Listening to the polar oceans

Monitoring and mapping marine ecosystems using passive and active acoustics

Sebastian Menze

Thesis for the degree of Philosophiae Doctor (PhD)
University of Bergen, Norway
2020

UNIVERSITY OF BERGEN

Listening to the polar oceans

Monitoring and mapping marine ecosystems using passive and active acoustics

Sebastian Menze

Thesis for the degree of Philosophiae Doctor (PhD)
at the University of Bergen

Date of defense: 12.06.2020

Year: 2020

Title: Listening to the polar oceans

Name: Sebastian Menze

Print: Skipnes Kommunikasjon / University of Bergen

Scientific environment

This PhD has been written at Institute of Marine Research (IMR), as part of the SI_ARCTIC project (Research Council of Norway grant 228896). The major part of this work was conducted at the IMR's oceanography and climate group in Bergen, with occasional stays at the University Centre of Svalbard and fieldwork onboard IMR's research vessels. The formal educational institution has been the Geophysical Institute at the University of Bergen. The two passive acoustic papers of this thesis are part of an ongoing collaboration with colleagues from the ocean acoustics departments of the Alfred Wegener Institute for Polar and Marine Research and the Woods Hole Oceanographic Institution.

Acknowledgements

I am genuinely thankful for the advice, support, opportunities and trust I received from my supervisors Randi B. Ingvaldsen and Peter M. Haugan. Thank you for the many motivating words, new perspectives and freedom to follow my ideas. I am looking forward to future projects already. I would also like to thank Jan Erik Stiansen and my colleagues at the oceanography and climate group at the IMR for three highly enjoyable years in a stimulating and balanced work environment. It would not have been the same without the many discussions, coffees and beers with my fellow PhD students Kjersti, Sigrid, Håvard and Marcos, thank you for going through the ups and downs of PhD life together with me. Special thanks also belong to Melissa Chierici, Anna Nikolopoulos and Martin Biuw for providing motivation, opportunities and feedback at just the right moments, and Elisabeth Jones, Angelika Renner and Midoli Goto for a great cruise to the Southern Ocean. I would also like to thank the crew onboard IMR's research vessels for their dedicated efforts for marine science and making us researchers feel at home onboard.

I thank Ilker Fer and Joachim Reuder for the guidance I received at the Geophysical Institute at the University of Bergen. Many thanks also belong to the place where my passion for ocean acoustics was ignited, the ocean acoustics group of the Alfred Wegener Institute. Thank you for all the fruitful discussions and feedback Olaf Boebel, Daniel P. Zitterbart and Ilse van Opzeeland.

So many people contributed to making this PhD possible, that I can name but a few. But the two that lay the foundations and supported me all the way were my parents Annelore and Horst. You always had my back, tolerated all my exotic ideas and encouraged me to find things out for myself, I am deeply grateful. My sister Sabine, Andreas and little Jonathan made life brighter with each visit, and greatly helped to charge my batteries for the final PhD months. The mountains and fjords of Norway became a source of energy and meaning for me, the many unforgettable tours with friends and the BSI friluft group contributed much to the growth of this PhD. I especially thank Carsten, Johan, Martin, Daniel and Achim for being solid partners on

the wall and in life, and Ryan, AK, Hugo, Tim, Felix, Henning, Ronja, Astrid, Steffi, Omar, Borgar, Karl and Haakon.

"The fact that whale and human music have so much in common even though our evolutionary paths have not intersected for 60 million years, suggests that music may predate humans--that rather than being the inventors of music, we are latecomers to the musical scene"

Gray, P., Krause, B., Atema, J., Payne, R., Krumhansl, C., Baptista, L. (2001). The Music of Nature and the Nature of Music. *Science*. 291(1). 52-54

Abstract

This interdisciplinary thesis uses active and passive acoustics to study the polar marine ecosystems. The polar oceans are some of the most remote, harshest and least well studied environments of the planet, and also the regions where climate change and the associated changes in marine ecosystems happen fastest. The four papers that comprise this thesis are based on acoustic data from moored and vessel-mounted instruments and cover different aspects of the Arctic and Antarctic marine ecosystems.

Vessel-mounted Acoustic Doppler Current Profiler (ADCP) data was used to map circulation patterns in the highly dynamical Fram Strait region. Such unstructured ADCP data is relatively seldom used in regional studies due to challenges associated with the interpretation of temporal and spatial variability. This was addressed by compiling a large data set, binning, different spatial interpolation methods and discussion of individual sections. The analysis showed that the Yermak Pass Branch can be as important as the Svalbard Branch in transporting Atlantic Water into the Arctic Ocean. The ADCP data was thereafter combined with vessel-mounted echosounder data and numerical modelling to investigate the impact of Atlantic Water circulation on plankton and fish distribution within four major troughs that cut into the Svalbard shelf. The Hinlopen Trough received the strongest and most direct Atlantic Water inflow and showed stronger acoustic backscatter from fish and zooplankton than the shelf, shelf break, and deep ocean. These results suggest that the balance between throughflow and retention creates favourable habitats in the trough for fish, benthic organisms and marine mammals.

Passive acoustic data was used to study the sources and seasonal variation of ambient sound in the deep Southern Ocean. Passive acoustic monitoring has the advantage of autonomously and non-invasively gathering data over large spatial and temporal scales. The Southern Ocean, one of the last acoustically pristine oceans due to its remoteness and lack of infrastructure, is particularly well suited for such studies. Recordings from two moored recorders showed that ambient sound levels were strongly affected by the sea ice cover and local wind stress. Sound produced by marine mammals formed

choruses that could be detected as population specific peaks in the long-term spectral averages. The temporal and spatial variation of these marine mammal choruses suggests seasonal patterns in migration and behaviour. A method to estimate the spatial distribution of acoustic sources (e.g. vocalizing animals) based on such chorus recordings was developed and tested, to resolve for marine mammal distribution and migration in ocean areas that are too large or remote to survey with traditional methods. Simulated annealing was used to estimate the distribution of acoustic sources on a geodesic grid, and the robustness of the method was tested with simulated scenarios using both drifting acoustic recorders (Argo floats) and a moored array as acoustic receivers. The results showed that inversion accuracy is only moderately reduced by inaccuracies in the sound propagation model. To then calculate the distribution of the vocalizing animals from the estimated acoustic source pressure distribution, the population specific call rates and source levels need to be considered.

The four papers that comprise this thesis showed how encompassing the whole spectrum of acoustical oceanography, from echosounder and ADCP surveys to the analysis of passive acoustic recordings, allows us to study marine ecosystems from different angles. The papers use both a bottom-up approach, by mapping ocean currents and their impact on plankton and fish distribution, and direct approach towards the highest trophic levels, by monitoring the acoustic presence of vocalizing marine mammals. This thesis suggests multiple approaches to use acoustics to observe the under-sampled polar oceans and shows how utilizing often overlooked features in acoustic data can enhance our understanding of sparsely observed processes in remote ocean areas.

List of Publications

1. Menze, S., Ingvaldsen, R. B., Haugan, P., Beszczynska-Moeller, A., Fer, I., Sundfjord, A., & Falk-Petersen, S. (2019). **Atlantic Water pathways along the north-western Svalbard shelf mapped using vessel-mounted current profilers**. *Journal of Geophysical Research: Oceans*, 124(3), pp.1699–1716, https://doi.org/10.1029/2018JC014299

2. Menze S., Nikolopoulos A., Hattermann T., Gjøsæter H., Albretsen J. and Ingvaldsen R. B. (2020) **Productive detours – comparing Atlantic Water inflow and acoustic backscatter in the major troughs along the Svalbard shelf** *submitted to Progress in Oceanography*

3. Menze, S., Zitterbart, D. P., van Opzeeland, I., & Boebel, O. (2017). **The influence of sea ice, wind speed and marine mammals on Southern Ocean ambient sound**. *Royal Society Open Science*, 4(1), 160370, https://doi.org/10.1098/rsos.160370

4. Menze, S., Zitterbart, D. P., Biuw, M., & Boebel, O. (2019). **Estimating the spatial distribution of vocalizing animals from ambient sound spectra using widely spaced recorder arrays and inverse modelling**. *The Journal of the Acoustical Society of America*, 146(6), 4699–4717. https://doi.org/10.1121/1.5139406

Contents

1. Introduction

The ocean is almost impenetrable for light and near transparent for sound, which is why many marine animals and oceanographic measurement technologies use sound to gather physical and ecological information. Acoustical instruments are non-invasive and can cover ranges far larger than optical and point-measuring in-situ sensors. Combined with autonomous moored, drifting or moving platforms they can provide year-round data from remote data-deficient regions. Acoustic sensing can be divided into two categories: active acoustics, probing the environment by emitting an acoustic signal and analysing the returning reflections, and passive acoustics, listening to the naturally occurring sound in an environment. Active acoustic sensing has most applications in fishery science (Godø et al., 2014) and physical oceanography (Gilcoto et al., 2009), whereas passive acoustic monitoring has mainly been used for naval applications and marine mammal science (Mellinger et al., 2007).

This interdisciplinary thesis uses both active and passive acoustics to study polar marine ecosystem from two sides of the marine food-web: bottom-up, mapping ocean currents and their impact on plankton and fish distribution, and directly from the top, monitoring the acoustic presence and distribution of marine mammals. Complex passive and active acoustic observational datasets are combined with hydrodynamic and acoustic ocean models to utilize often overlooked features of acoustic data from the polar oceans. Due to their remoteness, large scale and harsh climate, the polar oceans and ecosystems are challenging to observe with in-situ sensor, visual and catch based methods. They are also among the fastest warming oceans on the planet, rendering it important to maximize the information that can be obtained from the area's sparse acoustic observations.

The first part of this thesis focuses on active acoustic data and the bottom-up approach to ecosystem monitoring. Paper one presents data from Acoustic Doppler Current Profilers (ADCPs) and uses spatial interpolation techniques to map Atlantic Water (AW) circulation. Paper two combines backscatter data from ADCPs and echosounders

with numerical model simulations to investigate the impact of the AW circulation in troughs on the shelf ecosystem.

The second part of this thesis focuses on passive acoustic recordings. Paper three analyses a three-year time series of ocean ambient sound and discusses the temporal and spatial variation in the contribution of different physical and biological sources. Paper four presents a method of estimating the spatial distribution of sound sources (e.g. marine mammals) from ambient sound recordings by sparse hydrophone arrays, combining acoustic propagation models and computational parameter estimation. An illustration of a simplified marine ecosystem and the active and passive approach to acoustic ecosystem monitoring is shown in Figure 1. The four papers that comprise this thesis are located at their respective sides of the schematic food-web.

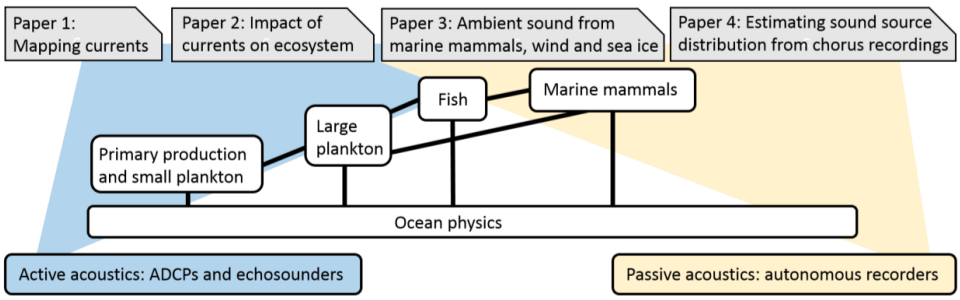

Figure 1: *Organization of the papers into an active and passive approach (blue and yellow fields) to acoustic ecosystem monitoring. A simplified model of a polar marine ecosystem is shown in the white boxes and short descriptions of the papers are given in the grey boxes.*

This synthesis is structured as follows: section 2 describes the scientific background, the study areas and gives an overview of previous research. Section 3 describes each paper's data, methods and research questions and section 4 contains summaries of the four papers. Section 5 discusses the major results and sets them in context with previous studies.

2. Scientific background

2.1 Physics of underwater sound

Whereas light and the major part of the electromagnetic spectrum are strongly attenuated over distances larger than ~10 m in seawater, sound waves are only weakly attenuated and propagate approximately four times faster in the ocean than the atmosphere. Marine mammal vocalizations or other loud signals below 1 kHz can be detected over hundreds of kilometres from the source (Dushaw & Menemenlis, 2014; Wang et al., 2016). This renders acoustic waves optimal to probe the marine environment but also makes for a very noisy acoustic environment due to the many sources of underwater ambient sound.

The propagation of soundwaves in the ocean depends on the sound speed profile, sea floor and surface properties and absorption. Absorption is an effect of the viscosity of water, chemical reactions (magnesium sulphate and boric acid ions) and heat loss (Lurton, 2002) and depends on frequency, temperature, salinity and depth. In addition to absorption, sound energy is also attenuated by reflection and refraction at the sea surface and sea floor. Since sound speed in the ocean is not constant but varies with density, acoustic waves can also be refracted and reflected inside the water column (Stranne et al., 2017). Minima in the ocean sound speed profile create waveguides (also termed sound channels or ducts) where acoustic waves are trapped in the channel due to the curvature of the sound speed profile. In tropical and mid-latitude oceans, a deep sound channel exists that allows soundwaves to propagate over large distances due to the reduced sea floor and surface interaction. In the polar oceans the sound speed minimum is found at the surface, generating upward refracting sound speed profiles. How far sound waves can propagate in this surface channel depends on the presence and properties of sea ice (Hope et al., 2017).

The propagation of sound waves can be modelled by solving the acoustic wave equation using varying approximations. One of the simplest models is geometrical spreading, where one assumes the wave propagates like an expanding sphere until it

reaches the seafloor and surface and then spreads as an expanding cylinder. It only incorporates absorption and energy loss due to the expanding wave front but is a good first approximation of the logarithmic transmission loss over distance curve (Lurton, 2002). A more sophisticated approach that also includes interference effects is to approximate the wave front with a set of plane waves that propagate along ray paths expanding from the source. This approach is termed raytracing and can include the effect of spatially variable seafloor, sound speed and sea surface properties (Porter, 1987; Porter & Liu, 1994). Other models use normal modes and parabolic equations to solve the acoustic wave equation (Abawi et al., 1997; Etter, 2009).

2.2 Active acoustic monitoring

Active acoustic sensing of ocean properties involves analysing the strength and frequency of reflected acoustic signals (echosounders) or the modification of acoustic signals between source and receiver (tomography). One of the first uses of acoustics for marine science was the development of the echosounder, or SONAR (sound navigation and ranging), to measure seafloor depth based on the travel time of the returning echo. This led to the discovery that sound is not only reflected off the seafloor, but also from fish and other marine organisms in the water column (Lurton, 2002). Modern sonar systems use multiple frequencies or broadband transducers, that allow for species classification of the scattering organisms (Korneliussen et al., 2016)

The strength of the backscatter varies with the signal's frequency. How much sound energy is reflected at which frequency depends on the shape and density of the scattering object, which can be described with the impulse response (returning signal strength over frequency or time). The Doppler frequency shift of the returning echo can be used to measure the speed and movement direction of the scattering objects. ADCPs use this effect and measure ocean current profiles using backscatter from passively drifting particles and organisms (Gilcoto et al., 2009). In addition to providing current profiles, the backscatter strength of ADCPs can also be used to study biomass and particle distribution in the water column (Berge et al., 2014; Gostiaux & van Haren, 2010; Griffiths, 2002).

These active acoustic technologies have the advantage of providing quantitative data with both absence and presence information, even if the study objects do not emit sound themselves. Calibrating the echosounders with reference spheres and determining the species composition (and size) of the scattering layers with targeted trawls, allows for biomass and species abundance estimates (Ona et al., 2009). Such combined acoustic and trawl surveys have become a common tool to estimate fish and zooplankton stock sizes (Simmonds & MacLennan, 2008) and study animal behaviour and movement (Berge et al., 2014; Godø et al., 2013; Kaartvedt et al., 2008). Active acoustic sensing is more range restricted than passive acoustic sensing, as echosounders and ADCPs can only sample between 10s and 1000s of meters range, depending on the signal frequency. Mounting echosounders and ADCPs to ships and moving platforms allows for the generation of transects and spatial data (Savidge & Amft, 2009), whereas mooring them to the sea floor or fixed structures generates useful time series (Beszczynska-Moller et al., 2012; Cisewski et al., 2010). Recent developments in source and receiver array and data processing technology allow to not only measure backscatter profiles underneath the ship but also within hundreds of km range around the receiver and source array (Gong et al., 2014; Makris et al., 2018; Wang et al., 2016). This ocean acoustic waveguide remote sensing method requires large towed source and receiver arrays. These could be more invasive than vessel-mounted echosounders since loud sounds in the hearing range of marine organisms are used (Risch et al., 2014).

2.3 Passive acoustic monitoring

Passive acoustic monitoring (PAM) is the recording and analysis of sound in an environment. The rise in affordable autonomous recording technologies and computing power to analyse large datasets increased the methods prevalence and effectiveness. One of the major advantages of this technology is its capacity to autonomously and non-invasively gather data over large spatial and temporal scales, independent of visual conditions. The sound in an environment is also termed the “soundscape” or “acoustic environment” and can be divided into physical, biological and anthropogenic sources (Krause & Farina, 2016; Pijanowski et al., 2011). Soundscapes consist of transient

sounds (e.g. animal vocalizations), and continuous sounds (e.g. traffic noise). The continuous part of the soundscape is often termed “ambient noise” or “acoustic background”. In this thesis the term “ambient sound” is used.

In the ocean, sound is generated by physical sources: sea surface motion (breaking waves, oscillating bubble clouds, etc.), seismic activity, sea and shelf ice; anthropogenic sources: shipping, seismic surveys and construction; and biological sources: marine mammals, fish and crustaceans (Carey & Evans, 2011; Wenz, 1962; Wilcock et al., 2014). The analysis of sound recordings can be split into two approaches, detecting, classifying and localizing transient signals or analysing the temporal and spatial variation in averaged ambient sound spectra (Au & Hastings, 2008). Analysis of the transient sound is useful to detect the presence and local acoustic activity of different sound sources, and even localize and track sound sources (Urazghildiiev & Clark, 2013). Combining acoustic cue detection with statistical methods such as distance sampling allows for abundance estimates of vocalizing species (Marques et al., 2013; Thomas & Marques, 2012). Analysis of the spectral shape and spatio-temporal variation of ambient sound can be used to study the sound generating processes behind it. The sound of marine mammal populations vocalizing over extended periods of time adds up to quasi-continuous “choruses” which create characteristic peaks in marine sound spectra (Nieukirk et al., 2012). These choruses show marked seasonal and spatial patterns (Leroy et al., 2018).

Ocean ambient sound is thought to increase in many ocean basins, mainly due to increased marine traffic and seismic surveys (Frisk, 2012; McDonald et al., 2008; Miksis-Olds et al., 2013). This has led to concerns about the impact of anthropogenic noise on marine mammals, as increasing anthropogenic noise levels can mask marine mammal communication and affect the animals behaviour, foraging and mating success (Clark et al., 2009; Tyack, 2008).

PAM can be realized using different technical approaches (Van Parijs et al., 2009). Many studies use autonomous recorders attached to oceanographic moorings or underwater structures and generate time series that can be compared for different

mooring sites (Mellinger et al., 2007). Another approach is to tow hydrophone arrays to study the spatial distribution of sound sources and use beamforming or triangulation to locate sound sources (Wang et al., 2016; Yack et al., 2013). Moored recorders in high latitude areas were used to show that some whales overwinter at high-latitude and migration patterns are more differentiated than previously thought (Magnúsdóttir & Lim, 2019; Van Opzeeland et al., 2013; Stafford et al., 2012).

The major drawback of PAM is that animals can only be detected when they are vocalizing, providing only presence but not absence data. The detectability of acoustic signals varies with time and space, due to variation in ambient sound, transmission loss between source and receiver, signal source level, shape and frequency and signal emission rate. These factors need to be taken into account when interpreting signal detection rates, especially when inferring source density and distribution from passive signal detection rates. Helble et al. (2013) showed that that the detectability of humpback vocalizations can vary by an order of magnitude.

Using careful analysis and interpretation, PAM is a powerful method to close observation gaps in areas that are challenging to survey otherwise. PAM is also used to quantify physical processes in remote regions, such as offshore precipitation (Nystuen et al., 2008), glacier calving (Pettit, 2012), sea ice deformation and earthquakes (Dziak et al., 2015).

2.4 The polar oceans

The Southern Ocean and the Arctic Ocean are both high-latitude, ice covered polar oceans, but different in several key aspects. The Arctic Ocean is encircled by land and covers a far smaller area than the vast Southern Ocean surrounding Antarctica. The only deep connection of the Arctic Ocean to the global ocean circulation is through the Fram Strait between Greenland and Svalbard. Thus, processes and changes occurring in Fram Strait are important locally as well as for the global climate system (Aagaard et al., 1985; Rudels et al., 2015). Figure 2 compares the bathymetry of the Arctic and Antarctic and highlights this thesis's study regions.

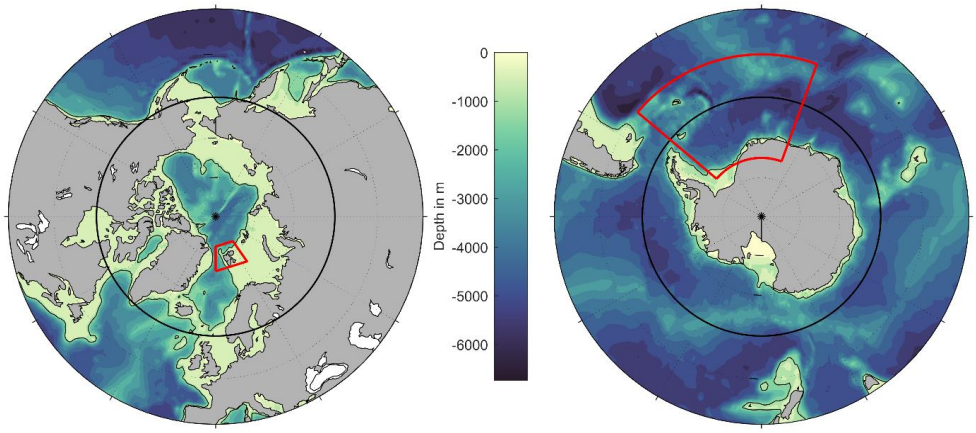

Figure 2: *Comparison of the bathymetry and size of the Arctic Ocean and Nordic seas (left panel) and Southern Ocean (right panel), from 40 to 90 °N/°S. Study regions of this thesis are encircled by red lines. The 0 and 1000 m isobath are marked with black contours, the thick black circles mark 60 °N/°S. The bathymetry was derived from the ETOPO1 dataset (Amante & Eakins, 2009).*

The Southern Ocean can be defined in multiple ways, but generally describes the Ocean surrounding Antarctica, south of approx. 60°S. Here the Atlantic, Pacific and Indian Ocean connect in complex circulation patterns. The air-sea gas exchange, water mass transformations and deep water formation occurring here strongly impact global climate (Marshall & Speer, 2012; Sabine et al., 2004). In comparison with the ocean north of 60°N whose area is ~50 % shallow (50–200 m) shelves (Bluhm et al., 2015), the Southern Ocean is several thousand meters deep with shorter and deeper (~500 m) shelves (Hunt et al., 2016). Whereas the Arctic sea ice cap consists of both first- and multi-year ice, sea ice in the Southern Ocean is generally first-year ice, meaning it only lasts for one winter. This results in different sea ice properties and dynamics, and different adaptations of the ice-dependent species (Gradinger, 1999; Spindler, 1990; Stammerjohn et al., 2012).

Both the Southern and Arctic Ocean ecosystems are undergoing rapid changes due to global warming and ocean acidification (Rhein et al., 2013). High latitude regions are experiencing the fastest climate change due to a combination of oceanic and

atmospheric feedback mechanisms that are termed polar amplification (Pithan & Mauritsen, 2014). The ongoing anthropogenic emission of greenhouse gases not only raises atmospheric temperature and moisture, but also impacts the oceanic heat content and circulation, global wind patterns, and significantly alters the global carbon cycle (Stocker et al., 2013). Half of the anthropogenic heat and CO_2 is absorbed by the oceans (Cheng et al., 2017; Resplandy et al., 2018; Sabine et al., 2004) resulting in an unprecedentedly fast ocean acidification, challenging the fitness and reproduction of many marine organisms, especially carbonate shell forming plankton (AMAP, 2013; Hönisch et al., 2012). The increased ocean temperature and acidity results in large-scale habitat shifts that threatens populations with geographical or other adaptation limitations, such as tropical coral reefs and sea ice dependent species in the Arctic (Hoegh-Guldberg & Bruno, 2010). It is thus of paramount importance to map and monitor the sensitive and fast changing polar oceans.

Such observations are mainly gathered with vessel-based surveys, mooring arrays and satellites. Despite the harsh climate, the relative closeness of the Arctic Ocean to harbours and settlements renders it better sampled than the vast and remote Southern Ocean, which is only sporadically surveyed and contains few mooring arrays compared to its size. Profiling Argo floats have greatly improved the remote area data coverage for temperature and salinity data and are increasingly capable of sampling the ice-covered waters of the Southern Ocean (Klatt et al., 2007). However, more complex observations of, e.g. ocean currents, chemical parameters or biological parameters like species abundance, distribution and behaviour remain sparse throughout most of the polar oceans. To fill this observational gap, novel platforms and sensors have been developed that can provide data autonomously, over longer timescales and larger areas. Examples are water- or air-borne autonomous vehicles, bio-geo-chemical and acoustic Argo floats, ice tethered platforms, long-lasting animal-borne tags, and autonomous sensors on moorings and vessels of opportunity. The following two sections summarize results from recent observational efforts and discuss the oceanography and ecology of the two study regions in more detail.

2.5 The Arctic Ocean and Svalbard region

Atlantic Water is a major source of heat, nutrients and organisms to the Arctic Ocean and is thus an important component of the global climate system (Bluhm et al., 2015). It flows into the Arctic Ocean via two major pathways: the Barents Sea, where it gets significantly cooled and modified (Smedsrud et al., 2013), and around Svalbard, where it transports the majority of heat into the Arctic Ocean (Pnyushkov et al., 2015). Figure 3 shows a schematic map of the AW circulation and gateways into the Arctic Ocean. AW enters the Arctic Ocean as a boundary current flowing around Svalbard, in Fram Strait this current is termed the West Spitsbergen Current (WSC). The WSC splits into three branches that partly reunite and continue as the Arctic Circumpolar Boundary Current (ACBC) north of Svalbard, where it transports AW around and into the Eurasian and American Basin (Aksenov et al., 2011; Crews et al., 2019; Koenig et al., 2017).

The flow through the two major Atlantic gateways is monitored by mooring arrays: one across the Barents Sea opening covering the AW inflow (Ingvaldsen et al., 2004) and one across Fram Strait monitoring AW inflow and Arctic Water outflow (Beszczynska-Moller et al., 2012). The ACBC is monitored with mooring arrays north of the Barents Sea, the Laptev Sea and in the Canada Basin (Pérez-Hernández et al., 2019; Pnyushkov et al., 2015; Renner et al., 2018). Mooring and survey data (Beszczynska-Moller et al., 2012) show warming of the AW inflow since monitoring started in 1997. Propagation of anomalously warm AW can be traced along the ACBC (Ivanov et al., 2012; Polyakov et al., 2011), warming the interior Arctic Ocean (Polyakov et al., 2013). As a result of this, the Arctic sea ice cover is not only melting due to increased atmospheric heat flux, but also increasing heat flux from the ocean (Carmack et al., 2015; Onarheim et al., 2014; Polyakov et al., 2017). Arctic sea ice extent and thickness are declining rapidly, and a complete loss of summer sea ice within this century is likely if greenhouse gas emissions continue unchanged (Serreze & Meier, 2019). North of Svalbard, heat from AW continues to diminish the sea ice cover even in winter (Onarheim et al., 2014).

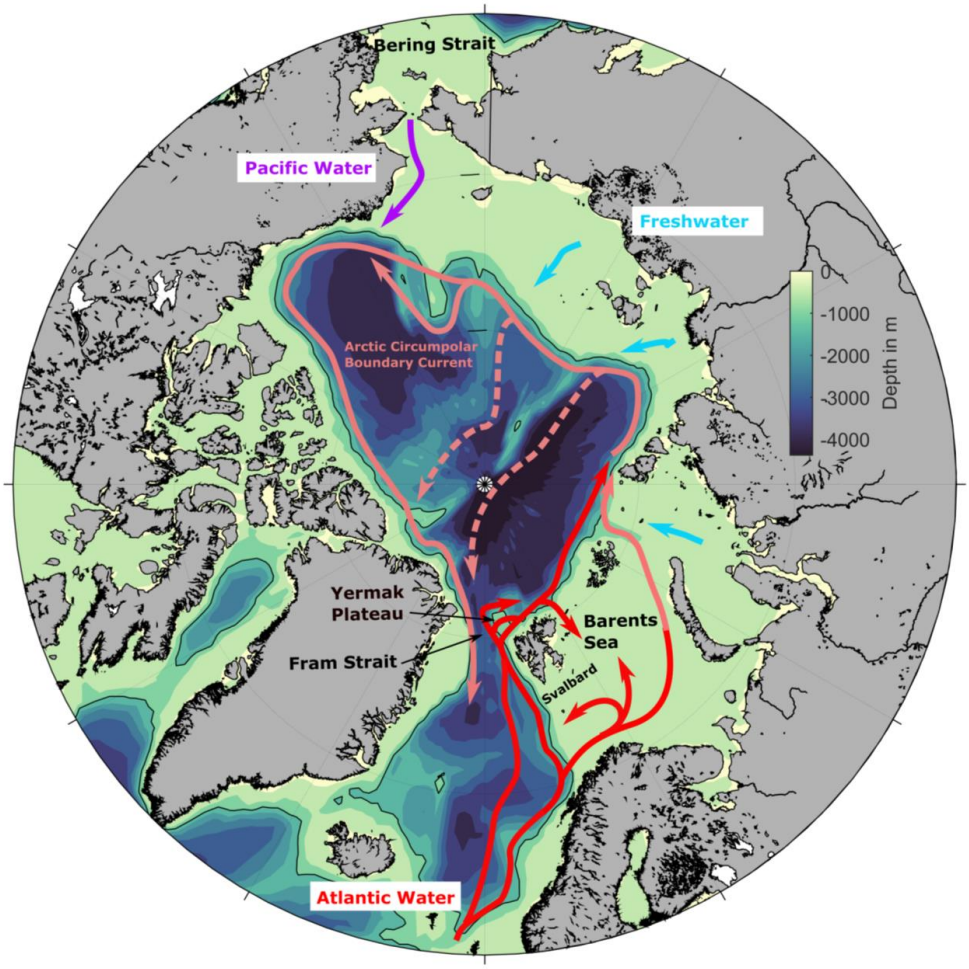

Figure 3: *Schematic map of inflow into the Arctic Ocean and the pathways of Atlantic Water. The 0 and 1000 m isobath are marked with black contours. The bathymetry was derived from the ETOPO1 dataset (Amante & Eakins, 2009).*

The warming of the AW inflow (Beszczynska-Moller et al., 2012; Walczowski et al., 2012) can be traced into the interior Arctic Ocean and contributes to sea ice loss. (Polyakov et al., 2017). The pathways AW takes into the Arctic and along the shelf are only roughly known from hydrographic sections, drifter and model studies (Cokelet et al., 2008; Gascard et al., 1995; Wekerle et al., 2017). Recent high-resolution models showed that considerable amounts of AW follow short pathways over the Yermak

Plateau into the Arctic instead of longer pathways around the plateau (Crews et al., 2019; Koenig et al., 2017). Detailed knowledge of the AW pathways is important to assess how much heat is lost to the atmosphere and surrounding water masses before the AW encounters sea ice. Due to the warming AW inflow and melting sea ice cover, the Barents Sea, Svalbard shelf and Arctic Ocean are experiencing increasing "Atlantification" i.e. a change from colder and stratified Arctic water masses to a warmer and less stratified water column (Lind et al., 2018; Polyakov et al., 2017).

The AW also carries nutrients, plankton and organisms northwards, extending the realm of boreal species into the Arctic (Hop et al., 2019). The circulation patterns in the Arctic have a strong impact on the distribution of drifting, as well as mobile and sessile species, that feed on advected organic matter or local primary production fuelled by advected nutrients (Hunt et al., 2016; Vernet et al., 2019; Wassmann et al., 2015; Wassmann et al., 2019). The increasing "Atlantification" along the Svalbard shelf and in the Barents Sea leads to habitat loss for Arctic species and habitat gain for Boreal/Atlantic species. Recent surveys found Atlantic blue mussels and Mackerel in Isfjorden (Berge et al., 2005, 2015), and annual large-scale surveys of the Barents Sea revealed a marked decrease of Arctic habitat and species and an increase in Boreal species (Fossheim et al., 2015), concurring with an observed change from bottom-dwelling benthivore fish to larger piscivorous fish (Frainer et al., 2017).

The shrinking sea ice cover shifts the ice edge further north-east and leads to a habitat decline for ice dependent species, such as ice algae, polar bears (Lone et al., 2018; Stern & Laidre, 2016) and ice-associated seals (Hamilton et al., 2015). The replacement of lipid-rich arctic plankton species with less lipid-rich boreal species is thought to affect predator-prey relationships and propagate within the food-web (Falk-Petersen et al., 2009; Mayzaud et al., 2016). The mismatch between species that depend on the shrinking sea ice cover off the shelf and their prey on the shelf and shelf break could further threaten the survival of ice-associated species (Hamilton et al., 2017).

In contrast, the sea ice decline opens new habitats for pelagic and boreal species, especially in areas where AW inflow of nutrients fuels the local primary production

(Randelhoff et al., 2018; Wassmann et al., 2015). Baleen whales are expected to migrate further north-east of Svalbard with decreasing sea ice cover due to favourable feeding conditions (Falk-Petersen et al., 2014). Marine mammal distribution around Svalbard corresponds well with topographically steered currents, fronts and tidewater glaciers (Storrie et al., 2018). Blue whales (among other species) were often sighted in the Isforden and Hinlopen trough area, where they likely feed on aggregations of zooplankton (Goldbogen et al., 2011). The reduction of sea ice along the Svalbard shelf and in the Barents Sea might benefit the endangered blue whale and fin and humpback whale populations, but threatens the already endangered ice-dependent walrus and bowhead whale populations (Węsławski et al., 2000). In addition to this habitat loss, the expected increase in marine traffic in an ice-free Arctic Ocean is a potential disturbance to endemic marine mammal populations (Gabriele et al., 2018; Halliday et al., 2017). Compared to the remote Southern Ocean, the North Atlantic and Arctic Ocean receive high levels of anthropogenic noise from marine traffic and seismic surveys (Ahonen et al., 2017; Haver et al., 2017; Van Parijs et al., 2009).

2.6 The Southern Ocean

The Southern Ocean is characterized by its deep shelves, large seasonal sea ice cover, strong winds and zonal circulation patterns. A map of the major circulation patterns and fronts in the Southern Ocean is shown in Figure 4. In this region, no landmasses block zonal flow around the planet in neither the atmosphere nor the ocean. Bands of strong westerly winds drive the earth's largest current system: the Antarctic circumpolar current (ACC). The frontal zones south (Antarctic Polar Front or Antarctic Convergence) and north (Sub-Antarctic Front) of the ACC efficiently act as boundaries for meridional water mass transport, isolating Antarctic water masses and ecosystems from the sub-Antarctic domain (Hunt et al., 2016). At the Antarctic Polar Front, cold Antarctic waters submerge below warmer Antarctic intermediate waters, creating a sharp sea surface temperature front. The Antarctic coastal current flows westward along the Antarctic coast, opposite to the ACC, and is driven by winds off the Antarctic continent. These winds also lead to the formation of large and stable polynyas where

the sea ice is pushed northwards. They are characterized by high primary production and are important habitats for marine mammals, as they provide both prey and access to air (Arrigo et al., 2015). The front between the coastal current and the ACC is termed the Antarctic divergence, a zonal band where North Atlantic Deep Water rises upwards and mixes with surface waters. In the Ross and Weddell Sea large gyres connect the coastal current and the ACC. Cold and saline bottom water formed near and underneath the ice shelves in this area, constitutes an important component of the global thermohaline circulation (Fahrbach et al., 1995).

The coastal currents transport numerous tabular icebergs (calved from Antarctica's vast ice shelves) into the Weddell Sea gyre, creating a northward iceberg drift that is often termed "Iceberg alley". The Antarctic sea ice cover is generally seasonal, with only small amounts of multi-year ice surviving the summer. The extent of the sea ice varies with the position of the Antarctic polar front from year to year (Hunt et al., 2016). No clear trend is discernible for Antarctic sea ice melt, as some regions are losing while others gain sea ice, which is likely related to the isolation of Antarctic waters as well as a change in freshwater and wind conditions (Stammerjohn et al., 2012). With continuing greenhouse gas emissions, sea ice extent is also expected to decline in the Antarctic (Stocker et al., 2013). Ocean acidification is another consequence of continued greenhouse gas emissions, as the Southern Ocean surface waters are projected to be aragonite undersaturated within 2100, stressing calcifying plankton (Bednaršek et al., 2012; Orr et al., 2005).

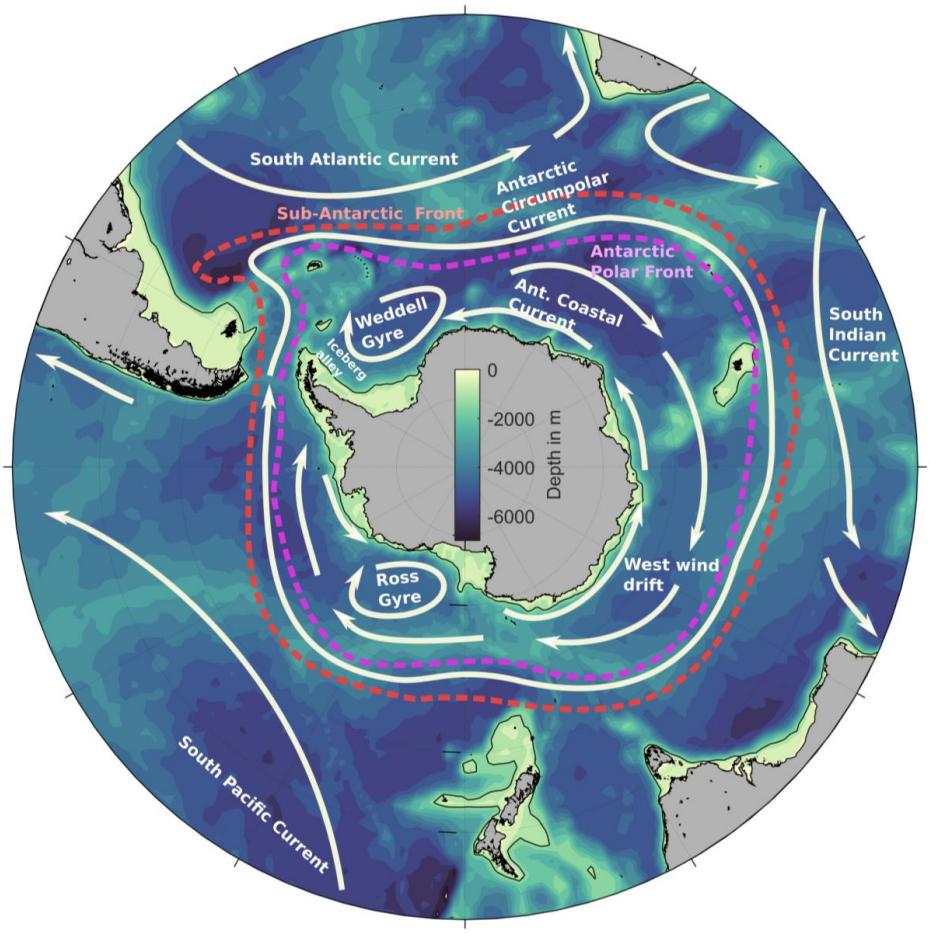

Figure 4: *Schematic map of the major currents and fronts in the Southern Ocean. The 0 and 1000 m isobath are marked with black contours. The bathymetry was derived from the ETOPO1 dataset (Amante & Eakins, 2009).*

The Southern Ocean is the habitat of approx. 50% of the world's marine mammals (in terms of biomass, Perrin et al. 2009) and contains one of the largest single-species biomasses on Earth: Antarctic krill (*Euphausia superba*). Antarctic krill is a key species for the Southern Ocean ecosystem, which is characterized by short food chains (plankton - krill - whale) but complex and dynamic food webs (Ainley et al., 2010). In contrast to the Arctic, Southern Ocean primary production is not primarily limited by the major nutrients nitrate and phosphate but mainly the trace element iron (Bakker et

al., 2002). Naturally occurring primary production (and corresponding aggregations of higher trophic levels) is highest in the coastal polynyas, the marginal ice zone, along the shelf and frontal areas where nutrient rich deep water reaches the surface (Arrigo et al., 2008; Nicol et al., 2000). The distribution of krill is less homogenous around Antarctica than for other zooplankton species. Approximately 70% of the stock is located in the Atlantic sector between the Antarctic Peninsula and the Scotia Sea (Atkinson et al., 2008; Siegel, 2005). Advection of krill towards the South Orkney islands and South Georgia is an important food source for the large marine mammal population in the Scotia Sea (Atkinson et al., 2008). Krill has been fished commercially on the shelves of the Scotia Sea since the 1970s (Nicol et al., 2012).

Dense aggregations of krill along oceanic fronts and topographic features or under the sea ice render lunge feeding of baleen whales extremely effective (Friedlaender et al., 2014; Goldbogen et al., 2007, 2011). These feeding grounds sustain large populations of baleen whales, most of which perform annual migrations between low-latitude breeding and high-latitude feeding grounds. Recent long-term PAM studies found that the migration patterns of humpback whales, and likely also other whales, is more differentiated than previously thought, as some whales overwinter in the coastal polynyas (Van Opzeeland et al., 2013). Contrary to blue, humpback and fin whales which avoid the sea ice cover, Antarctic minke whales are closely associated to the sea ice and feed of krill aggregations beneath the ice (Friedlaender et al., 2014; Herr et al., 2019; Kelly et al., 2014). They are frequently observed deep within the ice pack, surfacing in leads or breaking through thin ice.

Antarctic minke whales are the only Southern Ocean marine mammal species still subject to industrial whaling. Given the conflicts surrounding whaling of Antarctic minke whales, reliable data on this species distribution and abundance is needed. Visual surveys of Antarctic marine mammals are only possible in summer and require extensive funding to cover vast areas, and are thus only conducted every ~10 years (Williams et al., 2014). To cover the seasonal, interannual and spatial (within the sea ice) observation gaps, efforts to create a circum-Antarctic array of autonomous acoustic recorders are underway (Van Opzeeland et al., 2014).

3. This study

3.1 Research questions

The objective of this PhD thesis is to use acoustic methods to study polar marine ecosystems, with emphasis on utilizing features of passive and active acoustic data that are often neglected. Acoustic data can be challenging to interpret due to the size and complexity of the datasets, concurring spatio-temporal variability and many sources of sound in the ocean. This interdisciplinary thesis outlines a combination of approaches and methods to study polar marine ecosystem with different acoustic instruments, focusing on the research questions that are outlined below. The studies uses both a bottom-up approach and a direct approach towards the highest trophic levels. Figure 5 gives a visual overview of the topics and methods addressed in this thesis.

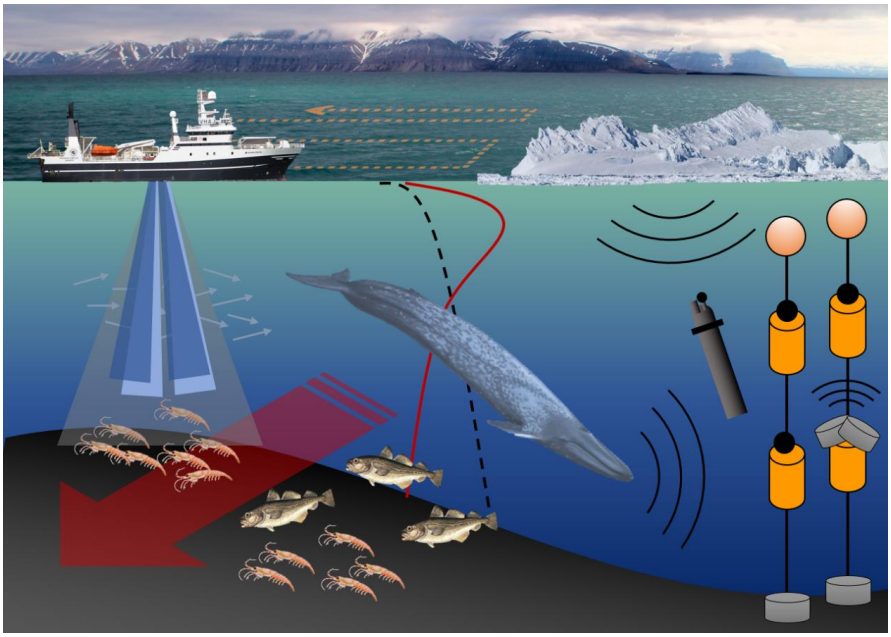

Figure 5: *Illustration of the research topics and methods covered in this thesis: vessel-mounted Acoustic Doppler Current Profilers and echosounders to measure ocean currents and backscatter are depicted on the left side, a typical polar sound speed*

(dashed line) and temperature (red line) profile in the middle and acoustic recorders in oceanographic moorings and an Argo float on the right side.

Can unstructured ADCP data reveal persistent circulation patterns and the pathways of AW along the Svalbard shelf? Even though AW flow into the Arctic is relatively well studied, few observations exist on the pathways that AW takes between the northern Fram Strait and the Nansen Basin. This can be investigated using vessel-mounted ADCP observations (shown as blue beams underneath the vessel in Figure 5), although this type of data is challenging to interpret as it contains both spatial and temporal variation and is fairly hetereogenous in space and time. Knowing the pathways AW takes around Svalbard impacts not only our understanding of local hydrography and ecology but is also useful to investigate the Arctic's heat and volume fluxes. In the first paper, a compilation of vessel-mounted ADCP observations was used to investigate the flow of AW west and north of Svalbard.

Are the spatial patterns in backscatter from zooplankton and fish recorded with echosounders and ADCPs along the Svalbard shelf linked to AW circulation? Analysis of the vessel-mounted ADCP data showed that a considerable amount of AW enters the trough systems along the Svalbard shelf. In these troughs, especially the Hinlopen Trough, backscatter values from zooplankton and fish are higher than in most other regions along the shelf. This could be related to topographically steered inflow of nutrients and organic matter with the AW (red arrow in Figure 5). In the second paper we addressed these issues evaluating observed backscatter and simulations with a high-resolution regional ocean model.

Which sound sources contribute to the Southern Ocean soundscape, and which spatial and temporal patterns can be identified using moored autonomous recorders? The sources and variability of ambient sound in the offshore Southern Ocean have not been comprehensively studied before. The Southern Ocean is a critical habitat for the endangered Antarctic Blue whales and other marine mammals, which rely on sound for communication, foraging and orientation. Studying the natural variability and spatio-temporal patterns of ambient sound encountered by Southern Ocean marine

mammals forms a useful baseline for comparative studies and future assessments. Another important motivation was to study marine mammal acoustic presence throughout the whole year, as almost no observational data exists on the distribution and behaviour of Southern Ocean marine mammals in winter. In addition, the scarcity of anthropogenic sound sources in Southern Ocean allows the study of undisturbed ambient sound. The third paper addresses these issues using long term recordings of the Southern Ocean soundscape. A schematic drawing of the moored recorders is shown on the right side of Figure 5.

How can the spatio-temporal patterns in animal choruses be used to study the distribution of vocalizing animals? The third paper documented that the Southern Ocean marine mammal choruses exhibit distinct spatio-temporal patterns. This stimulated the development of an inverse theory to estimate the distribution of vocalizing animals from the spatial variation in animal chorus intensity. Due to the Southern Oceans remoteness, size and harsh climate considerable uncertainty exists on the spatial distribution of marine mammals, especially in winter. The fourth paper presents and tests a method to estimate sound source (e.g. marine mammals) distribution year-round over ocean-basin scales that requires only sparse recorder arrays.

3.2 Data

This thesis is based on a wide spectrum of data from both observations and models. The first paper is based on vessel-mounted ADCP data gathered during 10 surveys in four consecutive summers (2014–2017), described in further detail in the paper. The bathymetry of the study area was extracted from the IBCAO dataset (Jakobsson et al., 2012).

The second paper is based on backscatter data from organisms using ADCP and echosounder data from 6 summer surveys with RV Helmer Hanssen from 2014 to 2019. Parts of the ADCP dataset were also used in the first paper, but then for investigating the ocean currents. The backscatter observations were compared to circulation and

inflow timeseries derived from existing model fields from an eddy-permitting high-resolution Regional Ocean Modelling System (ROMS) named S800 (Crews et al., 2018, 2019; Hattermann et al., 2016). The backscatter profiles were also compared to particle tracks simulated with the TRACMASS algorithm (Döös, 1995) using the S800 model fields. The S800 model horizontal grid size is 800m x 800m and it has terrain following vertical coordinates. The S800 model was run for the years 2007 to 2010 and was forced using atmospheric reanalysis data and modelled freshwater discharge from glaciers (Hattermann et al., 2016).

The third paper is based on data from underwater recorders from March 2008 to December 2010. The moorings were part of the Alfred Wegener Institutes oceanographic mooring array along the Greenwich meridian and in the Weddell Sea, whose data is available at the PANGEA repository (https://www.pangaea.de/). We compared the acoustic recordings to wind speed values extracted from the European Centre for Medium-Range Weather Forecasts (ECMWF) global ERA-Interim reanalysis dataset (Dee et al., 2011). To compare ambient sound and sea ice we used remote sensing data from the Advanced Microwave Scanning Radiometer Earth Observing System (AMSR- E, Spreen et al. 2008).

The fourth paper is purely methodological and uses simulated scenarios to test the new inverse method. To set up the simulations and model underwater sound propagation we used ETOPO-1 bathymetry (Amante & Eakins, 2009) and sound speed profiles from the World Ocean Atlas mean annual climatology (Dushaw et al., 2013).

3.3 Methods

This section contains short summaries of the methods applied in the four papers. Complete descriptions of the methods can be found in each paper.

For paper one, the raw ADCP data was post-processed and averaged into 5-min temporal bins and 5-m depth bins. Misalignment of current vectors was removed, and acoustic interference with the sea floor, CTD cable, nets, and due to ringing was semi-automatically removed from the data set using the ADCP editing program gautoedit.

Spatial and temporal binning and spatial interpolation were used to analyse the scattered ADCP data. We interpolated regular latitude-longitude style current vector grids from the scattered observations using objective mapping (Bretherton et al., 1976; Gandin, 1966) and divergence free radial basis functions (Vennell & Beatson, 2009). Objective mapping uses the observations' autocorrelation to fit a weight function, and then calculates regular grid values by weighted averaging over the nearby observations. When using a Gaussian weight function to interpolate the u (north-south) and v (east-west) components separately, the strongest features in the dataset are enhanced but the interpolated current field is not volume conserving. To interpolate current fields from scattered observations that are also volume conversing we used divergence free radial basis functions, an approach that combines function approximation with the conservation equations (MacMahan et al., 2012).

In the second paper, echosounder and ADCP backscatter was converted to the Nautical Area Scattering Coefficient and compared to the hydrodynamic simulations. Multi-frequency scrutinization and target strength analysis of the echosounder data were conducted with the Large Scale Survey System (LSSS) post-processing system (Korneliussen et al., 2006; Korneliussen et al., 2016). For this study the target categories were collected into drifting organisms (plankton, young-of-the-year fishes and mesopelagic fishes) and all larger fishes (not drifting with the ocean currents). The AW inflow and recirculation in the four major troughs along the Svalbard shelf were characterized using existing S800 model fields. AW Transport time series were compared to the principal components of current velocity from across-trough sections. Particle tracking was used to investigate the connectivity between the upstream shelf-break and the troughs.

Paper three compares ambient sound spectra and timeseries with local sea ice concentration and wind speed, using time series analysis. Time series of marine mammal chorus amplitude were calculated from the recordings by subtracting fitted spectra from the averaged ambient sound spectra in each chorus frequency band.

Paper four describes how these chorus time series can be used to estimate the distribution of sound sources (i.e. vocalizing animals) using an approach derived from geophysical inverse theory (Tarantola, 2005). This method was initially developed in the authors MSc thesis (Menze, 2015), but was refined during the PhD period. The simulations, analysis and interpretation of the test scenarios were produced during the PhD period. The estimation method comprises of a forward model to simulate the transmission loss between possible source locations and the recorder array and a parameter estimation algorithm that searches the source distribution creating the least misfit between the observed and modelled chorus levels. Two propagation models were successfully implemented in the forward model: geometrical spreading and the ray trace model BELLHOP (Porter, 1987). The distribution of sound sources on a geodesic grid was then estimated by using a "simulated annealing" numerical optimization algorithm.

4. Summary of papers

4.1 Paper 1: Atlantic Water pathways along the north-western Svalbard shelf mapped using vessel-mounted current profilers

A large amount of warm AW enters the Arctic as a boundary current through Fram Strait (in the WSC) and is the major oceanic heat source to the Arctic Ocean. This inflow is an important parameter of the climate system and for the Arctic ecosystems. It is monitored by an array of moorings and annual surveys in Fram Strait, but few observations exist of AW pathways north of Fram Strait. We mapped the circulation patterns and AW pathways around Svalbard using vessel-mounted ADCP data from 10 surveys during 4 consecutive summers (2014-2017). Despite the heterogenous nature of this compiled data set, persistent circulation patterns could be discerned.

The scattered ADCP data were interpolated onto a regular grid using objective mapping (which highlighted the dataset's dominant features but using correlation functions that were not volume conserving) and with divergence free radial basis functions (that are volume conserving). Both interpolations agreed well with each other and showed a meandering boundary current west of Svalbard and a more homogeneous AW flow, centred around the 1000 m isobath north of Svalbard. Along the north-western Svalbard shelf, the WSC splits into the shallow Svalbard Branch, the Yermak Branch that follows the slope of the Yermak Plateau, and the Yermak Pass Branch flowing across the plateau. In all summers, we observed a northward jet between 79 and 80 °N and the 1000 and 500 m isobaths, before the WSC divided into the three branches. North of Svalbard, the shallow Svalbard Branch reunited with the Yermak Pass Branch between 10 and 15 °E and a part of the AW circulated within Hinlopen Trough. The calculated volume transport around Svalbard of 2 Sv in the upper 500 m compares well with model results and previous observations. Our results show that the Yermak Pass Branch can be as important as the Svalbard Branch in transporting AW across the Yermak Plateau during summer, matching recent modelling studies.

4.2 Paper 2: Productive detours – comparing Atlantic Water inflow and acoustic backscatter in the major troughs along the Svalbard shelf

In this paper we evaluated AW circulation and acoustic backscatter along the north-western Svalbard shelf to study the impact of topographically steered trough currents on local ecology, focusing on the four largest trough systems: the Isfjorden, Kongsfjorden, Hinlopen and Kvitøya troughs. The Svalbard shelf is a transition zone between Boreal, Arctic and coastal ecosystems that is experiencing rapid warming and sea ice loss, and habitat loss for Arctic and habitat gain for Atlantic species.

We compared backscatter data from vessel-mounted echosounders with data from Acoustic Doppler Current Profilers and evaluated the results towards circulation from a high-resolution regional ocean model. Compared to the shelf, shelf break and deep ocean, average backscatter was strongest in the troughs, especially data from Hinlopen Trough showed strong average backscatter in both the demersal and surface layer.

All four troughs experience topographically steered recirculation (in-and-outflow) of AW, with more pronounced seasonality (strongest in winter) west than north of Svalbard. The Hinlopen and Isfjorden troughs receive the strongest AW inflow. Particle tracking showed that the Hinlopen Trough receives direct inflow from the AW boundary current, whereas the Isfjorden and Kongsfjorden trough mainly receive inflow from shelf and upper shelf break. The troughs showed retention inside the recirculation patterns, and this balance between throughflow and retention likely creates favourable feeding habitats in the troughs for fish, benthic organisms and marine mammals. We suggest that the recirculating flow increases acoustic backscatter in the troughs and attracts fish and other predators through three mechanisms: an increase in local production through the advection of nutrients and phytoplankton, direct advection of zooplankton, and retention of organisms inside the troughs.

4.3 Paper 3: The influence of sea ice, wind speed and marine mammals on Southern Ocean ambient sound

This paper describes the natural variability of ambient sound in the Atlantic sector of the Southern Ocean. This is an acoustically pristine ocean area due to its large distance to sources of anthropogenic noise (shipping and seismic surveys) and thus ideal to gather baseline data and study the natural variation of ambient sound in relation to sea ice, sea state and marine mammal vocalizations. Over a three-year period, two autonomous recorders were moored along the Greenwich meridian (66 and 69 °S) to collect underwater passive acoustic data, which was compared to sea ice and wind speed time series.

We found that ambient sound levels were strongly affected by the seasonal variation of the sea ice cover, which dampens sea surface motion caused by wind and waves. This results in low correlation between local wind speed and sound levels during austral winter. With increasing sea ice concentration, area and thickness, sound levels decreased while the relative contribution of distant sources increased. We found a robust correlation between local wind speed and ambient sound above 500 Hz under open ocean conditions in austral summer.

Marine mammal sounds formed a substantial part of the overall acoustic environment, comprising calls produced by Antarctic blue whales (*Balaenoptera musculus intermedia*), fin whales (*Balaenoptera physalus*), Antarctic minke whales (*Balaenoptera bonaerensis*) and leopard seals (*Hydrurga leptonyx*). The combined sound energy of a group or population vocalizing during extended periods formed species specific choruses that contributed specific peaks to the ambient sound spectra. The Antarctic minke whale chorus was loudest during austral winter and repeatedly showed a diel pattern that coincided with the diel vertical migration of zooplankton. The Antarctic blue and fin whale contributions were loudest in austral autumn and the leopard seal chorus only audible from December to mid-January. The temporal and spatial variation of these marine mammal choruses suggests seasonal patterns in

migration and/or calling behaviour. When controlling for variation in behaviour and sound propagation these signals could be used to study the distribution and/or migration of the vocalizing animals.

4.4 Paper 4: Estimating the spatial distribution of vocalizing animals from ambient sound spectra using widely spaced recorder arrays and inverse modelling

In paper three we described the spatial and temporal patterns in the choruses of four marine mammal species in the Southern Ocean. In this paper we present a method to estimate the distribution of sound sources (i.e. vocalizing animals) from such chorus recordings and test the method with a set of simulated scenarios. This is an approach to resolve for the spatial distribution of vocalizing marine mammals with very sparse unsynchronized arrays in ocean areas that are too large or remote to survey with traditional methods. This method was initially developed in the authors MSc thesis (Menze, 2015), but was refined during the PhD period. The simulations, analysis and interpretation of the test scenarios were produced during the PhD period.

The challenge with interpreting the spatial and temporal patterns in marine mammal choruses is that a higher chorus level does not imply a higher density of animals, due to the nonlinearity of underwater sound propagation and the large and unknown number and location of sources involved. For a given location, increased chorus level can be caused by a combination of processes: an increase in number of vocalizing animals, increase in source level, increase in call rate, decreasing distance to the vocalizing animals or decreasing transmission loss between the vocalizing animals and the recorder. We address these issues using methods from Bayesian geophysical inverse theory to estimate the distribution of sound sources that would generate the observed set of chorus recordings.

To solve this under-determined inverse problem, we used simulated annealing to estimate the distribution of acoustic sources (i.e. vocalizing marine mammals) on a geodesic grid. Employing a sound propagation model, the approach included calculating a transmission loss matrix, which connects all grid nodes and recorders. Two propagation models were successfully implemented: geometrical spreading and the ray trace model BELLHOP.

The robustness of the proposed method was tested in a modelling study with simulated marine mammal distributions in the Atlantic sector of Southern Ocean using both drifting acoustic recorders (Argo floats) and a moored array as acoustic receivers. The results show that inversion accuracy mainly depends on the number and location of the recorders and correlates with the entropy of the estimated source distribution. Tests with different transmission loss models indicated that inversion accuracy is affected only moderately by inevitable inaccuracies in transmission loss models. The presented method can be applied to marine mammal choruses, but also to other problems involving a large number of signal sources that can be observed by a sparse array of receivers, such as bird, fish, crustacean and insect choruses. Once a sufficient number of recorders is recovered from the mooring array in the Southern Ocean, the chorus inversion method could be applied to these recordings.

5. Discussion and Outlook

This thesis connects the fields of physical oceanography, ocean acoustics, marine ecosystem and marine mammal science and shows how acoustic sensing and advanced data analysis can be used to study polar marine ecosystems from both the basis and the top of the food-web. The active acoustic approach led to the mapping of circulation patterns that influence marine ecosystems (paper one) and investigation into the connection between these currents and fish and plankton backscatter in troughs along the shelf (paper two). The passive acoustic approach led to time series of marine mammal acoustic presence (paper three) and the development and testing of an inverse method to estimate the spatial distribution of the vocalizing animals (paper four).

The datasets that form the basis of the presented papers are large, noisy and complex, but they also contain unique information that could be extracted with careful analysis. Unstructured along-track ADCP data with few distinct transect lines are seldomly utilized, yet paper one demonstrates that useful current maps can be created with proper processing and interpolation. This ADCP dataset could also be used in a second way, as paper two demonstrates that also the backscatter data from vessel-mounted ADCPs provides meaningful information. Paper three and four demonstrate that what is often considered background noise in under water recordings, contains information on the recording location's sea-surface-motion and marine mammal presence, behaviour and distribution.

Paper one shows that the analysis of sparse ADCP data can give robust transport estimates and circulation maps. The transport estimate of 2 Sv of AW flowing around Svalbard agrees well with other studies (Koenig et al., 2017; Pérez-Hernández et al., 2017, 2019; Wekerle et al., 2017). The ADCP data confirmed that the Yermak Pass Branch is an important pathway of AW into the Arctic. The Svalbard Branch and Yermak Branch have been observed frequently (Aagaard et al., 1987) but few observations existed of the Yermak Pass Branch before this study. It has previously only been observed by two acoustically tracked floats (Gascard et al., 1995) and in model simulations (Crews et al., 2019; Koenig et al., 2017; Wekerle et al., 2017). Even

though most modern research vessels are equipped with ADCPs, not all research expeditions make use of the ADCP data. Paper three demonstrated that the compilation of large ADCP datasets from multiple surveys and "vessels of opportunity" can provide relevant insights into regional circulation patterns. This demonstrates the value of collecting underway survey data even if it is not analysed immediately. Increasingly, such ADCP and other survey data is stored into open repositories for later use and analysis, enhancing the potential for future studies.

The compiled ADCP data also suggested that AW enters the Hinlopen Trough on the western side and exits on the eastern side, transporting heat, organic matter and nutrients into the trough. To investigate whether this could benefit the local ecosystem, spatial patterns in backscatter observations from ADCPs and echosounders were compared to high-resolution ocean model results. Average backscatter was higher in the investigated troughs than on the shelf, the shelf break and in the deep ocean. Especially the Hinlopen Trough exhibited high backscatter values from fish in the demersal and plankton in the surface layer. Although all four troughs experienced topographically steered in- and out-flow of AW, the Hinlopen Trough received the strongest and most direct inflow of AW from the boundary current. The balance between AW in- and out-flow and retention in the troughs likely renders them a favourable habitat for both sessile and mobile species and forms a steady organic matter supply for the benthos (Meyer et al., 2015). It can be expected that the trough ecosystems will become even more "Atlantic" with the ongoing warming of the AW inflow and sea ice reduction, extending the Atlantic domain all the way north-east of Svalbard (Fossheim et al., 2015; Polyakov et al., 2017; Vihtakari et al., 2018). The topographically steered in- and out-flow currents are likely varying with the AW volume transport, which has remained relatively stable since observations started in 1997 (Beszczynska-Moller et al., 2012; Nilsen et al., 2016). Model studies that cover several decades, not just the 4 years of S800 data analysed in paper four, could be used to investigate whether the AW inflow into the troughs is changing with global warming.

The increasing atmospheric and oceanic warming in the Arctic reduces the sea ice cover, which changes not only the distribution of species but also marine traffic, fishing and resource extraction. PAM studies in the Arctic showed a near continuous presence of noise from seismic surveys, especially in summer and fall (Ahonen et al., 2017; Moore et al., 2012). With the decreasing ice cover, marine traffic and industrial activity in the Arctic are expected to significantly increase, especially when the North-East passage between Europe and Asia becomes ice-free (Smith & Stephenson, 2013).

In contrast to the anthropogenic sound present in the Arctic (Ahonen et al., 2017; Haver et al., 2017; Moore et al., 2012), the Southern Ocean acoustic environment remains almost acoustically pristine and is a prime location to study the natural variation of ocean ambient sound. The recordings presented in paper three showed that wind stress, sea ice and marine mammals are the major contributors to ambient sound between 10 and 1000 Hz in the offshore areas of the Southern Ocean. Southern Ocean ambient sound is strongly connected to the annual cycle: sea-surface-generated sound decreased with growing sea-ice concentration, thickness and extent, and marine mammal vocal activity followed annually reoccurring patterns. The dataset provided insight into both physical (sea surface motion and sea ice deformation) and biological (marine mammal vocal activity) processes.

The detection and analysis of transient vocalizations is a reliable method to study the acoustic presence and behaviour of vocalizing marine mammals within the detection range of the recorder, i.e. the distance to the recorder where an incoming signal is still discernible and not masked by the ambient sound (Mellinger et al., 2007). In this thesis, paper three and four show that also the analysis of the ambient sound itself is a powerful tool to study marine mammals. The detection range of transient sounds (vocalizations) varies strongly with ambient sound, signal amplitude and frequency, and transmission loss between the source and receiver (Helble et al., 2013), but is roughly between 20 to 150 km for blue whales in the Southern Ocean (Samaran et al., 2010). In contrast, ambient sound is a combined acoustic signal that is integrated over a far larger area, up to thousands of kilometres away from the recorder (Carey & Evans, 2011; Chapp et al., 2005). The analysis of ambient sound is an efficient method to study prevalent acoustic

events over ocean basin scales, such as noise from sea surface motion or choruses from large groups of vocalizing animals (groups large enough to produce a chorus that is louder than the ambient sound from other sources in the area).

Marine mammal choruses have not only been observed in the Southern Ocean, but also from fin whales in the Mid and North Atlantic (Nieukirk et al., 2012), fin and blue whales in the North Pacific (Burtenshaw et al., 2004; Curtis et al., 1999) and Indian Ocean (Leroy et al., 2018), Pygmy blue and Antarctic blue whales around Australia (McCauley et al., 2018), and fin and possibly bowhead whales in the Arctic (Ahonen et al., 2017). Similar to the choruses recorded in the Southern Ocean, the temporal and spatial variation of these choruses suggests seasonal patterns in marine mammal distribution (migration) and/or behaviour.

Tests with simulated scenarios in paper four showed that it is possible to resolve for marine mammal spatial distribution from such chorus recordings, despite the under-determinedness of this inverse problem. The scenarios demonstrated that the inversion accuracy depends on both the number of recorders and their placement in relation to gradients in the chorus sound field. The test scenarios indicated that the accuracy of the estimates is only moderately affected by inaccuracies in the underwater sound propagation model. These simulations were an important first step for developing and towards applying the inverse method to real chorus recordings. The inverse method could alleviate the large knowledge gaps concerning Southern Ocean marine mammal distribution and migration. This is especially relevant for the critically endangered Antarctic blue whales (Cooke, 2018) and for Antarctic minke whales that partially reside within the sea ice, which hampers visual survey efforts (Herr et al., 2019; Williams et al., 2014). Calculating reliable abundance estimates from acoustic recordings requires improved knowledge of the acoustic behaviour of the observed population, i.e. how often and loud the animals vocalize, and how this varies with the seasons and individuals within the populations. Such information could be gathered using acoustic tags and small-scale hydrophone arrays that can resolve for sound source location and source level. The observed connection between Antarctic minke whale calling behaviour and the diel vertical migration of krill points to a connection between

feeding and calling behaviour, that has also been observed for northern minke whales (Risch et al., 2013). Thus, PAM could potentially not only be used to monitor and map Antarctic minke whale presence but also their feeding on aggregations of krill. The decrease in recorder price and increase in battery and memory capacity render it possible to deploy moored arrays with enough recorders for chorus inversion. Such a large-scale mooring array is currently under development in the Southern Ocean (Van Opzeeland et al., 2014). Once a sufficient number of concurrent recordings is available, the inversion method could be applied to data from this array. Paper number four is a first exploration of using marine mammal chorus recordings to study marine mammal distribution. Future research is planned to optimize the method and to integrate it with established statistical methods to obtain estimates with confidence intervals.

The simulations in paper four also show that Argo floats can be a useful platform to record ambient sound and estimate sound source distribution. Argo floats are autonomously profiling measurement platforms that drift passively with ocean currents to measure ocean temperature, salinity and other biogeochemical parameters (Argo, 2018). They greatly enhanced data coverage in remote ocean regions and are a major part of the global ocean observation system to monitor climate change (Riser et al., 2016). They could prove to be a more cost-effective solution than large-scale passive acoustic mooring arrays, that require extensive ship time for mooring deployment and recovery. Argo floats with hydrophones have already been developed and used to track beaked whales (Matsumoto et al., 2013), study ambient sound and precipitation (Nystuen et al., 2011) and track floats under sea ice (Klatt et al., 2007). To be able to receive data from the floats via the Iridium or Argos network, the recordings need to be processed onboard the float, so that only averaged spectra and acoustic detections need to be transmitted. If today's ~3000 Argo floats would also monitor ocean ambient sound, the distribution and migration of frequently vocalizing fin and blue whales could be monitored in near-real time. Such a large-scale ambient sound dataset could also be useful to study precipitation, air-sea-gas exchange and anthropogenic noise in the open ocean (Nystuen et al., 2011, 2008). Acoustic Argo floats could be interdisciplinary measurement platforms to study marine ecosystems both from the bottom (physical

oceanography and primary production) and from the top, by recording sound from vocalizing marine mammals.

The four papers that comprise this thesis showed how encompassing the whole spectrum of acoustical oceanography, from echosounder and ADCP surveys to the analysis of passive acoustic recordings, allows us to study marine ecosystems from different angles. This thesis suggests multiple approaches to use acoustics to observe the under-sampled polar oceans and could show how utilizing often overlooked features in acoustic data can enhance our understanding of sparsely observed processes in remote ocean areas.

6. References

Aagaard, K., Swift, J. H., & Carmack, E. C. (1985). Thermohaline circulation in the Arctic Mediterranean Seas. *Journal of Geophysical Research*, *90*(C3), 4833. https://doi.org/10.1029/JC090iC03p04833

Aagaard, K., Foldvik, A., & Hillman, S. R. (1987). The West Spitsbergen Current: Disposition and water mass transformation. *Journal of Geophysical Research: Oceans*, *92*(C4), 3778–3784. https://doi.org/10.1029/JC092iC04p03778

Abawi, A. T., Kuperman, W. A., & Collins, M. D. (1997). The coupled mode parabolic equation. *J. Acoust. Soc. Am.*, *102*(1), 233–238. https://doi.org/10.1121/1.419819

Ahonen, H., Stafford, K. M., de Steur, L., Lydersen, C., Wiig, Ø., & Kovacs, K. M. (2017). The underwater soundscape in western Fram Strait: Breeding ground of Spitsbergen's endangered bowhead whales. *Marine Pollution Bulletin*, *123*(1–2), 97–112. https://doi.org/10.1016/j.marpolbul.2017.09.019

Ainley, D., Ballard, G., Blight, L. K., Ackley, S., Emslie, S. D., Lescroël, A., et al. (2010). Impacts of cetaceans on the structure of Southern Ocean food webs. *Marine Mammal Science*, *26*(2), 482–498. https://doi.org/10.1111/j.1748-7692.2009.00337.x

Aksenov, Y., Ivanov, V. V., Nurser, A. J. G., Bacon, S., Polyakov, I. V., Coward, A. C., et al. (2011). The arctic circumpolar boundary current. *Journal of Geophysical Research: Oceans*, *116*(9). https://doi.org/10.1029/2010JC006637

Amante, C., & Eakins, B. W. (2009). ETOPO1 1 Arc-Minute Global Relief Model: Procedures, Data Sources and Analysis. *NOAA Technical Memorandum NESDIS NGDC-24, National Geophysical Data Center, NOAA*. https://doi.org/10.7289/V5C8276M

AMAP. (2013). *AMAP Assessment 2013: Arctic Ocean Acidification*. Oslo, Norway: Arctic Monitoring and Assessment Programme (AMAP).

Argo. (2018). Argo float data and metadata from Global Data Assembly Centre (Argo GDAC). SEANOE. https://doi.org/10.17882/42182

Arrigo, K. R., van Dijken, G. L., & Bushinsky, S. (2008). Primary production in the Southern Ocean, 1997-2006. *Journal of Geophysical Research: Oceans*, *113*(8), 1997–2006. https://doi.org/10.1029/2007JC004551

Arrigo, K. R., van Dijken, G. L., & Strong, A. L. (2015). Environmental controls of marine productivity hot spots around Antarctica. *Journal of Geophysical Research: Oceans*, *120*(8), 5545–5565. https://doi.org/10.1002/2015JC010888

Atkinson, A., Siegel, V., Pakhomov, E. A., Rothery, P., Loeb, V., Ross, R. M., et al. (2008). Oceanic circumpolar habitats of Antarctic krill. *Marine Ecology Progress Series*, *362*, 1–23. https://doi.org/10.3354/meps07498

Au, W. W. L., & Hastings, M. C. (2008). *Principles of Marine Bioacoustics*. New York, NY: Springer US. https://doi.org/10.1007/978-0-387-78365-9

Bakker, D. C. E., Zeldis, J., Law, C. S., Abraham, E. R., Safi, K., Jameson, G., et al. (2002). A mesoscale phytoplankton bloom in the polar Southern Ocean stimulated by iron fertilization. *Nature*, *407*(October), 695–702. https://doi.org/10.1038/35037500

Bednaršek, N., Tarling, G. A., Bakker, D. C. E., Fielding, S., Jones, E. M., Venables,

H. J., et al. (2012). Extensive dissolution of live pteropods in the Southern Ocean. *Nature Geoscience*, *5*(12), 881–885. https://doi.org/10.1038/ngeo1635

Berge, J, Johnsen, G., Nilsen, F., Gulliksen, B., & Slagstad, D. (2005). Ocean temperature oscillations enable reappearance of blue mussels Mytilus edulis in Svalbard after a 1000 year absence. *Marine Ecology Progress Series*, *303*, 167–175. https://doi.org/10.3354/meps303167

Berge, J, Heggland, K., Lønne, O. J., Cottier, F., Hop, H., Heggland, K., et al. (2015). First Records of Atlantic Mackerel (Scomber scombrus) from the Svalbard Archipelago , Norway , with Possible Explanations for the Extensions of Its Distribution. *Arctic Institute of North America*, *68*(1), 54–61.

Berge, Jørgen, Cottier, F., Varpe, Ø., Renaud, P. E., Falk-Petersen, S., Kwasniewski, S., et al. (2014). Arctic complexity: A case study on diel vertical migration of zooplankton. *Journal of Plankton Research*, *36*(5), 1279–1297. https://doi.org/10.1093/plankt/fbu059

Beszczynska-Moller, A., Fahrbach, E., Schauer, U., & Hansen, E. (2012). Variability in Atlantic water temperature and transport at the entrance to the Arctic Ocean, 1997-2010. *ICES Journal of Marine Science*, *69*(5), 852–863. https://doi.org/10.1093/icesjms/fss056

Bluhm, B. A., Kosobokova, K. N., & Carmack, E. C. (2015). A tale of two basins: An integrated physical and biological perspective of the deep Arctic Ocean. *Progress in Oceanography*, *139*, 89–121. https://doi.org/10.1016/j.pocean.2015.07.011

Bretherton F. P., Davis, R. E., & Fandry, C. B. (1976). A technique for objective analysis and design of oceanographic experiment applied to MODE-73. *Deep Sea Res.*, *23*(April 1975), 559–582.

Burtenshaw, J. C., Oleson, E. M., Hildebrand, J. A., McDonald, M. A., Andrew, R. K., Howe, B. M., & Mercer, J. A. (2004). Acoustic and satellite remote sensing of blue whale seasonality and habitat in the Northeast Pacific. *Deep Sea Research Part II: Topical Studies in Oceanography*, *51*(10–11), 967–986. https://doi.org/10.1016/j.dsr2.2004.06.020

Carey, W. M., & Evans, R. B. (2011). *Ocean Ambient Noise*. New York, NY: Springer New York. https://doi.org/10.1007/978-1-4419-7832-5

Carmack, E., Polyakov, I., Padman, L., Fer, I., Hunke, E., Hutchings, J., et al. (2015). Toward quantifying the increasing role of oceanic heat in sea ice loss in the new arctic. *Bulletin of the American Meteorological Society*, *96*(12), 2079–2105. https://doi.org/10.1175/BAMS-D-13-00177.1

Chapp, E., Bohnenstiehl, D. R., & Tolstoy, M. (2005). Sound-channel observations of ice-generated tremor in the Indian Ocean. *Geochemistry, Geophysics, Geosystems*, *6*(6), 1–14. https://doi.org/10.1029/2004GC000889

Cheng, L., Trenberth, K. E., Fasullo, J., Boyer, T., Abraham, J., & Zhu, J. (2017). Improved estimates of ocean heat content from 1960 to 2015. *Science Advances*, *3*(3), 1–11. https://doi.org/10.1126/sciadv.1601545

Cisewski, B., Strass, V. H., Rhein, M., & Krägefsky, S. (2010). Seasonal variation of diel vertical migration of zooplankton from ADCP backscatter time series data in the Lazarev Sea, Antarctica. *Deep-Sea Research Part I: Oceanographic Research Papers*, *57*(1), 78–94. https://doi.org/10.1016/j.dsr.2009.10.005

Clark, C., Ellison, W., Southall, B., Hatch, L., Van Parijs, S., Frankel, A., & Ponirakis, D. (2009). Acoustic masking in marine ecosystems: intuitions, analysis, and implication. *Marine Ecology Progress Series*, *395*, 201–222. https://doi.org/10.3354/meps08402

Cokelet, E. D., Tervalon, N., & Bellingham, J. G. (2008). Hydrography of the West Spitsbergen Current, Svalbard Branch: Autumn 2001. *Journal of Geophysical Research: Oceans*, *113*(1), 1–16. https://doi.org/10.1029/2007JC004150

Cooke, J. G. (2018). Balaenoptera musculus ssp. intermedia. *The IUCN Red List of Threatened Species*, *e.T41713A5*. https://doi.org/10.2305/IUCN.UK.2018-2.RLTS.T41713A50226962.en

Crews, L., Sundfjord, A., Albretsen, J., & Hattermann, T. (2018). Mesoscale Eddy Activity and Transport in the Atlantic Water Inflow Region North of Svalbard. *Journal of Geophysical Research: Oceans*, *123*(1), 201–215. https://doi.org/10.1002/2017JC013198

Crews, L., Sundfjord, A., & Hattermann, T. (2019). How the Yermak Pass Branch Regulates Atlantic Water Inflow to the Arctic Ocean. *Journal of Geophysical Research: Oceans*, *124*(1), 267–280. https://doi.org/10.1029/2018JC014476

Curtis, K. R., Howe, B. M., & Mercer, J. A. (1999). Low-frequency ambient sound in the North Pacific: Long time series observations. *J. Acoust. Soc. Am.*, *106*(6), 3189–3200. https://doi.org/10.1121/1.428173

Dee, D. P., Uppala, S. M., Simmons, a. J., Berrisford, P., Poli, P., Kobayashi, S., et al. (2011). The ERA-Interim reanalysis: Configuration and performance of the data assimilation system. *Quarterly Journal of the Royal Meteorological Society*, *137*(656), 553–597. https://doi.org/10.1002/qj.828

Döös, K. (1995). Interocean exchange of water masses. *Journal of Geophysical Research: Oceans*, *100*(C7), 13499–13514. https://doi.org/10.1029/95JC00337

Dushaw, B D, Worcester, P. F., Dzieciuch, M. A., & Menemenlis, D. (2013). On the time-mean state of ocean models and the properties of long range acoustic propagation. *Journal of Geophysical Research: Oceans*, *118*(9), 4346–4362. https://doi.org/10.1002/jgrc.20325

Dushaw, Brian D, & Menemenlis, D. (2014). Antipodal acoustic thermometry: 1960, 2004. *Deep Sea Research Part I: Oceanographic Research Papers*, *86*(C), 1–20. https://doi.org/10.1016/j.dsr.2013.12.008

Dziak, R. P., Bohnenstiehl, D. R., Stafford, K. M., Matsumoto, H., Park, M., Lee, W. S., et al. (2015). Sources and Levels of Ambient Ocean Sound near the Antarctic Peninsula. *Plos One*, *10*(4), e0123425. https://doi.org/10.1371/journal.pone.0123425

Etter, P. C. (2009). Review of ocean-acoustic models. *OCEANS 2009, MTS/IEEE Biloxi - Marine Technology for Our Future: Global and Local Challenges*, 1–6. Retrieved from http://ieeexplore.ieee.org/xpls/abs_all.jsp?arnumber=5422478

Fahrbach, E., Rohardt, G., Scheele, N., Schröder, M., Strass, V., & Wisotzki, A. (1995). Formation and discharge of deep and bottom water in the northwestern Weddell Sea. *Journal of Marine Research*, *53*(4), 515–538. https://doi.org/10.1357/0022240953213089

Falk-Petersen, S., Mayzaud, P., Kattner, G., & Sargent, J. R. (2009). Lipids and life strategy of Arctic Calanus. *Marine Biology Research*, *5*(1), 18–39.

https://doi.org/10.1080/17451000802512267
Falk-Petersen, S., Pavlov, V., Berge, J., Cottier, F., Kovacs, K. M., & Lydersen, C. (2014). At the rainbow's end: high productivity fueled by winter upwelling along an Arctic shelf. *Polar Biology*. https://doi.org/10.1007/s00300-014-1482-1
Fossheim, M., Primicerio, R., Johannesen, E., Ingvaldsen, R. B., Aschan, M. M., & Dolgov, A. V. (2015). Recent warming leads to a rapid borealization of fish communities in the Arctic. *Nature Climate Change*, *5*(7), 673–677. https://doi.org/10.1038/nclimate2647
Frainer, A., Primicerio, R., Kortsch, S., Aune, M., Dolgov, A. V., Fossheim, M., & Aschan, M. M. (2017). Climate-driven changes in functional biogeography of Arctic marine fish communities. *Proceedings of the National Academy of Sciences*, *114*(46), 12202–12207. https://doi.org/10.1073/pnas.1706080114
Friedlaender, A. S., Goldbogen, J. A., Nowacek, D. P., Read, A. J., Johnston, D., & Gales, N. (2014). Feeding rates and under-ice foraging strategies of the smallest lunge filter feeder, the Antarctic minke whale (Balaenoptera bonaerensis). *Journal of Experimental Biology*, *217*(16), 2851–2854. https://doi.org/10.1242/jeb.106682
Frisk, G. V. (2012). Noiseonomics: the relationship between ambient noise levels in the sea and global economic trends. *Scientific Reports*, *2*(1), 437. https://doi.org/10.1038/srep00437
Gabriele, C. M., Ponirakis, D. W., Clark, C. W., Womble, J. N., & Vanselow, P. B. S. (2018). Underwater Acoustic Ecology Metrics in an Alaska Marine Protected Area Reveal Marine Mammal Communication Masking and Management Alternatives. *Frontiers in Marine Science*, *5*(August), 1–17. https://doi.org/10.3389/fmars.2018.00270
Gandin, L. S. (1966). Objective analysis of meteorological fields. Translated from the Russian. Jerusalem (Israel Program for Scientific Translations). *Quarterly Journal of the Royal Meteorological Society*, *92*(393), 447–447. https://doi.org/10.1002/qj.49709239320
Gascard, J.-C., Richez, C., & Rouault, C. (1995). New insights on large-scale oceanography in Fram Strait: The West Spitsbergen Current. *Oceanography of the Arctic: Marginal Ice Zones and Continental Shelves*, *49*, 131–182. https://doi.org/10.1029/CE049p0131
Gilcoto, M., Jones, E., & Fariña-Busto, L. (2009). Robust estimations of current velocities with four-beam broadband ADCPs. *Journal of Atmospheric and Oceanic Technology*, *26*(12), 2642–2654. https://doi.org/10.1175/2009JTECHO674.1
Godø, O. R., Sivle, L. D., Patel, R., & Torkelsen, T. (2013). Synchronous behaviour of cetaceans observed with active acoustics. *Deep-Sea Research Part II: Topical Studies in Oceanography*, *98*, 445–451. https://doi.org/10.1016/j.dsr2.2013.06.013
Godø, O. R., Handegard, N. O., Browman, H. I., Macaulay, G. J., Kaartvedt, S., Giske, J., et al. (2014). Marine ecosystem acoustics (MEA): quantifying processes in the sea at the spatio-temporal scales on which they occur. *ICES Journal of Marine Science*, *71*(8), 2357–2369. https://doi.org/10.1093/icesjms/fsu116

Goldbogen, J. A., Pyenson, N. D., & Shadwick, R. E. (2007). Big gulps require high drag for fin whale lunge feeding. *Marine Ecology Progress Series*, *349*, 289–301. https://doi.org/10.3354/meps07066

Goldbogen, J. A., Calambokidis, J., Oleson, E., Potvin, J., Pyenson, N. D., Schorr, G., & Shadwick, R. E. (2011). Mechanics, hydrodynamics and energetics of blue whale lunge feeding: efficiency dependence on krill density. *Journal of Experimental Biology*, *214*(1), 131–146. https://doi.org/10.1242/jeb.048157

Gong, Z., Jain, A. D., Tran, D., Yi, D. H., Wu, F., Zorn, A., et al. (2014). Ecosystem scale acoustic sensing reveals humpback whale behavior synchronous with herring spawning processes and re-evaluation finds no effect of sonar on humpback song occurrence in the Gulf of Maine in fall 2006. *PLoS ONE*, *9*(10). https://doi.org/10.1371/journal.pone.0104733

Gostiaux, L., & van Haren, H. (2010). Extracting meaningful information from uncalibrated backscattered echo intensity data. *Journal of Atmospheric and Oceanic Technology*, *27*(5), 943–949. https://doi.org/10.1175/2009JTECHO704.1

Gradinger, R. (1999). Integrated abundance and biomass of sympagic meiofauna in Arctic and Antarctic pack ice. *Polar Biology*, *22*(3), 169–177. https://doi.org/10.1007/s003000050407

Griffiths, G. (2002). Comparison of acoustic backscatter measurements from a ship-mounted Acoustic Doppler Current Profiler and an EK500 scientific echo-sounder. *ICES Journal of Marine Science*, *53*(2), 487–491. https://doi.org/10.1006/jmsc.1996.0070

Halliday, W. D., Insley, S. J., Hilliard, R. C., de Jong, T., & Pine, M. K. (2017). Potential impacts of shipping noise on marine mammals in the western Canadian Arctic. *Marine Pollution Bulletin*, *123*(1–2), 73–82. https://doi.org/10.1016/j.marpolbul.2017.09.027

Hamilton, C D, Kovacs, K. M., Ims, R. A., Aars, J., Strøm, H., & Lydersen, C. (2017). Spatial overlap among an Arctic predator, prey and scavenger in the marginal ice zone. *Marine Ecology Progress Series*, *573*(January), 45–59. https://doi.org/10.3354/meps12184

Hamilton, Charmain D, Lydersen, C., Ims, R. A., & Kovacs, K. M. (2015). Predictions replaced by facts : a keystone species ' behavioural responses to declining arctic sea-ice. *Biology Letters*, *11*(20150803), 1–6. https://doi.org/10.1098/rsbl.2015.0803

Hattermann, T., Isachsen, P. E., von Appen, W.-J., Albretsen, J., & Sundfjord, A. (2016). Eddy-driven recirculation of Atlantic Water in Fram Strait. *Geophysical Research Letters*, *43*. https://doi.org/10.1002/2016GL068323

Haver, S. M., Klinck, H., Nieukirk, S. L., Matsumoto, H., Dziak, R. P., & Miksis-Olds, J. L. (2017). The not-so-silent world: Measuring Arctic, Equatorial, and Antarctic soundscapes in the Atlantic Ocean. *Deep Sea Research Part I: Oceanographic Research Papers*, (December 2016), 0–1. https://doi.org/10.1016/j.dsr.2017.03.002

Helble, T. A., D'Spain, G. L., Hildebrand, J. A., Campbell, G. S., Campbell, R. L., & Heaney, K. D. (2013). Site specific probability of passive acoustic detection of humpback whale calls from single fixed hydrophones. *The Journal of the*

Acoustical Society of America, *134*(3), 2556–2570. https://doi.org/10.1121/1.4816581

Herr, H., Kelly, N., Dorschel, B., Huntemann, M., Kock, K., Lehnert, L. S., et al. (2019). Aerial surveys for Antarctic minke whales (*Balaenoptera bonaerensis*) reveal sea ice dependent distribution patterns. *Ecology and Evolution*, (March), ece3.5149. https://doi.org/10.1002/ece3.5149

Hoegh-Guldberg, O., & Bruno, J. F. (2010). The impact of climate change on the world's marine ecosystems. *Science*, *328*(5985), 1523–1528. https://doi.org/10.1126/science.1189930

Hönisch, B., Ridgwell, A., Schmidt, D. N., Thomas, E., Gibbs, S. J., Sluijs, A., et al. (2012). The geological record of ocean acidification. *Science*, *335*(6072), 1058–1063. https://doi.org/10.1126/science.1208277

Hop, H., Assmy, P., Wold, A., Sundfjord, A., Daase, M., Duarte, P., et al. (2019). Pelagic Ecosystem Characteristics across the Atlantic Water Boundary Current from Rijpfjorden, Svalbard, to the Arctic Ocean During Summer (2010-2014). *Frontiers in Marine Science*, *6*(April), 1–21. https://doi.org/10.3389/fmars.2019.00181

Hope, G., Sagen, H., Storheim, E., Hobæk, H., & Freitag, L. (2017). Measured and modeled acoustic propagation underneath the rough Arctic sea-ice. *The Journal of the Acoustical Society of America*, *142*(3), 1619–1633. https://doi.org/10.1121/1.5003786

Hunt, G. L., Drinkwater, K. F., Arrigo, K., Berge, J., Daly, K. L., Danielson, S., et al. (2016). Advection in polar and sub-polar environments: Impacts on high latitude marine ecosystems. *Progress in Oceanography*, *149*, 40–81. https://doi.org/10.1016/j.pocean.2016.10.004

Ingvaldsen, R. B., Asplin, L., & Loeng, H. (2004). Velocity field of the western entrance to the Barents Sea. *Journal of Geophysical Research: Oceans*, *109*(C3), 1–12. https://doi.org/10.1029/2003JC001811

Ivanov, V. V., Alexeev, V. A., Repina, I., Koldunov, N. V., & Smirnov, A. (2012). Tracing atlantic water signature in the arctic sea ice cover east of Svalbard. *Advances in Meteorology*, *2012*. https://doi.org/10.1155/2012/20181810.1155/2012/201818

Jakobsson, M., Mayer, L., Coakley, B., Dowdeswell, J. A., Forbes, S., Fridman, B., et al. (2012). The International Bathymetric Chart of the Arctic Ocean (IBCAO) Version 3.0. *Geophysical Research Letters*, *39*(12), 1–6. https://doi.org/10.1029/2012GL052219

Kaartvedt, S., Torgersen, T., Klevjer, T. A., Røstad, A., & Devine, J. A. (2008). Behavior of individual mesopelagic fish in acoustic scattering layers of Norwegian fjords. *Marine Ecology Progress Series*, *360*(May), 201–209. https://doi.org/10.3354/meps07364

Kelly, N., Peel, D., & Bravington, M. V. (2014). Distribution and abundance of Antarctic minke whales in sea ice regions of East Antarctica: a summary of results. *IWC Scientific Committee Document SC/65b/IA15*, 1–22. Retrieved from papers2://publication/uuid/8DB308E1-6D8A-4614-8AE4-6802B9DAD44A

Klatt, O., Boebel, O., & Fahrbach, E. (2007). A profiling float's sense of ice. *Journal of Atmospheric and Oceanic Technology*, *24*(7), 1301–1308.

https://doi.org/10.1175/JTECH2026.1

Koenig, Z., Provost, C., Villacieros-Robineau, N., Sennéchael, N., Meyer, A., Lellouche, J. M., & Garric, G. (2017). Atlantic waters inflow north of Svalbard: Insights from IAOOS observations and Mercator Ocean global operational system during N-ICE2015. *Journal of Geophysical Research: Oceans*, *122*(2), 1254–1273. https://doi.org/10.1002/2016JC012424

Korneliussen, R. J., Ona, E., Eliassen, I., Heggelund, Y., Patel, R., & Godø, O. R. (2006). The large scale survey system – LSSS. *Proceedings Ofthe 29th Scandinavian Symposium on Physical Acoustics (Ustaoset)*.

Korneliussen, Rolf J., Heggelund, Y., Macaulay, G. J., Patel, D., Johnsen, E., & Eliassen, I. K. (2016). Acoustic identification of marine species using a feature library. *Methods in Oceanography*, *17*(December), 187–205. https://doi.org/10.1016/j.mio.2016.09.002

Krause, B., & Farina, A. (2016). Using ecoacoustic methods to survey the impacts of climate change on biodiversity. *Biological Conservation*, *195*(January 2016), 245–254. https://doi.org/10.1016/j.biocon.2016.01.013

Leroy, E., Samaran, F., Stafford, K., Bonnel, J., & Royer, J. (2018). Broad-scale study of the seasonal and geographic occurrence of blue and fin whales in the Southern Indian Ocean. *Endangered Species Research*, *37*, 289–300. https://doi.org/10.3354/esr00927

Leroy, E. C., Royer, J. Y., Bonnel, J., & Samaran, F. (2018). Long-Term and Seasonal Changes of Large Whale Call Frequency in the Southern Indian Ocean. *Journal of Geophysical Research: Oceans*, *123*(11), 8568–8580. https://doi.org/10.1029/2018JC014352

Lind, S., Ingvaldsen, R. B., & Furevik, T. (2018). Arctic warming hotspot in the northern Barents Sea linked to declining sea-ice import. *Nature Climate Change*, *8*(7), 634–639. https://doi.org/10.1038/s41558-018-0205-y

Lone, K., Kovacs, K. M., Lydersen, C., Fedak, M., Andersen, M., Lovell, P., & Aars, J. (2018). Aquatic behaviour of polar bears (Ursus maritimus) in an increasingly ice-free Arctic. *Scientific Reports*, *8*(1), 9677. https://doi.org/10.1038/s41598-018-27947-4

Lurton, X. (2002). *An introduction to underwater acoustics: principles and applications*. Springer. Retrieved from http://books.google.de/books?id=VTNRh3pyCyMC

MacMahan, J., Vennell, R., Beatson, R., Brown, J., & Reniers, A. (2012). Divergence-free spatial velocity flow field interpolator for improving measurements from adcp-equipped small unmanned underwater vehicles. *Journal of Atmospheric and Oceanic Technology*, *29*(3), 478–484. https://doi.org/10.1175/JTECH-D-11-00084.1

Magnúsdóttir, E. E., & Lim, R. (2019). Subarctic singers: Humpback whale (Megaptera novaeangliae) song structure and progression from an Icelandic feeding ground during winter. *PLoS ONE*, *14*(1), 1–26. https://doi.org/10.1371/journal.pone.0210057

Makris, N. C., Godø, O. R., Yi, D. H., Macaulay, G. J., Jain, A. D., Cho, B., et al. (2018). Instantaneous areal population density of entire Atlantic cod and herring spawning groups and group size distribution relative to total spawning

population. *Fish and Fisheries*, (March 2018), 201–213. https://doi.org/10.1111/faf.12331

Marques, T. A., Thomas, L., Martin, S. W., Mellinger, D. K., Ward, J. A., Moretti, D. J., et al. (2013). Estimating animal population density using passive acoustics. *Biological Reviews of the Cambridge Philosophical Society*, *88*(2), 287–309. https://doi.org/10.1111/brv.12001

Marshall, J., & Speer, K. (2012). Closure of the meridional overturning circulation through Southern Ocean upwelling. *Nature Geoscience*, *5*(3), 171–180. https://doi.org/10.1038/ngeo1391

Matsumoto, H., Jones, C., Klinck, H., Mellinger, D. K., Dziak, R. P., & Meinig, C. (2013). Tracking beaked whales with a passive acoustic profiler float. *The Journal of the Acoustical Society of America*, *133*(2), 731–40. https://doi.org/10.1121/1.4773260

Mayzaud, P., Falk-Petersen, S., Noyon, M., Wold, A., & Boutoute, M. (2016). Lipid composition of the three co-existing Calanus species in the Arctic: impact of season, location and environment. *Polar Biology*, *39*(10), 1819–1839. https://doi.org/10.1007/s00300-015-1725-9

McCauley, R. D., Gavrilov, A. N., Jolliffe, C. D., Ward, R., & Gill, P. C. (2018). Pygmy blue and Antarctic blue whale presence, distribution and population parameters in southern Australia based on passive acoustics. *Deep-Sea Research Part II: Topical Studies in Oceanography*, (August). https://doi.org/10.1016/j.dsr2.2018.09.006

McDonald, M. A., Hildebrand, J. A., Wiggins, S. M., & Ross, D. (2008). A 50 Year comparison of ambient ocean noise near San Clemente Island: A bathymetrically complex coastal region off Southern California. *The Journal of the Acoustical Society of America*, *124*(4), 1985–1992. https://doi.org/10.1121/1.2967889

Mellinger, D., Stafford, K., Moore, S., Dziak, R., & Matsumoto, H. (2007). An Overview of Fixed Passive Acoustic Observation Methods for Cetaceans. *Oceanography*, *20*(4), 36–45. https://doi.org/10.5670/oceanog.2007.03

Menze, S. (2015). Estimating fin whale distribution from ambient noise spectra using Bayesian inversion. *Master Thesis at the University of Bergen*, 1–117.

Meyer, K. S., Sweetman, A. K., Young, C. M., & Renaud, P. E. (2015). Environmental factors structuring Arctic megabenthos - a case study from a shelf and two fjords. *Frontiers in Marine Science*, *2*(April), 1–14. https://doi.org/10.3389/fmars.2015.00022

Miksis-Olds, J. L., Bradley, D. L., & Maggie Niu, X. (2013). Decadal trends in Indian Ocean ambient sound. *The Journal of the Acoustical Society of America*, *134*(5), 3464. https://doi.org/10.1121/1.4821537

Moore, S. E., Stafford, K. M., Melling, H., Berchok, C., Wiig, O., Kovacs, K. M., et al. (2012). Comparing marine mammal acoustic habitats in Atlantic and Pacific sectors of the High Arctic: Year-long records from Fram Strait and the Chukchi Plateau. *Polar Biology*, *35*(3), 475–480. https://doi.org/10.1007/s00300-011-1086-y

Nicol, S., Pauly, T., Bindoff, N. L., Wright, S., Thiele, D., Hosle, G. W., et al. (2000). Ocean circulation off east Antarctica affects ecosystem structure and sea-ice extent. *Nature*, *406*(6795), 504–507. https://doi.org/10.1038/35020053

Nicol, S., Foster, J., & Kawaguchi, S. (2012). The fishery for Antarctic krill - recent developments. *Fish and Fisheries*, *13*(1), 30–40. https://doi.org/10.1111/j.1467-2979.2011.00406.x

Nieukirk, S. L., Mellinger, D. K., Moore, S. E., Klinck, K., Dziak, R. P., & Goslin, J. (2012). Sounds from airguns and fin whales recorded in the mid-Atlantic Ocean, 1999–2009. *The Journal of the Acoustical Society of America*, *131*(2), 1102–1112. https://doi.org/10.1121/1.3672648

Nilsen, F., Skogseth, R., Vaardal-Lunde, J., & Inall, M. (2016). A Simple Shelf Circulation Model: Intrusion of Atlantic Water on the West Spitsbergen Shelf. *Journal of Physical Oceanography*, *46*(4), 1209–1230. https://doi.org/10.1175/jpo-d-15-0058.1

Nystuen, J., Riser, S., Wen, T., & Swift, D. (2011). Interpreted acoustic ocean observations from Argo floats. *The Journal of the Acoustical Society of America*. https://doi.org/10.1121/1.3587814

Nystuen, J. a, Amitai, E., Anagnostou, E. N., & Anagnostou, M. N. (2008). Spatial averaging of oceanic rainfall variability using underwater sound: Ionian Sea rainfall experiment 2004. *The Journal of the Acoustical Society of America*, *123*(4), 1952–1962. https://doi.org/10.1121/1.2871485

Ona, E., Mazauric, V., & Andersen, L. N. (2009). Calibration methods for two scientific multibeam systems. *ICES Journal of Marine Science*, *66*(6), 1326–1334. https://doi.org/10.1093/icesjms/fsp125

Onarheim, I. H., Smedsrud, L. H., Ingvaldsen, R. B., & Nilsen, F. (2014). Loss of sea ice during winter north of Svalbard. *Tellus, Series A: Dynamic Meteorology and Oceanography*, *66*(1), 1–9. https://doi.org/10.3402/tellusa.v66.23933

Van Opzeeland, I., Van Parijs, S., Kindermann, L., Burkhardt, E., & Boebel, O. (2013). Calling in the Cold: Pervasive Acoustic Presence of Humpback Whales (Megaptera novaeangliae) in Antarctic Coastal Waters. *PLoS ONE*, *8*(9), 1–7. https://doi.org/10.1371/journal.pone.0073007

Van Opzeeland, I., Samaran, F., Stafford, K. M., Findlay, K., Gedamke, J., Harris, D., & Miller, B. S. (2014). Towards Collective circum-Antarctic Passive Acoustic Monitoring : The Southern Ocean Hydrophone Network (SOHN). *Polarforschung*, *83*(2), 47–61.

Orr, J. C., Fabry, V. J., Aumont, O., Bopp, L., Doney, S. C., Feely, R. A., et al. (2005). Anthropogenic ocean acidification over the twenty-first century and its impact on calcifying organisms. *Nature*, *437*(7059), 681–686. https://doi.org/10.1038/nature04095

Van Parijs, S., Clark, C., Sousa-Lima, R., Parks, S., Rankin, S., Risch, D., & Van Opzeeland, I. (2009). Management and research applications of real-time and archival passive acoustic sensors over varying temporal and spatial scales. *Marine Ecology Progress Series*, *395*, 21–36. https://doi.org/10.3354/meps08123

Pérez-Hernández, M. D., Pickart, R. S., Pavlov, V., Våge, K., Ingvaldsen, R., Sundfjord, A., et al. (2017). The Atlantic Water boundary current north of Svalbard in late summer. *Journal of Geophysical Research: Oceans*, *119*, 7123–7138. https://doi.org/10.1002/2016JC012486

Pérez-Hernández, M. D., Pickart, R. S., Torres, D. J., Bahr, F., Sundfjord, A., Ingvaldsen, R., et al. (2019). Structure, transport and seasonality of the Atlantic

Water Boundary Current north of Svalbard: Results from a year-long mooring array. *Journal of Geophysical Research: Oceans*, 1–20. https://doi.org/10.1029/2018JC014759

Perrin, W. F., Würsig, B. G., & Thewissen, J. G. M. (2009). *Encyclopedia of Marine Mammals*. Academic Press. Retrieved from http://books.google.de/books?id=2rkHQpToi9sC

Pettit, E. C. (2012). Passive underwater acoustic evolution of a calving event. *Annals of Glaciology*, *53*(60), 113–122. https://doi.org/10.3189/2012AoG60A137

Pijanowski, B. C., Villanueva-Rivera, L. J., Dumyahn, S. L., Farina, A., Krause, B. L., Napoletano, B. M., et al. (2011). Soundscape Ecology: The Science of Sound in the Landscape. *BioScience*, *61*(3), 203–216. https://doi.org/10.1525/bio.2011.61.3.6

Pithan, F., & Mauritsen, T. (2014). Arctic amplification dominated by temperature feedbacks in contemporary climate models. *Nature Geoscience*, *7*(3), 181–184. https://doi.org/10.1038/ngeo2071

Pnyushkov, A. V., Polyakov, I. V., Ivanov, V. V., Aksenov, Y., Coward, A. C., Janout, M., & Rabe, B. (2015). Structure and variability of the boundary current in the Eurasian Basin of the Arctic Ocean. *Deep-Sea Research Part I: Oceanographic Research Papers*, *101*, 80–97. https://doi.org/10.1016/j.dsr.2015.03.001

Polyakov, I. V., Alexeev, V. A., Ashik, I. M., Bacon, S., Beszczynska-Moeller, A., Carmack, E. C., et al. (2011). Fate of early 2000s arctic warm water pulse. *Bulletin of the American Meteorological Society*, *92*(5), 561–566. https://doi.org/10.1175/2010BAMS2921.1

Polyakov, I. V., Bhatt, U. S., Walsh, J. E., Abrahamsen, E. P., Pnyushkov, A. V., & Wassmann, P. F. (2013). Recent oceanic changes in the Arctic in the context of long-term observations. *Ecological Applications*, *23*(8), 1745–1764. https://doi.org/10.1890/11-0902.1

Polyakov, I. V., Pnyushkov, A. V., Alkire, M. B., Ashik, I. M., Baumann, T. M., Carmack, E. C., et al. (2017). Greater role for Atlantic inflows on sea-ice loss in the Eurasian Basin of the Arctic Ocean. *Science*, *356*(6335), 285–291. https://doi.org/10.1126/science.aai8204

Porter, M. B. (1987). Gaussian beam tracing for computing ocean acoustic fields. *The Journal of the Acoustical Society of America*, *82*(4), 1349–1359. https://doi.org/10.1121/1.395269

Porter, M. B., & Liu, Y.-C. (1994). Finite-element ray tracing. *Theoretical and Computational Acoustics*, *2*, 947–956.

Randelhoff, A., Reigstad, M., Chierici, M., Sundfjord, A., Ivanov, V., Cape, M. R., et al. (2018). Seasonality of the Physical and Biogeochemical Hydrography in the Inflow to the Arctic Ocean through Fram Strait. *Frontiers in Marine Science*, *5*(June), 224. https://doi.org/10.3389/fmars.2018.00224

Renner, A. H. H., Sundfjord, A., Janout, M. A., Ingvaldsen, R. B., Beszczynska-Möller, A., Pickart, R. S., & Pérez-Hernández, M. D. (2018). Variability and Redistribution of Heat in the Atlantic Water Boundary Current North of Svalbard. *Journal of Geophysical Research: Oceans*, *123*(9), 6373–6391. https://doi.org/10.1029/2018JC013814

Resplandy, L., Keeling, R. F., Eddebbar, Y., Brooks, M. K., Wang, R., Bopp, L., et al. (2018). Quantification of ocean heat uptake from changes in atmospheric O 2 and CO 2 composition. *Nature*, *563*(7729), 105–108. https://doi.org/10.1038/s41586-018-0651-8

Rhein, M., Rintoul, S. R., Aoki, S., Campos, E., Chambers, D., Feely, R. A., et al. (2013). Observations: Ocean. In Intergovernmental Panel on Climate Change (Ed.), *Climate Change 2013: The Physical Science Basis. Contribution of Working Group I to the Fifth Assessment Report of the Intergovernmental Panel on Climate Change* (Vol. 9781107057, pp. 255–316). Cambridge, USA: Cambridge University Press. https://doi.org/10.1017/CBO9781107415324.010

Risch, D., Clark, C. W., Dugan, P. J., Popescu, M., Siebert, U., & Van Parijs, S. M. (2013). Minke whale acoustic behavior and multi-year seasonal and diel vocalization patterns in Massachusetts Bay, USA. *Marine Ecology Progress Series*, *489*, 279–295. https://doi.org/10.3354/meps10426

Risch, D., Corkeron, P. J., Ellison, W. T., & Van Parijs, S. M. (2014). Formal Comment to Gong et al.: Ecosystem Scale Acoustic Sensing Reveals Humpback Whale Behavior Synchronous with Herring Spawning Processes and Re-Evaluation Finds No Effect of Sonar on Humpback Song Occurrence in the Gulf of Maine in Fall 2006. *PLoS ONE*, *9*(10), e109225. https://doi.org/10.1371/journal.pone.0109225

Riser, S. C., Freeland, H. J., Roemmich, D., Wijffels, S., Troisi, A., Belbéoch, M., et al. (2016). Fifteen years of ocean observations with the global Argo array. *Nature Climate Change*, *6*(2), 145–153. https://doi.org/10.1038/nclimate2872

Rudels, B., Korhonen, M., Schauer, U., Pisarev, S., Rabe, B., & Wisotzki, A. (2015). Circulation and transformation of Atlantic water in the Eurasian Basin and the contribution of the Fram Strait inflow branch to the Arctic Ocean heat budget. *Progress in Oceanography*, *132*, 128–152. https://doi.org/10.1016/j.pocean.2014.04.003

Sabine, C. L., Feely, R. A., Gruber, N., Key, R. M., Lee, K., Bullister, J. L., et al. (2004). The oceanic sink for anthropogenic CO2. *Science (New York, N.Y.)*, *305*(5682), 367–71. https://doi.org/10.1126/science.1097403

Samaran, F., Adam, O., & Guinet, C. (2010). Detection range modeling of blue whale calls in Southwestern Indian Ocean. *Applied Acoustics*, *71*(11), 1099–1106. https://doi.org/10.1016/j.apacoust.2010.05.014

Savidge, D. K., & Amft, J. A. (2009). Circulation on the West Antarctic Peninsula derived from 6 years of shipboard ADCP transects. *Deep-Sea Research Part I: Oceanographic Research Papers*, *56*(10), 1633–1655. https://doi.org/10.1016/j.dsr.2009.05.011

Serreze, M. C., & Meier, W. N. (2019). The Arctic's sea ice cover: trends, variability, predictability, and comparisons to the Antarctic. *Annals of the New York Academy of Sciences*, *1436*(1), 36–53. https://doi.org/10.1111/nyas.13856

Siegel, V. (2005). Distribution and population dynamics of Euphausia superba: Summary of recent findings. *Polar Biology*, *29*(1), 1–22. https://doi.org/10.1007/s00300-005-0058-5

Simmonds, J., & MacLennan, D. N. (2008). *Fisheries Acoustics: Theory and Practice*. Wiley. Retrieved from https://books.google.no/books?id=ktUOvnfzB-

QC
Smedsrud, L. H., Esau, I., Ingvaldsen, R. B., Eldevik, T., Haugan, P. M., Li, C., et al. (2013). The role of the Barents Sea in the Arctic climate system. *Reviews of Geophysics*, *51*(3), 415–449. https://doi.org/10.1002/rog.20017
Smith, L. C., & Stephenson, S. R. (2013). New Trans-Arctic shipping routes navigable by midcentury. *Proceedings of the National Academy of Sciences of the United States of America*, *110*(13), 6–10. https://doi.org/10.1073/pnas.1214212110
Spindler, M. (1990). A Comparison of Arctic and Antarctic Sea Ice and the Effects of Different Properties on Sea Ice Biota. In U. Bleil & J. Thiede (Eds.), *Geological History of the Polar Oceans: Arctic versus Antarctic* (pp. 173–186). Dordrecht: Springer Netherlands. https://doi.org/10.1007/978-94-009-2029-3_10
Spreen, G., Kaleschke, L., & Heygster, G. (2008). Sea ice remote sensing using AMSR-E 89-GHz channels. *Journal of Geophysical Research*, *113*(C2), C02S03. https://doi.org/10.1029/2005JC003384
Stafford, K., Moore, S., Berchok, C., Wiig, Ø., Lydersen, C., Hansen, E., et al. (2012). Spitsbergen's endangered bowhead whales sing through the polar night. *Endangered Species Research*, *18*(2), 95–103. https://doi.org/10.3354/esr00444
Stammerjohn, S., Massom, R., Rind, D., & Martinson, D. (2012). Regions of rapid sea ice change: An inter-hemispheric seasonal comparison. *Geophysical Research Letters*, *39*(6), 1–8. https://doi.org/10.1029/2012GL050874
Stern, H. L., & Laidre, K. L. (2016). Sea-ice indicators of polar bear habitat. *Cryosphere*, *10*(5), 2027–2041. https://doi.org/10.5194/tc-10-2027-2016
Stocker, T. F., Dahe, Q., Plattner, G.-K., Alexander, L. V., Allen, S. K., Bindoff, N. L., et al. (2013). Technical Summary. *Climate Change 2013: The Physical Science Basis. Contribution of Working Group I to the Fifth Assessment Report of the Intergovernmental Panel on Climate Change*, 33–115. https://doi.org/10.1017/ CBO9781107415324.005
Storrie, L., Lydersen, C., Andersen, M., Wynn, R. B., & Kovacs, K. M. (2018). Determining the species assemblage and habitat use of cetaceans in the Svalbard Archipelago, based on observations from 2002 to 2014. *Polar Research*, *37*(1), 1463065. https://doi.org/10.1080/17518369.2018.1463065
Stranne, C., Mayer, L., Weber, T. C., Ruddick, B. R., Jakobsson, M., Jerram, K., et al. (2017). Acoustic mapping of thermohaline staircases in the arctic ocean. *Scientific Reports*, *7*(1), 1–9. https://doi.org/10.1038/s41598-017-15486-3
Tarantola, A. (2005). *Inverse Problem Theory and Methods for Model Parameter Estimation*. Philadelphia: Society for Industrial and Applied Mathematics.
Thomas, L., & Marques, T. A. (2012). Passive Acoustic Monitoring for Estimating Animal Density. *Acoustics Today*, *8*(3), 35. https://doi.org/10.1121/1.4753915
Tyack, P. L. (2008). Implications for marine mammals of large-scale changes in the marine acoustic environment. *Journal of Mammalogy*, *89*(3), 549–558.
Urazghildiiev, I. R., & Clark, C. W. (2013). Comparative analysis of localization algorithms with application to passive acoustic monitoring. *The Journal of the Acoustical Society of America*, *134*(6), 4418–4426. https://doi.org/10.1121/1.4824683
Vennell, R., & Beatson, R. (2009). A divergence-free spatial interpolator for large

sparse velocity data sets. *Journal of Geophysical Research*, *114*(C10), C10024. https://doi.org/10.1029/2008JC004973

Vernet, M., Ellingsen, I. H., Seuthe, L., Slagstad, D., Cape, M. R., & Matrai, P. A. (2019). Influence of Phytoplankton Advection on the Productivity Along the Atlantic Water Inflow to the Arctic Ocean, *6*(September), 1–18. https://doi.org/10.3389/fmars.2019.00583

Vihtakari, M., Welcker, J., Moe, B., Chastel, O., Tartu, S., Hop, H., et al. (2018). Black-legged kittiwakes as messengers of Atlantification in the Arctic. *Scientific Reports*, *8*(1), 1–11. https://doi.org/10.1038/s41598-017-19118-8

Walczowski, W., Piechura, J., Goszczko, I., & Wieczorek, P. (2012). Changes in Atlantic water properties: An important factor in the European Arctic marine climate. *ICES Journal of Marine Science*, *69*(5), 864–869. https://doi.org/10.1093/icesjms/fss068

Wang, D., Garcia, H., Huang, W., Tran, D. D., Jain, A. D., Yi, D. H., et al. (2016). Vast assembly of vocal marine mammals from diverse species on fish spawning ground. *Nature*, 1–18. https://doi.org/10.1038/nature16960

Wassmann, P., Kosobokova, K. N., Slagstad, D., Drinkwater, K. F., Hopcroft, R. R., Moore, S. E., et al. (2015). The contiguous domains of Arctic Ocean advection: Trails of life and death. *Progress in Oceanography*, *139*, 42–65. https://doi.org/10.1016/j.pocean.2015.06.011

Wassmann, P. F., Slagstad, D., & Ellingsen, I. (2019). Advection of mesozooplankton into the northern Svalbard shelf region. *Frontiers in Marine Science*, *6*(JUL), 1–10. https://doi.org/10.3389/fmars.2019.00458

Wekerle, C., Wang, Q., von Appen, W.-J., Danilov, S., Schourup-Kristensen, V., & Jung, T. (2017). Eddy-Resolving Simulation of the Atlantic Water Circulation in the Fram Strait With Focus on the Seasonal Cycle. *Journal of Geophysical Research: Oceans*, *122*(11), 8385–8405. https://doi.org/10.1002/2017JC012974

Wenz, G. M. (1962). Acoustic Ambient Noise in the Ocean: Spectra and Sources. *The Journal of the Acoustical Society of America*, *34*(12), 1936–1956. https://doi.org/10.1121/1.1909155

Węsławski, J. M., Hacquebord, L., Stempniewicz, L., & Malinga, M. (2000). Greenland whales and walruses in the Svalbard food web before and after exploitation. *Oceanologia*, *42*(1), 37–56.

Wilcock, W. S. D., Stafford, K. M., Andrew, R. K., & Odom, R. I. (2014). Sounds in the ocean at 1-100 Hz. *Annual Review of Marine Science*, *6*, 117–140. https://doi.org/10.1146/annurev-marine-121211-172423

Williams, R., Kelly, N., Boebel, O., Friedlaender, A. S., Herr, H., Kock, K. H., et al. (2014). Counting whales in a challenging, changing environment. *Scientific Reports*, *4*, 1–6. https://doi.org/10.1038/srep04170

Yack, T. M., Barlow, J., Calambokidis, J., Southall, B., & Coates, S. (2013). Passive acoustic monitoring using a towed hydrophone array results in identification of a previously unknown beaked whale habitat. *The Journal of the Acoustical Society of America*, *134*(3), 2589–95. https://doi.org/10.1121/1.4816585

Papers 1 to 4 attached

I

JGR Oceans

RESEARCH ARTICLE
10.1029/2018JC014299

Atlantic Water Pathways Along the North-Western Svalbard Shelf Mapped Using Vessel-Mounted Current Profilers

Sebastian Menze[1,2], Randi B. Ingvaldsen[1], Peter Haugan[1,2], Ilker Fer[2], Arild Sundfjord[3], Agnieszka Beszczynska-Moeller[4], and Stig Falk-Petersen[5]

[1]Institute of Marine Research, Bergen, Norway, [2]Geophysical Institute, University of Bergen, Bergen, Norway, [3]Norwegian Polar Institute, Tromsø, Norway, [4]Institute of Oceanology, Polish Academy of Sciences, Sopot, Poland, [5]Akvaplan-niva AS, Tromsø, Norway

Key Points:
- Atlantic water transport west and north of Svalbard estimated from sparse VM-ADCP data is 2 Sv in summer
- Yermak Pass Branch was observed in summer and can be as important as the Svalbard Branch for Atlantic water transport
- Atlantic water circulates within Hinlopen trench and strait

Supporting Information:
- Data Set S1

Correspondence to:
S. Menze,
sebastian.menze@hi.no

Citation:
Menze, S., Ingvaldsen, R. B., Haugan, P., Beszczynska-Moeller, A., Fer, I., Sundfjord, A., & Falk-Petersen, S. (2019). Atlantic water pathways along the north-western Svalbard shelf mapped using vessel-mounted current profilers. *Journal of Geophysical Research: Oceans*, *124*, 1699–1716. https://doi.org/10.1029/2018JC014299

Received 23 JUN 2018
Accepted 12 FEB 2019
Accepted article online 28 FEB 2019
Published online 15 MAR 2019
Corrected 11 MAY 2019

This article was corrected on 11 MAY 2019. See the end of the full text for details.

Abstract A large amount of warm Atlantic water (AW) enters the Arctic as a boundary current through Fram Strait (West Spitsbergen Current [WSC]) and is the major oceanic heat source to the Arctic Ocean. Along the north-western Svalbard shelf, the WSC splits into the shallow Svalbard Branch, the Yermak Branch that follows the slope of the Yermak Plateau, and the Yermak Pass Branch flowing across the plateau. The WSC has previously been studied using moorings, dedicated oceanographic transects, and models. In this study, we mapped the circulation patterns and AW flow around Svalbard using Vessel-Mounted Acoustic Doppler Current Profiler data from multiple surveys during four consecutive summers (2014–2017). Despite the scattered nature of this compiled data set, persistent circulation patterns could be discerned. Spatial interpolation showed a meandering boundary current west of Svalbard and a more homogeneous AW flow, centered around the 1,000-m isobath north of Svalbard. In all summers, we observed a northward jet between 79 and 80°N and the 1,000- and 500-m isobaths, before the WSC divided into the three branches. North of Svalbard, the shallow Svalbard Branch reunited with the Yermak Pass Branch between 10 and 15°E and a part of the AW circulated within Hinlopen Trench. The calculated volume transport of 2 Sv in the upper 500 m compares well with model results and previous observations. Our results further show that the Yermak Pass Branch can be as important as the Svalbard Branch in transporting AW across the Yermak Plateau during summer.

Plain Language Summary We mapped how seawater flows from the Atlantic into the Arctic Ocean around the Svalbard archipelago. To know where and how much water flows from the Atlantic into the Arctic Ocean is important because Atlantic water is the major source of heat, nutrients, and plankton for the Arctic Ocean. Heat from Atlantic water plays a role in the increased melting of sea ice, and the nutrients and plankton drifting with the currents are a major food supply for the Arctic marine ecosystem. We mapped the ocean currents with acoustic current meters that are mounted to research vessels that surveyed the area west and north of the Svalbard archipelago. We found that the Atlantic water flowing around Svalbard can take three different pathways: the shallow Svalbard Branch close to the north-western edge of Svalbard, the Yermak Branch that follows the slope of an underwater plateau north-west of Svalbard, and the Yermak Pass Branch that flows across the plateau and which has not been observed in summer before. We also showed that Atlantic water circulates within Hinlopen trench, a large passage splitting the archipelago, which could create a local ecological hot spot due to the favorable nutrient and plankton supply.

1. Introduction

Atlantic water (AW) flows along the western and northern Svalbard shelf with the West Spitsbergen Current (WSC). This current transports the majority of heat and biological material into the Arctic and has been a focus of oceanographic research since Nansen's expedition in 1893. The circulation patterns around Svalbard have been extensively studied using ocean models, mooring arrays, and oceanographic transects, but an observation-based high-resolution map of AW pathways and large-scale circulation has not been available so far. In this paper, we compiled and analyzed a large data set of acoustic Doppler current profiler observations to study the average circulation patterns.

The Arctic Ocean is connected with the northern Atlantic and Pacific oceans through four main gateways: Fram Strait, the Barents Sea, Bering Strait, and through the Canadian Arctic Archipelago. AW enters the Arctic along two major pathways, the Barents Sea Branch, transporting on average 1.8 Sv (10^6 m^3/s; Skagseth et al., 2008), and the Fram Strait Branch (historically called the WSC), transporting an average 3 Sv of AW (Beszczynska-Moller et al., 2012). The AW passing through the shallow Barents Sea loses substantial amounts of heat before entering the Eurasian Basin (Smedsrud et al., 2013), and the AW passing through Fram Strait, the major deepwater connection of the Arctic to the World Ocean, is the largest heat source for the Arctic Ocean (Rudels et al., 2015). Exchange of water masses and heat has been monitored by regular surveys and a mooring array in Fram Strait since 1997 (Beszczynska-Moller et al., 2012). The WSC is a topographically steered boundary current, which is strongest but also most variable in winter (von Appen et al., 2016). It sheds eddies that facilitate the south-westward recirculation of AW (Hattermann et al., 2016) and AW transport into Nansen Basin (Crews et al., 2018). Along the north-western Svalbard shelf, the WSC splits into the shallow Svalbard Branch (SB), the Yermak Branch that follows the slope of the Yermak Plateau (YB), and the Yermak Pass Branch (YPB) flowing across the plateau (Koenig et al., 2017; Wekerle et al., 2017).

Knowing the circulation patterns and AW pathways around Svalbard is essential to assess the impacts of oceanic heat, volume, salt, and carbon transport on local and pan-Arctic climate. It has been shown that with warming AW inflow, the winter sea ice cover north of Svalbard shrinks and air temperature rises (Ivanov et al., 2012; Onarheim et al., 2014; Piechura & Walczowski, 2009). Recent observations in the Eurasian Basin showed that oceanic heat increasingly contributes to sea ice loss, as AW heat can more easily reach the under-ice boundary layer when stratification weakens and AW shoals (Ivanov et al., 2016; Polyakov et al., 2017).

Understanding the chemical and biological oceanography of the Arctic Ocean is not possible without in-depth understanding of the import and export of water, sea ice, nutrients, carbon, and organisms (Berge et al., 2012; Falk-Petersen et al., 2007; Helland-Hansen & Nansen, 1912). Given the low light and nutrient levels in the Arctic Oceans, the pathways and distribution of advected organisms and nutrients have a strong impact on the ecosystem of the Arctic Basin (Wassmann et al., 2015). The Fram Strait region is of special ecological importance for several reasons: (1) the AW transports large amounts of nutrients, phytoplankton, and zooplankton into the Arctic Ocean and shelf seas (Wassmann et al., 2015); (2) the transpolar ice drift transports sediments, particulate matter, and ice fauna into the Fram Strait that are released during the melting processes (Berge et al., 2012; Proshutinsky et al., 2015); and (3) the increased inflow of AW and declining sea ice has opened up large areas between northern Spitsbergen and Franz Josef Land for new primary production (Falk-Petersen et al., 2014; Onarheim et al., 2014). The declining sea ice and changing oceanographic conditions north and west of Svalbard also affect the migration and distribution of mobile organisms such as marine mammals, fish, and sea birds (Descamps et al., 2016; Falk-Petersen et al., 2014; Haug et al., 2017). Mapping the flow of AW around Svalbard contributes to the baseline knowledge of physical oceanography in the studied region that in turn affects local and pan-Arctic climate and ecosystems.

2. Materials and Methods

The study is based on an observational data set collected using Vessel-Mounted Acoustic Doppler Current Profilers (VM-ADCPs) and Lowered Acoustic Doppler Current Profilers (L-ADCPs) during the summer months of four consecutive years (2014–2017). The surveys covered the Svalbard Shelf and the southern Yermak Plateau and are described in the following section.

2.1. Surveys

Our data set comprises of 10 surveys with RV Helmer Hanssen, RV Håkon Mosby, and RV Oceania in June–September 2014 to 2017. Other research vessels entered the study area during our study period, but we limited our analysis to 10 surveys due to varying VM-ADCP data availability and quality. The survey tracks and stations are displayed in Figure 1, and detailed information about each survey and the instrumentation can be found in Table 1. Four SI_ARCTIC project surveys with RV Helmer Hanssen provided a full data set of VM-ADCP, L-ADCP, and CTD (conductivity, temperature, and depth) data. On these surveys, a vessel-mounted 76.8-kHz RDI Workhorse Mariner ADCP continuously profiled currents in the upper 500 m and was set to record with a vertical bin size of 8 m. We used the software VMDAS (Vessel-

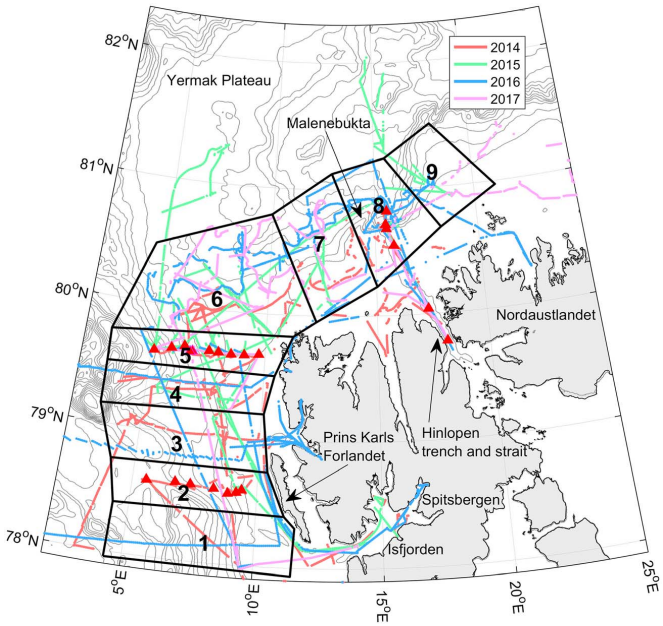

Figure 1. Map of Vessel-Mounted Acoustic Doppler Current Profilers tracks and averaging boxes. The color marks the year of each track: 2014: red; 2015: green; 2016: blue; and 2017: magenta. Bathymetry contours are shown with 200-m intervals (IBCAO; Jakobsson, 2012). The red triangles mark Lowered Acoustic Doppler Current Profiler (L-ADCP) stations. Gaps in the Vessel-Mounted Acoustic Doppler Current Profilers tracks are due to missing or low-quality data.

Table 1
Overview of the Surveys Used to Compile the VM-ADCP Data Set

Date	Survey name/project	Vessel	Data	VM-ADCP frequency	Number of bins	Bin size (m)
20 August to 3 September 2014	SI_ARCTIC	RV Helmer Hanssen	CTD, L-ADCP, VM-ADCP	76.8 kHz	100	8
7 to 17 August 2014	Carbonbridge	RV Helmer Hanssen	VM-ADCP	76.8 kHz	50	8
26 August to 5 September 2014	UNIS AGF214 survey HM2014618	RV Håkon Mosby	VM-ADCP	76.8 kHz	100	8
7 to 14 September 2014	UiB survey HM2014619	RV Håkon Mosby	VM-ADCP	76.8 kHz	100	8
12 to 21 August 2015	UiB survey HM2015617	RV Håkon Mosby	VM-ADCP	76.8 kHz	100	8
19 August to 5 September 2015	SI_ARCTIC	RV Helmer Hanssen	CTD, VM-ADCP	76.8 kHz	100	8
21 August to 1 September 2016	UNIS AB320	RV Helmer Hanssen	VM-ADCP	76.8 kHz	65	8
21 June to 22 July 2016	AREX IOPAN	RV Oceania	VM-ADCP	153.6 kHz	100	8
2 to 16 September 2016	SI_ARCTIC	RV Helmer Hanssen	CTD, L-ADCP, VM-ADCP	76.8 kHz	100	8
21August to 7 September 2017	SI_ARCTIC	RV Helmer Hanssen	CTD, L-ADCP, VM-ADCP	76.8 kHz	100	8

Note. CTD, conductivity, temperature, and depth; L-ADCP, Lowered Acoustic Doppler Current Profiler; VM-ADCP, Vessel-Mounted Acoustic Doppler Current Profilers.

Mounted Data Acquisition System) from RDI instruments to record the VM-ADCP and navigational data. During most of the CTD casts, current profiles were recorded with a downward looking 300-kHz RDI Workhorse Sentinel L-ADCP system using 8-m bins, while temperature and salinity data were collected following standard routines using a 911plus CTD system manufactured by Seabird. In addition to the VM-ADCP data from the four SI_ARCTIC surveys, we used VM-ADCP data from summer time surveys with RV Håkon Mosby, RV Helmer Hanssen, and RV Oceania (instrument frequency and bin size for each cruise are given in Table 1).

2.2. VM-ADCP Postprocessing

The VM-ADCP data were processed with the CODAS processing software package (Hummon, 2016), using 5-min temporal bins and 5-m depth bins. Misalignment of current vectors was removed, and acoustic interference with sea floor, CTD cable, nets, and due to ringing was semiautomatically removed from the data set using the VM-ADCP editing program gautoedit. Automatic thresholding algorithms rejected data with a jitter larger than 0.15 m/s and with a *percentage good* flag lower than 50%. After postprocessing, 49.5% of the bins in the VM-ADCP data set were rejected or missing. To ensure consistency between the surveys, all VM-ADCP profiles were binned vertically in 10-m bins between 10 and 700 m (the first bin centered around 15 m). This data set is available as netcdf file under the following link: https://doi.org/10.21335/NMDC-1323631641.

2.3. L-ADCP Postprocessing

The L-ADCP data were processed using the MATLAB-based inversion software LDEO (Version 4.2; Visbeck, 2002). In the upper layers, VM-ADCP data were used as a constraint for the inversion, whereas bottom echoes were used as a constraint for the lower layers. The average velocity error of the L-ADCP profiles was 0.03 m/s, and the bin size was set to 10 m.

3. Data Analysis

Current measurements obtained with VM-ADCPs (and often also with L-ADCP) vary in both time and space, rendering it a challenging data set to interpret. In this study we used three different approaches to interpret our heterogenous data set: (1) annual binning in polygonal boxes to compare spatial and temporal variability, (2) spatial interpolation to map persistent circulation patterns (objective mapping [OM] and radial basis functions), and (3) discussion of individual L-ADCP sections.

For both the VM-ADCP and L-ADCP current profiles, the along- and across-slope current components were calculated by rotating the current vectors according to the slope aspect in their respective locations. Slope aspect was calculated from the IBCAO bathymetry (Jakobsson et al., 2012), which was smoothed beforehand with a 2-D low-pass filter set to 18-km length. All analyses described here were done in MATLAB 2016a. The corresponding code and a tutorial can be found in this GitHub repository: https://github.com/sebastian-menze/Processing-and-analysis-of-large-ADCP-datasets.

3.1. Detiding Using the AOTIM Tidal Model

Tidal currents inferred from the AOTIM-5 tidal model (Padman & Erofeeva, 2004) were subtracted from the VM-ADCP and L-ADCP data sets. Tides on the shelf surrounding Svalbard can be as strong as 30 cm/s. The AOTIM-5 model has a 5-km resolution and provides estimates for the four most energetic tidal components in the Arctic: M_2, S_2, K_1, and O_1. AOTIM-5 is frequently used to detide ocean velocity data in the Arctic and has provided reliable estimates of barotropic tides (Fer et al., 2010; Meyer et al., 2017). Lacking a suitable model, we did not remove baroclinic tides from our data (discussed further in section 5.1).

3.2. Spatial Interpolation

We applied two different interpolation methods to the VM-ADCP data to visualize and map the general circulation patterns and estimate AW transport along the shelf: OM (also often termed objective analysis) and divergence-free radial basis functions (DF-RBFs).

3.2.1. Objective Mapping

We used OM to interpolate scattered VM-ADCP data onto a regular grid of current vectors. The interpolation is based on all available depth-averaged VM-ADCP observations, consisting of 10 surveys in August–September 2014–2017 (Table 1). The interpolation was conducted prior to rotating the current vectors into

along- and across-isobath components, separately interpolating the east and north velocity components. Combining the VM-ADCP data of multiple surveys improves the spatial coverage and smooths out the temporal variability, yielding a pattern more representative of the large-scale mean circulation.

OM (Bretherton et al., 1976) is an interpolation method used to generate a smooth and regular data grid from scattered data points (similar to interpolation techniques such as kriging). During the interpolation, data points are weighed according to a Gaussian function. It is defined by the standard deviation σ, which describes the *similarity radius*, within which the current field is sufficiently autocorrelated, and the interpolation error E, which describes the relative error we allow during the interpolation. Thus, the OM method requires that the semivariance (autocorrelation) function of the data field has a Gaussian shape.

To confirm this and estimate the similarity radius σ of the VM-ADCP data set, we calculated the average cross-semi-variance of the depth-averaged (between 0- and 500-m depth) current vectors u (northward) and v (eastward) for all profiles in the VM-ADCP data set:

$$\gamma_{i,r} = \frac{1}{\sum i \,\epsilon\, r} \left(\sum u_i - u_{i\,\epsilon\, r}\right)^2 \left(\sum v_i - v_{i\,\epsilon\, r}\right)^2,$$

where $\gamma_{i,\,r}$ denotes the cross-semi-variance of the current vector u and v for profile i in the distance bin (radius) r from profile i and $i \,\epsilon\, r$ are the indices of all profiles within distance bin r. We then estimated the median variogram that represents the cross-semi-variance of u and v as a function of distance (Figure S1). In addition, we fitted the following Gaussian function to each profile's variogram:

$$\widehat{\gamma}_r = (\gamma_{\max} - \gamma_{\min})\left(1 - e^{-\frac{r^2}{\sigma^2}}\right),$$

where $\widehat{\gamma}_r$ is the fitted cross-semi-variance, $\gamma_{\max}$ and $\gamma_{\min}$ are the maximum and minimum cross-semi-variances, r is the radius, and σ is the standard deviation that describes the similarity radius in which the current vectors are sufficiently correlated. The resulting distribution of standard deviations (similarity radii) is displayed in Figure S1. The median similarity radius is 58 km, and the 10th and 90th percentiles are 20 and 109 km, respectively. We also calculated the spatial autocorrelation of the u and v component separately using Moran's index and found the autocorrelation dropping to zero above 25-km distance (Figure S2). Based on the two measures, we choose to use a standard deviation σ of 25 km and an interpolation error of 0.4 for the OM algorithm.

The interpolated current field's uncertainty is quantified by the error between the interpolated and observed data (Figure S3). We choose to discard bins with a combined error larger than 0.8 and which were covered less than two summers. Due to the scattered nature of the VM-ADCP data set, not all summers and regions were covered equally (Figure S4). The OA interpolation algorithm is not mass and volume conserving and exhibits convergence and divergence zones of $\pm 0.15\ s^{-1}$ (Figure S5).

3.2.2. Interpolation With Divergence Free Radial Basis Functions

The current fields were also interpolated using DF-RBFs (Vennell & Beatson, 2009). The principle behind this method is to approximate the vector field as the sum of a set of 2-D spline functions whose weights determine the u and v vectors and that are centered at a subset of the data points. In contrast to OM, the DF-RBFs interpolate the u and v vector simultaneously and conserve volume and mass flux in the current field. In cases such as ours, where the observed current vectors contain both temporal and spatial variability (are divergent) the DF-RBFs minimize but do not eliminate divergence in the interpolated vector field. DF-RBFs are especially suitable to extract eddies and meanders from scattered current observations (Rogowski et al., 2014). We followed the method of Vennell and Beatson (2009) and added additional coastal constrains to the interpolation that require the streamfunction of the vector field to be constant along the coastline, as suggested by Vennell and Beatson (2006). For each interpolation, we used the depth-averaged and detided VM-ADCP data and 7% of the observation locations as uniformly distributed center locations for the RBFs and additional RBF centers along the IBCAO coastline.

A difference between OM and DF-RBF interpolation is that OM interpolation emphasizes the dominant features in the scattered data set and produces a smooth field, whereas DF-RBFs aim to fit the potentially noisy observations as close as possible and are thus easily confused by noisy observations or temporal variation. Since OM is based on a spatially weighted averaging it can handle *noisy* data from multiple surveys that

contain both spatial and temporal variability well and emphasizes the dominant features in the scattered data set. The resulting field, however, is not volume and mass conserving. Due to the simplicity of the method, eddies and meanders are interpolated correctly only with multiple crossings, whereas DF-RBFs can interpolate eddies and meanders correctly even with a single crossing. Based on this, we used DF-RBF interpolation to reveal details and temporal variability in the horizontal fields within regions and between months, while we used OM to investigate the along-path AW transports.

3.3. Polygonal Boxes

To compare the scattered VM-ADCP data along the shelf break, we averaged the VM-ADCP profiles in nine polygonal boxes with roughly uniform topography, distributed along bottom depth contours. The averaged section in each box covers the upper 700 m of the water column and the slope between the 2,500- and 0-m isobath (with 200-m bin width). The boundaries of all boxes are marked by black lines in Figure 1. The boundaries of each box are listed in Table S1, while Figure S6 shows the average slope profile for each box.

3.4. Transport Estimates

We calculated the net volume transport into the Arctic Ocean from both the detided L-ADCP and detided VM-ADCP data. For the L-ADCP sections, we calculated the net transport through the entire section, the net transport of AW (using $T > 2$ °C; Beszczynska-Moller et al., 2012), and the net transport in the upper 500 m.

We used three different approaches to estimate transport in the upper 500 m from the VM-ADCP data. Each approach uses the OM current field derived from the VM-ADCP data as the focus was on the dominant features of the AW flow and whether this transport decreases northward/northeastward.

The first approach compares transport along isobaths (2,500 to 0 m, 200-m bin width) between the different polygonal boxes (Figure 1). These transport sections were calculated for each box by multiplying the along-slope current (rotated using the local azimuth at each grid point) averaged in each isobath bin by the average cross-sectional area of each isobath bin. Net transport in each box was calculated by summation of the estimated along-slope transports, calculated separately for all isobath bins in the box.

The second approach followed the steps of the first, but instead of rotating the u and v vectors of the objectively mapped data set using local azimuth angles, we used the average azimuth of each box. We thus calculate the poleward transport through each box with respect to each box's orientation.

For the third approach, we calculated transport through a series of transects using the depth-averaged OM current field. Locations of transects in relation to the boxes and the OM data set are illustrated in Figure S7.

4. Results

4.1. Averaged VM-ADCP Sections

Sections of along-slope flow, averaged in the nine boxes, are compared for four consecutive summers in Figure 2. Coverage of the sections varied between the years; however, some persistent flow patterns can be discerned.

The southernmost box, that is, Box 1, contains a strong jet with the current speed up to 0.5 m/s at approximately 78°N, reflecting the WSC core. In 2014 and 2016 the jet, located between the 2,000- and 1,000-m isobaths, was strongly baroclinic (strongest at the surface), whereas in 2017 it was narrower, constant with depth and centered around the 500-m isobath.

Box 2 was covered only sparsely, but the available data do not indicate a strong jet as in Box 1. However, northward flow centered near the 1,000-m isobath was observed in 2014, 2016, and 2017. No data are available near the 1,000-m isobath from 2015.

The current sections in Box 3 (west of Kongsfjorden) show large differences between the years. The patterns indicate two northward flowing cores with a southward flowing recirculation branch between them. Box 4 shows a fast (approximately 30 cm/s) northward flowing jet, observed in 2014–2016. In 2014 and 2016 a surface intensified jet was found between the 1,000- and 5,00-m isobaths in contrast to summer 2015 when three separate northward flowing branches occurred, possibly related to eddies, instabilities, and recirculation.

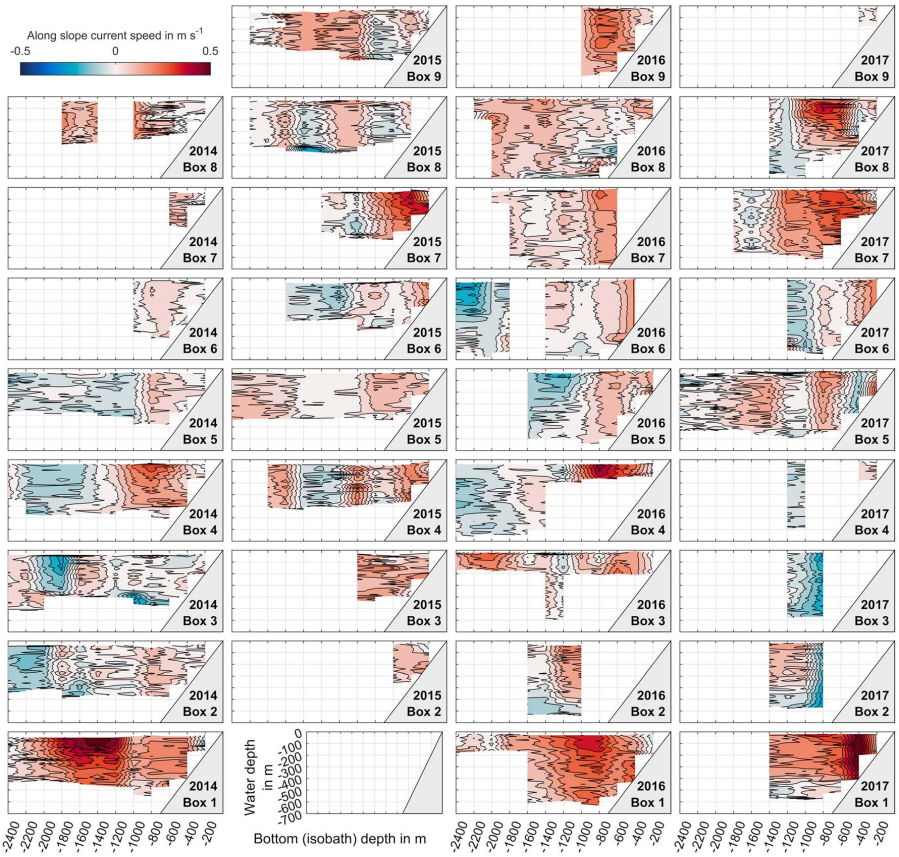

Figure 2. Sections of along-slope currents in a regular isobath coordinate system, averaged within the individual isobath bins for the Boxes 1–9. The red hues mark along-slope flow into the Arctic (north-eastward), while the blue hues indicate the along-slope flow out of the Arctic (to the south-west). Contour lines are drawn every 0.05 m/s, and the color scale ranges from −0.5 to 0.5 m/s. Bottom (isobath) depth is marked as a grey patch.

Box 5 shows a northward surface intensified jet of approximately 20 cm/s between the 1,000- and 500-m isobaths in all years. The jet had a very similar location and strength in all observed years and was the most persistent current in the VM-ADCP data set. West of this jet a recirculation current that varied considerably in width, depth, and strength was observed in all years. In 2015 and 2017 we observed an additional northward current with the highest speeds between 100- and 500-m depth, west of the recirculation current.

Box 6 on the Yermak Plateau was only sparsely sampled, but data from 2015, 2016, and 2017 show that highest northeastern current speeds were found on the shelf above the 500-m isobath. The current sections also indicate southwestward flow offshore of the 1,000-m isobath. A strong barotropic (constant with depth) boundary current was found again in Box 7 with its speed, width, and location varying between years. The current, centered around the 700-m isobath, was fastest (approximately 40 cm/s^{-1}) in 2015 and 2017 and slower (approximately 20 cm/s) in 2016. It was not covered in 2014.

Box 8 displays large interannual variability of the boundary current that is likely related to the irregular bathymetry of the area (Malenebukta canyon). In 2017 a strong surface intensified jet was observed between the 1,000 and 500-m isobaths. Box 9 was only sparsely sampled, but current profiles from 2015 and 2016 indicate a broad boundary current along the slope.

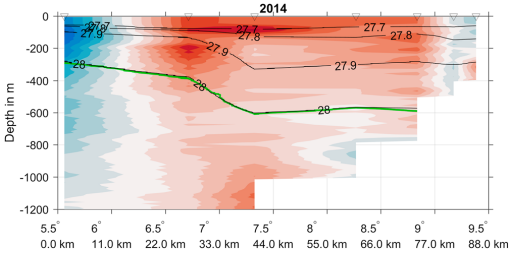

Figure 3. Lowered Acoustic Doppler Current Profiler section along 78.6°N (Box 2). The colored contours show the along-slope current speed ranging from −0.3 to 0.3 m/s^{-1} (color scale can be found in Figure 4), the black contours represent potential density ρ_θ, and the green line depicts the 2 °C isotherm. The triangles mark the locations of stations.

4.2. L-ADCP Sections

The available L-ADCP sections are displayed in Figures 3–5. The L-ADCP section measured in Box 2 in 2014 (Figure 3) agrees well with the averaged VM-ADCP section and shows a wide northward surface intensified boundary current (the WSC) between the 2,000 and 500-m isobaths. A southward recirculating current can be found offshore of the 2,000-m isobath. The L-ADCP sections measured in Box 5 (Figure 4) agree well with the averaged VM-ADCP sections and show a strong and slightly surface intensified boundary current between the 800- and 500-m isobaths in all fully covered sections. Offshore of this flow, a southward recirculating current was observed in 2014. In 2017, only a single station of this transect (marked with a black triangle in Figure 4) was sampled 2 times (23 August and 5 September 2017).

The transect along the Hinlopen trench and across the adjacent shelf showed a similar eastward boundary current centered around the 1,000-m isobath all available years (Figure 5). Unfortunately, no data are available from 2015 and the full width of the boundary current was not sampled. In the Hinlopen trench, the flow was mainly directed along the trench axis that is tilted with a 330° azimuth relative to north. Between 80 and 80.6°N a strong northwestward flow was observed each year with the highest velocity in the upper 100 m. In 2017 we also observed a strong southward current within the Hinlopen strait, south of 80°N.

To compare our L-ADCP and VM-ADCP data to previous studies, we defined AW as water warmer than 2 °C (Beszczynska-Moller et al., 2012). In the L-ADCP sections the lower boundary of AW is indicated by the 2 °C isotherm (green line). West of Svalbard, AW extends to approximately 500-m depth (the AW maximum depth is between 300 and 600 m; Figures 3 and 4), and north of Svalbard the AW layer reaches slightly deeper to approximately 600 m (Figure 5).

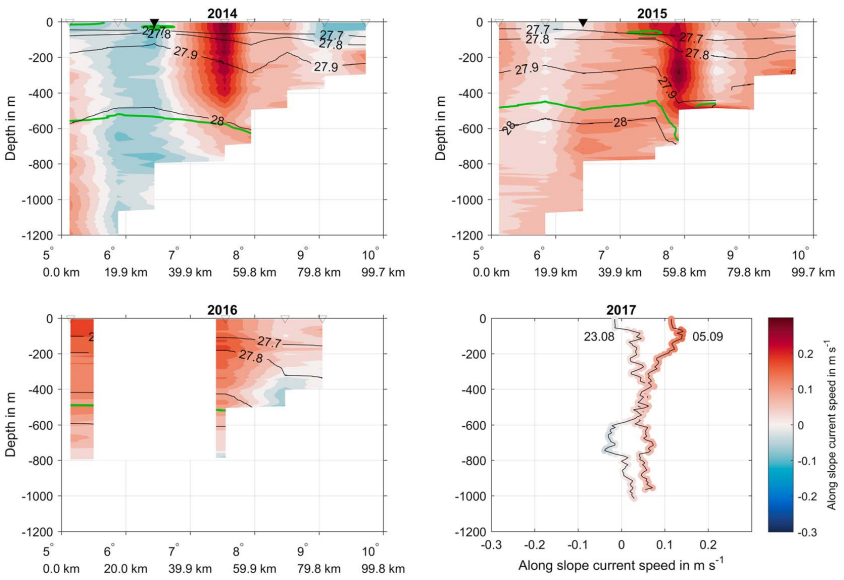

Figure 4. Lowered Acoustic Doppler Current Profiler sections along 79.7°N (Box 5). The colored contours show the along-slope current speed, the black contours represent potential density ρ_θ, and the green line depicts the 2 °C isotherm. The triangles mark the stations, and the filled black triangles mark the location of the two profiles measured in 2017.

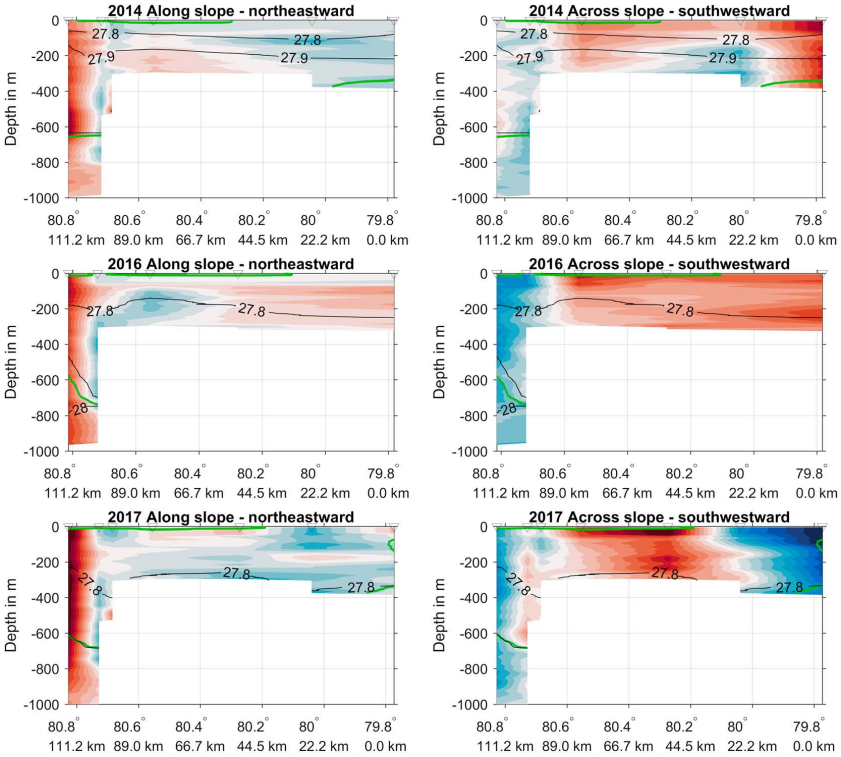

Figure 5. L-ADCP sections along the Hinlopen trench in Box 7 (16°E). The colored contours show the along- and across-slope (shelf break) current speed ranging from −0.3 to 0.3 m/s (color scale can be found in Figure 4), the black contours represent potential density ρ_Θ, and the green line the 2 °C isotherm. The triangles mark the stations.

4.3. Depth-Averaged Current Fields

Maps of the depth averaged (20–500 m) VM-ADCP observations and interpolated current fields for different months and years are shown in Figures 6 and 7. Figure 6 focuses on the WSC and Yermak Plateau and Figure 7 on the shelf and trenches north of Svalbard. The AW boundary current is visible as a strong north-eastward flow along the shelf slope to the west and north of Svalbard.

The observed and interpolated circulation patterns show the WSC meandering in relation to the variable slope bathymetry (in August 2014 and 2015; Figures 6a and 6b). The OM interpolation (Figure 6f) shows divergent and convergent patterns west of Svalbard related to eddies and recirculation. The DF-RBF interpolation extracted some of these eddies and meanders successfully, especially in August 2017 on the Yermak Plateau (Figure 6d).

Between 5 and 10°E and 79 and 80°N, the interpolations indicate a persistent northward boundary current toward the Yermak Plateau (Figure 6). The OM implies that this jet splits into three branches: the narrow and shallow SB that follows the 200-m isobath, the YB flowing along the western slope of the Yermak Plateau, and the YPB that branches off the YB toward east at approximately 80.5°N and 6°E and reunites with the SB near 11°E (Figure 6f). Since the OM interpolation is based on the available data at all times, this does not mean that all the three branches are present at all times. The SB was discernible as strong and narrow jet in the observations and DF-RBF interpolations from August 2015, September 2016, and September 2017. The YB was discernible as meandering flow in August 2015,

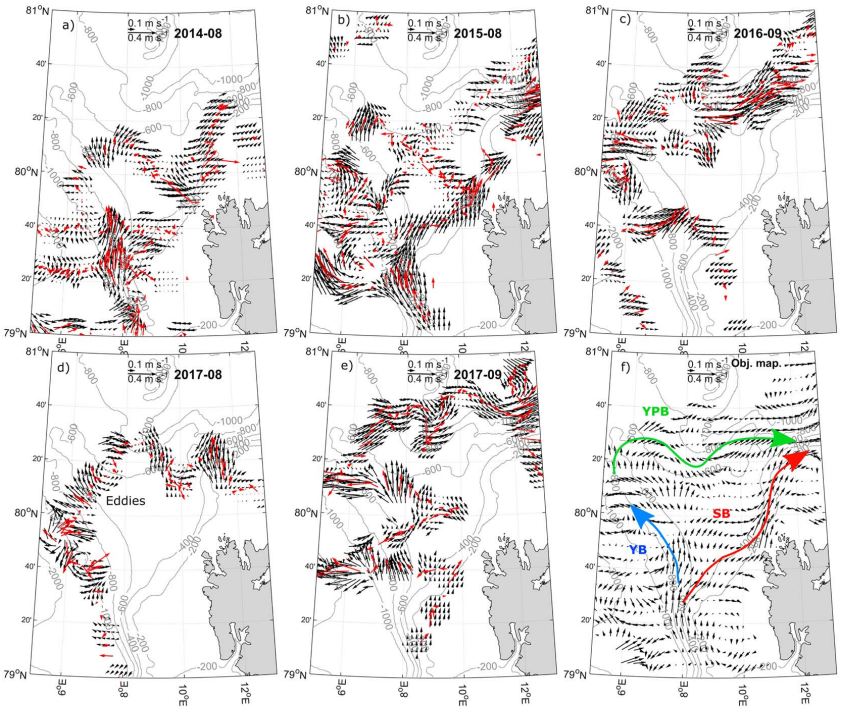

Figure 6. Maps of the observed and interpolated currents on Yermak Plateau. (a–e) The observed currents (red arrows) and divergence-free radial basis function interpolation (black arrows) during months with enough data coverage. Interpolated vectors further than 10 km from the observations are not shown. (f) The objective mapping interpolated current field using all available data. The colored arrows indicate the Atlantic Water branches visible in the objective mapping field and panels a to e: SB, Svalbard Branch (red); YB, Yermak Branch (blue); YPB, Yermak Pass Branch (green).

September 2016, and August and September 2017 and the YPB as meandering flow in September 2016 and 2017.

The OM interpolation suggests that the narrow SB moves toward the shelf around 79.7°N and roughly follows the 400-m isobath north and north-west of Svalbard, whereas the YPB roughly follows the 600-m isobath, and has a much broader and meandering structure. East of 10°E and 80°N the boundary current meanders less and forms a persistent flow that follows the slope (Figure 7). Smaller topographic features such as Malenebukta (north of the Hinlopen trench) seem to have little impact on the large-scale circulation pattern. In the Hinlopen trench, we observed an inflow on the western side and a strong northward outflow on the eastern side.

A map of the OM interpolation error can be found in Figure S3 and shows that the interpolation was least certain (highest interpolation error) in areas with meandering currents west of Svalbard (west of 10°E and south of 79°N), north of 80.5°N on the Yermak Plateau and the sparsely sampled shelf east of 18°E. The boundary current branches between 79°N and Hinlopen Strait are robustly interpolated with significantly less interpolation error.

4.4. Transport Estimates

The three different VM-ADCP-based estimates of the net transport around Svalbard (box average with a local azimuth and a box average azimuth, and transects) are given in Tables S2 and S3. West of Svalbard, we found a northward transport in the upper 500 m ranging between 0.7 and 2.6 Sv for the box method

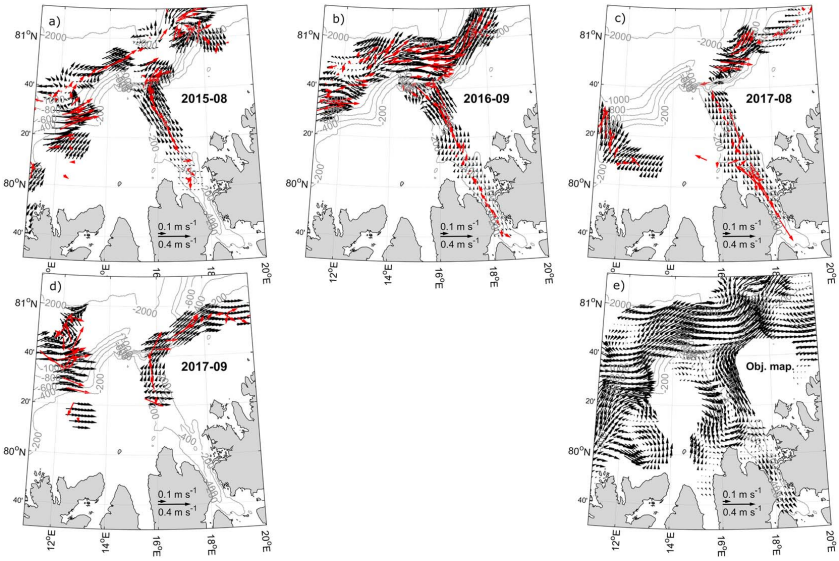

Figure 7. Maps of the observed and interpolated currents north of Spitsbergen. (a–d) The observed currents (red arrows) and divergence-free radial basis function interpolation (black arrow) during month with enough data coverage. Interpolated vectors further than 10 km from the observations are not shown. (e) The objective mapping interpolation using all available data.

and 0.4–4.4 Sv for the transect method; the large range is related to the sparse sampling of the area. Both the box average and transect approach produce a similar transport estimate of about 2 Sv from 79.6°N and poleward (Boxes 4–8, shown in Figure 8). We estimated a transport of 0.8 Sv in the SB and 1.9 Sv in the YPB, based on transects through the interpolated VM-ADCP data set. Because of the uncertainty in the width of the meandering and filamentous YPB, the YPB transport is an order of magnitude estimate and is not as accurate as the SB estimate. The box-averaged transport estimates using the local azimuth (red) are very similar to those using a box-average azimuth (blue).

We also calculated transport from the L-ADCP sections in Boxes 2 and 5 (Table 2). The lateral extent of the L-ADCP section in Box 7 proved too short to obtain reliable transport values. We calculated the total net transport through each section, the net AW transport (water warmer than 2 °C), and net transport in the upper 500 m. The values compare well to the VM-ADCP transport estimates. The AW transport values are similar to the transport in the upper 500 m, because AW was mainly confined to the upper 500 m (Figures 3 and 4).

5. Discussion

The region west and north of the Svalbard archipelago, the northernmost extension of the North Atlantic, is of particular interest with regard to the oceanic heat input to the Arctic Ocean. AW carried northward brings heat, thereby affecting thermal conditions as well as the sea ice cover (e.g., Beszczynska-Möller et al., 2012; Onarheim et al., 2014). The Atlantic current also supplies the region with nutrients and drifting organisms like zooplankton (Basedow et al., 2018; Kosobokova & Hirche, 2009) and micronekton (Knutsen et al., 2017), thereby fueling life north of Svalbard and in the Arctic Ocean (Bluhm et al., 2015; Wassmann et al., 2015). Thus, knowledge about general circulation and transports as well as details of the flow is essential. In this study, we investigated the large-scale AW flow along the western and northern Svalbard shelf break based on a large heterogeneous summer time ADCP data set. We found a persistent boundary current along the shelf slope and a variable offshore flow west of Svalbard, three different AW branches over and around

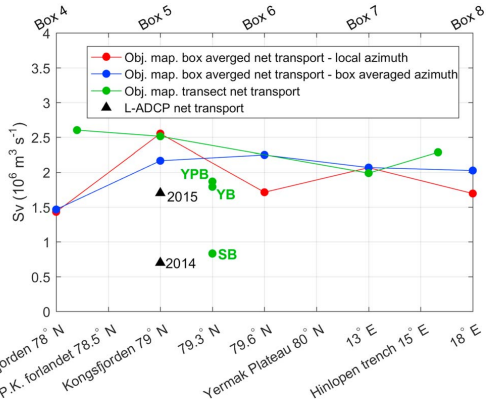

Figure 8. A comparison of net along-slope transport estimates in the upper 500 m around Svalbard: from the Kongsfjord opening to north of Hinlopen trench. The colored lines display transport estimated from the Vessel-Mounted Acoustic Doppler Current Profilers objective mapping data set: blue indicates net along-slope transport calculated by rotating all velocity vectors with the average azimuth of each box, red indicates net along-slope transport calculated by rotating each velocity vector with its local azimuth (slope aspect), and green indicates net along-slope transport calculated through a series of transects (locations displayed in Figure S7). The bold green abbreviations mark the transport estimates for the Yermak Branch (YB), Yermak Pass Branch (YPB), and Svalbard Branch (SB), while the black triangles mark the transport based on the Lowered Acoustic Doppler Current Profiler (L-ADCP) transects.

the Yermak Plateau, and a persistent boundary current along the northern Svalbard shelf slope that is a continuation of the YPB and SB.

5.1. Uncertainty and Limitations

Ocean currents are challenging to measure and interpret, as they vary in both time and space. Common approaches to this problem are limiting the spatial variation by analyzing data from a fixed location (moorings and repeated stations) or limiting the temporal variation by analyzing *snapshots* of the current field (remote sensing and quasi-synoptic transects). In this study, a collection of current measurements that contains both temporal and spatial variability was analyzed with different methods: L-ADCP sections and spatial interpolation to elucidate the spatial variability, and box averaging to analyze the spatiotemporal changes.

How reliable are these methods for separating spatial and temporal variability, and how persistent is the observed circulation system? The box-averaged sections show varying locations and strength of the AW flow each year, but the general flow pattern is similar between the years (Figure 2) and corresponds well with the more sparse L-ADCP sections (Figures 3–5). Although the VM-ADCP data set consists of snapshots of the current field that vary in both space and time, we conclude that careful interpretation of the box averaging and spatial interpolation allows separation of the spatial and temporal variation. However, the objectively mapped areas with sparse data or data from only a single year should be treated with caution, as they might not represent the average circulation pattern accurately. A map of data coverage is shown in Figure S4. Boxes 1, 2, 3, and 9 were sampled less frequently and less uniform than the other boxes, which is reflected in the fluctuating transport estimates for these boxes, that were therefore not shown in Figure 8. We thus focus our discussion and conclusions on the areas with reliable data coverage: Boxes 4–8 and the Hinlopen trench.

The averaging radius used for OM supresses spatial patterns smaller than 25 km and thus effectively filters out eddies that have radii of 5–8 km in the study area (Crews et al., 2018). Also, note that OM is biased to potentially underestimating rather than overestimating current speeds (Thomson & Emery, 2001). In our study area, the growth period for instabilities in summer is approximately 2 days (von Appen et al., 2016). Our L-ADCP sections were measured during 2–3 days and could thus contain variability from current meanders in addition to the observed persistent north-eastward flow.

The AOTIM-5 tidal model is barotropic and cannot represent the baroclinic currents caused by interference effects and internal waves excited by tidal flow. Strong baroclinic tides and internal waves have been shown to occur along the Barents Sea opening, the YB, and the shelf and slopes around Svalbard (Fer et al., 2015; Kurkina & Talipova, 2011; Padman et al., 1992; Skarðhamar et al., 2015). Fer et al. (2015) estimated that around the Yermak Plateau, approximately 50% of the M_2 tidal energy is converted to internal tides that

Table 2
Along-Slope Transport Estimated From the L-ADCP Sections West of Svalbard

	L-ADCP section along 79.7°N - Box 5		L-ADCP section along 78.6°N - Box 2
Year	2014	2015	2014
Net transport in Sv	1.4	2.3	2.3
Net AW (Θ > 2 °C) transport in Sv	0.9	1.7	1.3
Net transport in the upper 500 m in Sv	0.7	1.7	1.2

Note. L-ADCP, Lowered Acoustic Doppler Current Profiler.

are trapped along the topography. As a result, the velocity fields detided using the barotropic tidal model can contain errors. To assess the sensitivity to detiding, we compared the OM interpolation current field based on the VM-ADCP data before and after the removal of tides. The current fields show almost identical patterns (Figures S8 and S9), indicating that the size of the data set and the interpolation scale filter out most tidal currents. The discrepancies between the two current fields are mainly found between 80 and 81°N on the western Yermak Plateau, a region that was only sparsely sampled. Given our focus on the depth-averaged circulation patterns, the SB and YPB, and the limited effect of barotropic tides on our results, we conclude that the AOTIM-5 model removes tidal currents sufficiently well for our purposes.

Since the u and v components of the current fields are interpolated independently during the OM interpolation, the resulting current field is not volume and mass conserving (divergence/convergence displayed in Figure S5). The DF-RBF interpolation, on the other hand, is volume and mass conserving but cannot handle inconsistent data from multiple surveys and gives noisy estimates when too much temporal variation is present in the data set. We used DF-RBFS to interpolate data only from within a month. Figures 6 and 7 compare the circulation fields from the two different interpolation methods and show similar features and circulation patterns. The similarity between OM and monthly DF-RBF current fields, and the consistency of the 2-Sv transport estimates from Boxes 4 to 8, indicates that our findings in Boxes 4–8 and the Hinlopen trench are robust.

5.2. Circulation Patterns and Pathways

The observed current patterns agree well with previous observations and modeling results. Already Helland-Hansen and Nansen (1912) found that a part of the WSC recirculates westward and another part splits into several branches flowing northward and eastward. The presence of the SB and YB has been confirmed frequently since then (Aagaarda et al., 1987), whereas the YPB has been observed and modeled less frequently. It has previously only been observed by acoustically tracked floats (Gascard et al., 1995) and in model simulations (during winter by Hattermann et al., 2016; Koenig et al., 2017; and Crews et al., 2018, and during the entire year by Wekerle et al., 2017). Our observations show that the YPB also exists in summer (Figures 6 and 7). Both the SB and YPB flow over shallow areas with tidal speeds up to 0.2 m/s (Fer et al., 2015; Padman & Erofeeva, 2004), resulting in oscillatory flow patterns and lateral and horizontal mixing.

We found that the circulation patterns from high-resolution models (Hattermann et al., 2016; Koenig et al., 2017; Wekerle et al., 2017) agree well with our observations, especially in pointing out the importance of the YPB for AW transport into the Arctic. The strength and pathways of AW flow around Svalbard are forced by multiple factors: the large-scale oceanic and atmospheric circulation system (Chatterjee et al., 2018; Kawasaki & Hasumi, 2016), the local wind field (Inall et al., 2015), topography, instabilities, and eddies (Hattermann et al., 2016; von Appen et al., 2016; Wekerle et al., 2017). The average large-scale AW flow is confined to slopes, plateaus, and trenches, implying that the bottom topography is a major controlling factor. However, the strength of the three AW branches likely varies with time and season and is related to external forcing such as the strength of the North Atlantic gyres, the wind field, and the instability of the WSC and the rate of eddy formation (Chatterjee et al., 2018; Kawasaki & Hasumi, 2016; Wekerle et al., 2017).

Observations from annual IOPAN summer cruises showed a strong but variable WSC in VM- and L-ADCP measurements between 78 and 79°N and 8 and 12°E, along the shelf break west of Prins-Karls Forland (Walczowski et al., 2005; Walczowski & Piechura, 2006). This agrees with the WSC we observed in the averaged sections (Figure 2) and the objectively mapped data set (Figure 6). In 2003, Walczowski et al. (2005) observed a broad WSC core west of Isfjorden (their section S) between the 1,500- and 200-m isobaths. This concurs with our averaged section in Box 1 that shows a similarly strong along-slope current. Their section Z agrees with our averaged section from Box 2, as both sections show a weaker along-slope current than in Box 1 and some southward flow. Our averaged sections from Box 3 and their section EB agree as well, showing a stronger along-slope northward flow than in Box 2 and a southward flow that varies between the years.

The averaged sections roughly agree with the mooring array and transect observations of Beszczynska-Moller et al. (2012). They observed the WSC core between the 1,200- and 200-m isobaths along the 78.8°N section (west of the northern tip of Prins-Karls Forland). The OM interpolation does not show a strong

northward WSC at this section, but in the areas 50 km south and north of the 78.8°N section. The averaged section in Box 3 (that cover the 78.8°N section) only shows a strong WSC in 2015, and variable currents in 2014 and 2016 (similar to Box 2), whereas Boxes 1 and 4 show a strong boundary current in all sufficiently sampled years. These disparities and discontinuities illustrate the strong temporal and spatial variability of the WSC and can be attributed to undersampling and the scattered nature of our data set. Our snapshot ADCP measurements in Boxes 1 to 3 do most likely not represent the undulating, recirculating, and unstable parts of the WSC reliably. Boxes 4–8 and the Hinlopen trench show better data coverage and correspondingly a more consistent circulation pattern and consistent transport estimates. The discontinuities and divergence in the OM interpolation west of Svalbard (Boxes 1–3) are likely related to eddy activity and recirculation events. The WSC is a highly dynamic current that can be both barotropically and baroclinically unstable (Teigen et al., 2010, 2011; von Appen et al., 2016). Mooring and modeling studies of the WSC and AW currents north of Svalbard agree that largest volume transport and most instabilities occur in winter (Beszczynska-Moller et al., 2012; Koenig et al., 2017; von Appen et al., 2016; Wekerle et al., 2017). Late summer is the period when the WSC is most stable, confirming that our efforts to map the average circulation pattern in the July–September period are purposeful.

North of Svalbard (Figures 6 and 7; north of 80.3°N, and east of 10°E) the SB and YPB join into a persistent boundary current that follows the large-scale features of the shelf slope. Interestingly, the steep canyon-like bathymetry feature termed Malenebukta (80.8°N, 14°E) does not deflect the average boundary current. However, this steep bathymetric structure likely renders the boundary current less stable as the current partly detaches from the slope. The location and strength of the boundary current agree with previous observations farther east and results of model studies (Aksenov et al., 2011; Cokelet et al., 2008; Crews et al., 2018; Pérez-Hernández et al., 2017; Pnyushkov et al., 2015; Vaage et al., 2016; Wekerle et al., 2017). The data coverage is not sufficient to detect whether, and if so where, the YB joins the boundary current.

Our data revealed an inflow of AW on the western side of the Hinlopen trench and outflow on its eastern side. Similar circulation patterns have been found farther east in Kvitøyrenna (Pérez-Hernández et al., 2017) and farther south in Isfjorden (Nilsen et al., 2016). Such circulation is important for bringing warm AW onto the shelf in the deeper trenches. The Hinlopen region is a hot spot for marine mammals (Storrie et al., 2018), which might be linked to the supply of AW facilitating suitable habitat conditions.

5.3. Barotropic and Baroclinic Currents

Analysis of ADCP time series from the mooring array along the 78.8°N (Fram Strait section) showed that the WSC was barotropically unstable during ~40% and baroclinically unstable during ~30% of the measurement record (Teigen et al., 2010, 2011). Further investigations revealed a distinct seasonal cycle in generation of instabilities and eddy kinetic energy: though the WSC is potentially unstable year round, it is most unstable in winter due to reduced stratification and stronger offshore currents related to winter cooling and gyre circulation in the Nordic Seas (von Appen et al., 2016). The eddies formed by the unstable WSC facilitate AW recirculation in Fram Strait (Hattermann et al., 2016) and, beyond the Yermak Plateau, AW transport from the boundary current into the Nansen Basin (Crews et al., 2018).

West of Svalbard, the averaged sections (Figure 2) and L-ADCP profiles (Figures 3 and 4) show a combination of barotropic (constant with depth) and baroclinic currents (surface intensified). The L-ADCP sections at 78.6 and 79.7°N (Figures 3 and 4) show a strong and slightly baroclinic boundary current in the 2 years the section was covered, which agrees well in terms of location and strength with the northward current along the 1,000-m isobath present in the averaged sections in Box 5 (Figure 2). The surface intensified boundary current observed in Box 5 is the most persistent feature in our data set and represents the WSC core before it splits into the three branches. Its persistence compared to other observed currents could be related to local forcing or simply the sparse and irregular sampling in other regions. Due to its baroclinicity (Figure 2), the branching WSC might not be as constrained to follow f/H contours in this area, compared to other slope areas. This could explain why both the SB and YPB can move slightly up-slope on their way across the Yermak Plateau (Figure 6). The combination of a barotropic and baroclinic WSC agrees well with previous studies (Nilsen et al., 2016; von Appen et al., 2016; Walczowski et al., 2005).

Pérez-Hernández et al. (2017) suggest that the boundary current is more barotropic close to the continental slope and more baroclinic (surface intensified) farther offshore as the AW layer expands within the current.

This agrees with the average VM-ADCP sections in Box 1 (Figure 2), where in 2014 and 2016 the boundary current was baroclinic and wide between the 2,000- and 1,000-m isobaths, whereas in 2017 it was barotropic, narrow, and centered at approximately the 500-m isobath.

Here we must note that our VM-ADCP data set mainly covers a depth range between 20 and 500 m; thus, the Polar Surface Water layer (approximately 10–50 m thick) is not properly represented in the VM-ADCP data set. Any shear currents related to the halocline are likely not resolved, since the VM-ADCP data above 20 m are mostly filtered out during postprocessing due to interference and bubble effects.

5.4. Transport

Since 1997 currents in Fram Strait have been monitored along 78.8°N (Box 3) by an array of moored current meters (point and profiling instruments) and CTD sensors (Beszczynska-Moller et al., 2012). Analysis of these data indicates a long-term mean northward AW ($\Theta > 2$ °C) transport of 3.0 Sv through Fram Strait, consisting of a boundary current (termed the WSC core in Beszczynska-Moller et al., 2012) transporting on average 1.8 Sv (1.3 Sv of AW) and a variable offshore current, transporting 2–6 Sv. Whereas the offshore current showed considerable seasonality (strongest in winter), the boundary current (WSC core) manifested little intra-annual and inter-annual variability. For the August–September period, the moorings recorded an average northward AW transport of 2.5 Sv. Beszczynska-Moller et al. (2012) defined AW as water warmer than 2 °C, which approximately covers the upper 500 m of the water column (Figures 3–5) and can thus be compared directly with our transport estimates.

The VM-ADCP data coverage was best in Boxes 4–8, and in Box 5 we estimated an along-slope transport of 1.5 Sv (box-average method) and 2.6 Sv (transect method) in the upper 500 m (Figure 8 and Tables S2 and S3). This compares well with the mooring-based average August–September AW transport estimates from Beszczynska-Moller et al. (2012). Transport estimates from the L-ADCP transects in the same region, on the other hand, gave northward AW transports of 0.9 and 1.7 Sv in 2014 and 2015 respectively (Table 2). Although this is close to the long-term mean of 1.3 Sv for AW slightly further south (Beszczynska-Moller et al., 2012), it is substantially lower than the VM-ADCP data and the August–September average from moorings. It is also somewhat lower than the 2 Sv of northward transport (in the upper 700 m) in the boundary current, and 1–3 Sv in the offshore current, as reported by Basedow et al. (2018) for the region in Boxes 3 and 4 based on L-ADCP data from January, May, and August 2014. Furthermore, is it lower than the AW transport estimates presented by Walczowski et al. (2005) based on L-ADCP data, but this is due to them using a wider definition of AW ($\Theta > 0$ °C instead of $\Theta > 2$ °C). Deviations between the transports based on L-ADCP and VM-ADCP are most likely related to the differences sampling methods (horizontal resolution and temporal average vs. snapshot).

The interannual variation of AW transport west of Svalbard is large. Transport estimates from a model study revealed average AW summer transports west of Svalbard of 2.1 Sv in 2014 and 1.3 Sv in 2015 (Koenig et al., 2017). Even larger differences were evident in our 2014 and 2015 L-ADCP transport estimates in Box 5 (Table 2). These differences illustrate the large variability in the offshore current as well as the considerable current variability due to WSC meanders and eddies (Hattermann et al., 2016; von Appen et al., 2016). Based on this, we find that averaging over all the years 2014–2016 to be the most reliable method for calculating average transports.

North of Svalbard (Boxes 6–8), the OM revealed along-slope transports of 1.7–2.2 Sv in the upper 500 m (Table S3), which is consistent with estimates of the mean AW transport of 2.3 Sv ($\Theta > 1$ °C) measured in the boundary current northeast of Svalbard (at 30°E) by Pérez-Hernández et al. (2017). Our results also show that the YPB, which sheds off the YB at approximately 80.5°N (Figure 7), can be as important as the SB in transporting AW across the Yermak Plateau during summer.

Averaged over all boxes with sufficient data coverage (Boxes 4–8), the most reliable estimate of the August–September AW transport northwest and north of Svalbard is 2 Sv. Recent yearlong mooring observations in the AW boundary current at 31°E show that the current velocity increases significantly over bottom depths of around 800 m—the depth of the Yermak Pass—in fall and winter (Renner et al., 2018). This supports the finding of Koenig et al. (2017) that the YPB is stronger in fall and winter and that this branch provides the overall largest inflow of AW from Fram Strait to the Arctic Ocean.

6. Conclusions

The transport estimates and circulation patterns, obtained from analysis of sparse VM-ADCP data, yield a realistic representation of averaged currents and transports. Collection of current profiling measurements from vessels can thus provide a large potential data source. In our study, we limited the number data sets to the cruises conducted by the authors. A more comprehensive collection using data from all vessels operated in the region merits further analysis. We found an average along-slope transport of 2 Sv of AW northwest and north of Svalbard, which agrees well with literature. The most persistent current pattern found in our study was the boundary current located between 79 and 80°N and between the 1,000- and 400-m isobaths, representing the WSC core. The WSC splits into the YB, YPB and SB, of which the latter two coalesce north of Svalbard and partly follow the trench systems along the shelf. AW enters the Hinlopen trench on the western side and exits on the eastern side, transporting heat and nutrients toward the shelf and strait that could boost local productivity. Based on our observations, we propose that the YPB is comparable to the SB in transporting AW into the Arctic Ocean in summer.

Acknowledgments

We would like to thank the crew and scientists onboard RV Helmer Hanssen, RV Håkon Mosby, and RV Oceania for collecting and sharing ADCP data. We would like to thank the Editor and two anonymous reviewers for helping to improve this manuscript. The ADCP data are available under the following link: https://doi.org/10.21335/NMDC-1323631641. We declare no competing interests. Financial support of the study comes from the Research Council of Norway through the project "The Arctic Ocean Ecosystem" – (SI_ARCTIC, RCN 228896) and from the Institute of Marine Research, Bergen. The work is a contribution to the Barents Sea Ecosystem Programs at Institute of Marine Research, Bergen. Carbonbridge data collection was supported through the Research Council of Norway (RCN 226415).

References

Aagaarda, K., Foldvik, A., & Hillman, S. R. (1987). The West Spitsbergen Current: Disposition and water mass transformation. *Journal of Geophysical Research*, *92*(C4), 3778–3784. https://doi.org/10.1029/JC092iC04p03778

Aksenov, Y., Ivanov, V. V., Nurser, A. J. G., Bacon, S., Polyakov, I. V., Coward, A. C., et al. (2011). The arctic circumpolar boundary current. *Journal of Geophysical Research*, *116*, C09017. https://doi.org/10.1029/2010JC006637

Basedow, S. L., Sundfjord, A., von Appen, W.-J., Halvorsen, E., Kwasniewski, S., & Reigstad, M. (2018). Seasonal variation in transport of zooplankton into the Arctic Basin through the Atlantic gateway, Fram Strait. *Frontiers in Marine Science*, *5*(June), 1–22. https://doi.org/10.3389/fmars.2018.00194

Berge, J., Varpe, Ø., Moline, M. A., Wold, A., Renaud, P. E., Daase, M., & Falk-Petersen, S. (2012). Retention of ice-associated amphipods: Possible consequences for an ice-free Arctic Ocean. *Biology Letters*, *8*(6), 1012–1015. https://doi.org/10.1098/rsbl.2012.0517

Beszczynska-Moller, A., Fahrbach, E., Schauer, U., & Hansen, E. (2012). Variability in Atlantic water temperature and transport at the entrance to the Arctic Ocean, 1997–2010. *ICES Journal of Marine Science*, *69*(5), 852–863. https://doi.org/10.1093/icesjms/fss056

Bretherton, F. P., Davis, R. E., & Fandry, C. B. (1976). A technique for objective analysis and design of oceanographic experiment applied to MODE-73. *Deep Sea Research*, *23*(April 1975), 559–582.

Chatterjee, S., Raj, R. P., Bertino, L., Skagseth, Ø., Ravichandran, M., & Johannessen, O. M. (2018). Role of Greenland Sea gyre circulation on Atlantic water temperature variability in the Fram Strait. *Geophysical Research Letters*, *45*, 8399–8406. https://doi.org/10.1029/2018GL079174

Cokelet, E. D., Tervalon, N., & Bellingham, J. G. (2008). Hydrography of the West Spitsbergen current, Svalbard Branch: Autumn 2001. *Journal of Geophysical Research*, *113*, C01006. https://doi.org/10.1029/2007JC004150

Crews, L., Sundfjord, A., Albretsen, J., & Hattermann, T. (2018). Mesoscale eddy activity and transport in the Atlantic water inflow region north of Svalbard. *Journal of Geophysical Research: Oceans*, *123*, 201–215. https://doi.org/10.1002/2017JC013198

Descamps, S., Aars, J., Fuglei, E., Kovacs, K. M., Lydersen, C., Pavlova, O., et al. (2016). Climate change impacts on wildlife in a High Arctic archipelago - Svalbard, Norway. *Global Change Biology*, (June), 1–13. https://doi.org/10.1111/gcb.13381

Falk-Petersen, S., Pavlov, V., Berge, J., Cottier, F., Kovacs, K. M., & Lydersen, C. (2014). At the rainbow's end: High productivity fueled by winter upwelling along an Arctic shelf. *Polar Biology*, *38*(1), 5–11. https://doi.org/10.1007/s00300-014-1482-1

Falk-Petersen, S., Pavlov, V., Timofeev, S., & Sargent, J. R. (2007). Climate variability and possible effects on arctic food chains: The role of Calanus. In J. B. Ørbæk, R. Kallenborn, I. Tombre, E. N. Hegseth, S. Falk-Petersen, & A. H. Hoel (Eds.), *Arctic Alpine Ecosystems and People in a Changing Environment* (Chap. 9, pp. 147–166). Berlin, Heidelberg: Springer.

Fer, I., Müller, M., & Peterson, A. K. (2015). Tidal forcing, energetics, and mixing near the Yermak Plateau. *Ocean Science*, *11*, 287–304. https://doi.org/10.5194/os-11-287-2015

Fer, I., Skogseth, R., & Geyer, F. (2010). Internal waves and mixing in the marginal ice zone near the Yermak Plateau. *Journal of Physical Oceanography*, *40*(7), 1613–1630. https://doi.org/10.1175/2010JPO4371.1

Gascard, J.-C., Richez, C., & Rouault, C. (1995). New insights on large-scale oceanography in Fram Strait: The West Spitsbergen Current. *Oceanography of the Arctic: Marginal Ice Zones and Continental Shelves*, *49*, 131–182. https://doi.org/10.1029/CE049p0131

Hattermann, T., Isachsen, P. E., von Appen, W.-J., Albretsen, J., & Sundfjord, A. (2016). Eddy-driven recirculation of Atlantic water in Fram Strait. *Geophysical Research Letters*, *43*, 3406–3414. https://doi.org/10.1002/2016GL068323

Haug, T., Bogstad, B., Chierici, M., Gjøsæter, H., Hallfredsson, E. H., Høines, Å. S., et al. (2017). Future harvest of living resources in the Arctic Ocean north of the Nordic and Barents Seas: A review of possibilities and constraints. *Fisheries Research*, *188*, 38–57. https://doi.org/10.1016/j.fishres.2016.12.002

Helland-Hansen, B., & Nansen, F. (1912). The Sea West of Spitsbergen. *Videnskapsselskapets Skrifter. I. Mat.-Naturv. Klasse* 1912, 12.

Hummon, J. (2016). CODAS ADCP processing documentation. Retrieved May 1, 2016, from https://currents.soest.hawaii.edu/docs/adcp_doc/codas_doc/

Inall, M. E., Nilsen, F., Cottier, F. R., & Daae, R. (2015). Shelf/fjord exchange driven by coastal-trapped waves in the Arctic. *Journal of Geophysical Research: Oceans*, *120*, 8283–8303. https://doi.org/10.1002/2015JC011277

Ivanov, V., Alexeev, V., Koldunov, N. V., Repina, I., Sandø, A. B., Smedsrud, L. H., & Smirnov, A. (2016). Arctic Ocean heat impact on regional ice decay: A suggested positive feedback. *Journal of Physical Oceanography*, *46*(5), 1437–1456. https://doi.org/10.1175/JPO-D-15-0144.1

Ivanov, V. V., Alexeev, V. A., Repina, I., Koldunov, N. V., & Smirnov, A. (2012). Tracing Atlantic water signature in the arctic sea ice cover east of Svalbard. *Advances in Meteorology*, *2012*, 1–11. https://doi.org/10.1155/2012/201818

Jakobsson, M., Mayer, L., Coakley, B., Dowdeswell, J. A., Forbes, S., Fridman, B., et al. (2012). The International Bathymetric Chart of the Arctic Ocean (IBCAO) version 3.0. *Geophysical Research Letters*, *39*, L12609. https://doi.org/10.1029/2012GL052219

Kawasaki, T., & Hasumi, H. (2016). The inflow of Atlantic water at the Fram Strait and its interannual variability. *Journal of Geophysical Research: Oceans*, *121*, 502–519. https://doi.org/10.1002/2015JC011375

Knutsen, T., Wiebe, P. H., Gjøsæter, H., Ingvaldsen, R. B., & Lien, G. (2017). High latitude epipelagic and mesopelagic scattering layers—A reference for future Arctic ecosystem change. *Frontiers in Marine Science*, *4*(November). https://doi.org/10.3389/fmars.2017.00334

Koenig, Z., Provost, C., Villacieros-Robineau, N., Sennéchael, N., Meyer, A., Lellouche, J. M., & Garric, G. (2017). Atlantic waters inflow north of Svalbard: Insights from IAOOS observations and Mercator Ocean global operational system during N-ICE2015. *Journal of Geophysical Research: Oceans*, *122*, 1254–1273. https://doi.org/10.1002/2016JC012424

Kosobokova, K., & Hirche, H. J. (2009). Biomass of zooplankton in the eastern Arctic Ocean—A base line study. *Progress in Oceanography*, *82*(4), 265–280. https://doi.org/10.1016/j.pocean.2009.07.006

Kurkina, O. E., & Talipova, T. G. (2011). Huge internal waves in the vicinity of the Spitsbergen Island (Barents Sea). *Natural Hazards and Earth System Sciences*, *11*(3), 981–986. https://doi.org/10.5194/nhess-11-981-2011

Meyer, A., Sundfjord, A., Fer, I., Provost, C., Villacieros Robineau, N., Koenig, Z., et al. (2017). Winter to summer oceanographic observations in the Arctic Ocean north of Svalbard. *Journal of Geophysical Research: Oceans*, *122*, 6218–6237. https://doi.org/10.1002/2016JC012391

Nilsen, F., Skogseth, R., Vaardal-Lunde, J., & Inall, M. (2016). A simple shelf circulation model: Intrusion of Atlantic water on the West Spitsbergen shelf. *Journal of Physical Oceanography*, *46*(4), 1209–1230. https://doi.org/10.1175/JPO-D-15-0058.1

Onarheim, I. H., Smedsrud, L. H., Ingvaldsen, R. B., & Nilsen, F. (2014). Loss of sea ice during winter north of Svalbard. *Tellus Series A: Dynamic Meteorology and Oceanography*, *66*, 1–9. https://doi.org/10.3402/tellusa.v66.23933

Padman, L., & Erofeeva, S. (2004). A barotropic inverse tidal model for the Arctic Ocean. *Geophysical Research Letters*, *31*, L02303. https://doi.org/10.1029/2003GL019003

Padman, L., Plueddemann, A. J., Muench, R. D., & Pinkel, R. (1992). Diurnal tides near the Yermak Plateau. *Journal of Geophysical Research*, *97*(C8), 12,639–12,652. https://doi.org/10.1029/92JC01097

Pérez-Hernández, M. D., Pickart, R. S., Pavlov, V., Våge, K., Ingvaldsen, R., Sundfjord, A., et al. (2017). The Atlantic water boundary current north of Svalbard in late summer. *Journal of Geophysical Research: Oceans*, *119*, 7123–7138. https://doi.org/10.1002/2016JC012486

Piechura, J., & Walczowski, W. (2009). Warming of the West Spitsbergen Current and sea ice north of Svalbard. *Oceanologia*, *51*(2), 147–164. https://doi.org/10.5697/oc.51-2.147

Pnyushkov, A. V., Polyakov, I. V., Ivanov, V. V., Aksenov, Y., Coward, A. C., Janout, M., & Rabe, B. (2015). Structure and variability of the boundary current in the Eurasian Basin of the Arctic Ocean. *Deep-Sea Research Part I: Oceanographic Research Papers*, *101*, 80–97. https://doi.org/10.1016/j.dsr.2015.03.001

Polyakov, I. V., Pnyushkov, A. V., Alkire, M. B., Ashik, I. M., Baumann, T. M., Carmack, E. C., et al. (2017). Greater role for Atlantic inflows on sea-ice loss in the Eurasian Basin of the Arctic Ocean. *Science*, *8204*(April). https://doi.org/10.1126/science.aai8204

Proshutinsky, A., Dukhovskoy, D., Timmermans, M., Krishfield, R., & Bamber, J. L. (2015). Arctic circulation regimes. *Philosophical Transactions of the Royal Society A: Mathematical, Physical and Engineering Sciences*, *373*(2052), 20140160. https://doi.org/10.1098/rsta.2014.0160

Renner, A. H. H., Sundfjord, A., Janout, M. A., Ingvaldsen, R. B., Beszczynska-Möller, A., Pickart, R. S., & Pérez-Hernández, M. D. (2018). Variability and redistribution of heat in the Atlantic water boundary current north of Svalbard. *Journal of Geophysical Research: Oceans*, *123*, 6373–6391. https://doi.org/10.1029/2018JC013814

Rogowski, P., Terrill, E., & Chen, J. (2014). Observations of the frontal region of a buoyant river plume using an autonomous underwater vehicle. *Journal of Geophysical Research: Oceans*, *119*, 7549–7567. https://doi.org/10.1002/2014JC010392

Rudels, B., Korhonen, M., Schauer, U., Pisarev, S., Rabe, B., & Wisotzki, A. (2015). Circulation and transformation of Atlantic water in the Eurasian Basin and the contribution of the Fram Strait inflow branch to the Arctic Ocean heat budget. *Progress in Oceanography*, *132*, 128–152. https://doi.org/10.1016/j.pocean.2014.04.003

Skagseth, Ø., Furevik, T., Ingvaldsen, R., Loeng, H., Mork, K. A., Orvik, K. A., & Ozhigin, V. (2008). Volume and heat transports to the Arctic Ocean via the Norwegian and Barents seas. *Arctic-Subarctic Ocean Fluxes: Defining the Role of the Northern Seas in Climate*, 45–64. https://doi.org/10.1007/978-1-4020-6774-7_3

Skarðhamar, J., Skagseth, Ø., & Albretsen, J. (2015). Diurnal tides on the Barents Sea continental slope. *Deep Sea Research Part I: Oceanographic Research Papers*, *97*, 40–51. https://doi.org/10.1016/j.dsr.2014.11.008

Smedsrud, L. H., Esau, I., Ingvaldsen, R. B., Eldevik, T., Haugan, P. M., Li, C., et al. (2013). The role of the Barents Sea in the Arctic climate system. *Reviews of Geophysics*, *51*, 415–449. https://doi.org/10.1002/rog.20017

Storrie, L., Lydersen, C., Andersen, M., Wynn, R. B., & Kovacs, K. M. (2018). Determining the species assemblage and habitat use of cetaceans in the Svalbard Archipelago, based on observations from 2002 to 2014. *Polar Research*, *37*(1), 1463065. https://doi.org/10.1080/17518369.2018.1463065

Teigen, S. H., Nilsen, F., & Gjevik, B. (2010). Barotropic instability in the West Spitsbergen Current. *Journal of Geophysical Research*, *115*, C07016. https://doi.org/10.1029/2009JC005996

Teigen, S. H., Nilsen, F., Skogseth, R., Gjevik, B., & Beszczynska-Möller, A. (2011). Baroclinic instability in the West Spitsbergen Current. *Journal of Geophysical Research*, *116*, C07012. https://doi.org/10.1029/2011JC006974

Thomson, R., & Emery, W. (2001). *Data analysis methods in physical oceanography*. Heidelberg: Elsevier.

Vaage, K., Pickart, R. S., Pavlov, V., Lin, P., Torres, D. J., Ingvaldsen, R., et al. (2016). The Atlantic water boundary current in the Nansen Basin: Transport and mechanisms of lateral exchange. *Journal of Geophysical Research: Oceans*, *121*, 6946–6960. https://doi.org/10.1002/2016JC011715

Vennell, R., & Beatson, R. (2006). Moving vessel acoustic Doppler current profiler measurement of tidal stream function using radial basis functions. *Journal of Geophysical Research*, *111*, C09002. https://doi.org/10.1029/2005JC003321

Vennell, R., & Beatson, R. (2009). A divergence-free spatial interpolator for large sparse velocity data sets. *Journal of Geophysical Research*, *114*, C10024. https://doi.org/10.1029/2008JC004973

Visbeck, M. (2002). Deep velocity profiling using lowered acoustic Doppler current profilers: Bottom track and inverse solutions. *Journal of Atmospheric and Oceanic Technology*, *19*(5), 794–807. https://doi.org/10.1175/1520-0426(2002)019<0794:DVPULA>2.0.CO;2

von Appen, W.-J., Schauer, U., Hattermann, T., & Beszczynska-Möller, A. (2016). Seasonal cycle of mesoscale instability of the West Spitsbergen Current. *Journal of Physical Oceanography*, *46*, 1231–1254. https://doi.org/10.1175/JPO-D-15-0184.1

Walczowski, W., Piechura, J., Osinski, R., & Wieczorek, P. (2005). The West Spitsbergen Current volume and heat transport from synoptic observations in summer. *Deep-Sea Research Part I: Oceanographic Research Papers*, *52*(8), 1374–1391. https://doi.org/10.1016/j.dsr.2005.03.009

Wassmann, P., Kosobokova, K. N., Slagstad, D., Drinkwater, K. F., Hopcroft, R. R., Moore, S. E., et al. (2015). The contiguous domains of Arctic Ocean advection: Trails of life and death. *Progress in Oceanography*, *139*, 42–65. https://doi.org/10.1016/j.pocean.2015.06.011

Wekerle, C., Wang, Q., von Appen, W.-J., Danilov, S., Schourup-Kristensen, V., & Jung, T. (2017). Eddy-resolving simulation of the Atlantic water circulation in the Fram Strait with focus on the seasonal cycle. *Journal of Geophysical Research: Oceans*, *122*, 8385–8405. https://doi.org/10.1002/2017JC012974

Erratum

In the originally published version of this article, the survey name given in the third row of Table 1 was incorrectly given as IMR survey S2014618. The correct survey name is UNIS AGF214 survey HM2014618; the error did not impact the scientific content of the paper, and has now been corrected. This may be considered the official version of record.

Journal of Geophysical Research: Oceans

Supporting Information for

Atlantic Water pathways along the north-western Svalbard shelf mapped using vessel-mounted current profilers

Sebastian Menze[1,2], Randi B. Ingvaldsen[1], Peter Haugan[1,2], Agnieszka Beszczynska-Moeller[3], Ilker Fer[2], Arild Sundfjord[4], Stig Falk-Petersen[5]

[1]Institute of Marine Research, Bergen, Norway

[2]Geophysical Institute, University of Bergen, Norway

[3]Institute of Oceanology, Polish Academy of Sciences, Sopot, Poland

[4]Norwegian Polar Institute, Tromsø, Norway

[5]Akvaplan-niva AS, Tromsø, Norway

Corresponding author: Sebastian Menze (sebastian.menze@hi.no)

Contents of this file

Introduction

This document contains figures and tables that show additional aspects of the VM-ADCP datasets described in the main text.

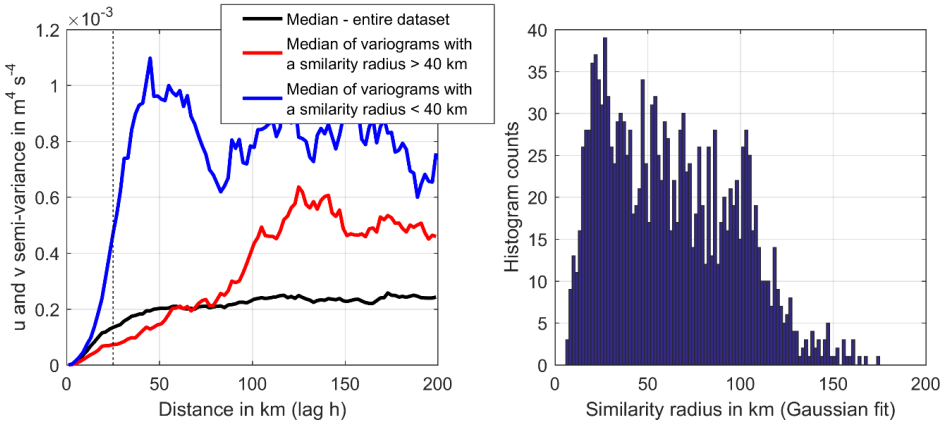

Figure S1. Left panel shows the median (solid black line) cross-semi-variance of the depth averaged VM-ADCP current dataset. The similarity radius was calculated for each data point as standard deviation of a Gaussian fit to each data point's cross-semi-variance. In the left panel, the red and blue line show the median cross-semi-variance for data points with a similarity radius larger or smaller than 40 km. The dashed black line indicates the 25 km standard deviation (averaging radius) chosen for the OM algorithm. Right panel shows the distribution of the similarity radius for the entire VM-ADCP dataset.

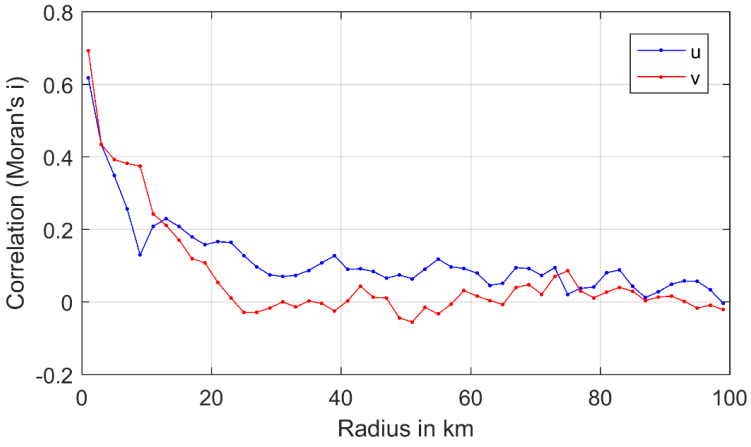

Figure S2. Spatial autocorrelation calculated using Moran's i for the u and v velocity components of the depth averaged VM-ADCP dataset.

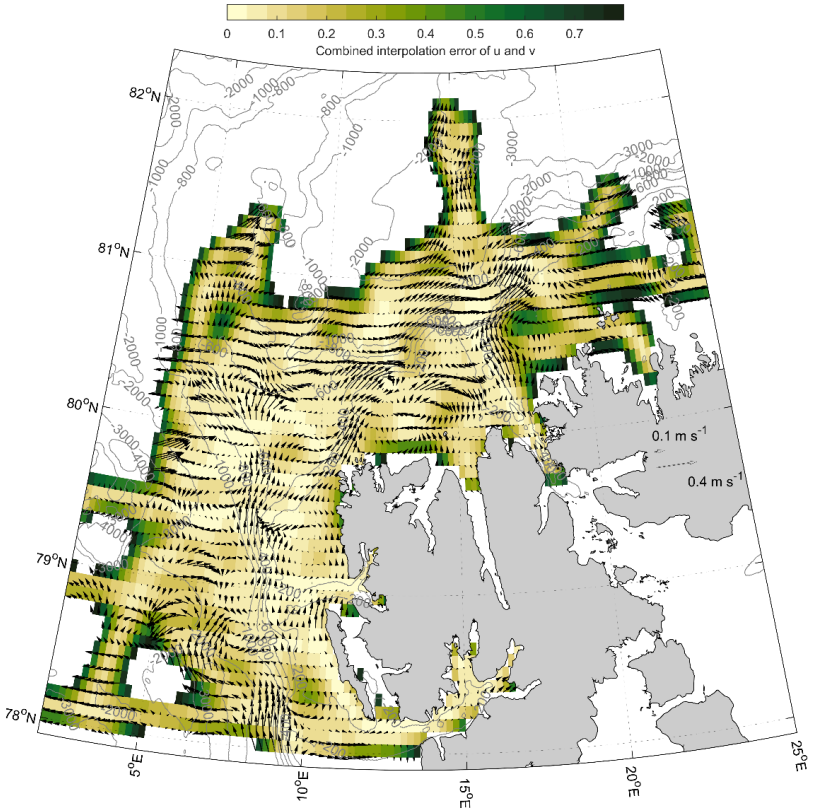

Figure S3. Map of the OM interpolated current field vectors and combined OM interpolation error of u and v, based on data gathered in July-September 2014-2017. Bathymetry contours were derived from IBCAO (Jackobsson, 2012).

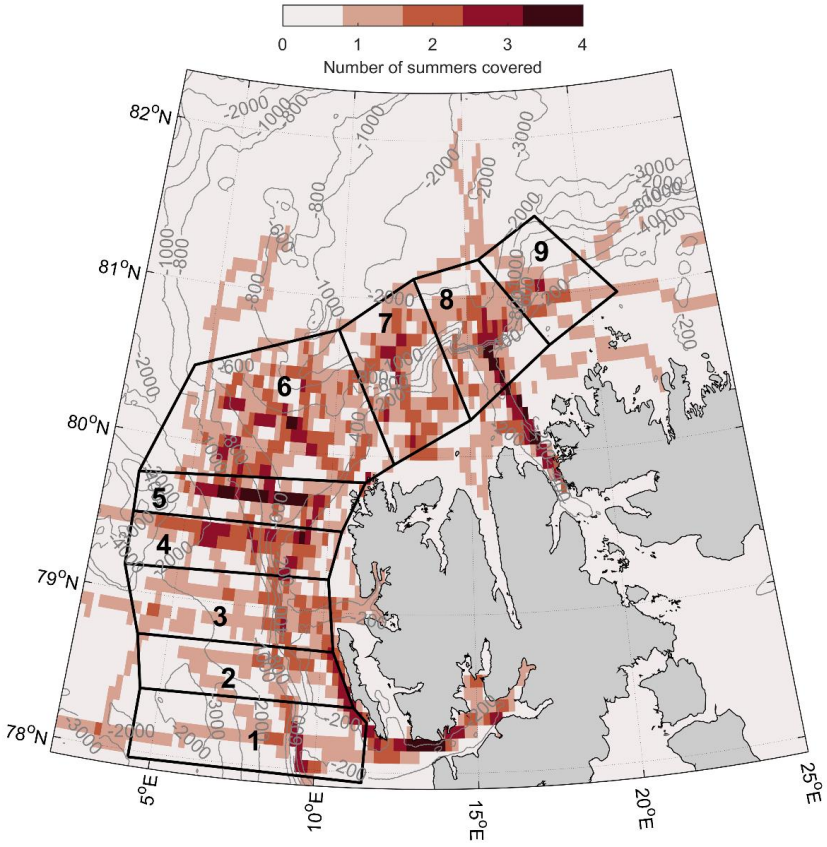

Figure S4. Map showing the number of summers with ADCP data for each bin of the interpolated current field (red hues) and averaging boxes (black lines). Bathymetry contours were derived from IBCAO (Jackobsson, 2012).

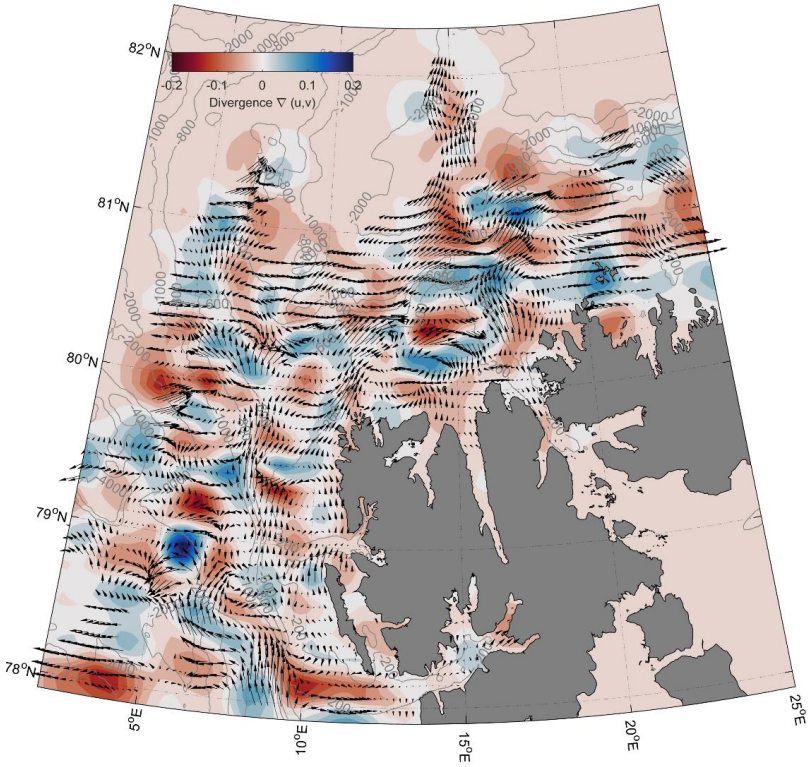

Figure S5. Map of the OM interpolated current field vectors and divergence (blue hues) and convergence (red hues) of the interpolated current field (in s^{-1}). Bathymetry contours were derived from IBCAO (Jackobsson, 2012).

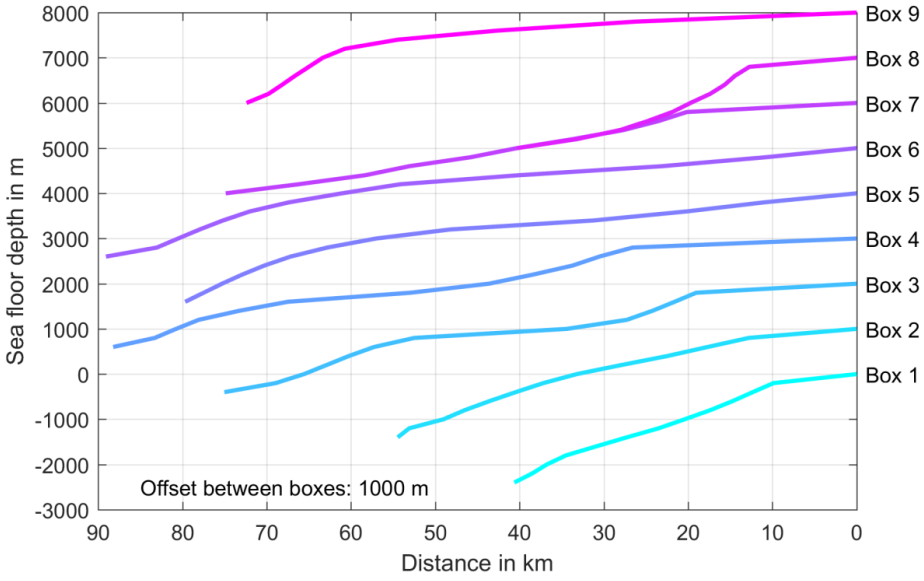

Figure S6. Average sea floor profile for each of the 9 averaging boxes based on IBCAO bathymetry. A 1000 m vertical offset was added for better visualization of the individual profiles.

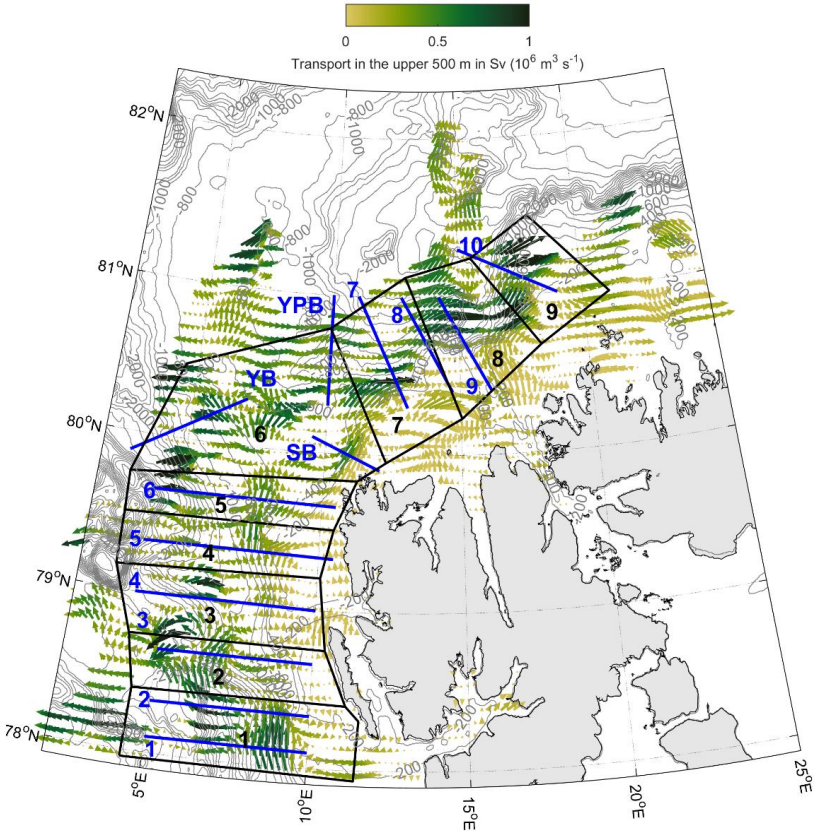

Figure S7. Map of OM interpolated de-tided depth-averaged flow between 20 and 500 m depth based on VM-ADCP data gathered in July-September 2014-2017. Colored arrows depict the interpolated flow field and associated transport in the upper 500 m. Blue transects (and numbers) are used to calculate transport along the slope and though the different branches. Black boxes and numbers indicate the averaging boxes.

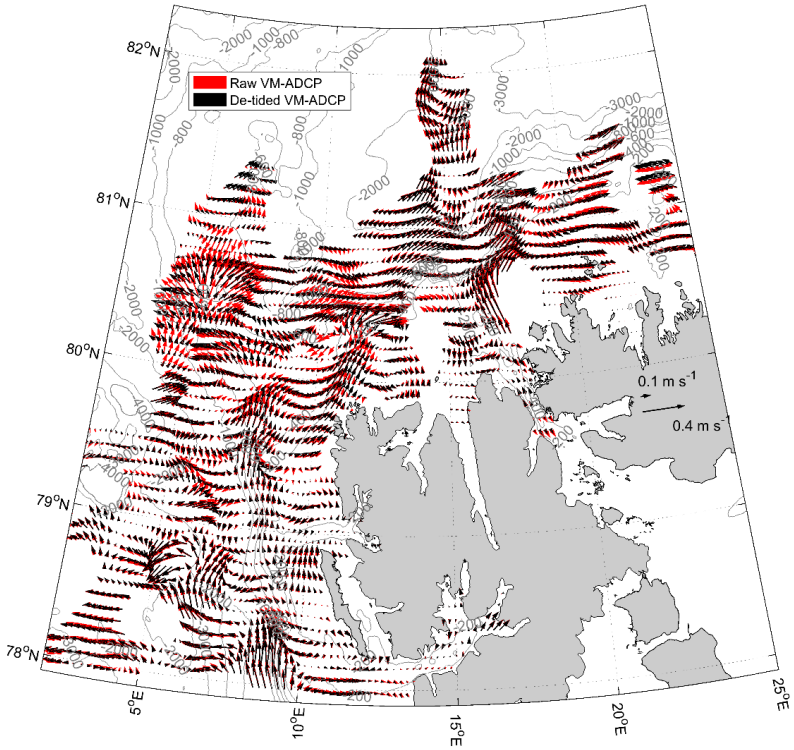

Figure S8. Map comparing the OM current fields based on raw (not de-tided) and de-tided VM-ADCP data (depth-averaged flow between 20 and 500 m).

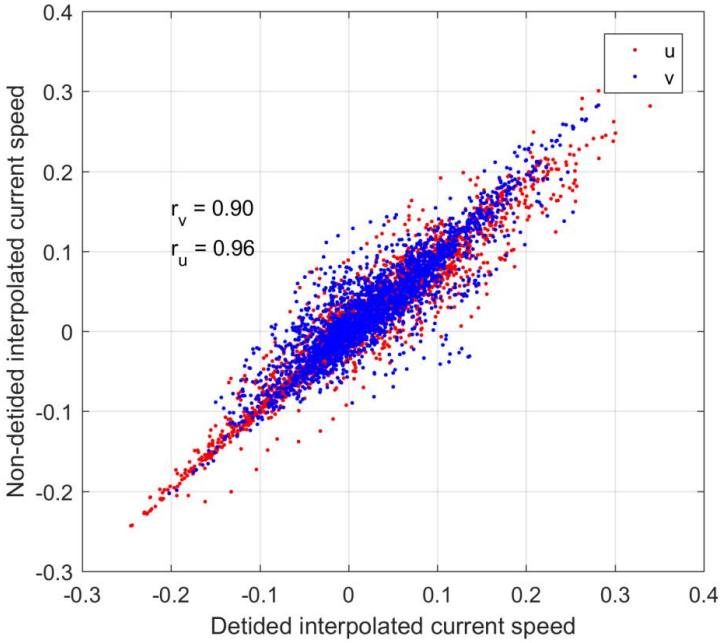

Figure S9. Scatter plot comparing the current speed vectors of OM current fields based on raw (not de-tided) and de-tided VM-ADCP data (depth-averaged flow between 20 and 500 m).

Box Nr.	Latitude	Longitude
1	77.9551 77.9344 78.3136 78.4042 78.3973	4.33042 11.4389 11.5431 11.1163 4.37436
2	78.3973 78.4042 78.7493 78.7367 78.3973	4.37436 11.1163 10.3818 4.01858 4.37436
3	78.7367 78.7493 79.2065 79.1572 78.7367	4.01858 10.3818 10.0949 3.22232 4.01858
4	79.1572 79.2065 79.5139 79.4957 79.1572	3.22232 10.0949 10.467 3.1906 3.22232
5	79.4957 79.5139 79.8302 79.7503 79.4957	3.1906 10.467 11.2157 3.13771 3.1906
6	79.7503 79.8302 79.9507 80.7893 80.4702	3.13771 11.2157 12.2305 9.94265 4.52037 3.13771
7	80.7893 79.9507 80.2309 81.1252 80.7893	9.94265 12.2305 15.0398 12.8566 9.94265
8	81.1252 80.2309 80.6803 81.2435 81.1252	12.8566 15.0398 18.2053 15.5312 12.8566
9	81.2435 80.6803 80.9711 81.5 81.2435	15.5312 18.2053 21.0828 18 15.5312

Table S1. Position of the averaging boxes displayed by black in Figure S7.

Transect (blue no in Figure S7)	Latitude	Longitude	Net along-slope transport in the upper 500 m in Sv
1	78.1, 78.1	5, 10	4.4
2	78.33, 78.33	5, 10	2.9
3	78.66, 78.66	5, 10	0.8
4	79, 79	4, 10	0.5
5	79.33, 79.33	4, 10.5	2.6
6	79.66, 79.66	4, 10.5	2.5
7	81, 80.3	11, 13	2.0
8	81, 80.4	12.7, 14.7	2.3
9	81, 80.4	14.2, 16.2	3.1
10	81.3, 81	15, 19	2.2
Svalbard Branch	80.1, 79.9	9.5, 12	0.8
Yermak Pass Branch	80.3, 81	10, 10	1.9
Yermak Branch	80.3, 79.88	7, 3	1.8

Table S2. Location and transport estimates for the blue transects displayed in Figure S7. Transects are sorted from southwest of Svalbard to northeast of Svalbard.

Box (black no in Figure S7)	Number of ADCP profiles in box	Net transport in Sv (along slope - local azimuth)	Net transport in Sv (through box - box average azimuth)
Box 1	65	1.9	2.2
Box 2	25	0.7	1.1
Box 3	27	1.0	0.5
Box 4	47	1.4	1.5
Box 5	110	2.6	2.2
Box 6	376	1.7	2.2
Box 7	162	2.1	2.1
Box 8	74	1.7	2.0
Box 9	59	2.9	3.6
Mean	105	1.8	1.9

Table S3. VM-ADCP profiles per box and transport estimates based on objective mapping for the black boxes displayed in Figure S7.

III

ROYAL SOCIETY OPEN SCIENCE

rsos.royalsocietypublishing.org

Research

Cite this article: Menze S, Zitterbart DP, van Opzeeland I, Boebel O. 2017 The influence of sea ice, wind speed and marine mammals on Southern Ocean ambient sound. *R. Soc. open sci.* **4**: 160370.
http://dx.doi.org/10.1098/rsos.160370

Received: 24 May 2016
Accepted: 1 December 2016

Subject Category:
Earth science

Subject Areas:
oceanography/ecology/acoustics

Keywords:
ocean ambient sound, ocean ambient noise, sea ice, Southern Ocean, Antarctic marine mammals, passive acoustic monitoring

Author for correspondence:
Sebastian Menze
e-mail: sebastian.menze@imr.no

Electronic supplementary material is available online at https://dx.doi.org/10.6084/m9.figshare.c.3647729.

THE ROYAL SOCIETY PUBLISHING

The influence of sea ice, wind speed and marine mammals on Southern Ocean ambient sound

Sebastian Menze[1,2], Daniel P. Zitterbart[1,3,4], Ilse van Opzeeland[1] and Olaf Boebel[1]

[1]Alfred Wegener Institute Helmholtz Centre for Polar and Marine Research, Bremerhaven, Germany
[2]Institute of Marine Research, Bergen, Norway
[3]Applied Ocean Physics and Engineering, Woods Hole Oceanographic Institution, Woods Hole, MA, USA
[4]Biophysics Group, Department of Physics, University of Erlangen-Nürnberg, Erlangen, Germany

SM, 0000-0002-2680-9794; DPZ, 0000-0001-9429-4350

This paper describes the natural variability of ambient sound in the Southern Ocean, an acoustically pristine marine mammal habitat. Over a 3-year period, two autonomous recorders were moored along the Greenwich meridian to collect underwater passive acoustic data. Ambient sound levels were strongly affected by the annual variation of the sea-ice cover, which decouples local wind speed and sound levels during austral winter. With increasing sea-ice concentration, area and thickness, sound levels decreased while the contribution of distant sources increased. Marine mammal sounds formed a substantial part of the overall acoustic environment, comprising calls produced by Antarctic blue whales (*Balaenoptera musculus intermedia*), fin whales (*Balaenoptera physalus*), Antarctic minke whales (*Balaenoptera bonaerensis*) and leopard seals (*Hydrurga leptonyx*). The combined sound energy of a group or population vocalizing during extended periods contributed species-specific peaks to the ambient sound spectra. The temporal and spatial variation in the contribution of marine mammals to ambient sound suggests annual patterns in migration and behaviour. The Antarctic blue and fin whale contributions were loudest in austral autumn, whereas the Antarctic minke whale contribution was loudest during austral winter and repeatedly showed a diel pattern that coincided with the diel vertical migration of zooplankton.

1. Introduction

Underwater ambient sound is created by the superposition of sounds from countless abiotic, biotic and anthropogenic acoustic sources; it is also termed the 'acoustic environment' [1] or 'ambient noise' [2]. This superposition renders it difficult to distinguish individual sound sources; however, ambient sound spectra can be used to study the different sound source types present within an environment and provide insights into the quality of an acoustic environment (e.g. potential masking effects due to anthropogenic noise).

In the ocean, sea surface processes, involving waves, wind stress, sea ice, precipitation and increasingly shipping form the chief sources contributing to ambient sound [2–4]. Wind stress is one of the major sources of ambient sound; the complex relation between wind speed and ambient sound varies with frequency and is strongest for frequencies above 500 Hz [2]. For the Pacific, Atlantic, Indian and Arctic Oceans, a growing body of literature reports increasing underwater sound levels caused by shipping and seismic exploration [5–9]. The Southern Ocean, on the other hand, is an acoustically pristine habitat due to its long distance from major shipping lanes and generally low levels of human activity. Anthropogenic sound sources rarely enter this region, mainly comprising sporadic research vessels and cruise ships that primarily target the Western Antarctic Peninsula area. The scarcity of such acoustically pristine habitats makes these invaluable in the context of passive acoustic monitoring (PAM) studies, as they can be used as a potential reference for trends in ocean ambient sound and to assess the natural variability of ambient sound. Nevertheless, only limited literature exists on the ambient sound conditions and trends in the Southern Ocean. Here, we analyse the temporal and spectral variation of Southern Ocean ambient sound over a 3-year period and discuss its relation to environmental factors such as wind speed and sea ice.

In regions closer to anthropogenic sound sources, evidence is accumulating that marine mammal communication, among other behaviours, is likely to be affected by increased ambient sound levels, particularly for baleen whale populations that are thought to rely on long-distance (low-frequency) communication [10–12]. Knowledge about the ambient sound marine mammals encounter in (and contribute to) the Southern Ocean's acoustic environment is limited and can provide valuable insights on how marine mammals interact with their acoustic environment in the relative absence of anthropogenic sound sources. Furthermore, multi-year passive acoustic records are important sources of year-round information on marine mammal distribution and behaviour. The Southern Ocean is thought to support more than 50% of the world's marine mammals in terms of biomass, many of which species have been subject to extensive exploitation [13]. Monitoring population recovery by means of visual surveys limits investigations to the austral summer months, when most regions in the Southern Ocean are accessible to vessels. PAM studies using autonomous recording units do not exhibit this seasonal bias [14]. For the Southern Ocean, various PAM applications have resulted in important findings, e.g. with respect to migration and distribution [15–17]. In addition to describing the ambient sound conditions in an important marine mammal habitat, we discuss how the vocal presence of the various marine mammal species relates to their spatio-temporal distribution and behaviour.

2. Material and methods

2.1. Moored recorders

Two autonomous underwater acoustic recorders (AURAL-M2, Autonomous Underwater Recorder for Acoustic Listening-Model 2, Multi-Électronique Inc.) were moored in the Atlantic sector of the Southern Ocean from March 2008 to December 2010 at 66°01′ S and 00°05′ E (Mooring ID: AWI-230-6) and at 69°00′ S and 00°00′ E (Mooring ID: AWI-232-9) [18]. Hereinafter, they will be identified as Aural 66° S and Aural 69° S. The mooring positions are shown in figure 1. Water depth at Aural 66° S was 3578 m, with the recorder moored at a depth of 260 m. Aural 69° S was moored 217 m deep in 3420 m deep waters. Permission to conduct fieldwork and deploy moorings in the Southern Ocean was granted by the German federal environmental agency (UBA permit number I 2.4-94003-3/207). The moorings consisted of Dyneema rope and carried multiple oceanographic devices. Details about the mooring set-up can be found in the electronic supplementary material, figures S1 and S2. Using a train wheel bottom weight and glass floats attached in regular intervals, an upright position of the moorings was achieved. Recorder depths varied within 2 m for Aural 66° S and 5 m for Aural 69° S due to currents shearing the moorings from their upright position.

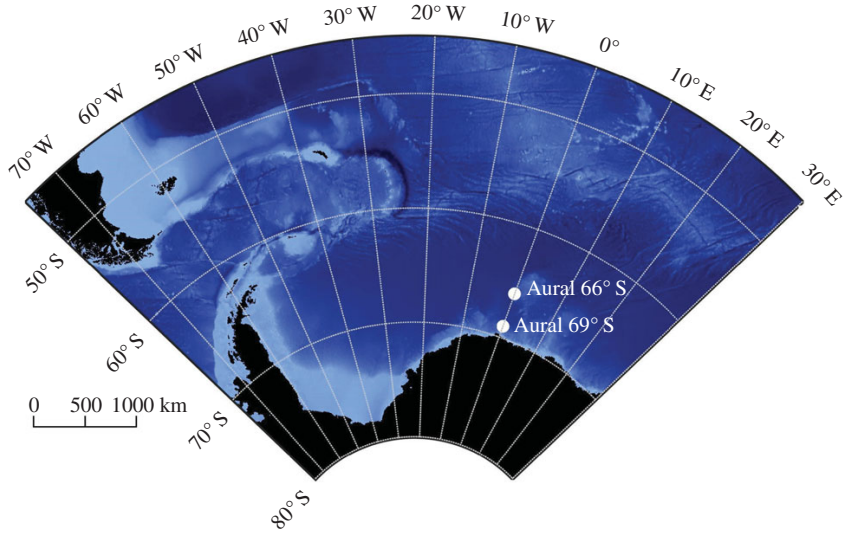

Figure 1. Map of mooring locations and 1 arc-min global relief model (ETOPO1) bathymetry [19].

Shear currents can induce strumming or flow noise into underwater acoustic recordings. In our recordings flow and strumming noises could not be discerned from manual screening of the 5-min spectrograms and power spectra, and were consequently assumed to have negligible impact on the results of this study. However, the shear current occasionally induced impulsive shackle noise at 69° S that contaminated some recordings between May and August in 2008 and June and October in 2009. The shackle noise could easily be identified by characteristic peaks between 40 and 60 Hz and occurred in so few recordings that we choose to not remove them from the dataset. Other than being occasionally visible as peaks in the long-term spectrogram and 50th and 95th percentile spectra of Aural 69° S, the shackle noise did not impact the results of this study.

The recorders were equipped with HTI-68-MIN (High Tech Inc.) hydrophones with a factory calibrated sensitivity of -164.6 dB re 1 V µPa^{-1}. The self-noise of the hydrophones was reported by the manufacturer as 54 dB re 1 µPa^2 Hz^{-1} at 10 Hz and 42 dB re 1 µPa^2 Hz^{-1} at 100 and 1000 Hz. According to the Aural's manufacturer, the recorder's electronic self-noise is flat within ±1 dB over the usable frequency range from 10 Hz to 15 kHz [20]. Assuming an electronic broadband self-noise of 10 bits (typical value according to the manufacturer) in addition to the hydrophones' self-noise, results in a recorder self-noise of 55.0 dB re 1 µPa^2 Hz^{-1} at 10 Hz and 45.4 dB re 1 µPa^2 Hz^{-1} at 100 and 1000 Hz. In addition, the spectra measured by both recorders contained narrow peaks (approx. 3 Hz wide) between 80 and 2000 Hz caused by additional electronic noise. They remained constant over time and can be easily identified in the spectra.

The Aural's system gain was set to 22 dB, resulting in a saturation sound pressure level of 149 dB re 1 µPa. The recorded ambient sound spectra never reached saturation values. The sound level calibrations are solely based on factory calibration, no further pre- or post-calibration was performed, nor did we apply any frequency-specific correction of hydrophone sensitivity. According to the manufacturer the recorders' frequency response is flat within ±1 dB over the usable frequency range [20]. Adding an electronic error of 10 bits (typical value according to the manufacturer) to the 1 dB pressure error, the recorders' total error becomes ±61.6 µPa. On the decibel scale this will amount to a change of ±1.56 dB re 1 µPa^2 Hz^{-1} for a 50 dB re 1 µPa^2 Hz^{-1} signal and ±0.05 dB re 1 µPa^2 Hz^{-1} for a 80 dB re 1 µPa^2 Hz^{-1} signal. The recorders used UTC time and were set to record with a sample rate of 32 768 Hz for 5 min every 4 h starting 00.00 h daily, resulting in 486 h of acoustic recordings. As a gross of the recorded spectra hit the systems noise floor above 10 kHz, we limited our analysis to ambient sound between 10 Hz and 10 kHz. Data were stored losslessly in 16 bit wav files. Owing to internal data handling problems with the recorder, every 48th file was lost [21]. Additional parameters of the recorders are listed in table 1.

Table 1. Properties of the deployed AURAL-M2 recorders.

combined recording period	11 Mar 2008–16 Dec 2010
recording period or Aural 66° S	8 Mar 2008–16 Dec 2010
recording period or Aural 69° S	11 Mar 2008–21 Dec 2010
position	66°01.13′ S 000°04.77′ E and 68°59.74′ S 000°00.17′ E
sample rate	32 768 Hz
bit depth	16 bit
sampling scheme	5-min recordings every 4 h
frequency range	10–16 384 Hz
dynamic range	59–149 dB re 1 µPa

2.2. Ambient sound spectra and marine mammal contributions

All data processing and analysis was performed using Matlab 2015a. As typical for ambient sound analysis, the power spectral density (PSD) was calculated using a pre-set averaging length, which was set to the full 5 min of each recording. The PSD was calculated and averaged after Welch's method [22] using a window length of 2 s, 50% overlap and a fast Fourier transform (FFT) size of 2 s. Using this approach to calculate the spectrum has the advantage of biasing away from transient sounds (such as nearby marine mammal call trains or sea-ice cracks) and towards the quasi-continuous ambient sound. The resulting spectra showed persistent peaks between 15 and 30 Hz as well as 90 and 1000 Hz that occurred annually. These peaks represent the local 'chorus-like' cumulative sound energy produced by different marine mammal species. Marine mammal vocalizations are transient sounds, but the local combined sound energy of a group or population vocalizing during extended periods adds up to a quasi-continuous sound signal that can dominate the underwater ambient sound over certain frequency bands. These parts of the acoustic environment are further referred to as *marine mammal contributions* (MMCs). Peaks in the spectra (MMCs) could be assigned to different species by manual perusal of the 5-min recordings and comparison with published records of marine mammal vocal repertoires. The following species' contribution could be detected in the PSD dataset (table 2): Antarctic blue whales (*Balaenoptera musculus intermedia*) [23,24], fin whales (*Balaenoptera physalus*) [23,24], Antarctic minke whales (*Balaenoptera bonaerensis*) [25] and leopard seals (*Hydrurga leptonyx*) [26]. The numbers after each species indicate the key references used to identify the vocalizations in our recordings and MMC peaks in the ambient sound spectra. Figure 2 shows an example spectrum (black line) with peaks that represent the contribution of Antarctic blue, Antarctic minke and fin whale vocalizations to the ambient sound. The frequency ranges each MMC covered were determined by measuring the width of the respective peaks, and the core frequency bands ($f_{\min}$ and $f_{\max}$) that best characterized each MMC were chosen manually to avoid interference between the different MMCs (table 2). Both Antarctic blue and fin whales vocalize between 15 and 25 Hz, thus the Antarctic blue whale contribution was best classified using the narrow peak between 26 and 28 Hz and fin whale contribution with the peak between 96 and 99 Hz. Owing to the overlapping frequency ranges of the MMCs, the PSD that each species contributed to ambient sound (PSD_{MMC}) was only calculated over each MMC's core frequency band ($f_{\min}$ to $f_{\max}$, column 3 in table 2) and not each MMC's entire frequency range (column 2 in table 2). Thus, all PSD_{MMC} values presented in this study represent the band-limited and not the total broadband sound energy each species contributes to ambient sound.

For each recording, the PSD_{MMC} in the four MMC core frequency bands was calculated by subtracting the estimated PSD without MMCs from the measured PSD. The hypothetical spectrum without the MMC ($PSD_{interpolated}$) was calculated by fitting an interpolation function to the measured PSD around each MMC frequency band (coloured lines in figure 2). The frequency ranges and interpolation functions used for each MMC are specified in table 2. The interpolation functions with the best fit to the MMC's frequency band were chosen manually for each MMC, and differed between species due to the different shape of the spectrum at the different MMC bands. For the Antarctic blue whale, Antarctic minke whale and leopard seal bands, power functions best represented the non-MMC spectrum. A polynomial function provided the best fit for the fin whale band due to the nearby Antarctic minke whale peak. To characterize how well the interpolated PSD represented the non-MMC part of the ambient sound, the fit between $PSD_{interpolated}$ and $PSD_{measured}$ was calculated for periods of MMC absence (electronic

Table 2. Spectral range and interpolation functions used to calculate PSD_{MMC}. In the interpolation functions θ_i represents the parameters that were fitted to each spectrum PSD_{dB}, the power spectral density in dB re 1 μPa^2 Hz^{-1} and f, the frequency in Hertz.

species	frequency range of MMC spectral peak	core frequency range used to calculate PSD_{MMC} ($f_{min} - f_{max}$)	interpolation function	frequency bands used to fit the interpolation function	correlation coefficient r^2 between interpolated and measured PSD_{dB} during MMC absence	average correlation coefficient r^2 between interpolated and measured PSD_{dB} in the frequency bands used to fit the interpolation function
Antarctic blue whales (*Balaenoptera musculus intermedia*)	15–28 Hz	26–28 Hz	power function: $PSD_{dB} = \theta_1 f^{\theta_2} + \theta_3$	10–15 and 30–50 Hz	—	0.97
fin whales (*Balaenoptera physalus*)	15–30 Hz and 97.5–98.5 Hz	96–99 Hz	4th degree polynomial: $PSD_{dB} = \theta_1 f^4 + \theta_2 f^3 + \theta_3 f^2 + \theta_4 f^1 + \theta_5$	50–95 and 101–150 Hz	0.99	0.92
Antarctic minke whales (*Balaenoptera bonaerensis*)	100–1000 Hz	105–300 Hz	power function: $PSD_{dB} = \theta_1 f^{\theta_2} + \theta_3$	30–97 and 500–1000 Hz	0.72	0.98
leopard seals (*Hydrurga leptonyx*)	300–400 Hz	320–350 Hz	same as used for the Antarctic minke whale band	same as used for the Antarctic minke whale band	0.95	same as used for the Antarctic minke whale band

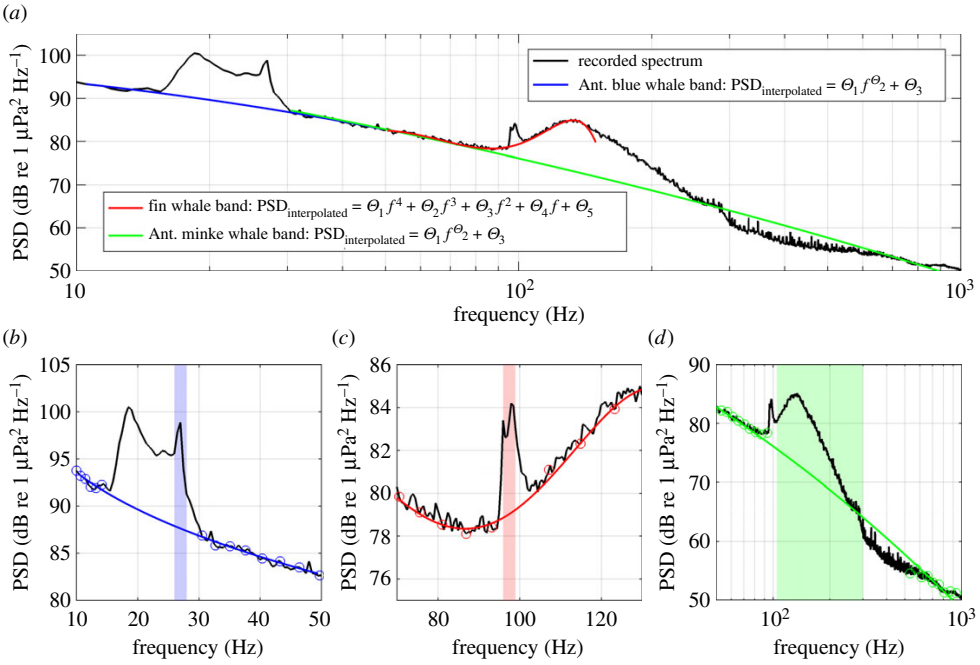

Figure 2. Example ambient sound spectrum with MMCs (visible as peaks) from Antarctic blue, Antarctic minke and fin whales and the respective interpolation functions used to calculate the non-MMC PSD. The black lines represent the measured PSD (at 66° S on 25 May 2008 12.00 h). (*a*) The three fitted interpolation functions in blue (Antarctic blue whale band), red (fin whale band) and green (Antarctic minke whale band). (*b–d*) Details of the measured spectra and interpolation function for each of the mentioned MMCs. The data points used to fit the interpolation functions to the measured spectra are displayed as circles and the frequency bands used to calculate the PSD_{MMC} are shaded in blue, red and green. In the interpolation functions, θ_i represents the parameters that were fitted to each spectrum; PSD_{dB}, the power spectral density in dB re 1 µPa^2 Hz^{-1} and *f*, the frequency in Hertz.

supplementary material, figure S3). For the fin whale frequency band, the correlation coefficient r^2 between $PSD_{interpolated}$ and $PSD_{measured}$ was 0.99, for the Antarctic minke whale band 0.72 and for the leopard seal band 0.95. As the Antarctic blue whale MMC was present year-round, we could not calculate the correlation coefficient between $PSD_{interpolated}$ and $PSD_{measured}$, but manual inspection of the fitted spectra confirmed that the interpolation function provided robust estimates of the non-MMC spectrum. The average correlation coefficient r^2 between $PSD_{interpolated}$ and $PSD_{measured}$ in the frequency bands used to fit the interpolation function (coloured circles in figure 2) was higher than 0.9 for all interpolation functions (table 2). Using interpolation functions to determine the non-MMC part of the ambient sound for each recording avoids biases that could arise from the temporal variation in abiotic ambient sound. To quantify the contribution of the different species (PSD_{MMC}), we averaged $PSD_{measured}$ and $PSD_{interpolated}$ over each MMC's respective core frequency band (table 2 and shaded areas in figure 2) and subtracted them from each other following

$$PSD_{MMC} = 10\log_{10}\left(\frac{\sum_{i=f_{min}}^{f_{max}} PSD_{measured}}{n_{f_{min}-f_{max}}} - \frac{\sum_{i=f_{min}}^{f_{max}} PSD_{interpolated}}{n_{f_{min}-f_{max}}}\right), \tag{2.1}$$

where PSD_{MMC} is the PSD of each species contribution to ambient sound in the four MMC core frequency bands in dB re 1 µPa^2 Hz^{-1}, $PSD_{measured}$ and $PSD_{interpolated}$ are PSD values in µPa^2 Hz^{-1}, f_{min} and f_{max} are the respective boundaries of each frequency band (table 2) and $n_{f_{min}-f_{max}}$ the sample size between f_{min} and f_{max}. The sample size was smallest for the Antarctic blue whale core frequency band ($n_{f_{min}-f_{max}} = 5$) and largest for the Antarctic minke whale core frequency band ($n_{f_{min}-f_{max}} = 382$). The PSD_{MMC} can only be measured when the MMC spectral peak is discernible in the power spectrum (i.e. when the MMC is

louder than other sound sources in the respective frequency band). This can be quantified as signal-to-noise ratio (SNR) using

$$\mathrm{SNR_{MMC}} = 10\log_{10}\left(\frac{\sum_{i=f_{\min}}^{f_{\max}} \mathrm{PSD_{measured}}}{n_{f_{\min}-f_{\max}}}\right) - 10\log_{10}\left(\frac{\sum_{i=f_{\min}}^{f_{\max}} \mathrm{PSD_{interpolated}}}{n_{f_{\min}-f_{\max}}}\right). \quad (2.2)$$

To ensure a rigid analysis, an MMC was defined as present when its $\mathrm{SNR_{MMC}}$ was higher than the pre-defined threshold of 1 dB.

2.3. Wind speed and sea-ice data

The zonal and meridional wind speed fields were extracted from the European Centre for Medium-Range Weather Forecasts interim climate reanalysis dataset (ERA-interim) [27]. The temporal resolution of the fields was selected to 12 h (at 00.00 and 12.00 h) and the spatial resolution as 0.25°.

Gridded sea-ice concentration data were obtained from the University of Bremen, based on their analysis of data from the Advanced Microwave Scanning Radiometer Earth Observing System (AMSR-E) [28]. The data consist of daily average values on a polar stereographic grid with a spatial resolution of 6 × 4 km. To correlate the gridded datasets with the two ambient sound time series, we calculated the average values of concentric circles in 50 km radius steps for each mooring location.

The Antarctic sea-ice extent time series was obtained from the National Snow and Ice Data Centre [29]. Sea-ice draught was measured by an upward looking sonar installed in the same mooring as Aural 69° S and the error-corrected sea-ice draught data obtained from the PANGEA database [30]. All correlation coefficients r in this study were calculated using Pearson's method [31].

3. Results

3.1. Spectra and band levels

The recorded spectral probability density over frequency is shown in figure 3. At frequencies above 1000 Hz, large parts of the spectra, visible as red clusters in the spectral probability density, met the recorders' noise floor. Between 15 and 100 Hz, the spectral probability density shows a bimodal distribution (two separated (red) areas of increased probability) that can be linked to the sea-ice conditions. The two white lines represent the average spectrum during ice-free and ice-covered periods and match the bimodal distribution. Neglecting the noise floor, the median, 5th and 95th percentile spectra are similar to a power law spectrum. However, peaks associated with marine mammal vocalizations (MMCs, table 2) can be found between 15 and 30 Hz as well as 90 and 1000 Hz. The spectra, furthermore, show narrow peaks (approx. 3 Hz wide) related to recorder internal electronic noise, which have a narrower bandwidth than the MMC peaks and stay constant over time.

The 3-year time series of PSDs, referred to as long-term spectrograms hereinafter, are displayed in figure 4. The temporal variation of the spectra follows a seasonal cycle, where the highest spectral levels occur in austral summer, between January and March, followed by a gradual decrease in spectral levels that can be associated with the growing sea-ice cover. In the long-term spectrogram from 69° S (figure 4*b*), the sound generated by moving shackles can be seen as faint dotted line at 40 and 57 Hz in 2008 and 2009.

3.2. Marine mammal contributions

The long-term spectrograms exhibit annually reoccurring horizontal lines between 15 and 30 Hz as well as 90 and 1000 Hz (figure 4, indicated by arrows), which intensify in amplitude seasonally. They are associated with marine mammal vocalizations and represent the local cumulative sound energy of all individuals of a species producing a specific call type. We analysed the temporal and spatial variation of $\mathrm{PSD_{MMC}}$ contributed by Antarctic blue, fin and Antarctic minke whales and leopard seals in their respective frequency bands (figure 5). The sound energy emitted by the characteristic broadband vocalizations of crabeater seals (*Lobodon carcinophaga*) was occasionally present in the long-term spectrograms between 500 and 1000 Hz (figure 4) [32], but was too faint for a robust analysis.

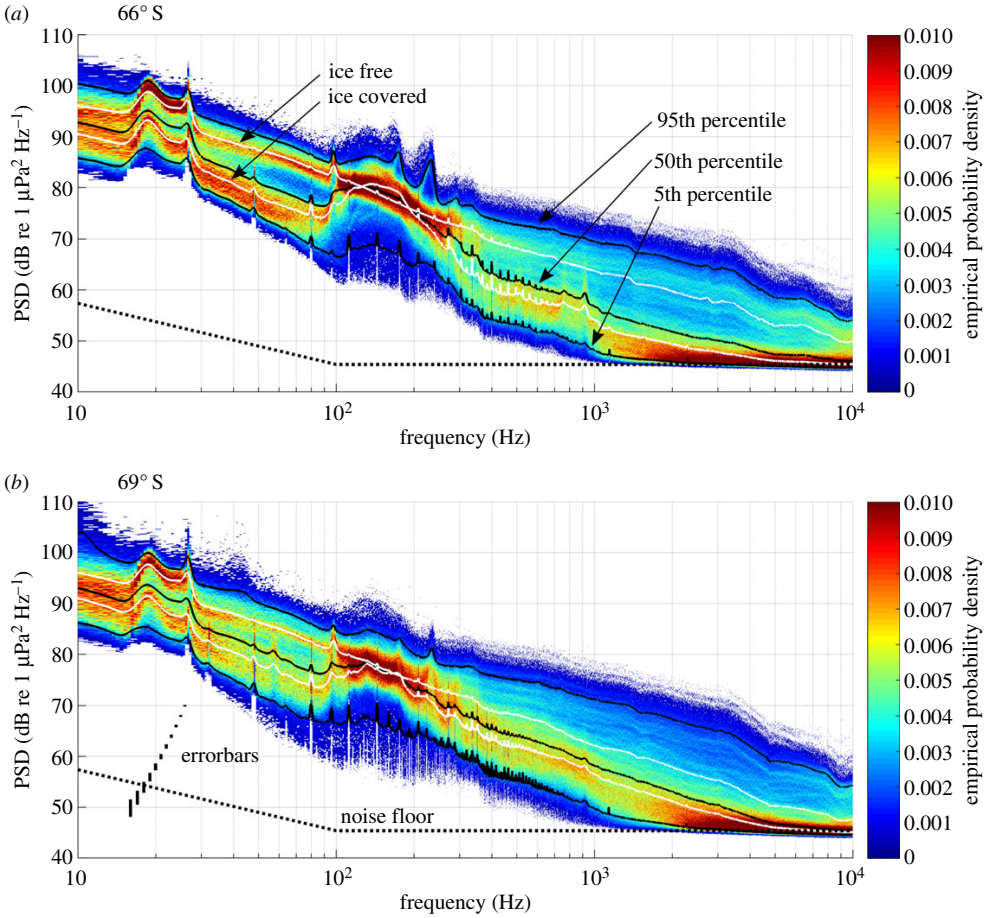

Figure 3. Spectral statistics at (*a*) 66° S and (b) 69° S (as based on factory calibration). Colour shows empirical spectral probability density as a function of frequency and spectral levels, the black solid lines the 5th, 50th and 95th percentile spectral levels and the white lines the average spectra during ice-covered (mean sea-ice concentration in 200 km radius $>$ 50%) and ice-free conditions (mean sea-ice concentration in 200 km radius $<$ 50%). The dashed lines show the system's noise floor. The vertical bars in (*b*) illustrate the error bars ($\pm$61.6 µPa) for signals from 50 to 70 dB re 1 µPa^2 Hz^{-1}.

3.2.1. Antarctic blue whales

Between 27 and 28 Hz, the most persistent peak in the long-term spectrograms (figure 4) is associated with Antarctic blue whale vocalizations. The recorded Antarctic blue whale contribution consists of so-called Z-calls, comprising three components [33], which are emitted between 18 and 27 Hz [24]. Owing to interference with fin whale vocalizations around 20 Hz and the remarkable stereotypy of the upper call component (Z-call), the Antarctic blue whale contribution is best represented by band levels between 26 and 28 Hz [34]. The blue whale contribution was recorded continuously, reaching highest PSD_{MMC} values in between February and June and lowest between September and December (figure 5*a*). Antarctic blue whale PSDs were similar at 66° S and 69° S from January to March and louder at 66° S compared with 69° S for the rest of the year.

3.2.2. Fin whales

Fin whales in the Southern Ocean emit pulsed calls with main energy around 20 and 89 or 99 Hz, depending on region [17,23]. In the long-term spectrograms (figure 4), the upper fin whale call component forms a narrow peak at 98 Hz, which is 9 Hz higher than measurements from fin whales off the West Antarctic Peninsula [23]. To exclude interference with Antarctic blue whale vocalizations, the PSD of the Antarctic fin whale contribution is best represented by the upper call component at 98 Hz.

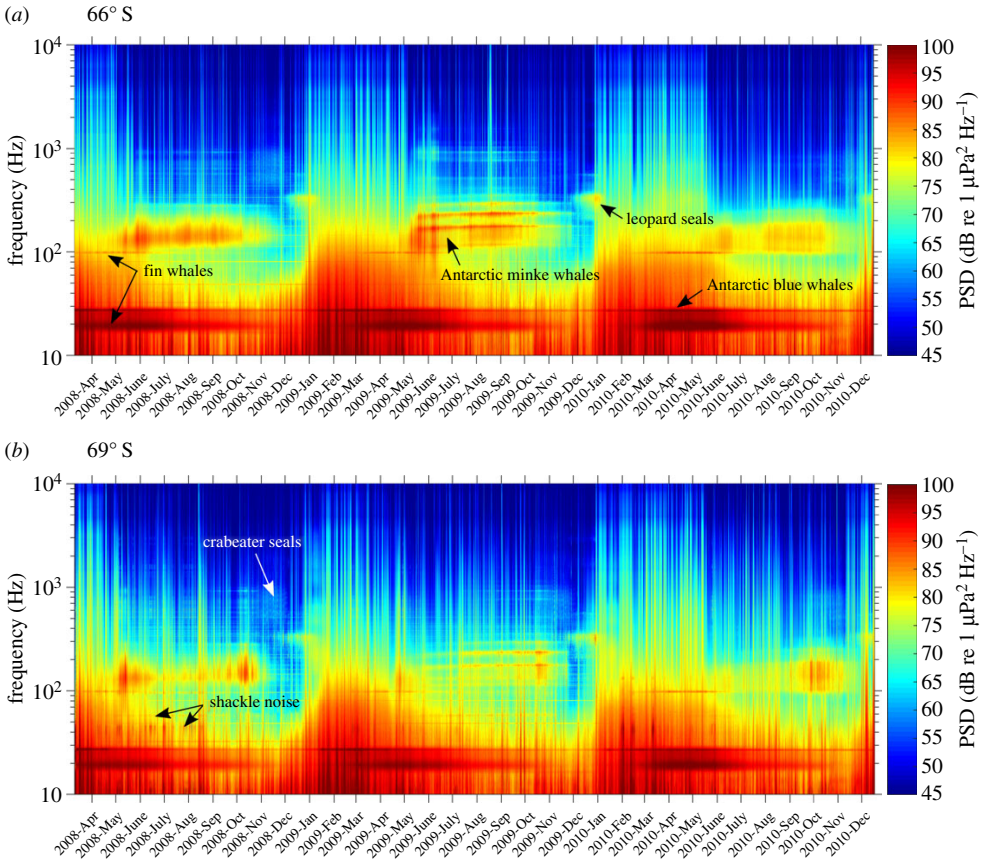

Figure 4. Long-term spectrograms of recordings from 66° S (*a*) and 69° S (*b*). PSD based on factory calibration.

The Antarctic fin whale contribution was present (SNR > 1 dB in the 96–99 Hz band) each year between March and July. Fin whale PSDs were generally louder at 66° S than 69° S, especially from April to July (figure 5*b*).

3.2.3. Antarctic minke whales

One of the most distinct patterns in the long-term spectrograms is observed between 100 and 300 Hz, reoccurring between May and November each austral winter (figure 4). It is associated with Antarctic minke whale vocalizations [25]. The PSDs of the Antarctic minke whale contribution differed by up to 10 dB between the two recording locations, with the contribution being louder at 66° S most of the year (figure 5*c*). At 66° S, Antarctic minke whale PSDs were highest between May and September, followed by a decrease in October and November. At 69° S, Antarctic minke whale PSD increased until October, followed by a sharp decrease in November. An exception to this pattern occurred in 2008, where Antarctic minke whale PSDs were stronger at 69° S compared with 66° S in the beginning of May, and increased at 66° S and decreased at 69° S until June. In the long-term spectrograms, the frequency characteristics of the Antarctic minke whale contribution varied from year to year (figure 4). However, throughout the recording period, the major part of the received Antarctic minke whale sound energy remained between 100 and 300 Hz.

On a much shorter time scale, the Antarctic minke whale acoustic contribution followed a diel cycle from the end of April to the beginning of August each year. Figure 6*a* displays the distribution of Antarctic minke whale PSD over a 24 h cycle (starting and ending at 12.00 UTC) at 66° S, normalized for each day between 0 and 1. The diel cycle's phase remained stable throughout the recording period, with Antarctic minke whale PSDs being louder at midnight than midday. The diel cycle was strongest in austral winter 2009 (electronic supplementary material, figure S4).

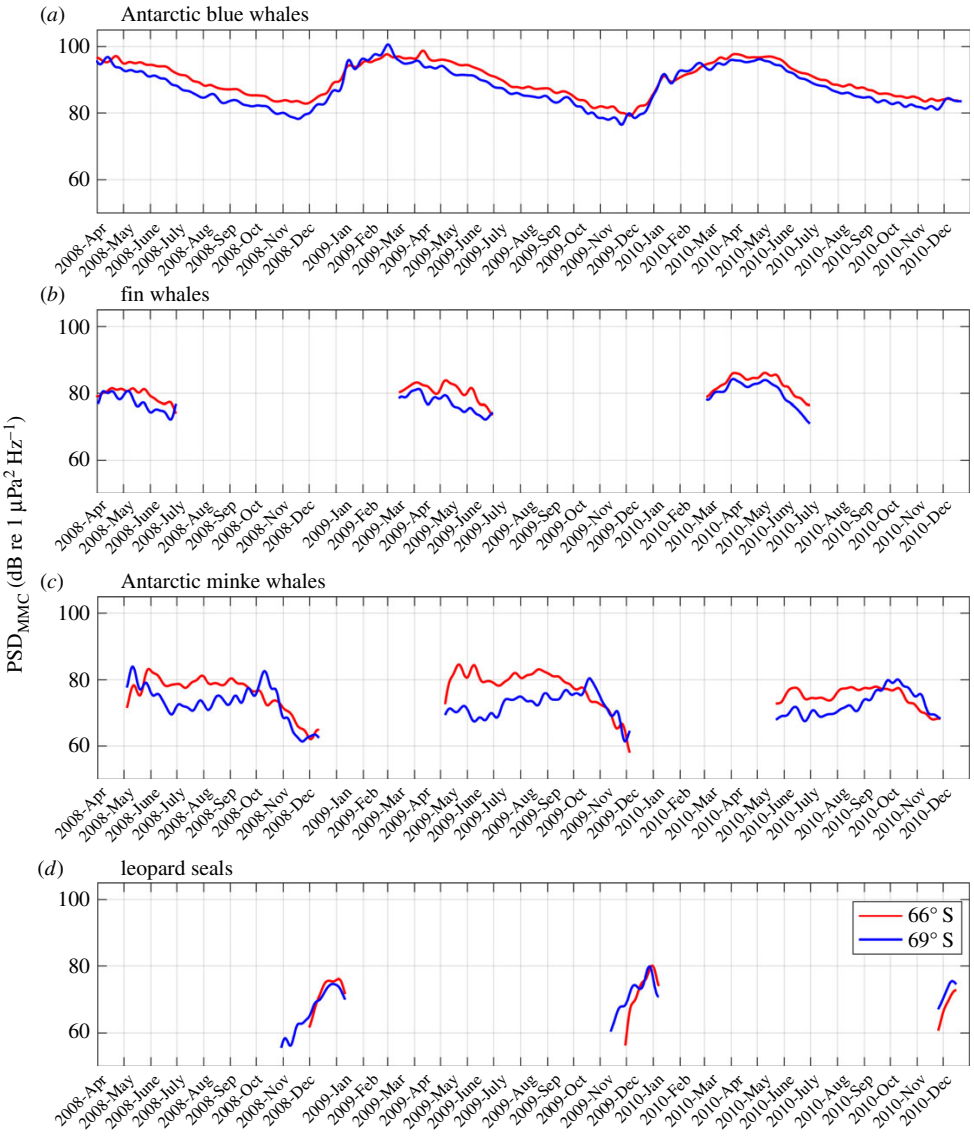

Figure 5. Comparison of marine mammal contribution PSD time series (low-pass filtered with a 7-day window Butterworth filter) between 66° S (red) and 69° S (blue) (as based on factory calibration): (*a*) Antarctic blue whale contribution (*Balaenoptera musculus intermedia*), (*b*) fin whale contribution (*Balaenoptera physalus*), (*c*) Antarctic minke whale contribution (*Balaenoptera bonaerensis*) and (*d*) leopard seal contribution (*Hydrurga leptonyx*). The PSD_{MMC} is only plotted where the SNR_{MMC} is above 1 dB. Note that PSD_{MMC} was averaged over different frequency bands: 26–28 Hz for Antarctic blue whales, 96–99 Hz for fin whales, 105–300 Hz for Antarctic minke whales and 320–350 Hz for leopard seals (table 2).

3.2.4. Leopard seals

Antarctic seals contribute distinctly to the underwater acoustic environment of the Southern Ocean [26]. Leopard seals are particularly vocally active (high density of calls) and their calls contain energy at frequencies low enough to contribute peaks to the long-term spectrograms. Peak energy of the contribution is found between 320 and 350 Hz, partly overlapping in frequency (but not the core frequency band f_{min} to f_{max}) with the Antarctic minke whale contribution (figure 4). The leopard seal contribution was loudest between December and January annually (figure 5*d*).

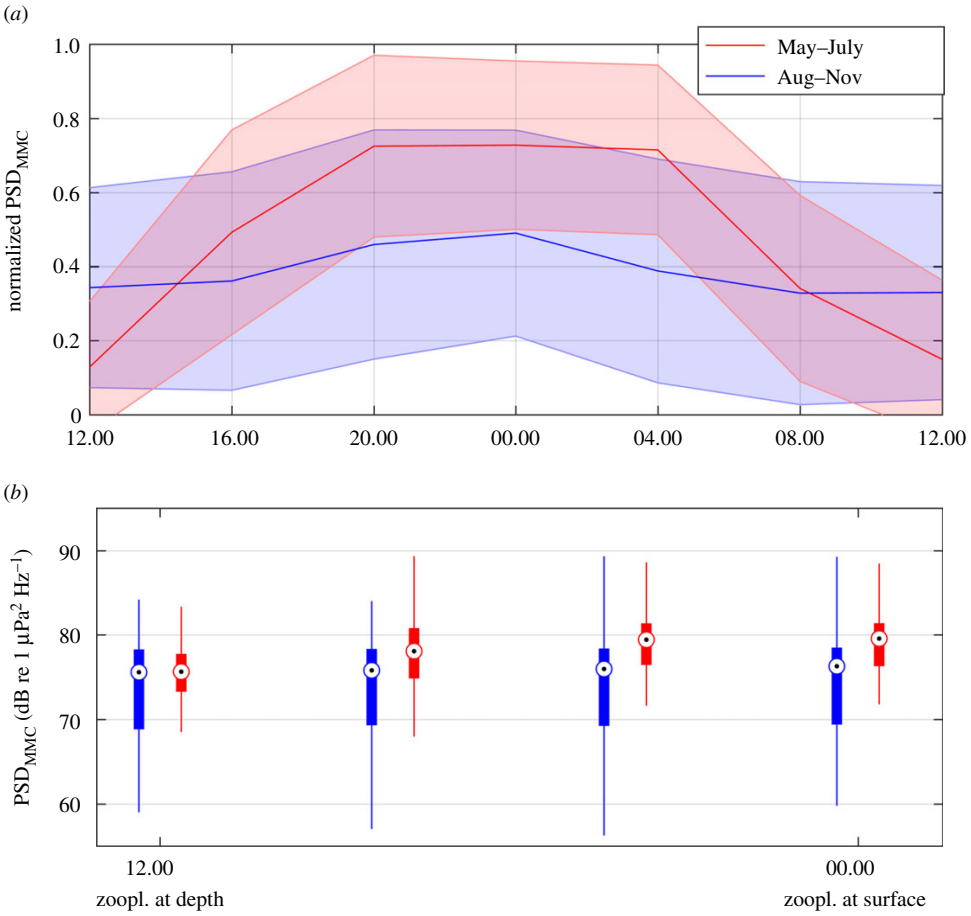

Figure 6. Seasonal presence of diel pattern in the Antarctic minke whale contribution in relation to the diel vertical migration (DVM) of zooplankton. (*a*) The averaged Antarctic minke whale PSD, normalized between 0 and 1 for each day, over the hour of day. Red represents the period between 1 May and 31 July, blue the period between 1 August and 30 November. Bold lines represent the average normalized PSD and shaded areas the standard deviations. (*b*) The relationship between Antarctic minke whale PSD (as based on factory calibration) and an idealized DVM pattern (zooplankton at depth during midday and at surface during midnight). The horizontal axis represents the idealized vertical position of zooplankton and the boxes Antarctic minke whale PSD averages for four vertical zooplankton positions (related to time of day). Points represent median values, thick lines 25th and 75th percentiles and thin lines the minimum and maximum values. Colour indicates the time periods corresponding to (*a*). The figure indicates that the timing of Antarctic minke whale vocal activity and DVM of zooplankton are connected during winter (polar night).

3.3. Relation to sea ice and wind speed

The impact of the physical environment on underwater sound levels was explored by comparing the average PSD in the frequency bands 30–80 and 500–1000 Hz with spatially averaged wind speed and sea-ice concentration as well as sea-ice draught and extent. These frequency bands were chosen to exclude interferences with the MMCs and to avoid the recorder noise floor. Both frequency bands show similar patterns over their respective bandwidth in the spectral probability density spectra (figure 3): a bimodal pattern related to sea ice for the 30–80 Hz band and a broad distribution for the 500–1000 Hz band, which indicates a differing response to the physical environment between the two bands.

Figure 7 compares the time series of PSD in the two bands and spatially averaged sea-ice concentration (percentage of area covered by sea ice), sea-ice draught (thickness of the submerged sea-ice layer) and extent (total area covered by sea ice). A scatterplot of the relationship between spatially averaged sea-ice concentration (within 500 km radius) and PSD is shown in figure 8*a*,*b*, where each marker represents a 5-min recording and marker colour encodes the recording month. The time series and scatter plots indicate an inverse relationship between sea-ice concentration and PSD, which is clearest

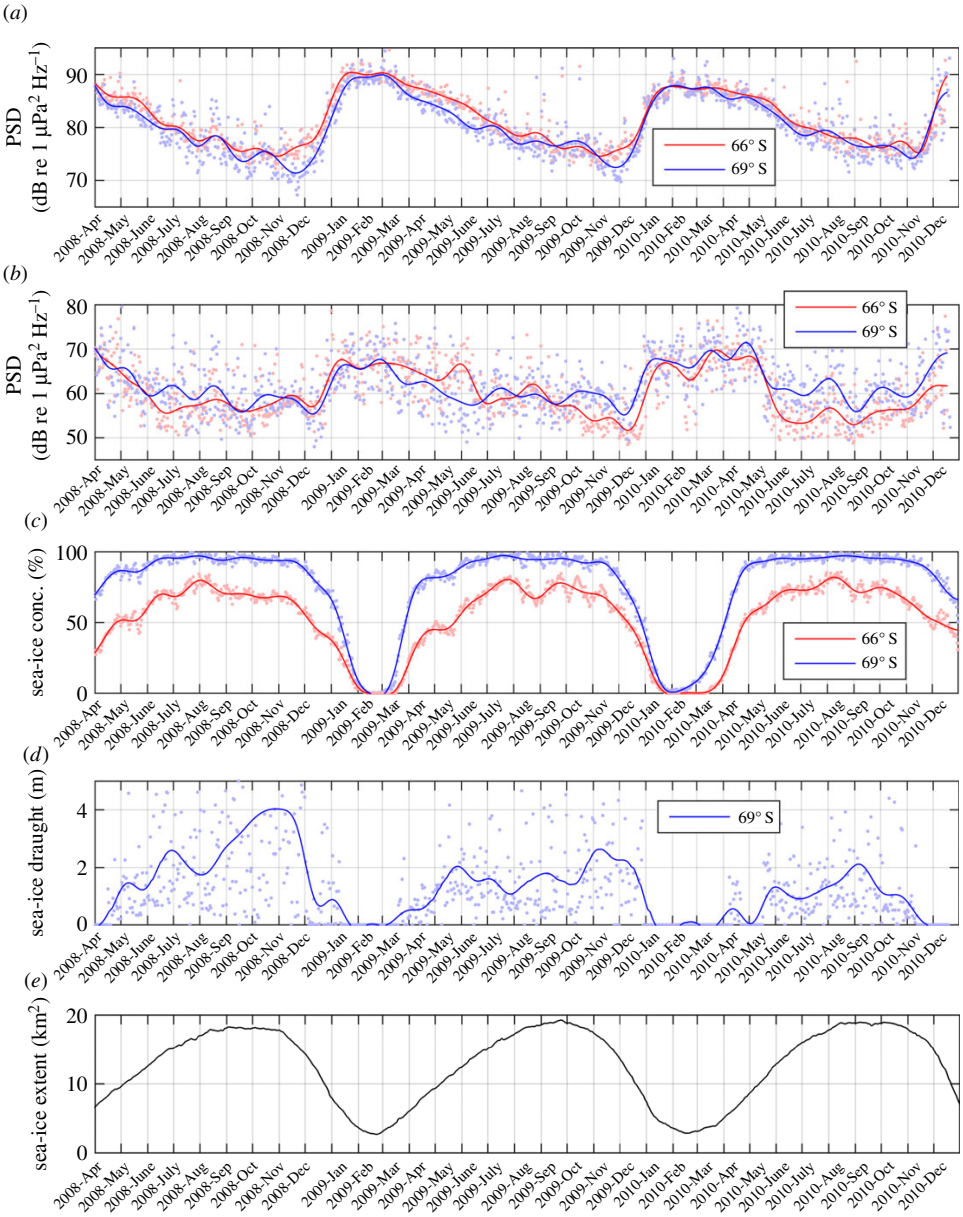

Figure 7. Comparison of ambient sound (as based on factory calibration) and sea-ice time series. (*a*,*b*) The average PSD of two frequency bands: 30–80 (*a*) and 500–1000 (*b*) Hz at both 66° S (red) and 69° S (blue). Each dot represents a 5-min recording, and the solid lines a 20-day running mean. (c) Spatially averaged sea-ice concentration (within 200 km radius) with the solid line representing a 20-day running mean. (*d*) The sea-ice draught at 69° S with the solid line representing a 20-day running mean. (*e*) The Antarctic sea-ice extent in square kilometres.

for the 30–80 Hz frequency band (dots in figure 8) and between February and July (blue hues in figure 8). Between August and November (yellow hues in figure 8), the PSD decreased even though the sea-ice concentration remained approximately constant, whereas between December and January, PSD and sea-ice concentration again showed an inverse relationship. For both frequency bands, the PSD continuously decreased throughout austral winter and reached lowest values in October and November, whereas the sea-ice concentration saturated already between June and August and the sea-ice extent reached its maximum in September and October (figure 7). Sea-ice draught (only measured at 69° S) increased continuously throughout austral winter and reached highest values around November. Throughout the

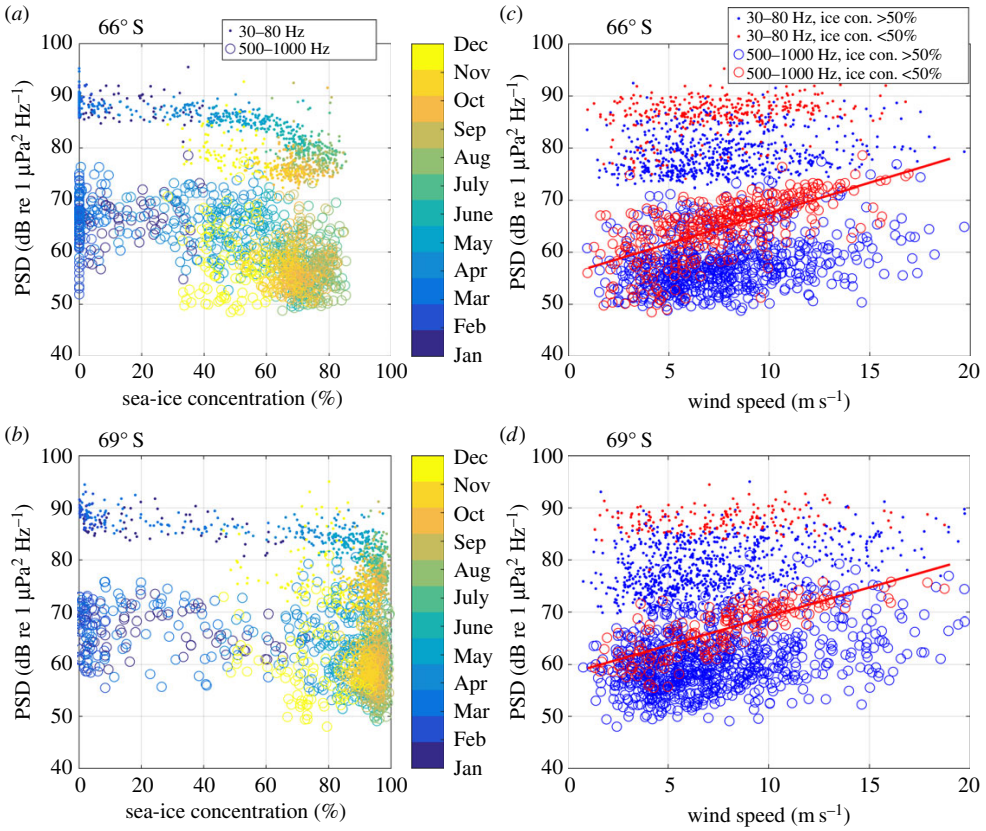

Figure 8. Relation between ambient sound levels (as based on factory calibration), wind speed and sea-ice concentration, each dot represents a 5-min recording. (*a*,*b*) The average PSD of two frequency bands (30–80 and 500–1000 Hz) over spatially averaged sea-ice concentration (within 500 km radius), with month represented by colour. (*c*,*d*) The average PSD of the two bands over spatially averaged wind speed (within 200 km radius), with ice-free conditions (sea-ice concentration smaller than 50%) represented by red markers and ice-covered conditions (sea-ice concentration larger than 50%) by blue markers. The red lines show a linear fit to the data points representing 500–1000 Hz PSD and wind speed under ice-free conditions. Average slope of linear fit was 1.13 and average correlation coefficient *r* was 0.7.

observed period, the annual maximum sea-ice draught decreased, whereas the sea-ice concentration showed no such trend. The sea-ice extent increased, especially in the Weddell Sea between January and May [35]. In the 30–80 Hz band, the annual minimum PSD (in November and December) increases, whereas the annual maximum PSD (January to March) decreases from 2009 to 2010. At both locations, the correlation between sea-ice concentration and PSD was strongest in the 30–80 Hz band (electronic supplementary material, figure S5); however, the spatial averaging radius corresponding to the strongest correlation was 200 km at 66° S ($r \approx -0.8$) compared with 2000 km at 69° S ($r \approx -0.9$).

Figure 9 shows maps of the correlation between wind speed in each ERA-interim cell and PSD under different sea-ice conditions. During ice-free conditions (average ice concentration in 200 km radius < 50%), wind speed strongly correlates ($r > 0.5$) with 500–1000 Hz PSD within a 200 km radius around both recorders' locations (figure 9*a*,*e*), whereas average PSD between 30 and 80 Hz correlates poorly with local wind speed (figure 9*c*,*d*). However, at 66° S wind speed and 30–80 Hz PSD correlate weakly ($r \approx 0.3$) over an area between 50° S and 70° S (figure 9*c*) during ice-free conditions. During ice-covered conditions (average ice concentration in 200 km radius > 50%), wind speed correlates weakly ($r \approx 0.3$) with 500–1000 Hz PSD within a 600 km radius for Aural 66° S (figure 9*b*) and within an area roughly indicating the coastal polynya for Aural 69° S. For both recorders, the 30–80 Hz PSD and wind speed correlate weakly in an area roughly indicating the coastal polynya, during ice-covered conditions. The relationship between local wind speed (averaged within 200 km radius) was also analysed as scatterplot (figure 8*c*,*d*). The response to increasing wind speed is similar at both locations: in the 30–80 Hz band, the PSD shows no substantial trend with increasing wind speed, both during ice-free and

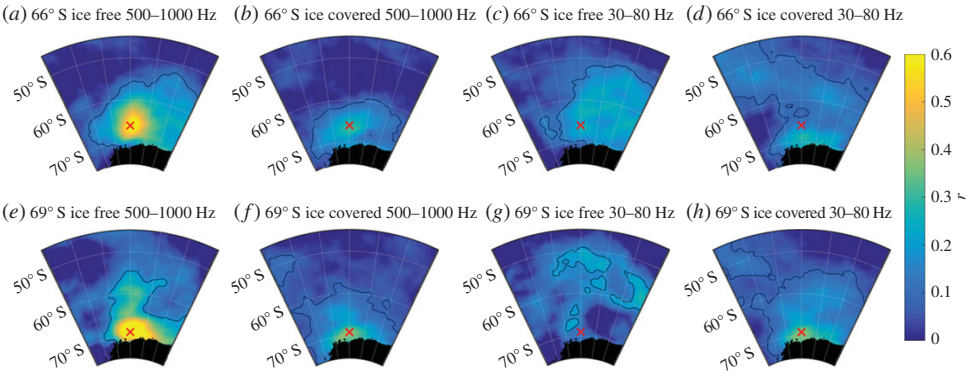

Figure 9. Maps showing the correlation between wind speed and average PSD in two frequency bands under ice-free (average sea-ice concentration in 200 km radius $< 50\%$) and ice-covered (average sea-ice concentration in 200 km radius $> 50\%$) conditions. The colour scale indicates the correlation coefficient r for each cell of the ERA-interim grid, the red cross marks each recorders location and the black contour lines encircles areas with $p > 0.001$, indicating a significant relation between PSD and wind speed. (*a–d*) Recordings from 66° S and (*e–h*) from 69° S. The correlation between average 500–1000 Hz PSD and wind speed (*a*,*e*) during ice-free conditions and (*b*,*f*) during ice-covered conditions. The correlation between average 30–80 Hz PSD and wind speed (*c*,*g*) during ice-free conditions and (*d*,*h*) during ice-covered conditions.

ice-covered conditions. In the 500–1000 Hz band, on the other hand, the PSD increases with increasing wind speed during ice-free conditions (slope of linear fit ≈1.13, $r = 0.7$), and shows no substantial trend during ice-covered conditions.

4. Discussion

The recorded long-term spectrograms represent the prevailing natural sound conditions in the Atlantic sector of the Southern Ocean, consisting of the cumulative emissions from air–sea-ice interaction, marine mammals and icebergs or shelf ice (approx. 200 km to the south of Aural 69° S). Ambient sound generated by shipping typically covers a frequency range from 10 to 1000 Hz and would be difficult to distinguish from sea-surface-generated sound in the ambient sound spectra [2]. However, due to the recorders' large distance to major shipping lanes (over 4000 km), ambient sound generated by shipping is likely to be of minor importance for our observations [36]. Ship-generated sound only dominated the spectrum when RV *Polarstern* approached the moorings containing the recorders (i.e. for deployment and recovery of the moorings). We thus assume that local and distant sea surface processes are the major abiotic sources of ambient sound in the Southern Ocean.

In the PSD dataset, the recorders' self-noise occurred as constant narrow peaks between 80 and 2000 Hz and broadband noise at frequencies above 1000 Hz. As the self-noise remained constant over time and the shackle noise occurred at frequencies away from the MMC bands, the PSD_{MMC} measurements were not affected. Owing to the self-noise's low amplitude and scarcity of the shackle noise, we assume that both had negligible impact on our analysis of the relation between environmental parameters and PSD. It did, however, limit our analysis to frequencies below 1000 Hz, as most spectra above that hit the systems noise floor.

4.1. Sea-surface-generated ambient sound

4.1.1. Wind stress

Wind stress at the sea surface generates sound between approximately 0.1 and 20 kHz [2,3]. The increase in sound levels with increasing wind speeds depends on wind speed and frequency and is largest for frequencies above 500 Hz [2]. Our observations show an approximately linear relationship (slope of linear fit ≈1.13, figure 8) between local wind speed (averaged within 200 km radius) and PSD under ice-free conditions in the 500–1000 Hz band, which is in accordance with other studies [2,4,37]. The large scatter in the relationship between local wind speed, sea ice and PSD can be attributed to the coarse sampling of the climate data (figure 8). The correlation between local wind speed and ambient sound levels (figures 8 and 9) is comparable with previous studies [38,39]. The low-frequency (10–500 Hz)

spectrum is dominated by the cumulative sound emitted from distant sources and surface waves [2], which explains the poor correlation between local wind speed and ambient sound levels below 500 Hz (figures 8 and 9). The lack of correlation between local wind speed and ambient sound during the presence of sea ice confirms the expectation that the sea-ice cover effectively shields the sea surface from direct wind stress and prevents local wind-generated sound. Figure S6 in the electronic supplementary material illustrates the changing relation between PSD and local wind speed for the summer and autumn of 2009 by comparing the long-term spectrogram with the local wind speed.

4.1.2. Local versus distant sound sources

South of the Antarctic Convergence Zone (i.e. south of 60° S), the sound speed minimum is located close to the sea surface, thus creating a surface sound duct [40]. Both recorders had been moored at the deeper end of this duct (electronic supplementary material, figure S7). According to Buckingham [41], under upward refracting conditions, ambient sound consists of a direct path (from local sources above the receiver) and a modal (mainly from distant sources) component. He, furthermore, inferred that sound levels decrease with depth, with the strongest gradients occurring in the modal component, in the upper 500 m and frequencies above 100 Hz [41]. However, as the depth difference between our recorders was only 43 m, we assume that the depth dependence of sound levels only had a minor impact on the observed PSD. In the 30–80 Hz band, Buckingham's theory predicts the dominance of the modal component, whereas in the 500–1000 Hz band, the theory predicts an overlap of the direct path and modal components [41].

Given that wind-induced surface motion is one of the major sound sources over the observed spectrum [2], the correlation maps between wind speed and PSD in figure 9 roughly indicate regions of significant noise contribution. The correlation maps indicate that during ice-free conditions, 500–1000 Hz PSD correlates strongly with local wind speed (approx. 200 km radius) and weakly with wind speed in a broad region around the recorder (approx. 600 km radius), whereas during ice-covered conditions 500–1000 Hz PSD only correlates weakly with wind speed in a broad region around the recorder (approx. 600 km radius). These results suggest that, in the 500–1000 Hz band, distant sources (modal component) dominate under ice-covered conditions, whereas local sources (direct path component) dominate under ice-free conditions. This is supported by the observation that the spatial averaging radius corresponding to the strongest correlation between sea-ice concentration and PSD was a magnitude larger at 69° S (surrounded by more sea ice) compared with 66° S (electronic supplementary material, figure S5). In the 30–80 Hz band, the correlation maps (figure 9) indicate the dominance of distance sources during both ice-free and ice-covered conditions. Under ice-covered conditions and for both frequency bands at 69° S, and for the 30–80 Hz band at 66° S, the correlation maps show highest values for a region indicative of the coastal polynya. This suggests that the polynyas around the Antarctic continent are important contributors of ambient sound during austral winter.

4.1.3. Sea ice as sink and source of underwater sound

The comparison between PSD and sea-ice concentration, draught and extent showed that a growing ice cover decreases ambient sound levels across the observed spectrum, with the strongest correlation in the 30–80 Hz band (figures 7 and 8). Low-frequency ambient is generated by sea surface motion, through a combination of several mechanisms [4,42]. The sea ice effectively attenuates surface motion, and thus reduces low-frequency (10–500 Hz) sound generated by surface waves. In addition to attenuating the local sound source mechanism, an increase in sea-ice extent, concentration, roughness and thickness will increase the attenuation of sound from distant sources [43]. The hypothesis that sea-ice thickness and roughness are important variables determining under-ice sound levels is supported by the fact that minimum PSD values in the 30–80 Hz band are reached while sea-ice draught measurements reach maximum values (approx. November, figure 7), which is after the sea-ice concentration and sea-ice extent reach maximum values (approx. July and September, figure 7). The increase of the annual minimum PSD in the 30–80 Hz band corresponds to the decrease of the annual maximum sea-ice draught (figure 7), whereas the decrease of the annual maximum PSD in the 30–80 Hz band probably corresponds to an increase of the annual minimum sea-ice extent (January to March) in the Weddell Sea [35]. The observation that, during winter, PSD values in the 30–80 Hz band were slightly lower at 69° S than 66° S, can be attributed to higher concentrations of sea ice (and a larger surrounding sea-ice area) at 69° S compared with 66° S. During winter, the 500–1000 Hz band PSD is slightly higher at 69° S than at 66° S (figure 7). The correlation maps (figure 9) suggest that the extra sound energy originates from the marginal sea-ice zone and ice-free areas of the coastal polynya. Overall, the observed relation between

ambient sound levels, sea-ice concentration and wind speed is comparable with the Arctic Ocean, where a 5–20 dB reduction of ambient sound levels was observed under sea ice [37].

In our observations, the net effect of the sea-ice cover is a reduction of ambient sound levels. However, sea ice is also a source of underwater sound, especially in the marginal sea-ice zone, where surface waves penetrate the ice floes [36,44]. Sea-ice-generated sound (icequakes) can contribute to ambient sound over the observed spectrum [2,36,44–46]. Icebergs and shelf ice can be intense sound sources (especially during calving events) and can contribute to ambient sound below 100 Hz [36,47]. Sound from the shelf ice edge (approx. 200 km from Aural 69° S and 500 km from Aural 66° S) could explain the increased PSD below 50 Hz at 69° S (figure 3). The effect of precipitation on ambient sound is not considered here, but has generally shorter and more localized effects on ambient sound than wind stress, and is of lesser importance than wind stress for the frequency bands analysed here (30–80 and 500–1000 Hz) [2].

4.2. Marine mammal contributions

Previous studies on the contribution of marine mammals to underwater ambient sound used relative metrics to describe the contribution (acoustic power method in [23], fin whale index in [48] and blue whale index in [49]), effectively describing the SNR of MMCs (termed signal in this context) to the abiotic ambient sound (termed noise in this context). This approach carries the risk of adding interference from abiotic sound fluctuations into the MMC measure. To avoid this, we calculated the strength of the MMC using absolute PSDs by subtracting interpolated abiotic spectra from the measured spectra (see §2.2). To illustrate the difference between the two metrics, figure 10 displays the Antarctic minke whale contributions SNR_{MMC} and PSD_{MMC}. The two time series exhibit different temporal patterns, peaking at different times. If the abiotic sound were roughly constant over time, the two time series would show similar patterns. But as the abiotic ambient sound shows substantial temporal variation, the SNR_{MMC} reflects both variation in the MMC (signal) and abiotic ambient sound (noise). To avoid this interference with abiotic sound fluctuation, we choose to analyse the MMCs using PSD_{MMC} as metric. Avoiding this interference is particularly relevant when sound energy contribution metrics are used to infer information on the animal's distribution and behaviour.

There are several other aspects that have to be borne in mind when deriving information on marine mammal occurrence and distribution from ambient sound spectra. The observed marine mammal PSDs only indicate periods of intense vocal activity, as sporadic calls will not be visible as peaks in the acoustic power spectra (too low SNR_{MMC}). Furthermore, marine mammal PSDs only contain information about the marine mammal presence, not absence (animals can be present in the area but not vocalize) and the vocalizing population could be sex or age segregated. For a given location, increased $PSDs_{MMC}$ could be caused by a combination of processes: an increase in number of vocalizing animals, increase in source level, increase in call rate, decreasing distance to the vocalizing animals or decreasing transmission loss between the vocalizing animals and the recorder.

The recorded $PSDs_{MMC}$ show annually reoccurring patterns that vary between species and recorder location (figure 5). It is important to note here that the PSDs of each species' contribution were only calculated over each MMC's core frequency band (f_{min} to f_{max}) and not each MMC's entire frequency range (table 2). Thus, a comparison of PSDs between different species or with abiotic sound sources is most informative when comparing relative patterns. The following sections discuss the species-specific observations.

4.2.1. Antarctic blue whales

Blue whale calls are recorded in all the world's oceans and distinct call types have been associated with specific subpopulations [50]. A persistent decrease in blue whale vocalization frequency has been observed globally and was also found in our recordings [34,51]. In the North Pacific and Indian Ocean, the spatial and temporal variation in blue whale vocal activity has been associated with annual migration patterns [34,38,52]. The observed inverse relation between sea-ice extent and Antarctic blue whale PSD indicates either latitudinal migration of vocalizing Antarctic blue whales or changes in vocal activity related to the seasonal cycle or sea ice. During austral summer and its limited sea-ice cover (January–March), Antarctic blue whale PSD is similar at 66° S and 69° S, while during austral winter (with high concentrations of sea ice), Antarctic blue whale PSD is stronger at 66° S than 69° S. Along the western shelf of the Antarctic Peninsula, Širović *et al*. [23] observed two annual peaks (March–May and October–November) in Antarctic blue whale vocal activity. The first of these peaks coincides with the Antarctic blue whale PSD peak and the minimum in sea-ice extent in this study, whereas an October–November

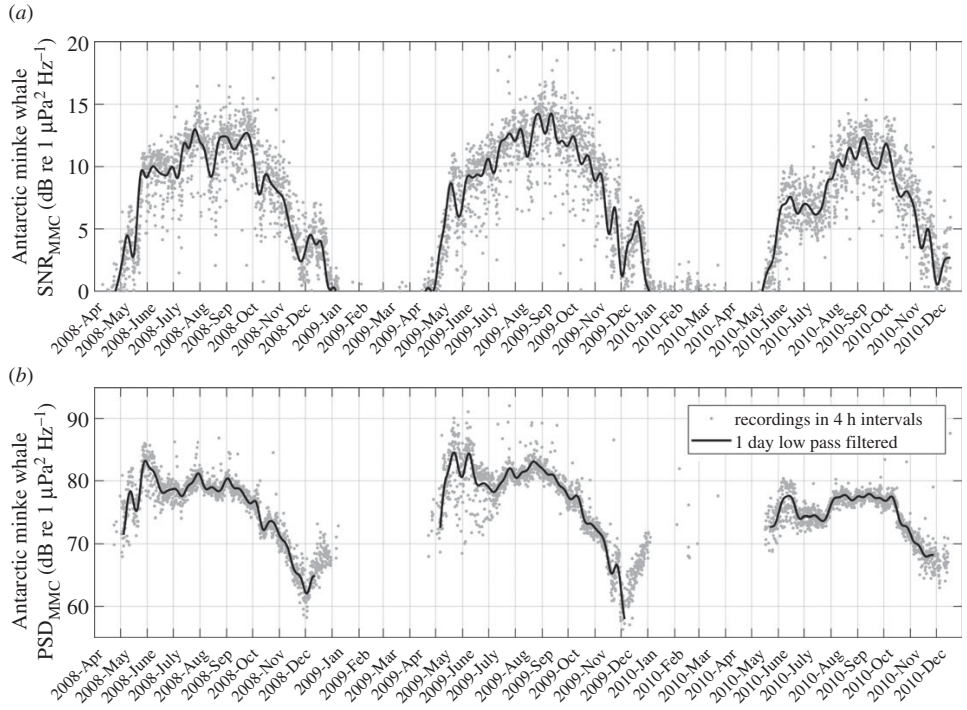

Figure 10. Comparison of the Antarctic minke whale contributions signal-to-noise ratio (SNR) and power spectral density (PSD, as based on factory calibration) recorded at 66° S. Grey dots represent values for each recording, black line the 1-day running mean. The PSD and SNR time series peak at different times and the May–June peak in PSD is absent from the SNR time series.

peak in vocal activity is absent in our data (figure 5*a*). Our observations match the Antarctic blue whale vocal activity pattern in the Drake Passage [36] and the Weddell Sea [49], where highest vocal activity was recorded in the end of summer and beginning of autumn (January–May). The 1996 stock of approximately 1700 Antarctic blue whales was estimated to be 0.7% the size of the pre-whaling stock (approx. 239 000 animals) [53]. Considering the sound produced by the contemporary population, the sound energy Antarctic blue whales contributed to the acoustic environment has probably been considerably higher before the depletion of stocks.

4.2.2. Fin whales

Owing to their low frequency (approx. 20 Hz) and high call rate, the pulsed vocalizations of fin whales are detectable as a peak in many recorded ambient sound spectra [54–56]. West of the Antarctic peninsula, fin whale vocal activity peaks annually between March and May [17,23], whereas fin whale PSD in our observations peaks between March and June, similar to vocal activity observations from Eastern Antarctica (approx. 67° S, approx. 70° E) [17]. The upper frequency component of the fin whale contribution west of the Antarctic Peninsula and in the Scotia Sea [17,23] is 9 Hz below the one we observed (at 98 Hz), whereas the fin whale contributions measured near Eastern Antarctica match our recordings [17]. The spectral offsets between the different recording locations suggest separate populations, which confirms Širović's findings [17], and indicates a connection between fin whales recorded in the Eastern Antarctic and the Atlantic sector of the Southern Ocean. The varying difference in fin whale PSD between 66° S and 69° S could be an indicator of latitudinal migration and the stronger fin whale PSD at 66° S compared with 69° S indicates that vocal activity or migration are influenced by the seasonal cycle or sea ice. Although the major part of each fin whale vocalization's sound energy is contained in the lower call component (approx. 20 Hz) [17], we only analysed the variation of the upper call component between 96 and 99 Hz to avoid interference with the Antarctic blue whale contribution. Given that fin whales could vary their use of the two call components, the PSD corresponding to

the lower call component might show a different pattern to the PSD we measured for the upper call component.

4.2.3. Antarctic minke whales

Antarctic minke whale vocalizations have only recently been identified and were previously known as 'Bioduck' signals [25]. Studies along the Weddell Sea coast and near the Australian coast most frequently observed Antarctic minke whale vocal activity in austral winter, and no vocal activity in austral summer [57,58]. A similar pattern was found in our recordings (figure 5*c*). The difference in Antarctic minke whale PSD between 66° S and 69° S suggests latitudinal migration of vocalizing minke whales or local changes in vocal behaviour. A part of the annual and spatial variation of PSD could also be caused by changes in transmission loss due to sea-ice growth and melting. Annually, Antarctic minke whale PSD peaked during May and October at 66° S, and during October and December at 69° S (except a unique peak in PSD at 69° S in May and June 2008). This suggests a southward migration of vocalizing Antarctic minke whales, or southward shift in vocal behaviour in austral spring. Antarctic minke whales frequently feed on dense patches of krill under sea ice [59]; the variation in Antarctic minke whale PSD could thus be linked to favourable prey and sea-ice conditions [60].

A connection between feeding and vocal behaviour is supported by the finding that the Antarctic minke whale contribution followed a diel cycle from the end of April to August (figure 6; electronic supplementary material, figure S1), with high vocal activity at midnight and less at midday. For northern minke whales, a similar diel cycle in vocal activity was observed in Massachusetts Bay and associated with feeding and mating [61]. The period when the Antarctic minke whale population's vocal behaviour follows a diel pattern overlaps with the time of minimal irradiance and growing sea-ice extent in the Southern Ocean. The diel calling cycle is thus probably not linked to irradiance cues from the sun. However, the diel vertical migration of zooplankton (DVM), including Antarctic krill (*Euphausia superba*), has been shown to occur in the polar night in the Atlantic sector of the Southern Ocean [62]. The occurrence of DVM coincides with the diel pattern in Antarctic minke whale PSD in time and space. Acoustic Doppler current profilers moored along the Greenwich meridian observed distinct DVM patterns from February to October at 66° S and between February and June at 69° S [63,64]. This coincides with the timing of the observed Antarctic minke whale PSD diel pattern. As typical for most DVM patterns, high zooplankton concentrations are found at the surface at night (when the Antarctic minke whale PSD was loudest) [62,63], and low concentrations during the day (figure 6*b*). Antarctic minke whales have been observed feeding directly under the sea surface, skimming the underside of sea ice for krill [59]. Given their under-ice feeding behaviour and the temporal and spatial overlap between DVM and diel PSD pattern, it is possible that at least from May to July, Antarctic minke whale vocalizations are connected to feeding. This connection could be in a mating context, attracting potential partners to favourable feeding locations (when krill is at the surface, midnight) or simply because feeding on krill at depth during midday limits simultaneous calling.

4.2.4. Leopard seals

Leopard seal vocalizations have been associated with mating: both sexes are known to produce a variety of calls [26]. Owing to their relatively short periods of intense vocal activity, leopard seal vocalizations are a minor source of ambient sound compared with the baleen whale contributions [26]. Along the Weddell Sea coast, leopard seal vocal activity has been observed between December and February and partly followed a diel pattern [26]. This agrees with the timing of the leopard seal contribution recorded at 66° S and 69° S (December to mid-January), although we found no persistent diel pattern in leopard seal PSD.

5. Conclusion

In contrast with the high levels of anthropogenic sound present in the Arctic [9], the Southern Ocean acoustic environment remains largely free of anthropogenic sound and can serve as reference for future ambient sound studies. We recorded substantial natural variability of ambient sound in the Southern Ocean. Our observations show that wind stress, sea ice and marine mammals are the major contributors of ambient sound between 10 and 1000 Hz in the offshore areas of the Southern Ocean. Sea-surface-generated sound dominates the ambient sound spectrum, except for the frequency bands containing MMCs. Figure 11 displays typical ambient sound spectra with respect to the sound sources. The

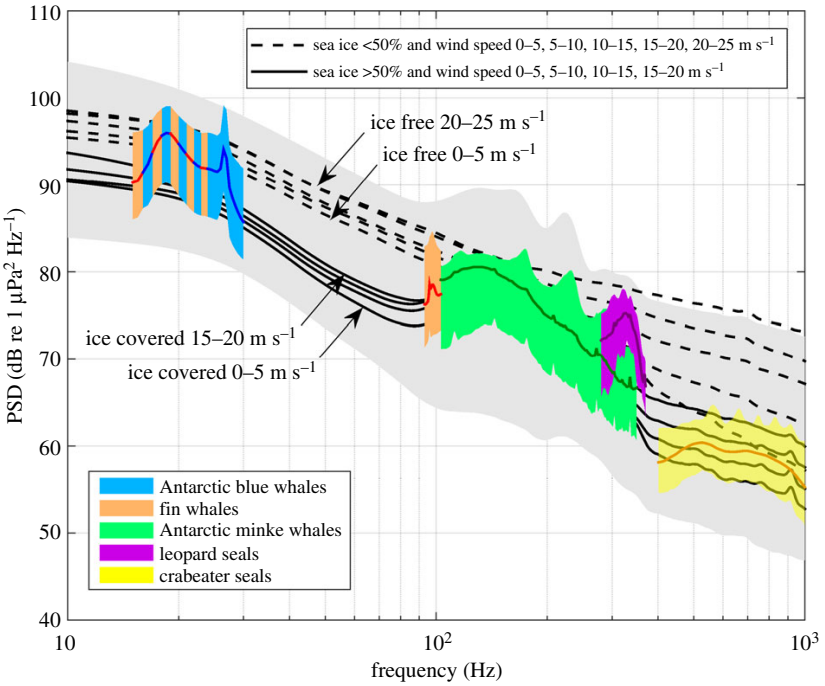

Figure 11. Typical features of the recorded ambient sound at 66° S. Grey area shows range of recorded spectra from 1st till 99th percentile, black lines show the average spectra at different wind speed and sea-ice conditions (averaged within 50 km radius), coloured spectra show averaged marine mammal contribution peaks and the coloured areas the respective 10th and 90th percentile peaks. The blue-red striped area indicates the frequency band between 15 and 25 Hz where the fin and Antarctic blue whale contribution overlap. Spectra have been filtered with running mean window between 5 and 50 Hz. PSD based on factory calibration.

black lines represent averaged spectra during different wind speed and sea-ice conditions. Our results confirm that sea ice reduces ambient sound levels by attenuating surface and acoustic waves, decouples the ambient sound from local wind speed and increases the dominance of distant sources. Southern Ocean ambient sound is strongly connected to the annual cycle: sea-surface-generated sound decreased with growing sea-ice concentration, thickness and extent, and marine mammal vocal activity followed annually reoccurring patterns.

The temporal and spatial variability of the MMCs contains information about behavioural and distribution patterns. Recording MMCs with a higher spatial resolution and combining these measurements with statistical and acoustic propagation models can render it possible to estimate the spatial distribution of vocalizing animals, which will improve our understanding of their behaviour, migration and habitat use.

Ethics. Permission to conduct fieldwork and deploy moorings in the Southern Ocean was granted by the German federal environmental agency (UBA permit no. I 2.4-94003-3/207).

Data accessibility. The ambient sound dataset and analysis code are available through the Dryad Digital Repository (http://dx.doi.org/10.5061/dryad.83s93) [65], ERA-interim data through the ECMWF website (http://www.ecmwf.int/), sea-ice concentration data through the University of Bremen (http://www.iup.uni-bremen.de/seaice/amsr/) and sea-ice draught data through the Pangea repository (https://doi.pangaea.de/10.1594/PANGAEA.821257).

Authors' contributions. S.M. carried out the data analysis and wrote the manuscript; D.P.Z. participated in the data analysis and helped drafting the manuscript together with I.v.O.; O.B. designed and coordinated the study, deployed the recorders and contributed to the discussions around the manuscript. All authors gave final approval for publication.

Competing interests. The authors have no competing interests.

Funding. The authors carried out the fieldwork and data analysis while employed at the Alfred Wegener Institute Helmholtz Centre for Polar and Marine Research.

Acknowledgements. We thank the crew of RV *Polarstern*, Matthias Monsees and Olaf Strothmann for the deployment and recovery of the recorders, Stefanie Spiesecke and Lars Kindermann for managing and cleaning up the raw data, and the AWI Ocean Acoustics Lab for making this paper possible. The ECMWF, National Snow and Ice Data Center and Axel Behrendt are thanked for sharing their data. We also thank W. E. Farrell, an anonymous reviewer and the associate editor for their constructive comments on the manuscript.

References

1. ISO 12913-1:2014 . 2015 Acoustics —soundscape— part 1: definition and conceptual framework.
2. Carey WM, Evans RB. 2011 *Ocean ambient noise*. New York, NY: Springer.
3. Wenz GM. 1962 Acoustic ambient noise in the ocean: spectra and sources. *J. Acoust. Soc. Am.* **34**, 1936–1956. (doi:10.1121/1.1909155)
4. Duennebier FK, Lukas R, Nosal EM, Aucan J, Weller RA. 2012 Wind, waves, and acoustic background levels at Station ALOHA. *J. Geophys. Res. C, Oceans* **117**, C03017. (doi:10.1029/2011JC007267)
5. McDonald MA, Hildebrand JA, Wiggins SM. 2006 Increases in deep ocean ambient noise in the Northeast Pacific west of San Nicolas Island, California. *J. Acoust. Soc. Am.* **120**, 711–718. (doi:10.1121/1.2216565)
6. Andrew RK, Howe BM, Mercer JA. 2011 Long-time trends in ship traffic noise for four sites off the North American West Coast. *J. Acoust. Soc. Am.* **129**, 642–651. (doi:10.1121/1.3518770)
7. Miksis-Olds JL, Bradley DL, Maggie Niu X. 2013 Decadal trends in Indian Ocean ambient sound. *J. Acoust. Soc. Am.* **134**, 3464. (doi:10.1121/1.4821537)
8. Frisk GV. 2012 Noiseonomics: The relationship between ambient noise levels in the sea and global economic trends. *Sci. Rep.* **2**, 437. (doi:10.1038/srep00437)
9. Moore SE, Stafford KM, Melling H, Berchok C, Wiig O, Kovacs KM, Lydersen C, Richter-Menge J. 2012 Comparing marine mammal acoustic habitats in Atlantic and Pacific sectors of the High Arctic: year-long records from Fram Strait and the Chukchi Plateau. *Polar Biol.* **35**, 475–480. (doi:10.1007/s00300-011-1086-y)
10. Clark C, Ellison W, Southall B, Hatch L, Van Parijs S, Frankel A, Ponirakis D. 2009 Acoustic masking in marine ecosystems: intuitions, analysis, and implication. *Mar. Ecol. Prog. Ser.* **395**, 201–222. (doi:10.3354/meps08402)
11. Castellote M, Clark CW, Lammers MO. 2012 Acoustic and behavioural changes by fin whales (*Balaenoptera physalus*) in response to shipping and airgun noise. *Biol. Conserv.* **147**, 115–122. (doi:10.1016/j.biocon.2011.12.021)
12. Williams R, Clark CW, Ponirakis D, Ashe E. 2014 Acoustic quality of critical habitats for three threatened whale populations. *Anim. Conserv.* **17**, 174–185. (doi:10.1111/acv.12076)
13. Perrin WF, Würsig BG, Thewissen JGM. 2009 *Encyclopedia of marine mammals*. New York, NY: Academic Press.
14. Van Parijs S, Clark C, Sousa-Lima R, Parks S, Rankin S, Risch D, Van Opzeeland I. 2009 Management and research applications of real-time and archival passive acoustic sensors over varying temporal and spatial scales. *Mar. Ecol. Prog. Ser.* **395**, 21–36. (doi:10.3354/meps08123)
15. Garland EC, Gedamke J, Rekdahl ML, Noad MJ, Garrigue C, Gales N. 2013 Humpback whale song on the Southern Ocean feeding grounds: implications for cultural transmission. *PLoS ONE* **8**, e79422. (doi:10.1371/journal.pone.0079422)
16. Dominello T, Širović A. 2016 Seasonality of Antarctic minke whale (*Balaenoptera bonaerensis*) calls off the western Antarctic Peninsula. *Mar. Mammal Sci.* **32**, 826–838. (doi:10.1111/mms.12302)
17. Širović A, Hildebrand JA, Wiggins SM, Thiele D. 2009 Blue and fin whale acoustic presence around Antarctica during 2003 and 2004. *Mar. Mammal Sci.* **25**, 125–136. (doi:10.1111/j.1748-7692.2008.00239.x)
18. Fahrbach E, de Baar H, Participants of the ANT-XXIV/3 expedition. 2010 The expedition of the Research Vessel 'Polarstern' to the Antarctic in 2008 (ANT-XXIV/3). *Ber. Polar Meeresforsch.* **606**, 1–232.
19. Amante C, Eakins BW. 2009 ETOPO1 1 arc-minute global relief model: procedures, data sources and analysis. NOAA Tech. Memo. NESDIS NGDC-24. Natl Geophys. Data Center, NOAA. (doi:10.7289/V5C8276M)
20. Multi-Électronique Inc. 2016 Autonomous underwater recorder for acoustic listening model 2—user guide, pp. 1–48.
21. Fahrbach E, Participants of the ANT-XXVII/2 expedition. 2011 The expedition of the Research Vessel 'Polarstern' to the Antarctic in 2010/11 (ANT-XXVII/2). *Ber. Polar Meeresforsch.* **634**, 1–242.
22. Welch P. 1967 The use of fast Fourier transform for the estimation of power spectra: a method based on time averaging over short, modified periodograms. *IEEE Trans. Audio Electroacoust.* **15**, 70–73. (doi:10.1109/TAU.1967.1161901)
23. Širović A, Hildebrand JA, Wiggins SM, McDonald MA, Moore SE, Thiele D. 2004 Seasonality of blue and fin whale calls and the influence of sea ice in the Western Antarctic Peninsula. *Deep. Res. II Top. Stud. Oceanogr.* **51**, 2327–2344. (doi:10.1016/j.dsr2.2004.08.005)
24. Širovic A, Hildebrand JA, Wiggins SM. 2007 Blue and fin whale call source levels and propagation range in the Southern Ocean. *J. Acoust. Soc. Am.* **122**, 1208–1215. (doi:10.1121/1.2749452)
25. Risch D *et al.* 2014 Mysterious bio-duck sound attributed to the Antarctic minke whale (*Balaenoptera bonaerensis*). *Biol. Lett.* **10**, 20140175. (doi:10.1098/rsbl.2014.0175)
26. Van Opzeeland I, Van Parijs S, Bornemann H, Frickenhaus S, Kindermann L, Klinck H, Plötz J, Boebel O. 2010 Acoustic ecology of Antarctic pinnipeds. *Mar. Ecol. Prog. Ser.* **414**, 267–291. (doi:10.3354/meps08683)
27. Dee DP *et al.* 2011 The ERA-interim reanalysis: configuration and performance of the data assimilation system. *Q. J. R. Meteorol. Soc.* **137**, 553–597. (doi:10.1002/qj.828)
28. Spreen G, Kaleschke L, Heygster G. 2008 Sea ice remote sensing using AMSR-E 89-GHz channels. *J. Geophys. Res.* **113**, C02S03. (doi:10.1029/2005JC003384)
29. Fetterer F, Knowles K, Meier W, Savoie M. 2016 *Sea ice index: Antarctic sea ice extent*. Boulder, CO: NSIDC Natl Snow Ice Data Center.
30. Behrendt A, Dierking W, Fahrbach E, Witte H. 2013 Sea ice draft measured by upward looking sonars in the Weddell Sea (Antarctica). Earth Syst. Sc. Data **5**, 209–226. (doi:10.1594/PANGAEA.785565)
31. Smith S. 2003 *Digital signal processing: a practical guide for engineers and scientists*. Newnes, Australia: Elsevier Science.
32. Klinck H, Mellinger DK, Klinck K, Hager J, Kindermann L, Boebel O. 2010 Long-range underwater vocalizations of the crabeater seal (*Lobodon carcinophaga*). *J. Acoust. Soc. Am.* **128**, 474–479. (doi:10.1121/1.3442362)
33. Rankin S, Ljungblad D, Clark C, Kato H. 2005 Vocalisations of Antarctic blue whales, *Balaenoptera musculus intermedia*, recorded during the 2001/2002 and 2002/2003 IWC/SOWER circumpolar cruises, Area V, Antarctica. *J. Cetacean Res. Manag.* **7**, 13–20.
34. Gavrilov AN, McCauley RD, Gedamke J. 2012 Steady inter and intra-annual decrease in the vocalization frequency of Antarctic blue whales. *J. Acoust. Soc. Am.* **131**, 4476. (doi:10.1121/1.4707425)
35. Parkinson CL, Cavalieri DJ. 2012 Antarctic sea ice variability and trends, 1979–2010. *Cryosphere* **6**, 871–880. (doi:10.5194/tc-6-871-2012)
36. Dziak RP *et al.* 2015 Sources and levels of ambient ocean sound near the Antarctic Peninsula. *PLoS ONE* **10**, e0123425. (doi:10.1371/journal.pone.0123425)
37. Roth EH, Hildebrand JA, Wiggins SM, Ross D. 2012 Underwater ambient noise on the Chukchi Sea continental slope from 2006–2009. *J. Acoust. Soc. Am.* **131**, 104–110. (doi:10.1121/1.3664096)
38. Curtis KR, Howe BM, Mercer JA. 1999 Low-frequency ambient sound in the North Pacific: long time series observations. *J. Acoust. Soc. Am.* **106**, 3189–3200. (doi:10.1121/1.428173)
39. Cato DH, Tavener S. 1997 Ambient sea noise dependence on local, regional and geostrophic wind speeds: implications for forecasting noise. *Appl. Acoust.* **51**, 317–338. (doi:10.1016/S0003-682X(97)00001-7)
40. Northrop J, Hartdegen C. 1980 Underwater sound propagation paths between Perth, Australia, and Bermuda: theory and experiment. NOSC Technical Report 585. San Diego, CA: Naval Ocean Systems Center.
41. Buckingham MJ. 1994 On surface-generated ambient noise in an upward refracting ocean. *Phil. Trans. R. Soc. Lond. A* **346**, 321–352. (doi:10.1098/rsta.1994.0024)
42. Yoon SW, Crum LA, Prosperetti A, Lu NQ. 1991 An investigation of the collective oscillations of a bubble cloud. *J. Acoust. Soc. Am.* **89**, 700–706. (doi:10.1121/1.1894629)
43. Diachok OI. 1976 Effects of sea-ice ridges on sound propagation in the Arctic Ocean. *J. Acoust. Soc. Am.* **59**, 1110–1120. (doi:10.1121/1.380965)
44. Pritchard RS. 1990 Sea ice noise-generating processes. *J. Acoust. Soc. Am.* **88**, 2830–2842. (doi:10.1121/1.399687)
45. Lewis JK, Denner WW. 1988 Arctic ambient noise in the Beaufort Sea: seasonal relationships to sea ice kinematics. *J. Acoust. Soc. Am.* **83**, 549–565. (doi:10.1121/1.396149)
46. Kinda GB, Simard Y, Gervaise C, Mars JI, Fortier L. 2013 Under-ice ambient noise in Eastern Beaufort Sea, Canadian Arctic, and its relation to environmental forcing. *J. Acoust. Soc. Am.* **134**, 77–87. (doi:10.1121/1.4808330)
47. Chapp E, Bohnenstiehl DR, Tolstoy M. 2005 Sound-channel observations of ice-generated tremor in the Indian Ocean. *Geochem. Geophys. Geosyst.* **6**, 1–14. (doi:10.1029/2004GC000889)
48. Nieukirk SL, Mellinger DK, Moore SE, Klinck K, Dziak RP, Goslin J. 2012 Sounds from airguns and fin whales recorded in the mid-Atlantic Ocean,

1999–2009. *J. Acoust. Soc. Am.* **131**, 1102–1112. (doi:10.1121/1.3672648)

49. Thomisch K, Boebel O, Clark C, Hagen W, Spiesecke S, Zitterbart D, Van Opzeeland I. 2016 Spatio-temporal patterns in acoustic presence and distribution of Antarctic blue whales *Balaenoptera musculus intermedia* in the Weddell Sea. *Endanger. Species Res.* **30**, 239–253. (doi:10.3354/esr00739)
50. McDonald M, Mesnick S. 2006 Biogeographic characterisation of blue whale song worldwide: using song to identify populations. *J. Cetacean Res. Manag.* **8**, 55–65.
51. McDonald M, Hildebrand J, Mesnick S. 2009 Worldwide decline in tonal frequencies of blue whale songs. *Endanger. Species Res.* **9**, 13–21. (doi:10.3354/esr00217)
52. Burtenshaw JC, Oleson EM, Hildebrand JA, McDonald MA, Andrew RK, Howe BM, Mercer JA. 2004 Acoustic and satellite remote sensing of blue whale seasonality and habitat in the Northeast Pacific. *Deep Sea Res. II Top. Stud. Oceanogr.* **51**, 967–986. (doi:10.1016/j.dsr2.2004.06.020)
53. Branch TA, Matsuoka K, Miyashita T. 2004 Evidence for increases in Antarctic blue whales based on Bayesian modelling. *Mar. Mammal Sci.* **20**, 726–754. (doi:10.1111/j.1748-7692.2004.tb01190.x)
54. Wilcock WSD, Stafford KM, Andrew RK, Odom RI. 2014 Sounds in the ocean at 1–100 Hz. *Ann. Rev. Mar. Sci.* **6**, 117–140. (doi:10.1146/annurev-marine-121211-172423)
55. Nichols RH. 2005 Some notable noises: monsters and machines. *IEEE J. Ocean. Eng.* **30**, 248–256. (doi:10.1109/JOE.2005.850878)
56. Watkins WA, Tyack P, Moore KE, Bird JE. 1987 The 20-Hz signals of finback whales (*Balaenoptera physalus*). *J. Acoust. Soc. Am.* **82**, 1901–1912. (doi:10.1121/1.395685)
57. Van Opzeeland I. 2010 Acoustic ecology of marine mammals in polar oceans. *Rep. Polar Mar. Res.* **619**, 1–332. (doi:10013/epic.36260)
58. Matthews D, Macleod R, McCauley RD. 2004 Bio-duck activity in the Perth Canyon. An automatic detection algorithm. In *Proc. of ACOUSTICS 2004*, pp. 63–66.
59. Friedlaender AS, Goldbogen JA, Nowacek DP, Read AJ, Johnston D, Gales N. 2014 Feeding rates and under-ice foraging strategies of the smallest lunge filter feeder, the Antarctic minke whale (*Balaenoptera bonaerensis*). *J. Exp. Biol.* **217**, 2851–2854. (doi:10.1242/jeb.106682)
60. Bombosch A, Zitterbart DP, Van Opzeeland I, Frickenhaus S, Burkhardt E, Wisz MS, Boebel O. 2014 Predictive habitat modelling of humpback (*Megaptera novaeangliae*) and Antarctic minke (*Balaenoptera bonaerensis*) whales in the Southern Ocean as a planning tool for seismic surveys. *Deep Sea Res. I Oceanogr. Res. Pap.* **91**, 101–114. (doi:10.1016/j.dsr.2014.05.017)
61. Risch D, Clark CW, Dugan PJ, Popescu M, Siebert U, Van Parijs SM. 2013 Minke whale acoustic behavior and multi-year seasonal and diel vocalization patterns in Massachusetts Bay, USA. *Mar. Ecol. Prog. Ser.* **489**, 279–295. (doi:10.3354/meps10426)
62. Flores H, van Franeker JA, Siegel V, Haraldsson M, Strass V, Meesters EH, Bathmann U, Wolff WJ. 2012 The association of Antarctic krill *Euphausia superba* with the under-ice habitat. *PLoS ONE* **7**, e31775. (doi:10.1371/journal.pone.0031775)
63. Cisewski B, Strass VH, Rhein M, Krägefsky S. 2010 Seasonal variation of diel vertical migration of zooplankton from ADCP backscatter time series data in the Lazarev Sea, Antarctica. *Deep. Res. I Oceanogr. Res. Pap.* **57**, 78–94. (doi:10.1016/j.dsr.2009.10.005)
64. Cisewski B, Strass VH. 2016 Acoustic insights into the zooplankton dynamics of the eastern Weddell Sea. *Prog. Oceanogr.* **144**, 62–92. (doi:10.1016/j.pocean.2016.03.005)
65. Menze S, Zitterbart D, Van Opzeeland I, Boebel O. 2016 Data from: The influence of sea ice, wind speed and marine mammals on Southern Ocean ambient sound. Dryad Digital Repository. (doi:10.5061/dryad.83s93)

Supplementary Figures related to the paper: The influence of sea ice, wind speed and marine mammals on Southern Ocean ambient sound

Sebastian Menze, Daniel P. Zitterbart, Ilse van Opzeeland and Olaf Boebel

Corresponding author:
Sebastian Menze, Institute of Marine Research, Bergen, Norway (sebastian.menze@imr.no, orcid.org/0000-0002-2680-9794)

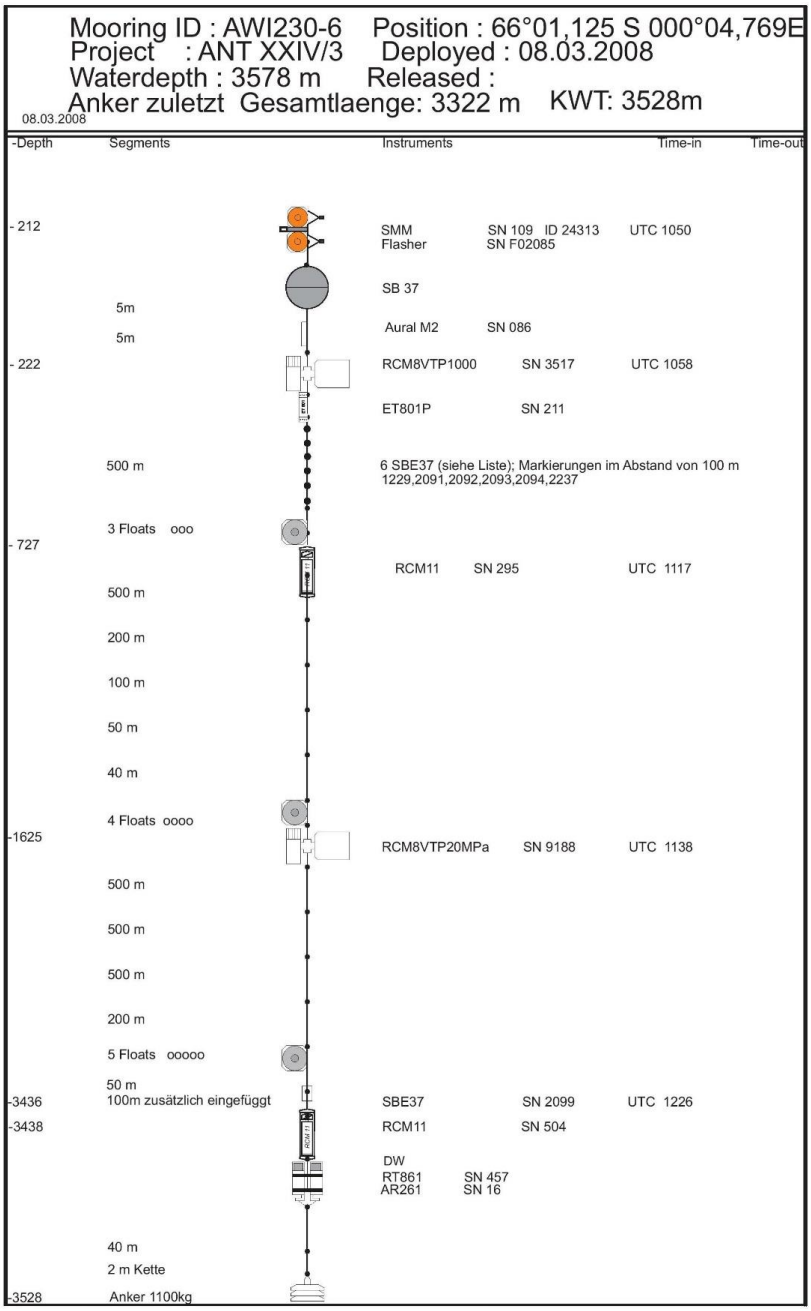

Supplementary Figure 1: Schematic representation of the mooring setup used to deploy Aural 66°S

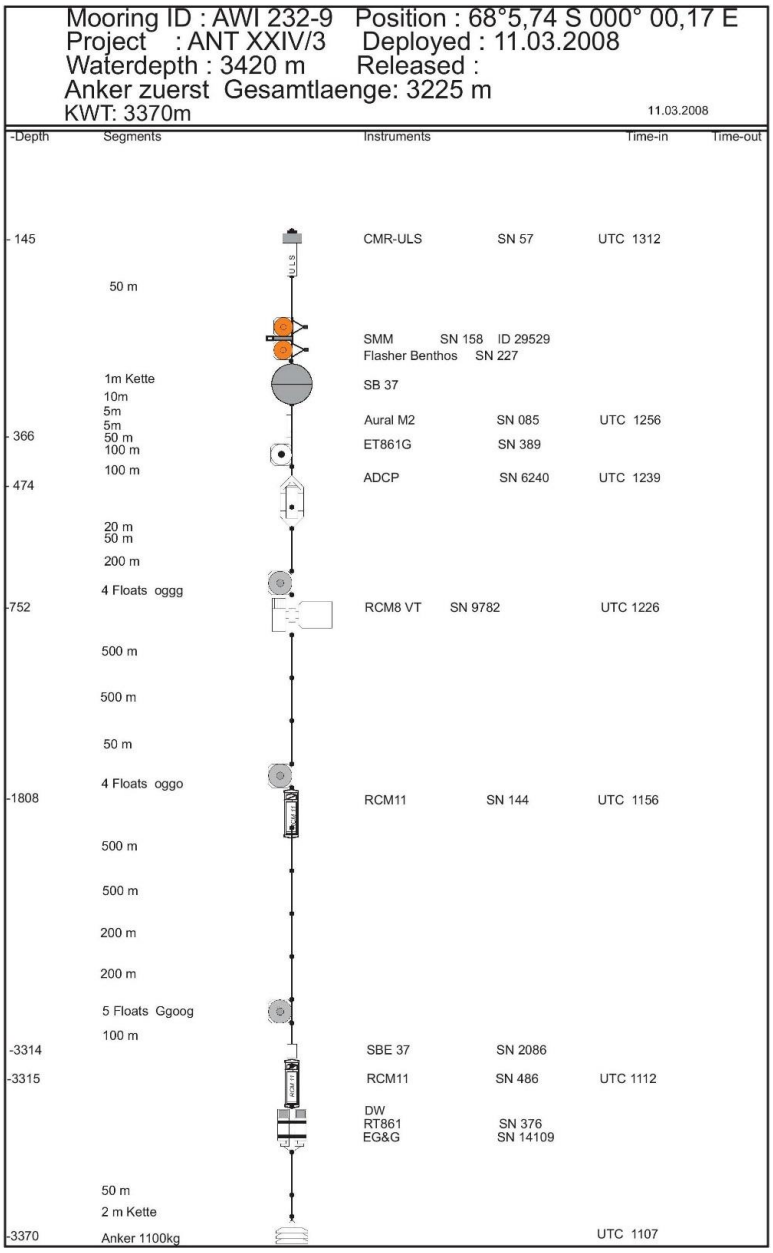

Supplementary Figure 2: Schematic representation of the mooring setup used to deploy Aural 69°S

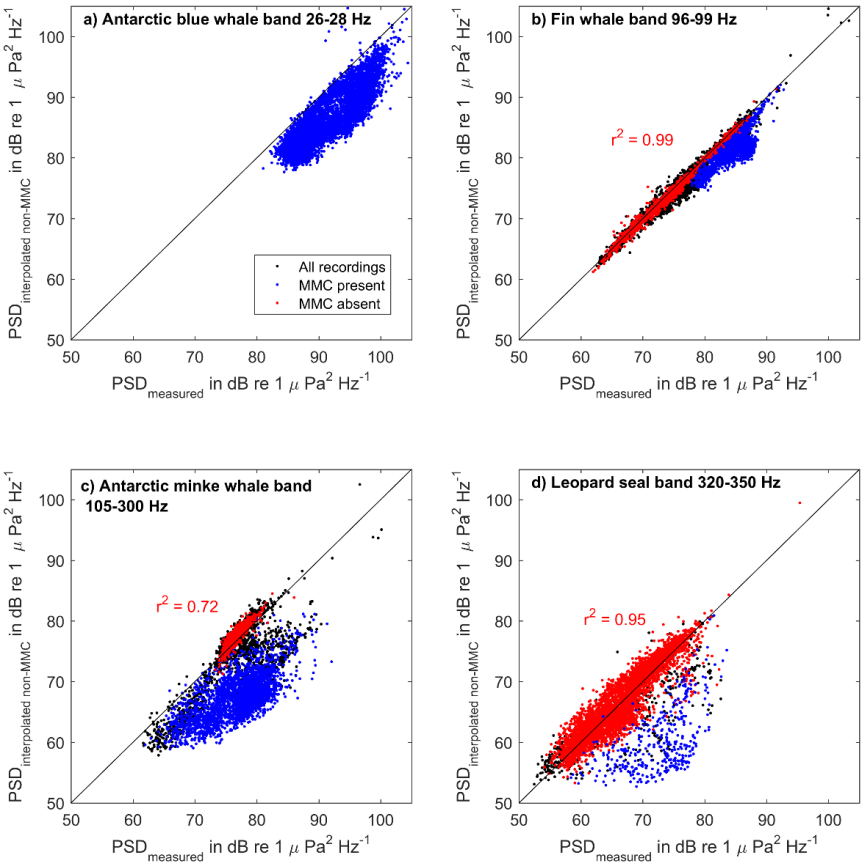

Supplementary Figure 3: Comparison of interpolated and measured PSD at 66°S in the marine mammal contribution frequency bands of a) Antarctic blue whales, b) Fin whales, c) Antarctic minke whales and c) Leopard seals. The black line indicates identical measured and interpolated PSD. Each dot represents a 5-min recordings, blue colour marks spectra where the respective MMC is present and red spectra where the respective MMC is absent.

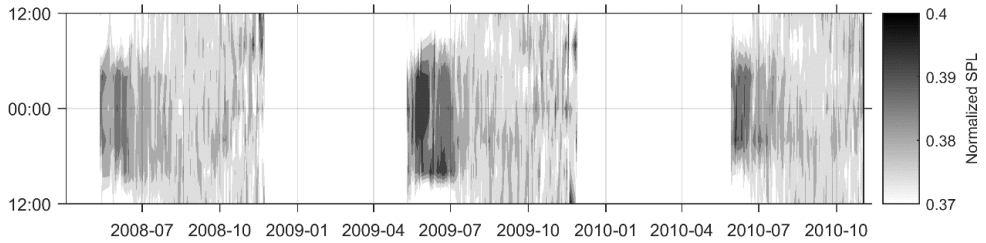

Supplementary Figure 4: Daily normalized Antarctic minke whale PSD at 66°S over time; vertical axis shows time of day (24-h cycle), horizontal axis shows the date and grey scale indicates the daily normalized Antarctic minke whale PSD. From May to July each year the black areas in the middle of the figure indicate a diel pattern, with intense vocal activity at midnight and weak vocal activity during midday. The broad grey areas indicate times where no diel pattern is present in the Antarctic minke whale PSD time series

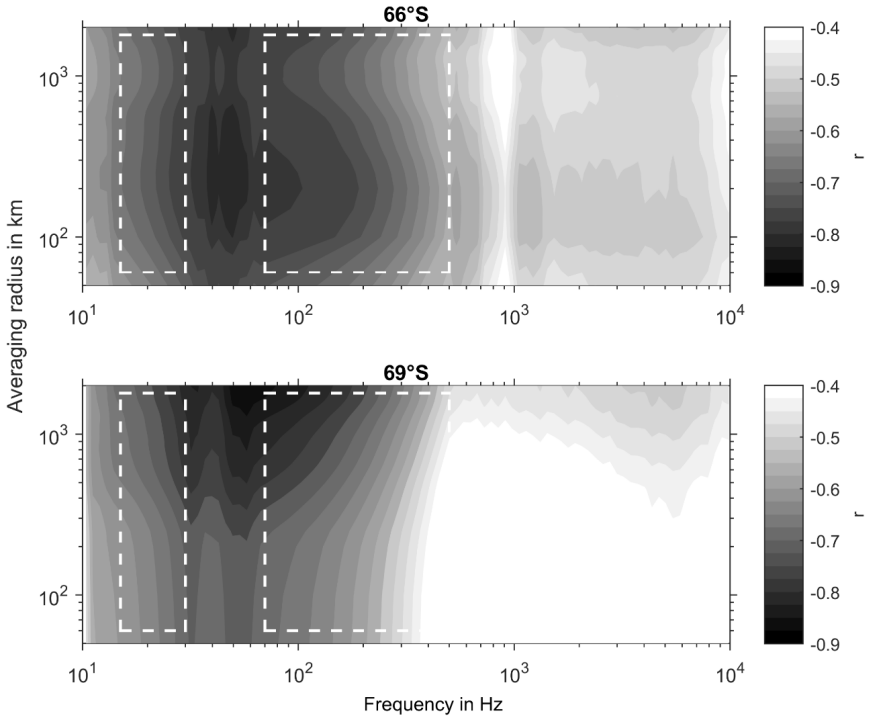

Supplementary Figure 5: Correlation between long-term spectrograms and sea ice concentration using different averaging radii around recorder location from February to July. Horizontal axis shows frequency, vertical axis the averaging radius and grayscale the correlation coefficient. Areas in white dashed box are interpolated correlation coefficients due to interference with marine mammal contributions, upper panel for Aural 66°S, lower for Aural 69°S

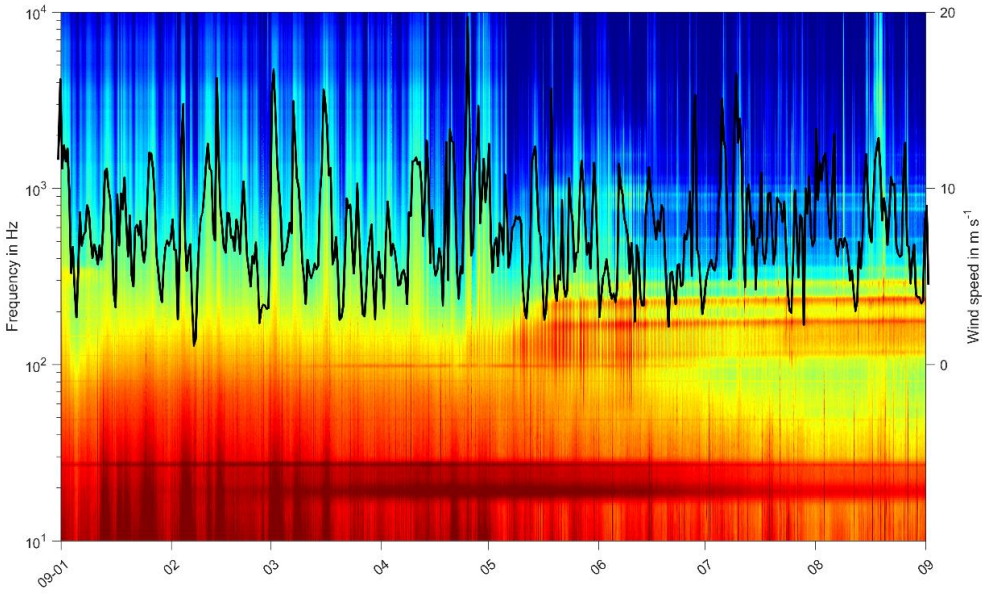

Supplementary Figure 6: Comparison of long-term spectrogram and average wind speed within a 200 km radius (Black line) at 66°S, Colour axis is the same as for Figure 4, ranging from 45 – 100 dB re 1 $\mu Pa^2\ Hz^{-1}$

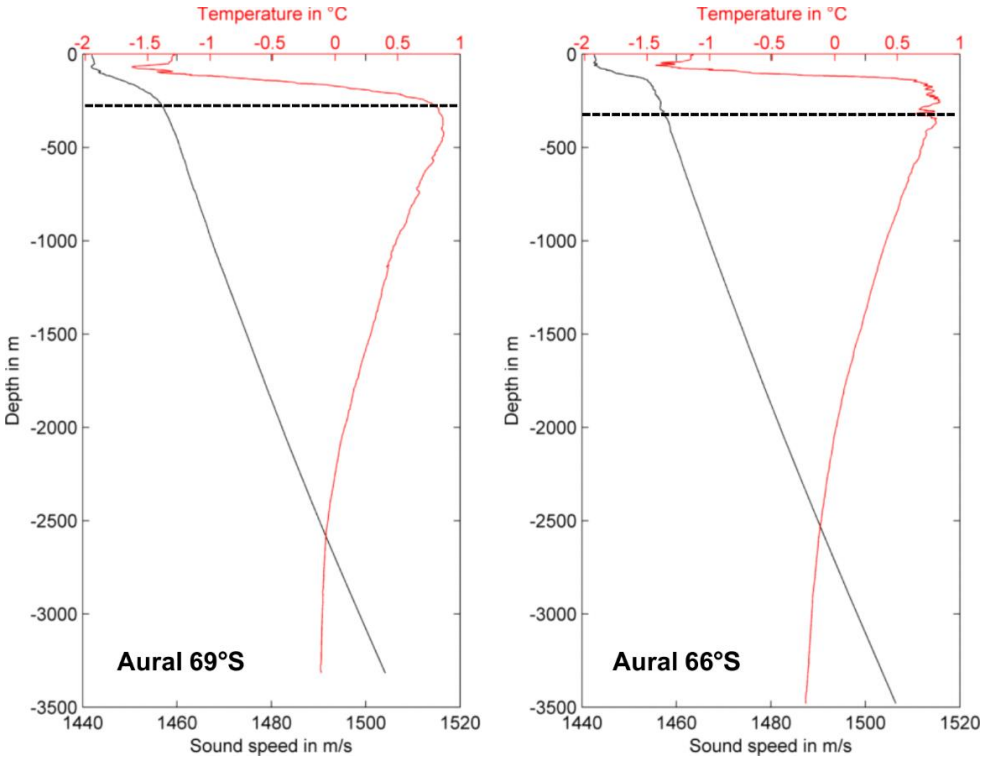

Supplementary Figure 7: Sound speed and temperature profiles measured at the mooring locations during deployment with RV Polarstern, using an SBE911plus CTD system. Dashed line indicates the depth of each recorder.

IV

Estimating the spatial distribution of vocalizing animals from ambient sound spectra using widely spaced recorder arrays and inverse modelling

Sebastian Menze,[1,a)] Daniel Zitterbart,[2,b)] Martin Biuw,[3] and Olaf Boebel[4]
[1]*Oceanography and Climate Group, Institute of Marine Research, P. O. Box 1870, Nordnes, Bergen, Norway*
[2]*Applied Ocean Physics and Engineering, Woods Hole Oceanographic Institution, 266 Woods Hole Road, Woods Hole, Massachusetts 02543-1050, USA*
[3]*Marine Mammal Group, Institute of Marine Research, Tromsø, Norway*
[4]*Ocean Acoustics Group, Alfred-Wegener-Institute, Helmholtz-Center for Polar and Marine Research, Klussmannstrasse 3d, 27570 Bremerhaven, Germany*

(Received 15 March 2019; revised 18 November 2019; accepted 18 November 2019; published online 31 December 2019)

The sound energy from marine mammal populations vocalizing over extended periods of time adds up to quasi-continuous "choruses," which create characteristic peaks in marine sound spectra. An approach to estimate animal distribution is presented, which uses chorus recordings from very sparse unsynchronized arrays in ocean areas that are too large or remote to survey with traditional methods. To solve this under-determined inverse problem, simulated annealing is used to estimate the distribution of vocalizing animals on a geodesic grid. This includes calculating a transmission loss (TL) matrix, which connects all grid nodes and recorders. Geometrical spreading and the ray trace model BELLHOP [Porter (**1987**). J. Acoust. Soc. Am. **82**(4), 1349–1359] were implemented. The robustness of the proposed method was tested with simulated marine mammal distributions in the Atlantic sector of the Southern Ocean using both drifting acoustic recorders [Argo (**2018**). SEANOE] and a moored array as acoustic receivers. The results show that inversion accuracy mainly depends on the number and location of the recorders, and can be predicted using the entropy and range of the estimated source distributions. Tests with different TL models indicated that inversion accuracy is affected only slightly by inevitable inaccuracies in TL models. The presented method could also be applied to bird, crustacean, and insect choruses. https://doi.org/10.1121/1.5139406

[JAC] Pages: 4699–4717

I. INTRODUCTION

Passive acoustic monitoring (PAM) is increasingly used to study the distribution and migration of vocalizing animals that are otherwise difficult to observe, such as marine mammals (Rogers *et al.*, 2013), birds (Dawson and Efford, 2009), fish (Wall *et al.*, 2013), insects, and amphibians (Pijanowski *et al.*, 2011). Most methods estimate population density and/or spatial distribution based on the detection of transient vocalizations (Marques *et al.*, 2013) recorded by single hydrophones or small-scale arrays. Here, we present an approach to estimate the distribution of vocalizing animals that utilizes ambient sound spectra from widely spaced recorder arrays (>100 km distance) and the cumulative sound energy emitted by a population, rather than signals from individual vocalizations. We developed this method to interpret recordings of low-frequency and far-ranging marine mammal vocalizations in the Southern Ocean, but it could also be applied to other situations involving a large number of signal sources, such as bird, crustacean, and insect choruses, which create a quasi-continuous chorus that is observed with a sparse array of receivers.

In the ocean, ambient sound (also often termed "ambient noise" or "soundscape") stems from sea surface motion, precipitation, sea ice motion, glacier calving, shipping, seismic surveys, marine mammals, fish, and crustaceans (Carey and Evans, 2011; McDonald *et al.*, 2008; Nieukirk *et al.*, 2012). The cumulative sound energy of a marine mammal population vocalizing during extended periods adds up to a "chorus-like" quasi-continuous signal, which can dominate ambient sound over certain frequency bands (Curtis *et al.*, 1999; Leroy *et al.*, 2018b; Seger *et al.*, 2016). Throughout the remainder of this paper, these parts of the ambient sound are referred to as marine mammal choruses (MMCs), though strictly speaking, they also contain energy from single, discernable calls. Hence, MMCs more accurately represent the acoustic power contributed in specific frequency bands by the target species. A recording containing Antarctic minke whale calls and the Antarctic minke and blue whale MMCs is shown in Fig. 1.

The contribution of the various sources to ambient sound can be determined by analyzing characteristic peaks and slopes in ambient sound spectra. The temporal variability of these spectra can be visualized with long-term spectral

[a)]Electronic mail: sebastian.menze@imr.no
[b)]Also at: Biophysics Group, Department of Physics, University of Erlangen-Nürnberg, Staudtstrasse 7/B2, 91058 Erlangen, Germany.

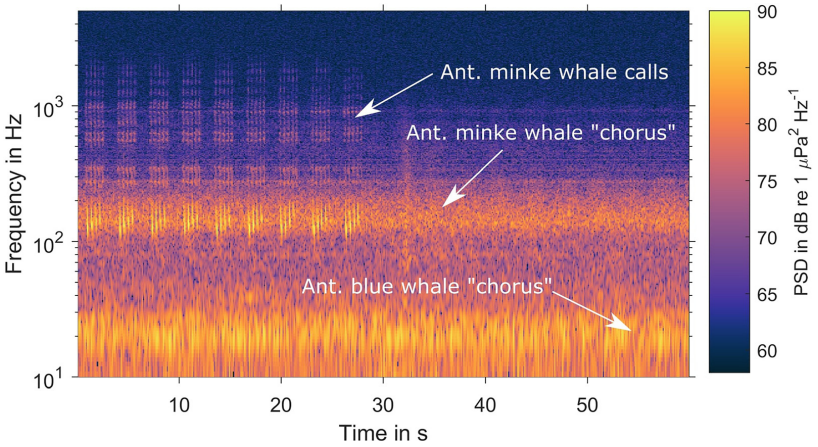

FIG. 1. (Color online) Spectrogram showing Antarctic minke whale calls and "chorus" (MMC) and Antarctic blue whale chorus (MMC). Recorded by a moored Aural M2 recorder (Multi-Electronique, Quebec, CA) on 5 September 2008 at 66°01.13′S and 0°04.77′E (sample rate, 32 768 Hz; spectrogram settings: fast Fourier transform (FFT), 8000 points; Hanning window, 50% overlap). The recordings are described in Menze *et al.* (2017).

averages (LTSA), which display the average power spectral density (PSD) of each recording over the recorder's deployment period. An example LTSA from the Southern Ocean is displayed in Fig. 2(a) (Menze *et al.*, 2017). The contribution of the air–sea–ice interaction to ambient sound can be seen as vertical lines, and the contribution of Antarctic blue whales (*Balaenoptera musculus intermedia*), fin whales (*Balaenoptera physalus*), Antarctic minke whales (*Balaenoptera bonaerensis*), and leopard seals (*Hydrurga leptonyx*) can be seen as horizontal lines in the LTSA (Menze *et al.*, 2017). The spectral peaks in Southern Ocean ambient sound related to Antarctic blue whales, fin whales, and Antarctic minke whales are displayed in Figs. 2(b)–2(d). The MMC sound energy can be calculated by subtracting fitted functions from the measured spectra, resulting in time series of MMC received levels (RL_{MMC}). Figure 2(e) compares Antarctic minke whale RL_{MMC} recorded at 66°S and 69°S; the time series show distinct north-south differences and co-varying patterns. MMCs have also been observed from fin whales in the Mid and North Atlantic (Nieukirk *et al.*, 2012), fin and blue whales in the North Pacific (Burtenshaw *et al.*, 2004; Curtis *et al.*, 1999) and Indian Ocean (Leroy *et al.*, 2018a), Pygmy blue and Antarctic blue whales around Australia (McCauley *et al.*, 2018), and fin and possibly Bowhead whales in the Arctic (Ahonen *et al.*, 2017), and exhibit extensive spatial as well as inter- and intra-annual variation. In this study, we explore how the information in such MMC patterns can be used to estimate the spatial distribution of a population of vocalizing animals.

Most approaches to estimate animal distribution or density from acoustic recordings focus on the detection of transient vocalizations, which can also be used to localize individual animals. The spacing, geometry, and clock accuracy of a recorder array, as well as the nature of the sound source, sound speed profile, and bathymetry, determine if and how accurately individual sound sources can be localized. If only a single hydrophone is present, it is often only possible to detect the number of calls per unit time (often termed call rate or acoustic activity) and RL_{MMC} at the hydrophone's location (Haver *et al.*, 2017; Van Opzeeland *et al.*, 2013; Van Parijs *et al.*, 2009). In shallow water with a dispersive waveguide and impulsive calls, range estimation is possible on a single hydrophone (Bonnel *et al.*, 2014; Marques *et al.*, 2011). In cases where the vocalizations propagate in a way that allows the identification of multipath arrival patterns or modes, it is also possible to estimate the call source level (SL), the distance from the recorder and source depth, in addition to the number of calls per unit time (Mouy *et al.*, 2012; Newhall *et al.*, 2012; Valtierra *et al.*, 2013). When arrays with small to medium spacing are used, it is possible to calculate the distance, bearing, and SL of transient sounds via time-difference-of-arrival (TDOA) or beamforming methods (Harris *et al.*, 2018; Širović *et al.*, 2007; Urazghildiiev and Clark, 2013; Urazghildiiev and Hannay, 2018; Wang *et al.*, 2016). However, when the array spacing becomes so large that a signal is no longer recorded by at least three hydrophones, or individual calls cannot be associated, tracking individual sound sources becomes challenging, and analysis is often limited to comparing the number of calls per unit time and RL_{MMC} at the different locations (Risch *et al.*, 2014; Thomisch *et al.*, 2016).

It is important to note the difference between density and distribution. In this study, we define density as the average number of vocalizing animals per km^2 within the entire study area, and we define spatial distribution as the number of animals per grid cell for a grid that tessellates the study area. The two most promising methods for estimating animal density from the detection of vocalizations are distance sampling and spatially explicit capture recapture methods (Harris *et al.*, 2013; Harris *et al.*, 2018; Kusel *et al.*, 2011; Kyhn *et al.*, 2012; Marques *et al.*, 2013; Martin *et al.*, 2013; Thomas and Marques, 2012; Ward *et al.*, 2012). However, due to their reliance on individual call detections, they work best on spatial scales smaller than ocean basins, and require an extensive recorder array (Carlén *et al.*, 2018; Harris *et al.*,

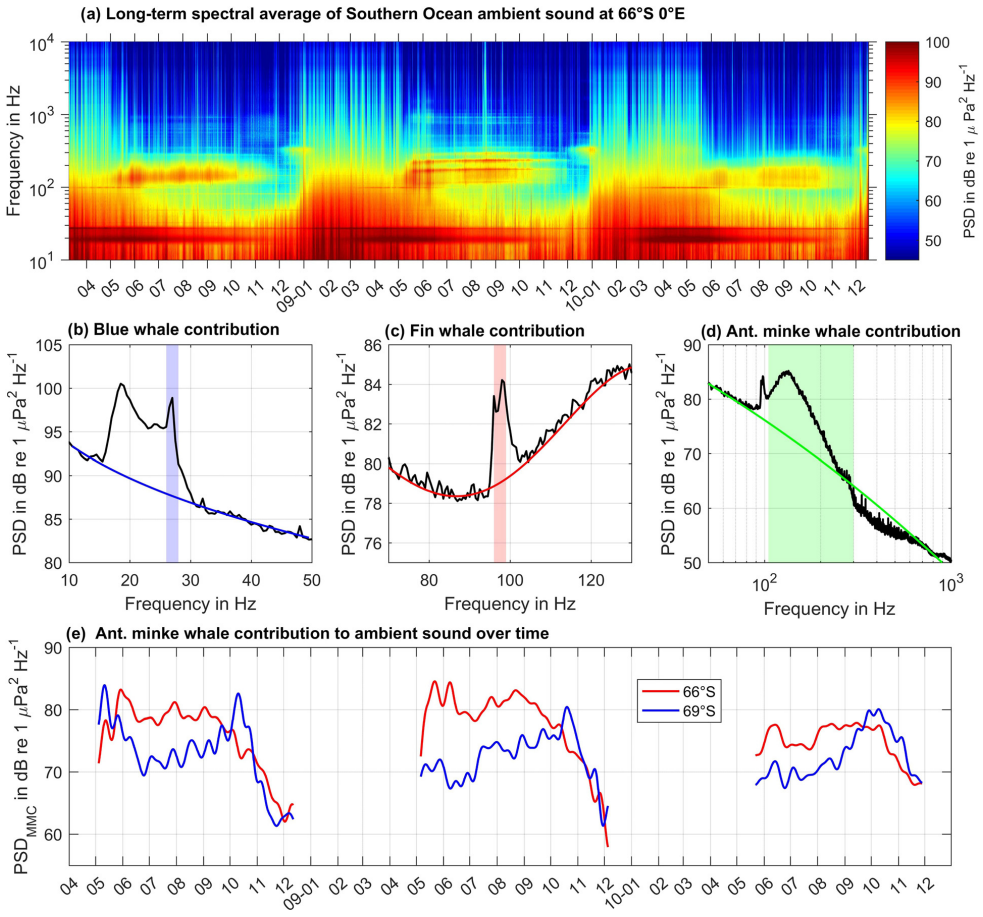

FIG. 2. (Color online) Ambient sound recordings from the Southern Ocean containing marine mammal contributions as described in Menze *et al.* (2017). (a) LTSA of recordings from 66°S, marine mammal contributions visible as horizontal streaks. (b),(c),(d) Marine mammal contribution peaks in example ambient sound spectrum. The black lines represent the measured PSD (at 66°S on 25 May 2008 12.00 h), the colored lines are three fitted interpolation functions and the colored areas are the frequency bands used to calculate the PSD_{MMC}. (e) Comparison of the Antarctic minke whale chorus (PSD_{MMC}) time series (low-pass filtered with a seven-day window Butterworth filter) between 66°S (red) and 69°S (blue).

2018). In this paper, we estimate the spatial distribution of acoustic sources instead of the density of acoustic sources in the study area.

Due to the complex and cumulative nature of the MMC to ambient sound, RL_{MMC} data have been rarely used to estimate animal distribution. Seger *et al.* (2016) combined MMC recordings and line transect surveys to investigate the spacing among singing Humpback whales. Mellinger *et al.* (2014) discussed an approach to estimate the density of vocalizing fin whales in a reference area around a single hydrophone using acoustic propagation modelling. The difficulty with interpreting the spatial and temporal patterns in RL_{MMC} is that a higher RL_{MMC} does not necessarily imply a higher density of animals due to the nonlinearity of underwater sound propagation and the large and unknown number and location of sources involved. For a given location, increased RL_{MMC} can be caused by a combination of processes: an increase in the number of vocalizing animals, an increase in SL, an increase in call rate, a decreasing distance to the vocalizing animals, or a decreasing TL between the vocalizing animals and the recorder. We address these issues by using a set of RL_{MMC} recordings in combination with acoustic propagation models and a parameter estimation algorithm to estimate the distribution of sound sources, which would generate the observed set of RL_{MMC} recordings. With additional information about the animals' SLs and call rates, it should then be possible to extend the presented approach further and provide an estimate of the number of animals per grid cell. As with any PAM method, we only estimate the distribution of vocalizing animals, while non-vocalizing animals present in the area cannot be detected.

This paper is structured into six sections. Section I is the Introduction and Sec. II describes the inversion method.

Section III describes simulated scenarios to test the robustness of the inversion method and how we quantified inversion accuracy. Section IV presents the results of the simulated test scenarios and relations between inversion accuracy and several metrics. Section V discusses these results and the feasibility of the inversion method. Conclusions are summarized in Sec. VI.

II. THE INVERSION METHOD

Estimating the spatial distribution (location and amplitude) of sound sources from a finite set of RL_{MMC} observations is an under-determined, non-linear inverse problem. Similar RL_{MMC} values could be caused by different source numbers, locations, and amplitudes, and the number of unknown parameters (location and amplitude) is much larger than the number of observations. Following the notation of the Bayesian geophysical inverse problem theory (Mosegaard and Sambridge, 2002; Tarantola, 2005), the RL_{MMC} observations form the data set $\mathbf{d}$, which is connected to the parameter set $\mathbf{m}$ through the forward model $\mathbf{d} = g(\mathbf{m})$. Here, the forward model $g(\mathbf{m})$ simulates the ambient sound created by a set of acoustic sources for which spatial distribution is described by the parameter set $\mathbf{m}$. To solve the inverse problem, we are sampling the joint posterior distribution that combines flat prior distributions over the parameters $\mathbf{m}$ and the least squares misfit between $\mathbf{d}$ and $g(\mathbf{m})$.

For inverse problems with a small number of parameters, the misfit function can be sampled using a grid search, i.e., calculating the misfit of all possible parameter combinations (also termed the search space). In our case, this is impossible since the number of parameters is in the hundreds to thousands, rendering the search space too large for a grid search. We therefore developed a parameter estimation algorithm that uses a Markov chain Monte Carlo (MCMC) algorithm to sample the misfit function and find the parameters with least misfit between observed and modelled RLs. This is a first exploration of the inverse theory approach toward estimating marine mammal distribution from chorus recordings. Sections II A–II C describe the different parts of the inversion method: the architecture of the forward model, prior estimates, assumptions, and the parameter estimation algorithm.

A. The forward model and *a priori* assumptions

Estimating RL_{MMC} requires knowledge about the number or sources (vocalizing marine mammals), their SL, location, and the TL between the source and recorder locations. The TL is not only influenced by the distance between the source and receiver, but also by the sound speed field, sea floor shape and properties, sea surface roughness, sea ice, and bubble clouds. Since it is computationally very costly to include all these parameters in a forward model, we make several assumptions to expedite the calculations.

Our first simplification of the forward model is neglecting time; since we are modelling the contribution of marine mammals to ambient sound, which is quasi-continuous on the scales of minutes to hours, we can simulate the transient vocalizations by a set of continuous sources of identical frequency. The continuous nature of ambient sound, and the marine mammal contribution to it, arises due to the many sources involved, the multipath propagation that spreads impulsive signals over time, and the repetitive and monotonous nature of many marine mammal vocalizations. Multipath propagation of underwater sound renders initially impulsive signals (such as the Antarctic minke whale calls in Fig. 1) into a quasi-continuous signal (such as the Antarctic minke whale "chorus" in Fig. 1) due to sea floor, internal, and surface reflections. We simulated this process for fin whale vocalizations and found that the pulse train can become a quasi-continuous signal at distances around 100 km away from the source (supplemental Figs. 1 and 2).[1] Since we assume a steady-state situation in our forward model, we observe the time scale so that our model is valid. We aim to estimate source distribution on a basin scale (thousands of km), where the signal travel times between source and recorder are on the scale of minutes to tens of minutes (an underwater sound signal needs approximately 11 min to travel 1000 km). Thus we assume that the SL, call rate, and location of the vocalizing marine mammals and TL are approximately constant on the time scale of 10–30 min. This implies that RL_{MMC} should be measured on the scale of minutes, ideally between 10 and 30 min, and the time steps between estimates of distribution need to be on the scale of hours. It is unlikely that the large-scale marine mammal distribution and TL change significantly on smaller time scales.

The second assumption is to neglect source depth in the forward model. This is deemed appropriate since the source depth mainly affects TL in the first tens of km (Weirathmueller *et al.*, 2013). Tagging of vocalizing blue whales indicated that calling occurs mainly at depths below 30 m (Lewis *et al.*, 2018).

The third assumption is to discretize and reduce the search space that is sampled by the parameter estimation algorithm. Since we neglect depth and time, the parameter set $\mathbf{m}$ only needs to describe the source locations and levels. Allowing arbitrary locations, SLs, and number of sources would require an overwhelming computational effort. We reduce the possible source locations to grid nodes. This grid is termed the simulated source grid. Using a rectangular latitude-longitude grid will result in an uneven distribution of nodes across ocean basin scales. Therefore, we calculated node positions with a geodesic algorithm that approximates the shape of a sphere using an icosahedron (Teanby, 2006). It is available as MATLAB code (MathWorks, Natick, MA), and was implemented into the forward model. The estimated received level, $\widehat{RL}_i$, at each recorder, i, is calculated as the (incoherent) sum of the acoustic power from all source grid nodes,

$$g(\boldsymbol{m}) = \widehat{RL}_i = 20\,\log_{10}\left(\sum_{j=1}^{n_{\text{nodes}}} 10^{(SL_j - TL_{ij})/20}\right),$$

where j is the source grid node index, n_{nodes} is the number of grid nodes, $SL_j = 20\,\log_{10}(SP_j)$ is the SL at each node, and TL_{ij} is the TL between a recorder i and the source at grid node j. For efficient computation, the TL between all grid nodes and recorders is calculated into a lookup TL matrix

using a sound propagation model. The two acoustic propagation models implemented for this study are presented in Sec. II B. The parameter estimation algorithm then needs to determine the source pressure at each node SP_j that produces the least misfit between model and observations. For this it is necessary to reduce the degrees of freedom of the inverse problem to allow the parameter estimation algorithm to find the best SP_j quickly. Instead of performing a grid search for the best SP_j (calculating the misfit of all possible parameter combinations), a fixed number of equally loud simulated sources is moved across the grid nodes. The number of simulated sources is set the same as the number of grid nodes $n_{\text{sources}} = n_{\text{nodes}}$. This allows all source location combinations ranging from one simulated source at each node to all simulated sources being at one node. The parameter set $\mathbf{m}$ is then defined as a vector containing the node index that describes where each simulated source is located. The source pressure at a given node is then defined as the sum of all simulated sources (animals) assigned to that node. The sound pressure of each source (animal) is defined as a fraction of the unknown cumulative source pressure (CSP, the total sound energy emitted by all vocalizing animals of the population) and n_{sources}. The source pressure SP_j at a given node j is thus calculated as the product of the number of simulated sources located at that node and the fraction of the CSP

$$SP_j = \left(\sum j \in \boldsymbol{m}\right)\frac{\text{CSP}}{n_{\text{nodes}}}.$$

The true value of the CSP is unknown, thus, it needs to be estimated on the basis of typical SLs, population sizes, and call rates as given in the literature. We assume that this could take any value (uniform distribution) between the extreme cases of CSP_{min} (only one animal volcanizing sporadically) and CSP_{max} (all possible existing animals volcanizing constantly).

We then solve the inverse problem (searching the minimum of the misfit function) for a predefined number $n_{\text{SA chains}}$ of CSP values between CSP_{min} and CSP_{max} independently. The SP_j estimate is then calculated as the median of the three best (smallest misfit) SA chains to smooth out potential artifacts of a single solution. For small sample sizes (small $n_{\text{SA chains}}$), taking the posterior median is a robust estimator of the parameters (Cronin *et al.*, 2009). The result of the inversion is the estimated source pressure grid, a map that shows where and how much sound pressure is emitted to create the recorded RL_{MMC}. We did not attempt to calculate animal densities from the estimated source pressure grid, but in cases where reliable estimates of animal call rate and SL are available, it should be possible to formulate multipliers that convert source pressure per area to number of animals per area. Conversely, for regions and species where population size is known with reasonable certainty, the migration of the entire vocalizing population could possibly be tracked. Figure 3 shows a flowchart of the inversion method, divided into knowns, prior, and posterior (after inversion) estimates. The inversion method was developed and tested with MATLAB2016a (MathWorks, Natick, MA) and Python2.7 (Python, Fredericksburg, VA).

B. Sound propagation models

The TL between the recorders, source grid nodes, and test scenario sources was calculated using two methods, geometrical spreading (Lurton, 2010) and raytracing, using the BELLHOP (Porter, 1987) model, although any other underwater sound propagation model may be used as well. Geometrical TL was calculated using a critical radius of 4000 m, where a transition from spherical to cylindrical propagation is assumed, as this value roughly represents the average ocean depth of the study area. For distances shorter than the critical radius, TL was calculated using spherical spreading and absorption only,

$$\text{TL}(r) = 20\,\log(r) + \alpha r,$$

where r is the distance from the source, and α is the absorption coefficient from the empirical equations of Francois and Garrison (1982). For distances larger than the critical radius, the equation

$$\text{TL}(r) = 20\,\log(r_{\text{critical}}) + 10\,\log\left(\frac{r}{r_{\text{critical}}}\right) + \alpha r$$

was employed, with r_{critical} being the critical radius. The distances between the source and receiver pairs were calculated using great circle lines to account for the curvature of the Earth.

Raytracing TL was calculated using the two-dimensional (2D) range dependent sound propagation model BELLHOP. Instead of calculating the TL between all source and receiver pairs, we simulated the three-dimensional (3D) sound field using a $2 \times N$-dimensional ($2 \times N$-D) approach, rotating a set of 2D slices (range and depth) in 5° steps, 360° degree around each source location. The bathymetry for each slice was obtained from the ETOPO-1 topography dataset (Amante and Eakins, 2009). The sound speed over range and depth for each slice was interpolated from the world ocean atlas mean annual climatology dataset (Dushaw *et al.*, 2013). The sea floor was assumed to be an elasto-acoustic half-space with a pressure wave sound speed of 1800 m s^{-1} and a density of 2.0 g cm^{-3}. Each acoustic source (i.e., whale) was assumed to be at 10 m depth, and all recorders were assumed to be at 100 m depth. Raytracing TL was only calculated for 150 Hz, and sea ice was not accounted for. The implications of these constraints will be discussed in Sec. V. We interpolated a latitude-longitude grid containing the TL at 100 m depth from the 72 range and depth slices for each source. The TL between each source and recorder was then retrieved from this grid. Example slices and interpolated TL values are shown in supplemental Fig. 3.[1]

The two TL models are compared to each other using source and recorder locations in the Weddell Sea (maps of the locations can be found in Secs. IV A–IV D) in Fig. 4. They show a robust correlation, but for close ranges and TL values less than 100 dB the geometrical spreading model overestimates TL in relation to the raytracing model, while it underestimates TL at far ranges and TL values higher than 100 dB. This is also illustrated in supplemental Fig. 4,[1]

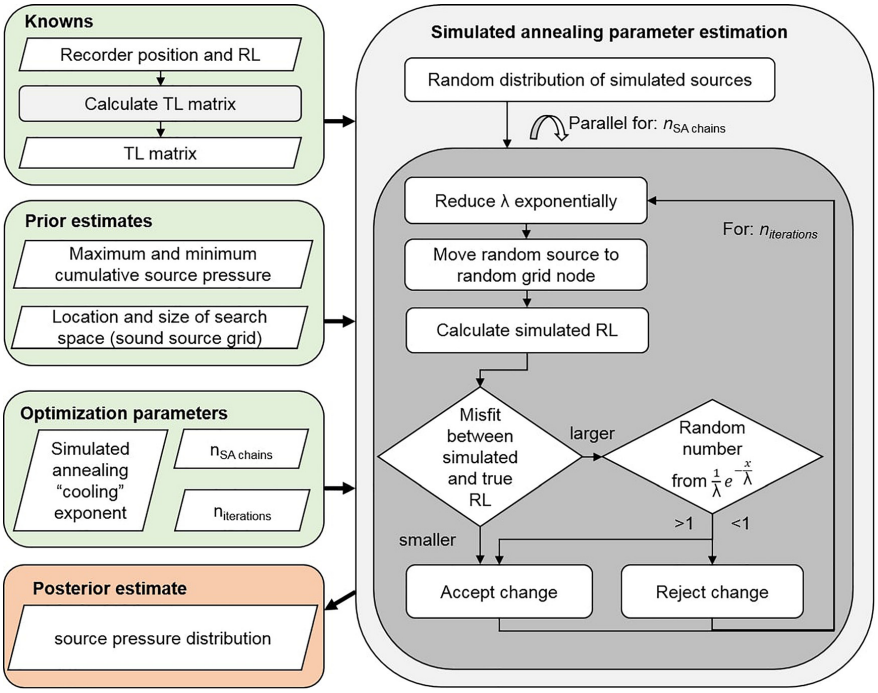

FIG. 3. (Color online) Flowchart of the inversion method and simulated annealing (SA) parameter estimation algorithm. Input variables are marked green, the output variables are marked red. Grey round boxes represent the computational parts of the method. λ is the SA "temperature" parameter that steers how much of an increase in misfit is tolerated at each iteration, and x is a random variable from the distribution $f(\lambda, x) = (1/\lambda)e^{-x/\lambda}$.

which compares the two models over a 1300 km section. It shows that geometrical spreading overestimates the TL in the first 500 km compared to BELLHOP. However, both the geometrical spreading and raytracing models provide a very similar logarithmic TL dependency. The performance and shortcomings of the two models are evaluated in Sec. V (Discussion).

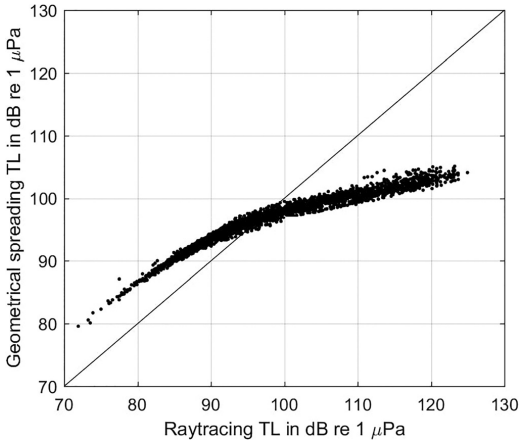

FIG. 4. Comparison of geometrical and raytracing TL models using source and receiver pairs in the Weddell Sea at 150 Hz. Detailed information on the receiver and source locations is given in Sec. III.

C. Parameter estimation

The parameter set **m** is defined as a vector containing the node indices that describe where each simulated source is located. Depending on the size and resolution of the grid, there are hundreds to thousands of grid nodes (=parameters). We sample the misfit function with a MCMC algorithm to find the global minimum within the search space. The movement of the algorithm through the search space is defined in the following manner: initially the simulated sources are distributed randomly (uniform distribution) over the grid nodes. Then, for each iteration, a simulated source is chosen randomly and moved to a random new grid node. Whether a move is accepted or rejected is governed by an acceptance rule. After the decision has been made, a new random move is generated. In this fashion, the algorithm moves through the search space for a fixed number of iterations.

Compared to the large number of parameters, the number of RL_{MMC} observations is very small (on the order of tens to hundreds). This implies that the inverse problem is highly under-determined, and the misfit function has many local minima. The local minima and the size of the search space render it challenging for the minimization algorithm to reach the global minimum. An algorithm that only follows

decreases in misfit may get trapped at a local minimum, while an algorithm that equally follows decreases and increases in misfit may not converge (get lost in the search space). Therefore, a suitable acceptance rule is essential for finding the global minimum.

We choose the simulated annealing (SA) acceptance rule (Kirkpatrick *et al.*, 1983). The SA algorithm always accepts decreases and increases in misfit with an exponential probability, which is reduced as the number of iterations increases. The probability to accept an increase in misfit is determined by the exponential probability density distribution $f(x;\lambda)$. An increase in misfit is accepted when a random number x, drawn from $f(x;\lambda)$ is larger than one. For each iteration, a new random number x is drawn from $f(x;\lambda)$,

$$f(x;\lambda) = \frac{1}{\lambda} e^{-x/\lambda},$$

where λ (termed the SA "temperature") is the mean of $f(x;\lambda)$, and the random variable x can range from 0 to ∞. With each iteration, λ is reduced following an exponential function:

$$\lambda = \left(1 - \frac{i_{\text{iteration}}}{n_{\text{iterations}}}\right)^{\varepsilon},$$

where ε is the SA "cooling" exponent ($\varepsilon > 0$), $i_{\text{iteration}}$ is the number of the current iteration, and $n_{\text{iterations}}$ is the total number of iterations. The cooling exponent ε determines how fast λ decreases with increasing numbers of iterations, i.e., it controls the speed of the transition from randomly accepting increases in misfit to always rejecting increases in misfit. We found that a cooling exponent between two and six works well, and use $\varepsilon = 2$ for all inversions in this study. A flowchart of the SA parameter estimations algorithm is displayed in Fig. 3. Given a sufficient number of iterations, the SA algorithm will converge toward the global minimum of the misfit function (Granville *et al.*, 1994).

To illustrate the parameter estimation process, Fig. 5 shows how λ is reduced over the iterations and how the misfit of the different SA chains is reduced over time. Each black line represents a solution (SA chain) moving through the search space. Each solution has a different CSP, which is the reason for the misfit offset between the different solutions already at the start of the iterations. Solutions with very large or very small CSP show large misfits between simulated and true RL over all iterations, whereas solutions with a fitting CSP converge toward lower misfit values after a few thousand iterations.

Figure 6 shows snapshots of the source pressure grid at different iteration stages for the same example scenario with 20 000 iterations and 13 recorders with an average distance of 300 km between the recorders. Initially, the simulated sources are distributed randomly (upper left panel). With increasing iterations the simulated sources are moved across the grid nodes, rendering the simulated source pressure grid increasingly similar to the true source pressure grid (lower right panel). The final estimate resolves the source distribution pattern well considering the small number of recorders

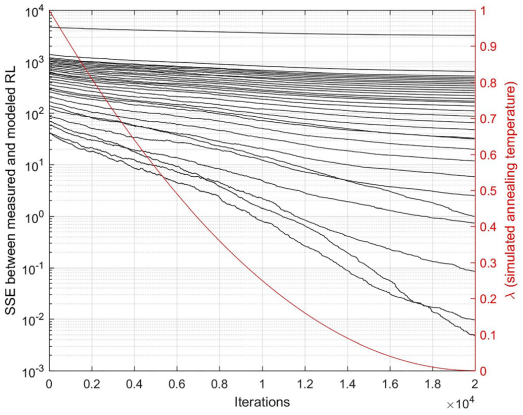

FIG. 5. (Color online) Misfit (SSE = sum of squared errors) between measured and modelled RLs over the iterations of the parameter estimation algorithm (black lines). The different black lines represent different SA chains ($n_{\text{SA chains}} = 32$, CSP between 10^{11} and 10^{13} μPa). The red line represents λ, the SA temperature [mean of $P(i,\lambda)$] over the iterations (SA cooling exponent $\varepsilon = 2$).

used. The gradient of incorrect sources in the upper left corner of the estimated source distribution represents excess sound energy in the forward model that is moved toward the boundaries of the search space to reduce the misfit between received and modelled RL, and will be discussed in Sec. V.

III. TEST SCENARIOS

The reliability and sensitivity of the inversion method was investigated using a set of test scenarios. All scenarios were created and analyzed using MATLAB2016a (MathWorks, Natick, MA) on a standard laptop, whereas the SA parameter estimation algorithm was executed on a high-performance computing cluster using 32 central processing units (CPUs) per scenario, computing each SA chain in parallel. The inversion and test scenario codes are available in the supplemental materials and a github repository.[1] The test scenarios were positioned in the Atlantic sector of the Southern Ocean between 45°S and 80°S and 65°W and 25°E. In all but the last test scenario, the simulated recorder array was a widely spaced mooring array identical to the HAFOS array of the Alfred Wegener Institute Helmholtz Centre for Polar and Marine Research (AWI; Van Opzeeland *et al.*, 2014; triangles in Fig. 6). The average array spacing, i.e., the distance between neighboring recorders, was 300 km. We plan to apply the inversion method to recordings from this array once they become available in the coming years. Detailed information on the inversion parameters and TL models used for each scenario are given in Table I.

We quantified the accuracy of each test scenario inversion using a metric similar to the simple matching coefficient (SMC; Sepkoski, 1974), which divides the sum of true positives and true negatives (number of matches) by the total set size. A SMC of zero means no overlap between two sets, and a SMC of one means a perfect match. We compared the true and estimated source pressure grids using two metrics: normalized accuracy (A_n) and binary accuracy (A_b). The

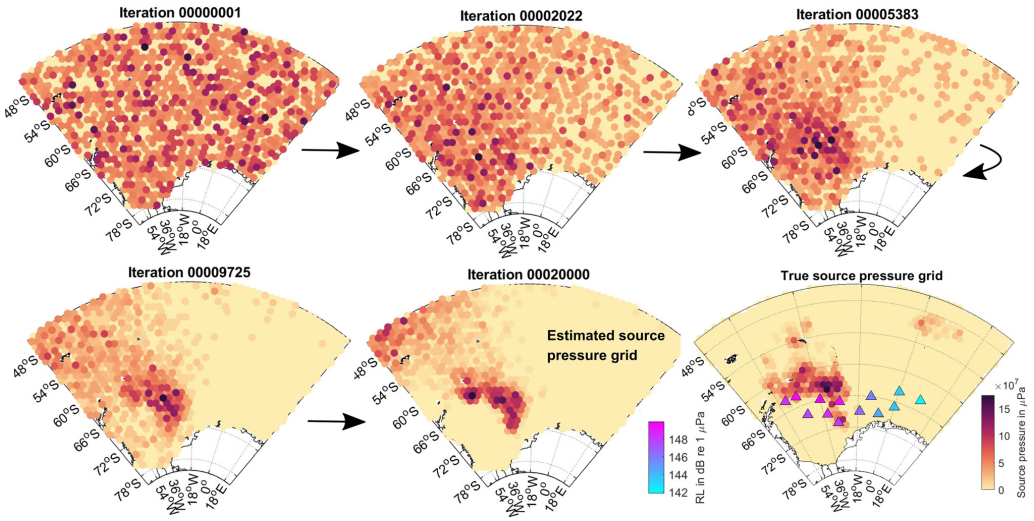

FIG. 6. (Color online) Schematic view of source pressure grid change during SA over 20 000 iterations. Colored dots represent the source pressure at each node in μPa (yellow to red hues, normalized for each panel). Lower right plot shows the true source pressure grid and recorder locations where the RLs in dB re 1 μPa are marked by blue and pink triangles. The color scales are only valid for the panels that show the estimated and true source pressure grid.

binary accuracy compares only presence-absence information, comparing two binary sets (truth and estimate) that are zero where the source pressure is zero, and one where the source pressure is greater than zero. The accuracy is then

$$\text{Accuracy} = \frac{\text{true positives} + \text{true negatives}}{\text{Number of nodes}} = \frac{\text{Number of matching nodes}}{\text{Number of nodes}}.$$

To compare not only presence/absence but also scalar patterns (ratio scale data), the normalized accuracy compares the true and estimated source pressures after normalizing the source pressure at each node into 50 different bin values between 0 and maximum true source pressure. Identical to the binary accuracy, the normalized accuracy is then defined as the number of matching nodes divided by the number of nodes but with 50 instead of 2 classes.

A. Random source distributions

The first test scenario's objective was to investigate the reliability and feasibility of the inversion method and find a metric that correlates with inversion accuracy and can be used when the method is applied to real data. Therefore, we applied the inversion method to 250 random source distributions, an array of 13 recorders with a spacing of approximately 300 km between adjacent recorders and a source pressure grid with 1328 nodes and 111 km distance between adjacent nodes. To simulate the patchy nature of marine mammal distributions, we created a latitude-longitude grid with a resolution of 0.1 arclength (11 km) and randomly assigned SLs to the grid bins of this fine scale source grid. This was realized in a three-step process: first, random noise with an f^{-5} spectrum was created (normalized between zero and one) and bins (output of the random number generator) with values below 0.75 set to zero, and bins with values above 0.75 were randomly assigned a value between 0 and 1 with an f^{-1} noise spectrum. The distribution was then thinned by setting bins back to zero where random noise (normalized between zero and one) with an f^{-2} spectrum was below 0.6. The resulting random distributions (an example distribution is shown in Fig. 7) show combinations of patchy and filamentous patterns not unlike the modelled habitat suitability distributions for Antarctic minke whales (Bombosch *et al.*, 2014; Herr *et al.*, 2019). We chose the spectral slope of the random distributions manually, yet other exponents or ways of simulating random source distribution to test the inversion method could be used equally well. To simulate source pressure distributions somewhat realistically, the normalized grid was then multiplied with a call rate of 0.5 (animals vocalizing 50% of the time) and source pressures of 10^9 μPa (180 dB re 1 μPa; Širović *et al.*, 2007). For each scenario, the respective "true" source pressure SP_j at each source pressure grid node (best possible inversion results) was calculated from the fine scale source grid by smoothing the fine scale grid with a 2D circular averaging filter, the radius of which is the average distance between the nodes (111 km), and then extracting the pressure value at each node's location from the smoothed grid. The node locations and true SP_j values of the source pressure grid are shown in Fig. 7(b), which also shows the location and RL of the recorder array. RLs at the recorder array were calculated using geometric spreading TL (the true TL), which was also implemented as the TL model for the inversion.

TABLE I. Overview of test scenarios.

Objective	Recorders	Number and type of replicate source distributions	"True" TL	TL model	Frequency (Hz)	$n_{\text{iterations}}$	$n_{\text{SA, chains}}$	CSP (μPa)	CSP_{min} and CSP_{max} (μPa)
Effect of different source distributions	Mooring array	250 random distributions	Geometrical spreading	Geometrical spreading	270	20 000	32	$2^{12} \pm 1^{12}$	1^{11} and 1^{13}
Effect of flawed TL model	Mooring array	100 random distributions on small grid	Geometrical spreading and BELLHOP raytracing	Geometrical spreading	150	15 000	30	$5^{11} \pm 3^{11}$	1^{11} and 1^{13}
Effect of number of SA chains	Mooring array	1 random distribution	Geometrical spreading	Geometrical spreading	150	15 000	5,10, 15,20, 25,30,35,40	2.3^{12}	1^{11} and 1^{13}
Effect of number of iterations	Mooring array	1 random distribution	Geometrical spreading	Geometrical spreading	150	1000,5000,10 000, 15 000,20 000, 25 000	32	2.3^{12}	1^{11} and 1^{13}
Effect of frequency	Mooring array	1 random distribution	Geometrical spreading	Geometrical spreading	27,98,150,270	15 000	32	2.3^{12}	1^{11} and 1^{13}
Effect of recorder number and location/ feasibility of drifting recorders	Argo floats	1 random distribution	Geometrical spreading	Geometrical spreading	150	20 000	32	1.6^{12}	1^{11} and 1^{13}

FIG. 7. (Color online) Example test scenario in the Weddell Sea. (a) shows the fine scale source grid where color indicates the amplitude of the acoustic sources (virtual whales) used to calculate the recorded RL (cyan-magenta triangles mark recorder location and respective RL). (b) shows the corresponding true amplitude of the source pressure grid nodes (best possible inversion result).

B. Inaccurate TL model

The second test scenario's objective was to investigate the effect of an incorrect and uncertain TL model on inversion success. We created 100 random source distributions using the same recorder array and random fine scale source grid generation as for the previous scenario (Sec. III A), but limited the source distribution to grid nodes between 62.5°S and 72°S and −49°E and 14°E to reduce the computational effort of the raytracing modelling. For each of the 100 distributions, 2 inversions were calculated. The first inversion was calculated with perfect TL knowledge, where both the true and forward model TLs were calculated using geometrical spreading. The second inversion was calculated with a flawed forward model TL, where the true TL was calculated using raytracing (as described in Sec. II A), but the forward model TL was calculated using geometrical spreading.

C. Robustness of inversion

We tested the robustness of the inversion method toward the number of SA chains and iterations, and the effect acoustic frequency has on inversion accuracy. We used geometrical spreading as the true and forward model TL and the same recorder array and source grid as for the previous scenarios. For a random distribution created by the method

described in Sec. III A, we ran 8 inversions using between 5 and 40 SA chains covering a CSP range between 10^{11} and 10^{13} μPa (with the true CSP being 2.3×10^{12} μPa). For the same distribution and CSP values, we ran 6 inversions with 32 SA chains and between 1000 and 25 000 iterations. The effect of acoustic frequency on inversion success was tested using the same distribution and CSP values and the acoustic frequencies 27, 98, 150, and 270 Hz, since they are the characteristic contributions of marine mammals to the Southern Ocean acoustic environment (Menze *et al.*, 2017).

D. Simulation of drifting recorders using Argo float tracks

The last scenario tested the feasibility of using drifting platforms, such as Argo floats (Argo, 2018), as a receiver array. We extracted the tracks of all Argo floats within the study area (between 45°S and 80°S and −65°E and 25°E) between the 1.1.2013 and 29.5.2013 from the Coriolis Global Data Assembly Center.[2] The Argo tracks are displayed in supplemental Fig. 5.[1] We created a random distribution using the method described for the previous scenarios. For each day between 1 January 2013 and 29 May 2013, we used the positions of the available Argo float profiles as recorder locations and ran an inversion using 20 000 iterations and 32 SA chains.

IV. RESULTS

A. Random source distributions and inversion accuracy

We estimated the area in which the inversion method produced reliable results by correlating the true and estimated source pressure at each node over the 250 random source distributions. The resulting map of correlation coefficients is displayed in Fig. 8. Correlation coefficients are high (>0.5) within an oval area centered around the recorder location. This area roughly corresponds to the area we termed the "trust zone," which we defined as the area where more than one recorder is present within a 1000 km radius. The trust zone could be defined equally well using other definitions, but we choose our approach as a first conservative approximation of the area in which we expect the recorder

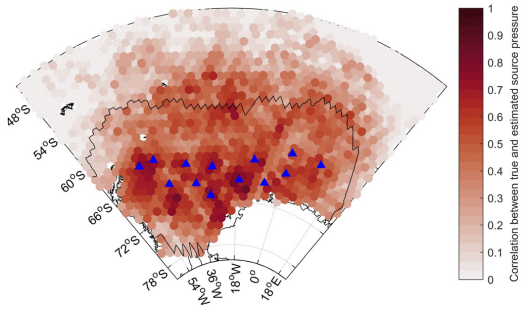

FIG. 8. (Color online) Map showing the correlation (red hues) between true and estimated source pressure over the 250 random distributions. Blue triangles mark recorder location. The black contour encircles the trust zone (more than one recorder present within a 1000 km radius).

setup and inversion algorithm to produce reliable results. This choice is discussed in more detail in Sec. V. The heterogenous patterns in correlation are likely artifacts caused by the small number of test scenarios.

We calculated the normalized and binary accuracy of the 250 inversions. The inversions proved remarkably successful given the small number (13) of recorders in the array, and accuracy values ranged between 0.2 and 1 with a median A_n of 0.7 and median A_b of 0.8 for nodes within the trust zone. Simulations confirmed that the A_n expected by chance is 0.3, and the A_b expected by chance is 0.5. Both the binary and normalized accuracies show a decreased inversion success when SP_j is calculated from only the best SA chain (solution) instead of the median of the three best SA chains. This is shown in Fig. 9(a), which compares the cumulative density function (CDF) of the normalized and binary accuracies for the 250 random source distributions. As indicated by the correlation map in Fig. 8, inversions were most successful within the trust zone. The CDF of accuracy within the trust zone and entire grid are compared in Fig. 9(b), confirming that the inversion was more accurate within the trust zone than across the entire grid. Hereinafter, all A_n and A_b values in the paper are calculated using only nodes within the trust zone if not stated otherwise.

The true and estimated CSPs within the trust zone are compared in Fig. 10. They agree well with a correlation coefficient of 0.9. To show example source distributions, Fig. 11 compares example true and estimated source distributions from the test scenario, sorted from best to worst normalized accuracy. The inversion method managed to estimate the presence and absence of sources well in most cases, even when no source was present in the trust zone or sources were distributed across multiple clusters. In some of the estimated source pressure grids, a gradient of sound sources is present at the boundary of the search space in the general direction of the true source distribution. As will be shown later, this represents excess sound energy in the forward model that is moved toward the boundaries of the search space to reduce the misfit between received and modelled RLs.

To investigate why some of the random source distributions could be estimated successfully while others could not, we compared the effect of several metrics on inversion accuracy and found that information entropy is one of the most useful metrics to predict inversion accuracy. Information entropy (Shannon, 1948) is a measure of information content (Borda, 2011), which reaches its maximum when the elements of the set are uniformly distributed. Using only nodes within the trust zone, the entropy $H(\mathrm{P}(\mathrm{SP}_j))$ of the estimated and true SP_j was calculated from the sample distribution $P(\mathrm{SP}_j)$ of the SP_j values in the following manner:

$$H(P(\mathrm{SP}_j)) = -\sum \mathrm{P}(\mathrm{SP}_j)\log(P(\mathrm{SP}_j)).$$

Source pressure distributions with high entropy contain a large variety of different SP_j values, whereas distributions with low entropy contained many similar SP_j values, mostly a high number of empty nodes with $\mathrm{SP}_j = 0$.

Figure 12(a) shows how inversion accuracy varies with the RL range of each source distribution and the misfit

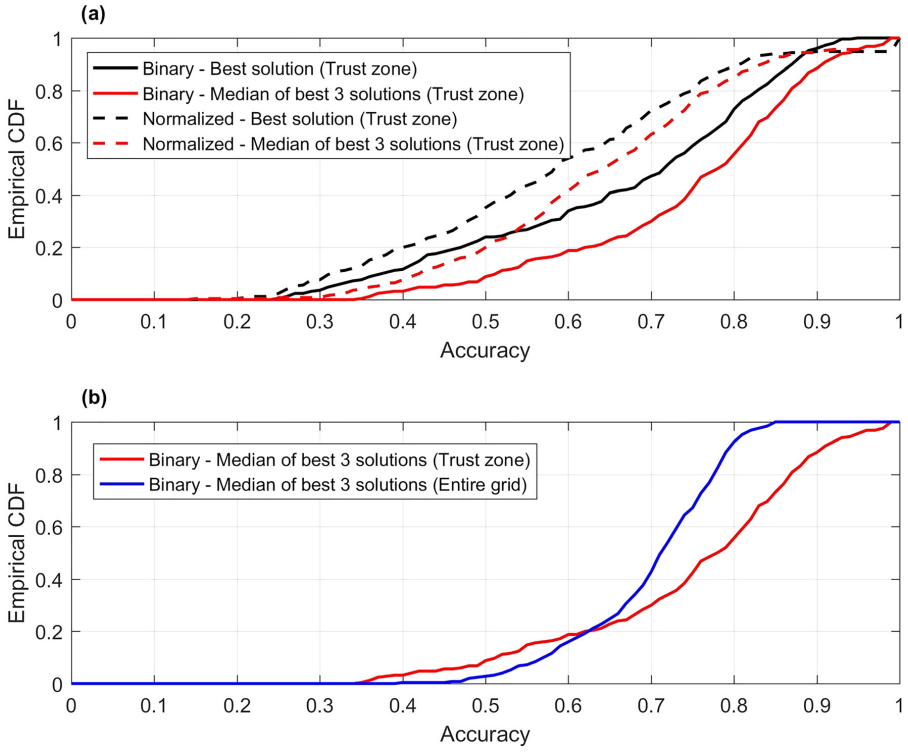

FIG. 9. (Color online) Comparison of the cumulative density functions (CDFs) of the accuracy values of the 250 random source distributions. (a) compares the accuracy of the best (black) and median of the three best SA chains (red). (b) compares the accuracy of the entire source grid and the source grid nodes within the trust zone.

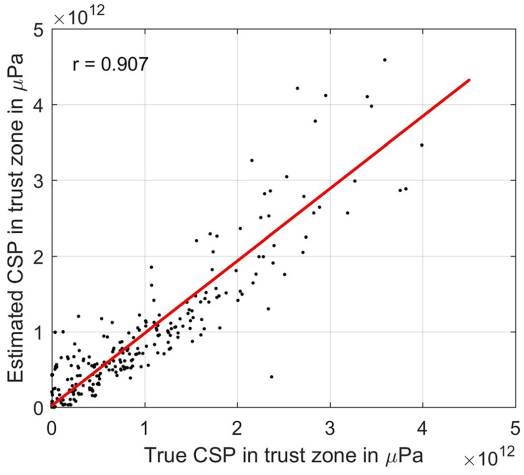

FIG. 10. (Color online) Comparison of the true and estimated CSPs in μPa. Each dot represents 1 of the 250 random source distributions. The red line is a linear fit to the data.

between true and simulated RL. Two clusters can be identified: a group of distributions with a RL range below 20 dB, which contains both low and high A_n values (0.4–1), and a cluster with RL ranges above 20 dB, which contains mainly high A_n values (0.6–0.9). Figure 12(c) shows that the cluster with RL ranges above 20 dB represents distributions closer to the recording array, which create a correspondingly larger RL range. The blue hues in the right cluster indicate a smaller average distance between sources and receivers ($<$2000 km). It is also separated from the other distributions through higher misfit values [yellow hues in Fig. 12(a)]. The cluster with RL ranges below 20 dB shows a large gradient of A_n values that corresponds to the gradient of true source pressure entropy (supplemental Fig. 6).[1] Accuracy shows an inverse relation to the entropy of the true source pressure [Fig. 12(b)], which also corresponds to an increase in CSP. This means that the inversion works best for distributions with low variance (such as many empty nodes) and less well for distributions with high variance. Accuracy is increasing with increasing misfit between true and estimated RLs [Fig. 12(e)] for misfit values between -100 and -50 dB, which also exhibit high estimated source pressure entropy values (yellow hues) and shows no clear relationship for misfit values above -50 dB. The entropy of the estimated source

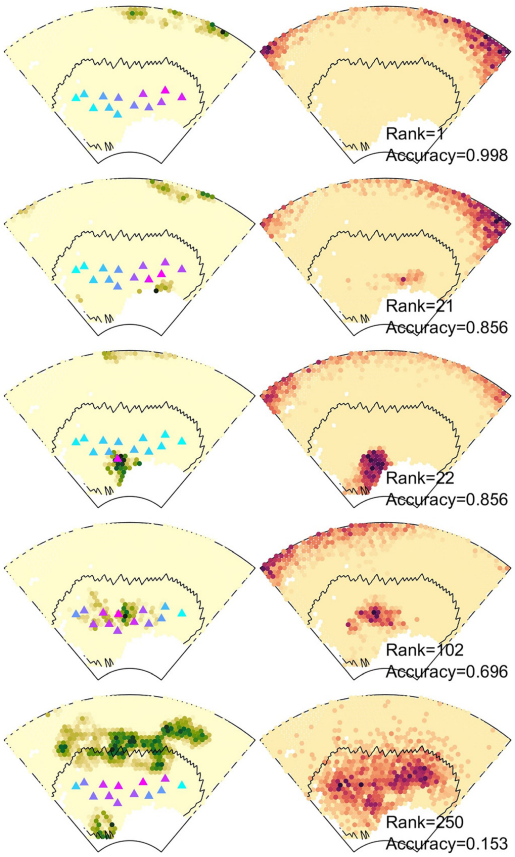

FIG. 11. (Color online) Various examples of true and estimated distributions sorted from the most accurate inversion (rank 1, $A_n = 0.996$) to the least accurate inversion (rank 250, $A_n = 0.162$). Maps in the left columns show the modelled source pressure grid and recorder locations (triangles, color indicates RL), and maps in the right columns show the estimated source pressure grid. Node color indicates the source pressure in μPa, normalized for each scenario (row). The black contours encircle the trust zone (more than one recorder present within a 1000 km radius).

pressure shows a marked relationship to accuracy [Fig. 12(f)]: accuracy decreases with increasing entropy of the estimated source pressure following a linear function ($r = 0.87$). However, the relationship between the entropy of the true and estimated source pressure is not linear and shows only limited correlation [Fig. 12(d)]. Another metric of the quality of the estimate is the width (variance) of the estimated source pressure distribution for each node. We compared the mean (averaged over all nodes) range of the best three source pressure estimates to normalized accuracy in Fig. 12(g). We used the range as an indicator of the variance due to the small number of solutions. Estimates with a small range (below 10^9 μPa) between the three best solutions show the highest accuracy, whereas estimates with a range larger than 10^9 μPa show a large spread in accuracy. This spread corresponds to a gradient in the entropy of the estimated source pressure (color). When only estimates with low entropy are considered (blue dots), a robust relation between the range of the estimates and accuracy exists.

The scatterplots in Fig. 12 show that the entropy and spread (variance) of the estimated source pressure can be used as a metric for inversion accuracy when no other information is available. The best inversion accuracy was achieved for estimated source distributions with low entropy, meaning that many nodes have similar values (are empty) and distributions were patchy; however, inversion was also successful for distributions with high entropy when the RL gradient/range was sufficiently high.

We also analyzed the true and false positive rates of the estimated source pressure grids, considering only source presence/absence information (supplemental Fig. 7[1]), and found that an increasing true positive rate corresponds to decreasing misfit and RL range, whereas an increasing false positive rate corresponds to increasing entropy of the estimated source pressure.

B. Effect of inaccurate TL model

The effect of a flawed TL model on inversion accuracy was tested by using 100 random distributions with the ray-tracing and geometrical spreading TL models. Figure 13 compares the inversion accuracy for inversion with a perfect and inaccurate TL model. Both the binary and normalized accuracies show a clear but small negative offset in the CDF (mean offset is 0.06) when the TL model is inaccurate compared to the perfect TL model. The inversion method still produced reliable source pressure grid estimates when complex multipath propagation of sound was approximated with a simple geometrical spreading model, at least for the deep ocean with upward refracting sound speed profile in the study area.

C. Sensitivity tests

Inversion accuracy was not impacted by changes in frequency. No significant change was detected among 27, 98, 150, and 270 Hz, and the binary accuracies were 0.83, 0.85, 0.85, and 0.87, respectively. However, inversion accuracy showed a marked relationship with the number of SA chains (solutions), which determines the resolution with which the CSP range is sampled. Figure 14 shows how inversion accuracy increases with an increasing number of SA chains. Within the trust zone, accuracy increases until around 20 solutions, whereas the accuracy of the entire grid increases continuously up to 40 solutions. This can also be seen when visually comparing the true [Fig. 14(b)] and estimated source pressure grids from inversions with an increasing number of SA chains [Figs. 14(c)–14(j)]. Five SA chains proved way too little to approximate the source distribution adequately, whereas inversions using 10–25 SA chains resolved the central cluster of sources but showed excess sound sources at the northern search space boundary. Inversion using more than 30 SA chains resolved the central cluster of sources and did not show excess sound sources at the search space boundaries. These results indicate that the inversion algorithm stores excess sound energy at the search space

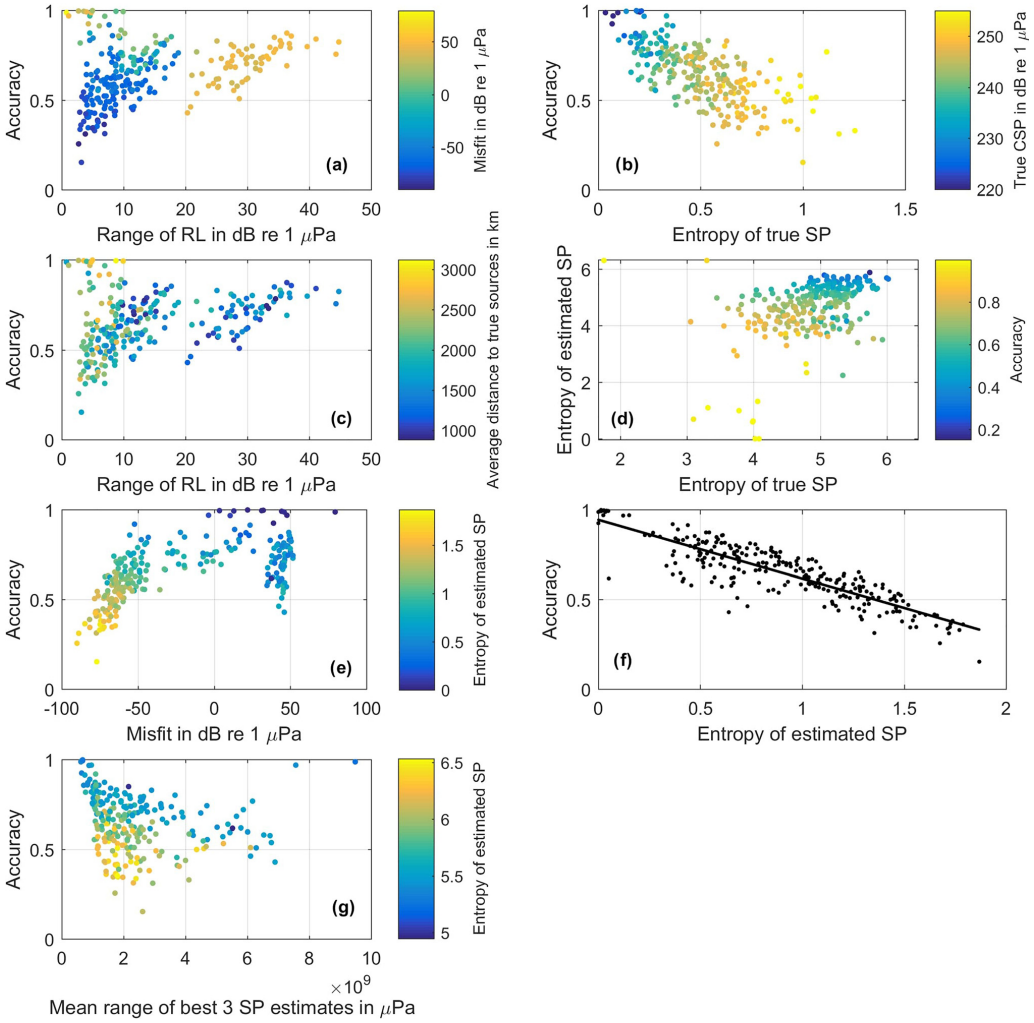

FIG. 12. (Color online) Scatterplots comparing the normalized inversion accuracy (A_n within the trust zone) and several metrics. Each dot represents 1 of the 250 random source distributions. (a) The range of RLs and the misfit between true and simulated RL (colors), (b) entropy of the true source pressure (SP) and true CSP (colors), (c) the range of RLs and the average distance between the true sources and recorders (colors), (d) entropy of the true and estimated SP (colors indicate accuracy), (e) misfit between true and estimated RL and entropy of the estimated source pressure, (f) entropy of the estimated source pressure, where the black line represents fitted linear function, and (g) the mean range of the three best estimated source pressure estimates and entropy of the estimated SP (color).

boundaries when the CSP distribution is too coarsely sampled (too few SA chains). The number of iterations to achieve successful inversion proved to be remarkably low (Fig. 15) in the test scenario. For the scenario described in Sec. III C, the increase in inversion accuracy flattened out after approximately 5000 iterations.

D. Simulation of drifting recorders using Argo float tracks

The suitability of Argo floats as drifting ambient sound recorders was tested using a random source distribution and the location of Argo float profiles over 71 days. The true source distribution, estimated source distribution, and recorder locations for six example days (sorted after inversion accuracy) are displayed in Fig. 16. When a sufficient number of Argo profiles (recorders) were present and their locations were spread evenly over the grid, inversion was successful with normalized accuracies up to 0.7 for the entire source grid. But, on days with very few or less evenly distributed floats, the inversion was unsuccessful. To investigate the necessary conditions for successful inversion, the scatterplots in Fig. 17 compare normalized accuracy over the number and location of recorders and the node entropy of

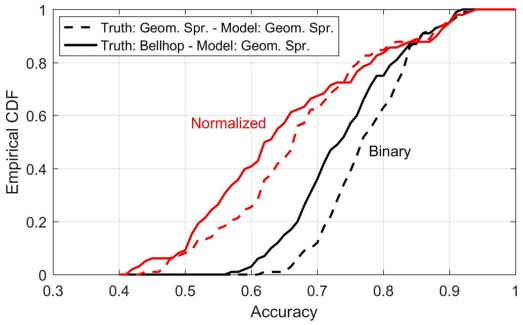

FIG. 13. (Color online) Comparison of the CDFs of accuracy (red, normalized accuracy; black, binary accuracy) of the 100 random source distribution estimates within the trust zone. The dashed lines show the accuracy for inversions with a perfect TL model, where the true and forward model TLs were both calculated using geometrical spreading. The solid lines show the accuracies for inversions with a flawed TL forward model, where the true TL was calculated using raytracing with BELLHOP, whereas the forward model TL was calculated using geometrical spreading.

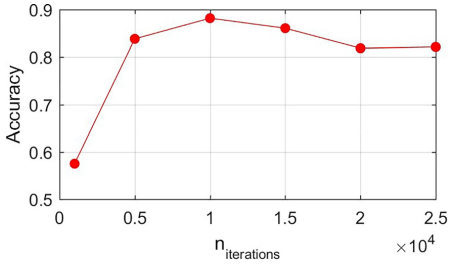

FIG. 15. (Color online) Binary inversion accuracy over the number of iterations for the test scenario.

the estimated source pressure. Whereas the entropy $H(P(\mathrm{SP}_j))$ quantifies the flatness of the source pressure *sample distribution*, the node entropy $H(\mathrm{SP}_j)$ determines the flatness of the source pressure grid directly by summing over the nodes

$$H(\mathrm{SP}_j) = -\sum \mathrm{SP}_j \log(\mathrm{SP}_j).$$

Both entropy metrics are low when the source pressure distribution has a low variance (many similar values, mainly empty nodes) and high when the source pressure distribution has a high variance.

We found that when less than 15 recorders were present, inversion accuracy ranged between 0.4 and 0.75, whereas accuracy was between 0.6 and 0.75 when more than 15 recorders were present. We found a close and almost linear relationship between the RL range and inversion accuracy, independent of the number or recorders. This indicates that inversion accuracy depends on both the number of recorders and the RL gradient (range). As for the 250 random source distributions in the first test scenario, we found a close relationship between inversion accuracy and the entropy of the estimated source pressure. In this scenario, the relationship between node entropy and accuracy was linear. Normalized accuracies were above 0.7 on 45% of the simulated days.

V. DISCUSSION

The test scenarios showed that it is possible to estimate the distribution of sound sources from ambient sound using widely spaced recorder arrays, but also demonstrated the limitations of the method and explored the prerequisites for successful inversion. Sections V A–V D interpret the results of the test scenarios and discuss the feasibility to apply this inversion method to real ambient sound data.

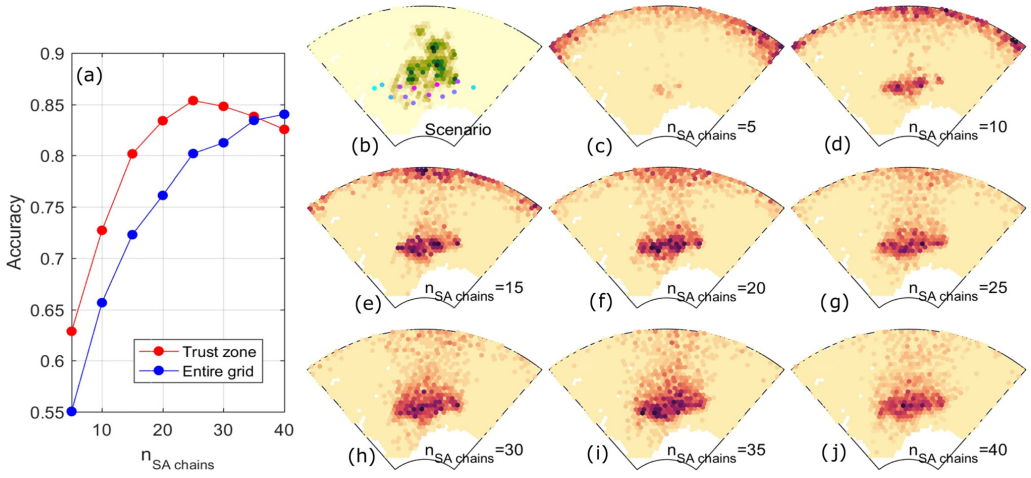

FIG. 14. (Color online) The effect of the number of SA) chains on inversion accuracy. (a) shows how binary accuracy in the trust zone and entire grid increases with increasing number of SA chains. (b) shows the test scenario source distribution (green hues) and RL (blue-pink hues). (c)–(j) show the estimated source pressure grid for inversion using 5–40 SA chains.

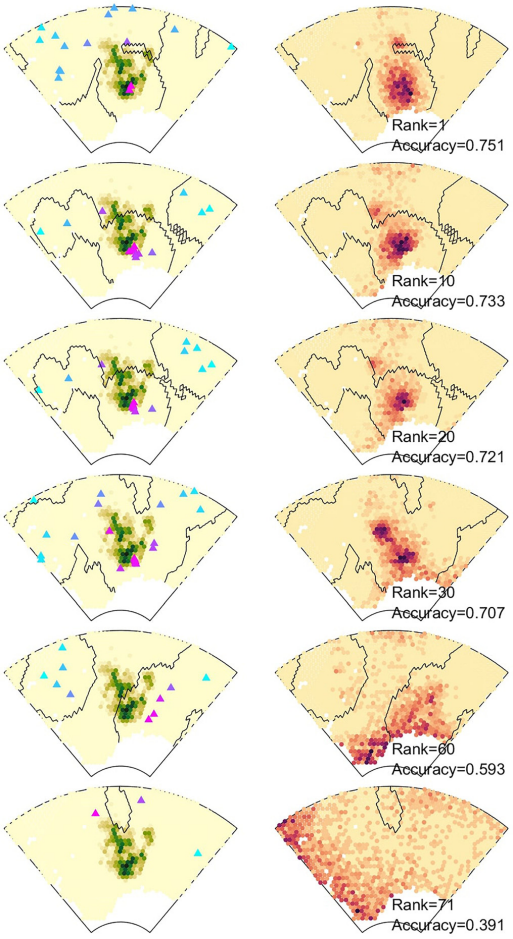

FIG. 16. (Color online) Example true and estimated distributions, sorted from best inversion to worst (rank 71) using normalized accuracy over the entire grid. Maps on the left show the true source pressure grid and recorder (Argo float) locations (triangles, color indicates RL), and maps of the right show the estimated source pressure grid. Node color indicates the source pressure in μPa, normalized for each scenario (row). The black contours encircle the trust zone (more than one recorder present within a 1000 km radius).

A. Accuracy and reliability of the inversion method

The random distribution and Argo float test scenarios showed that inversion accuracy can be predicted using the entropy and spread of the estimated source pressure grid [Figs. 12(f) and 17(b)] and range or gradient of the RLs [Figs. 12(c) and 17(c)]. Both the test scenarios with fixed recorders and random source distributions, and Argo float scenario with variable recorders and a fixed source distribution, indicated that an inversion is likely inaccurate when the estimated sources distribution has a high entropy and accurate when the source distribution has low entropy (many empty nodes and a patchy distribution). The reason for this is likely that the misfit function does not have a pronounced

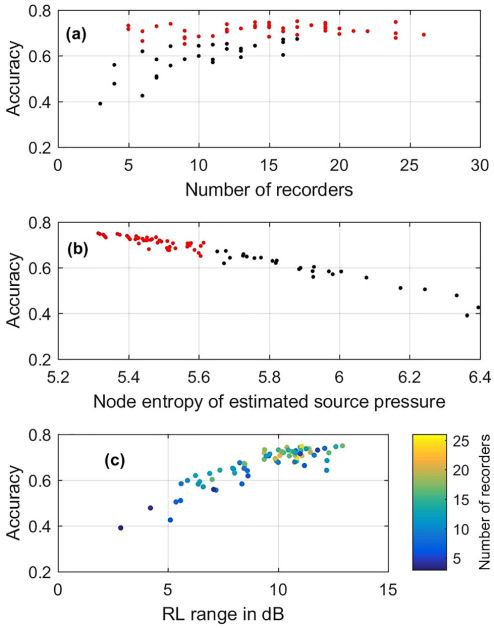

FIG. 17. (Color online) Scatterplots comparing normalized inversion accuracy over the entire grid for several metrics. (a) Number of recorders (Argo floats), (b) node entropy of the estimated source pressure, (c) range of RL values and number or recorders (color). Red dots indicate inversions with a node entropy of the estimated source pressure below 5.65.

global minimum when the inversion algorithm does not have sufficient information (too few recorders or too small RL gradient), forcing the parameter estimation algorithm to spread the sources over the search space. The comparisons between accuracy and RL range [Fig. 12(c) and 17(c)] demonstrated that an increased RL gradient, and resulting increase in RL information, benefits inversion accuracy, but inversion can also be successful with small RL gradients when the true source distribution contains no sources in the trust zone or has a low entropy (many empty nodes).

The test scenario with fixed recorders and random source distributions showed an inverse relationship between inversion accuracy and true source pressure entropy [Fig. 12(b)], indicating that the recorder array used in this scenario is most suitable to locate clustered distribution and regions with no sources. This could be related to a lack of gradients in the RL dataset for more uniform source distributions. Adding more recorders to the array and adjusting the spacing of the array would increase the information present in the RL dataset and, thus, improve the inversion accuracy. The effect of recorder array geometry on inversion accuracy will be studied with further simulations that would extend the scope of this paper.

It was crucial to test the effect of an inaccurate TL model on inversion accuracy, since TL models are only, more or less, a rough approximation of the true TL as it is challenging to model underwater sound propagation correctly. Most available models are only 2D, do not include

sea ice, and are computationally expensive. In high latitude oceans, such as the Weddell Sea, the effect of sea ice on TL can be profound, but few operational TL models that include TL from sea ice exist. We therefore compared the inversion accuracy of 100 random distributions with a perfect and a flawed TL model (Fig. 13). When using a flawed TL model, by approximating the true raytracing TL with a geometrical spreading model, the accuracy of the CDF shifted, on average, 0.06 toward smaller values. This means that inversion accuracy is only slightly affected by the flawed TL model in our study area (open upward refracting ocean), and thus simple TL models (such as geometrical spreading) could be used for inversions based on real data. This is likely the case due to the long distances and many source-receiver pathways of the inverse problem. Since the recorder array is widely spaced, small-scale variations in TL are not resolved, and the many pathways likely average out TL errors. As long as the TL model resolves the non-linear gradient of the TL on the scale of hundreds to thousands of km (supplemental Fig. 4[1]), inversion accuracy is only slightly decreased when approximating true TL with the geometrical spreading model. If this holds for ocean areas with more complex propagation characteristics than the deep offshore Southern Ocean remains to be studied with further simulations. Ocean areas with waveguides or complex topography will likely need more sophisticated TL forward models for successful inversion.

The area in which the inversion produces reliable estimates, the trust zone, was approximated by studying the correlation between the true and estimated source pressures of hundreds of random source distributions (Fig. 8). Such an approach could also be applied to estimate the trust zone when real data are used. The size and shape of the trust zone depends on the number and location of recorders; placing a large number or recorders uniformly over the study area is likely the best way to record a suitable dataset for inversion. This is supported by the results of the ARGO float simulations (Fig. 17). Within the trust zone, the inversion algorithm successfully estimated the CSP for most of the 250 random source distributions ($r = 0.9$; Fig. 10). It is important that the pressure values are not biased since the source pressure at each node is the basis of eventually estimating the number of animals per area by multiplying source pressure per area with (yet unknown) species specific coefficients. Increasing the number of SA chains, which determines how many different CSP samples are calculated, can likely increase this correlation even more.

The sensitivity tests (Figs. 14 and 15) showed that successful estimates of source distribution can be computed with reasonable effort ($\sim$10 000 iterations and 30 SA chains for the Weddell Sea test scenario). As expected, the more SA chains are used for the inversions, the better the estimate becomes. Using too few SA chains under-samples the CSP distribution, resulting in estimates with either a too low or too high CSP. The parameter estimation algorithm stores this excess sound energy (which cannot be located sufficiently) at the boundaries of the search space to match the general gradient of RL in the recorder array (Fig. 14). It was expected that accuracy increases with an increasing number of iterations until a certain value is reached; however, the comparatively small number of iterations needed to calculate accurate inversions was smaller than expected. This means that the source grid size and resolution and the number of recorders can be increased with realizable computational effort.

Another important aspect is that that the recorders need to be calibrated sufficiently because biases in the RL data could affect inversion accuracy, and the inversion method relies on absolute RL values and small gradients. However, the inaccurate TL test scenario (Fig. 13) showed that small errors in the forward model are tolerated by the inversion method, thus, small errors in RL should be tolerated similarly by the inversion method. Ideally each recording device should be calibrated before deployment. If this is not possible, the gain should be chosen so that part of the recorded spectra hit the noise floor of the recording device. This noise floor can then be compared to the factory calibration values of the hydrophone and recording device, and eventual offsets detected. An example of this post-deployment calibration check can be found in Menze *et al.* (2017). It is also a suitable way of quantifying the recorders self-noise. If it is too high, faint MMC peaks in the ambient sound might not be detected.

B. Requirements for successful inversion

To apply the inversion method to real MMC data and get reliable source pressure distribution estimates, several perquisites need to be fulfilled. First, the number of recorders needs to be large enough, and they need to record a large enough RL_{MMC} gradient. For the Weddell Sea scenario, already up to ten recorders can be sufficient, but more are preferred (Figs. 12 and 17). The recorders are best spread evenly over the study area to record as much RL gradient (large range of RL values) as possible to maximize the information content of the RL dataset. One of the most important requirements is that the MMC to ambient sound should be detectable in the first place. This depends not only on the number of vocalizing animals in the area but also on noise from shipping, seismic surveys, and sea surface motion. In regions with high marine traffic, the MMC peaks are likely masked by shipping noise, leading to a lack of RL_{MMC} measurements and low inversion accuracy. The inversion method is thus most suitable in remote regions far away from anthropogenic activity, which are also difficult to survey with traditional methods due to their remoteness. The inversion method is based on minimizing the misfit between recorded and modelled RL_{MMC}, thus, offsets and biases in the recorded RL_{MMC} can lead to erroneous inversion results. The recorders need to be properly calibrated to provide reliable RL_{MMC} data. Second, the number of iterations and solutions needs to be sufficiently high. Third, the source pressure grid should be large enough to cover all possibly expected source locations and have an adequate resolution (distance between grid nodes). Fourth, the TL matrix between the recorders and grid nodes should be calculated as accurately as possible.

C. Argo floats as ambient sound recorders

The Argo float test scenario showed that ambient sound data from drifting recorders could successfully be used for inversion (Fig. 17). However, the test also showed that successful inversion in the study area was only possible on approximately 45% of the simulated days, and on the other days there were too few profiles or profiles at unfavorable locations. This is related to the sparse number of Argo floats in the Southern Ocean (Reeve *et al.*, 2016); mid latitude areas have much better Argo float coverage than high latitude areas, thus, Argo floats are likely suitable for inversions in most of the world's oceans with the current Argo float array.

To obtain ambient sound data suitable for MMC inversion from Argo floats, several specifications need to be fulfilled. The location of the float needs to be known [the float needs to surface to get a global positioning system (GPS) fix or be localized acoustically]. The float needs to be able to record 5–30 min of sound in the right frequency band and sufficient dynamic range with a calibrated hydrophone. Furthermore, the floats would need to be able to calculate and transmit a power spectrum of the recording. Finally, all floats need to record at approximately the same time and date. The timing does not need to be accurate on the scale of seconds but should agree on the scale of minutes to ensure that only spatial variability of the MMC is recorded. To ensure consistency, the float should also stay at a fixed depth. It is likely most practical to record ambient sound for 10 min at the floats drifting depth (approximately 1000 m) before the float surfaces to measure a temperature and salinity profile. The technology to record ambient sound and transmit spectra with Argo floats has already been developed and successfully tested (Matsumoto *et al.*, 2013; Nystuen *et al.*, 2011), but a large transnational effort is necessary to create and deploy an Argo float array sufficient for MMC inversion. We propose that the scope of future Argo float deployments not only contain oceanographic and bio-geo-chemical sensors but also a calibrated hydrophone and necessary data processing capabilities, which cannot only be used to study marine mammal distribution but also rain fall rate and air–-sea–ice interaction (Cazau *et al.*, 2018; Ma *et al.*, 2005).

D. Application of the inversion method

We could demonstrate that successful inversion off MMCs is possible with the HAFOS mooring array (Van Opzeeland *et al.*, 2014). Inversion should be possible with all four MMCs (Blue, fin, and Antarctic minke whales, and leopard seals) and could allow year-round monitoring of the distribution of vocalizing marine mammals in the Weddell Sea. To obtain values of animal distribution and density (average number of animals in study area), the source pressure (SP) per area values needs to be multiplied with the population specific call rate (CR) and SL values

$$\frac{n_{\text{animals}}}{\text{area}} = \frac{\text{SP}}{\text{area}} \text{CR}\, 10^{\text{SL}/20}.$$

Reliable values for CR and SL are very difficult to obtain and, therefore, we did not investigate such density estimation yet. These multipliers are likely not constant with time and region and similar to the multipliers used in call detection estimation methods (Thomas and Marques, 2012). In addition to MMCs in the Southern Ocean, the inversion method could be applied to the MMC of fin whales in the Mid and North Atlantic (Nieukirk *et al.*, 2012), fin and blue whales in the North Pacific (Curtis *et al.*, 1999), fin and possibly Bowhead whales in the Arctic (Ahonen *et al.*, 2017), and fin and blue whales in the Indian Ocean (Leroy *et al.*, 2018a). Data from the widely spaced recorder arrays used in these studies show temporal and spatial patterns in RL_{MMC} suggestive of seasonal migration.

VI. CONCLUSION

We presented and tested an approach to estimate the distribution of vocalizing marine mammals based on inverse modelling and the spatial variation in ambient sound spectra instead of the detection of individual, transient vocalizations. Despite the under-determinedness of this inverse problem, the parameter estimation algorithm successfully estimated the spatial distribution of sound sources in a set of test scenarios, which showed that inversion accuracy depends on the number (and gradient) of RL observations, number of SA chains, and sound source distribution entropy. The accuracy of the estimates is only slightly affected by inevitable inaccuracies in the TL model. Test simulations indicated that drifting platforms, such as Argo floats, can be suitable to gather MMC data. Applying the method to ambient sound recordings from the Southern Ocean renders it possible to study the distribution and migration of vocalizing marine mammals on unpreceded spatial scales and temporal resolution, and compliments existing visual and acoustic estimation methods. The approach we explored in this paper could also be applied to recordings of other species that generate chorus-like sounds, e.g., insects, amphibians, and birds, provided that the sounds propagate far enough and are generated often enough to form a chorus. Calibrated recorders are used, and the TL between the recorders and sound sources can be sufficiently modelled.

ACKNOWLEDGMENTS

We would like to thank Randi Ingvaldsen and the Institute of Marine Research for providing supervision, funding (Research council of Norway Grant No. 228896), and scientific freedom to S.M., and the Office of Naval Research for funding D.Z. with Grant No. N00014-18-1-2811. We also thank the reviewers and Len Thomas for their feedback. The authors declare no competing interests.

[1]See supplementary material at https://doi.org/10.1121/1.5139406 for a pdf with the supplementary figures and a zip folder containing the code used for this study. The supplementary material can also be found in the github repository https://github.com/sebastianmenze/ambient-sound-inversion

[2]See http://www.argodatamgt.org/Access-to-data/Argo-data-selection (Last viewed 2/23/2018).

Ahonen, H., Stafford, K. M., de Steur, L., Lydersen, C., Wiig, Ø., and Kovacs, K. M. (**2017**). "The underwater soundscape in western Fram Strait: Breeding ground of Spitsbergen's endangered bowhead whales," Mar. Pollut. Bull. **123**(1-2), 97–112.

Amante, C., and Eakins, B. W. (**2009**). "ETOPO1 1 arc-minute global relief model: Procedures, data sources and analysis, in *NOAA Technical Memorandum NESDIS NGDC-24*, National Geophysical Data Center, NOAA, available at https://doi.org/10.7289/V5C8276M (Last viewed 5/1/2016).

Argo (**2018**). "Argo float data and metadata from Global Data Assembly Centre (Argo GDAC)" (SEANOE), available at http://doi.org/10.17882/42182.

Bombosch, A., Zitterbart, D. P., Van Opzeeland, I., Frickenhaus, S., Burkhardt, E., Wisz, M. S., and Boebel, O. (**2014**). "Predictive habitat modelling of humpback (*Megaptera novaeangliae*) and Antarctic minke (*Balaenoptera bonaerensis*) whales in the Southern Ocean as a planning tool for seismic surveys," Deep Sea Res., Part I **91**, 101–114.

Bonnel, J., Thode, A. M., Blackwell, S. B., Kim, K., and Macrander, A. M. (**2014**). "Range estimation of bowhead whale (*Balaena mysticetus*) calls in the Arctic using a single hydrophone," J. Acoust. Soc. Am. **136**(1), 145–156.

Borda, M. (**2011**). *Fundamentals in Information Theory and Coding* (Springer, Berlin).

Burtenshaw, J. C., Oleson, E. M., Hildebrand, J. A., McDonald, M. A., Andrew, R. K., Howe, B. M., and Mercer, J. A. (**2004**). "Acoustic and satellite remote sensing of blue whale seasonality and habitat in the Northeast Pacific," Deep Sea Res., Part II **51**(10-11), 967–986.

Carey, W. M., and Evans, R. B. (**2011**). *Ocean Ambient Noise* (Springer, New York).

Carlén, I., Thomas, L., Carlström, J., Amundin, M., Teilmann, J., Tregenza, N., Tougaard, J., Koblitz, J. C., Sveegaard, S., Wennerberg, D., Loisa, O., Dähne, M., Brundiers, K., Kosecka, M., Kyhn, L. A., Ljungqvist, C. T., Pawliczka, I., Koza, R., Arciszewski, B., Galatius, A., Jabbusch, M., Laaksonlaita, J., Niemi, J., Lyytinen, S., Gallus, A., Benke, H., Blankett, P., Skóra, K. E., Acevedo-Gutiérrez, A. (**2018**). "Basin-scale distribution of harbour porpoises in the Baltic Sea provides basis for effective conservation actions," Biol. Conserv. **226**, 42–53.

Cazau, D., Bonnel, J., and Baumgartner, M. (**2018**). "Wind speed estimation using acoustic underwater glider in a near-shore marine environment," IEEE Trans. Geosci. Remote Sens. **57**, 2097–2106.

Cronin, B., Stevenson, I. H., Sur, M., and Körding, K. P. (**2009**). "Hierarchical Bayesian modeling and Markov chain Monte Carlo sampling for tuning-curve analysis," J. Neurophysiol. **103**, 591–602.

Curtis, K. R., Howe, B. M., and Mercer, J. A. (**1999**). "Low-frequency ambient sound in the North Pacific: Long time series observations," J. Acoust. Soc. Am. **106**(6), 3189–3200.

Dawson, D. K., and Efford, M. G. (**2009**). "Bird population density estimated from acoustic signals," J. Appl. Ecol. **46**(6), 1201–1209.

Dushaw, B. D., Worcester, P. F., Dzieciuch, M. A., and Menemenlis, D. (**2013**). "On the time-mean state of ocean models and the properties of long range acoustic propagation," J. Geophys. Res. Oceans **118**(9), 4346–4362, https://doi.org/10.1002/jgrc.20325.

Francois, R. E., and Garrison, G. R. (**1982**). "Sound absorption based on ocean measurements. Part II: Boric acid contribution and equation for total absorption," J. Acoust. Soc. Am. **72**(6), 1879–1890.

Granville, V., Krivanek, M., and Rasson, J. P. (**1994**). "Simulated annealing: A proof of convergence," IEEE Trans. Pattern Anal. Mach. Intell. **16**(6), 652–656.

Harris, D., Matias, L., Thomas, L., Harwood, J., and Geissler, W. H. (**2013**). "Applying distance sampling to fin whale calls recorded by single seismic instruments in the northeast Atlantic," J. Acoust. Soc. Am. **134**(5), 3522–3535.

Harris, D. V., Miksis-Olds, J. L., Vernon, J. A., and Thomas, L. (**2018**). "Fin whale density and distribution estimation using acoustic bearings derived from sparse arrays," J. Acoust. Soc. Am. **143**(5), 2980–2993.

Haver, S. M., Klinck, H., Nieukirk, S. L., Matsumoto, H., Dziak, R. P., and Miksis-Olds, J. L. (**2017**). "The not-so-silent world: Measuring Arctic, equatorial, and Antarctic soundscapes in the Atlantic Ocean," Deep Sea Res., Part I **122**, 95–104.

Herr, H., Kelly, N., Dorschel, B., Huntemann, M., Kock, K., Lehnert, L. S., Siebert, U., Viquerat, S., Williams, R., and Scheidat, M. (**2019**). "Aerial surveys for Antarctic minke whales (*Balaenoptera bonaerensis*) reveal sea ice dependent distribution patterns," Ecol. Evol. March, **9**, 5664–5682.

Kirkpatrick, S., Gelatt, C. D., and Vecchi, M. P. (**1983**). "Optimization by simulated annealing," Science **220**(4598), 671–680.

Kusel, E. T., Mellinger, D. K., Thomas, L., Marques, T. A., Moretti, D., and Ward, J. (**2011**). "Cetacean population density estimation from single fixed sensors using passive acoustics," J. Acoust. Soc. Am. **129**(6), 3610–3622.

Kyhn, L. A., Tougaard, J., Thomas, L., Duve, L. R., Stenback, J., Amundin, M., Desportes, G., and Teilmann, J. (**2012**). "From echolocation clicks to animal density—Acoustic sampling of harbor porpoises with static dataloggers," J. Acoust. Soc. Am. **131**(1), 550–560.

Leroy, E., Samaran, F., Stafford, K., Bonnel, J., and Royer, J. (**2018a**). "Broad-scale study of the seasonal and geographic occurrence of blue and fin whales in the Southern Indian Ocean," Endanger. Species Res. **37**, 289–300.

Leroy, E. C., Royer, J.-Y., Bonnel, J., and Samaran, F. (**2018b**). "Long-term and seasonal changes of large whale call frequency in the Southern Indian Ocean," J. Geophys. Res. Oceans **123**, 8568–8580, https://doi.org/10.1029/2018JC014352.

Lewis, L. A., Calambokidis, J., Stimpert, A. K., Fahlbusch, J., Friedlaender, A. S., McKenna, M. F., Mesnick, S. L., Oleson, E. M., Southall, B. L., Szesciorka, A. R., and Širović, A. (**2018**). "Context-dependent variability in blue whale acoustic behaviour," R. Soc. Open Sci. **5**(8), 180241.

Lurton, X. (**2010**). *An Introduction to Underwater Acoustics: Principles and Applications* (Springer, Berlin).

Ma, B. B., Nystuen, J. A., and Lien, R.-C. (**2005**). "Prediction of underwater sound levels from rain and wind," J. Acoust. Soc. Am. **117**(6), 3555.

Marques, T. A., Munger, L. M., Thomas, L., Wiggins, S. M., and Hildebrand, J. A. (**2011**). "Estimating North Pacific right whale *Eubalaena japonica* density using passive acoustic cue counting," Endanger. Species Res. **13**(3), 163–172.

Marques, T. A., Thomas, L., Martin, S. W., Mellinger, D. K., Ward, J. A., Moretti, D. J., Harris, D., and Tyack, P. L. (**2013**). "Estimating animal population density using passive acoustics," Biol. Rev. Cambridge Philos. Soc. **88**(2), 287–309.

Martin, S. W., Marques, T. A., Thomas, L., Morrissey, R. P., Jarvis, S., Dimarzio, N., Moretti, D., and Mellinger, D. K. (**2013**). "Estimating minke whale (*Balaenoptera acutorostrata*) boing sound density using passive acoustic sensors," Mar. Mammal Sci. **29**, 142–158.

Matsumoto, H., Jones, C., Klinck, H., Mellinger, D. K., Dziak, R. P., and Meinig, C. (**2013**). "Tracking beaked whales with a passive acoustic profiler float," J. Acoust. Soc. Am. **133**(2), 731–740.

McCauley, R. D., Gavrilov, A. N., Jolliffe, C. D., Ward, R., and Gill, P. C. (**2018**). "Pygmy blue and Antarctic blue whale presence, distribution and population parameters in southern Australia based on passive acoustics," Deep Sea Res., Part II **157-158**, 154–168.

McDonald, M. A., Hildebrand, J. A., Wiggins, S. M., and Ross, D. (**2008**). "A 50 year comparison of ambient ocean noise near San Clemente Island: A bathymetrically complex coastal region off Southern California," J. Acoust. Soc. Am. **124**(4), 1985–1992.

Mellinger, D. K., Küsel, E. T., Harris, D., Thomas, L., and Matias, L. (**2014**). "Estimating singing fin whale population density using frequency band energy," J. Acoust. Soc. Am. **136**(4), 2275.

Menze, S., Zitterbart, D. P., van Opzeeland, I., and Boebel, O. (**2017**). "The influence of sea ice, wind speed and marine mammals on Southern Ocean ambient sound," R. Soc. Open Sci. **4**(1), 160370.

Mosegaard, K., and Sambridge, M. (**2002**). "Monte Carlo analysis of inverse problems,' Inverse Probl. **18**, R29–R54.

Mouy, X., Hannay, D., Zykov, M., and Martin, B. (**2012**). "Tracking of Pacific walruses in the Chukchi Sea using a single hydrophone," J. Acoust. Soc. Am. **131**(2), 1349.

Newhall, A. E., Lin, Y.-T., Lynch, J. F., Baumgartner, M. F., and Gawarkiewicz, G. G. (**2012**). "Long distance passive localization of vocalizing sei whales using an acoustic normal mode approach," J. Acoust. Soc. Am. **131**(2), 1814–1825.

Nieukirk, S. L., Mellinger, D. K., Moore, S. E., Klinck, K., Dziak, R. P., and Goslin, J. (**2012**). "Sounds from airguns and fin whales recorded in the mid-Atlantic Ocean, 1999–2009," J. Acoust. Soc. Am. **131**(2), 1102–1112.

Nystuen, J., Riser, S., Wen, T., and Swift, D. (**2011**). "Interpreted acoustic ocean observations from Argo floats," J. Acoust. Soc. Am. **129**, 2400.

Pijanowski, B. C., Villanueva-Rivera, L. J., Dumyahn, S. L., Farina, A., Krause, B. L., Napoletano, B. M., Gage, S. H., and Pieretti, N. (**2011**). "Soundscape ecology: The science of sound in the landscape," BioScience **61**(3), 203–216.

Porter, M. B. (**1987**). "Gaussian beam tracing for computing ocean acoustic fields," J. Acoust. Soc. Am. **82**(4), 1349–1359.

Reeve, K. A., Boebel, O., Kanzow, T., Strass, V., Rohardt, G., and Fahrbach, E. (**2016**). "A gridded data set of upper-ocean hydrographic properties in the Weddell Gyre obtained by objective mapping of Argo float measurements," Earth Syst. Sci. Data **8**(1), 15–40.

Risch, D., Castellote, M., Clark, C. W., Davis, G. E., Dugan, P. J., Hodge, L. E., Kumar, A., Lucke, K., Mellinger, D. K., Nieukirk, S. L., Popescu,

C. M., Ramp, C., Read, A. J., Rice, A. N., Silva, M. A., Siebert, U., Stafford, K. M., Verdaat, H., and Van Parijs, S. M. (**2014**). "Seasonal migrations of North Atlantic minke whales: Novel insights from large-scale passive acoustic monitoring networks," Mov. Ecol. **2**(1), 24.

Rogers, T. L., Ciaglia, M. B., Klinck, H., and Southwell, C. (**2013**). "Density can be misleading for low-density species: Benefits of passive acoustic monitoring," PloS One **8**(1), e52542.

Seger, K. D., Thode, A. M., Urbán-R., J., Martínez-Loustalot, P., Jiménez-López, M. E., and López-Arzate, D. (**2016**). "Humpback whale-generated ambient noise levels provide insight into singers' spatial densities," J. Acoust. Soc. Am. **140**(3), 1581–1597.

Sepkoski, J. J. (**1974**). "Quantified coefficients of association and measurement of similarity," J. Int. Assoc. Math. Geol. **6**(2), 135–152.

Shannon, C. E. (**1948**). "A mathematical theory of communication," Bell Syst. Tech. J. **27**, 379–423.

Širović, A., Hildebrand, J. A., and Wiggins, S. M. (**2007**). "Blue and fin whale call source levels and propagation range in the Southern Ocean," J. Acoust. Soc. Am. **122**(2), 1208–1215.

Tarantola, A. (**2005**). *Inverse Problem Theory and Methods for Model Parameter Estimation* (Society for Industrial and Applied Mathematics, Philadelphia, PA).

Teanby, N. A. (**2006**). "An icosahedron-based method for even binning of globally distributed remote sensing data," Comput. Geosci. **32**, 1442–1450.

Thomas, L., and Marques, T. A. (**2012**). "Passive acoustic monitoring for estimating animal density," Acoust. Today **8**(3), 35.

Thomisch, K., Boebel, O., Clark, C., Hagen, W., Spiesecke, S., Zitterbart, D., and Van Opzeeland, I. (**2016**). "Spatio-temporal patterns in acoustic presence and distribution of Antarctic blue whales *Balaenoptera musculus* intermedia in the Weddell Sea," Endanger. Species Res. **30**, 239–253.

Urazghildiiev, I. R., and Clark, C. W. (**2013**). "Comparative analysis of localization algorithms with application to passive acoustic monitoring," J. Acoust. Soc. Am. **134**(6), 4418–4426.

Urazghildiiev, I. R., and Hannay, D. E. (**2018**). "Passive acoustic detection and estimation of the number of sources using compact arrays," J. Acoust. Soc. Am. **143**(5), 2825–2833.

Valtierra, R. D., Glynn Holt, R., Cholewiak, D., and Van Parijs, S. M. (**2013**). "Calling depths of baleen whales from single sensor data: Development of an autocorrelation method using multipath localization," J. Acoust. Soc. Am. **134**(3), 2571–2581.

Van Opzeeland, I., Samaran, F., Stafford, K. M., Findlay, K., Gedamke, J., Harris, D., and Miller, B. S. (**2014**). "Towards collective circum-Antarctic passive acoustic monitoring: The Southern Ocean hydrophone network (SOHN)," Polarforschung **83**(2), 47–61.

Van Opzeeland, I., Van Parijs, S., Kindermann, L., Burkhardt, E., and Boebel, O. (**2013**). "Calling in the cold: Pervasive acoustic presence of humpback whales (*Megaptera novaeangliae*) in Antarctic coastal waters," PLoS One **8**(9), 1–7.

Van Parijs, S., Clark, C., Sousa-Lima, R., Parks, S., Rankin, S., Risch, D., and Van Opzeeland, I. (**2009**). "Management and research applications of real-time and archival passive acoustic sensors over varying temporal and spatial scales," Mar. Ecol.: Prog. Ser. **395**, 21–36.

Wall, C. C., Simard, P., Lembke, C., and Mann, D. A. (**2013**). "Large-scale passive acoustic monitoring of fish sound production on the West Florida Shelf," Mar. Ecol.: Prog. Ser. **484**, 173–188.

Wang, D., Garcia, H., Huang, W., Tran, D. D., Jain, A. D., Yi, D. H., Gong, Z., Jech, J. M., Godø, O. R., Makris, N. C., and Ratilal, P. (**2016**). "Vast assembly of vocal marine mammals from diverse species on fish spawning ground," Nature **531**, 366–370.

Ward, J. A., Thomas, L., Jarvis, S., Dimarzio, N., Moretti, D., Marques, T. A., Dunn, C., Claridge, D., Hartvig, E., and Tyack, P. (**2012**). "Passive acoustic density estimation of sperm whales in the Tongue of the Ocean, Bahamas," Mar. Mammal Sci. **28**, 444–455.

Weirathmueller, M. J., Wilcock, W. S. D., and Soule, D. C. (**2013**). "Source levels of fin whale 20 Hz pulses measured in the Northeast Pacific Ocean," J. Acoust. Soc. Am. **133**(2), 741–749.

Correction:

The vertical and horizontal label of Figure 12d should read “Node entropy” instead of just “Entropy”, and the caption “(d) node entropy of the true and estimated SP”.

Supplementary materials to the paper

Estimating the spatial distribution of vocalizing animals from ambient sound spectra using widely spaced recorder arrays and inverse modelling

by Sebastian Menze, Daniel Zitterbart, Martin Biuw and Olaf Boebel

Corresponding author: Sebastian Menze, Institute of Marine Research, Bergen, Norway

sebastian.menze@imr.no

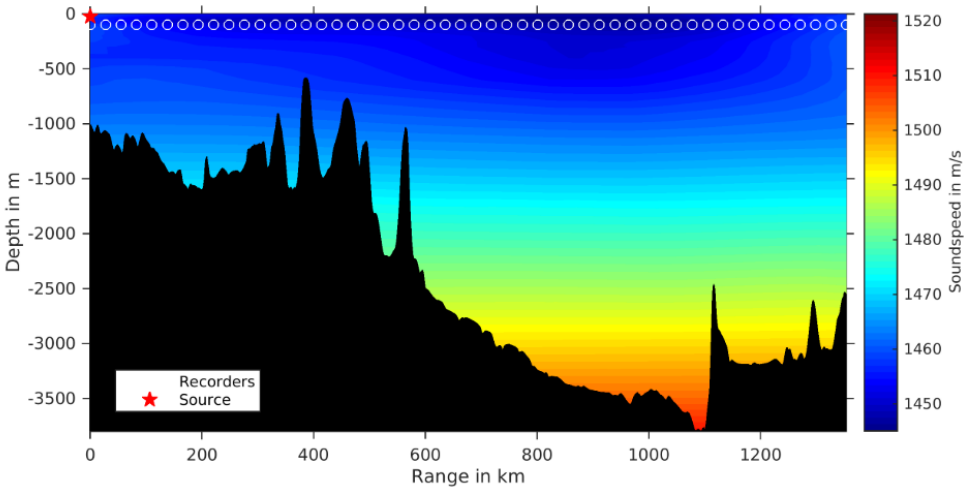

Suppl. Figure 1: Bathymetry and sound speed of section for which impulse responses were modelled. Bathymetry extracted from ETOPO-1 dataset, Sound speed from world ocean atlas mean climatology dataset. Red star represents the location of the sound source and the white circles the receiver locations.

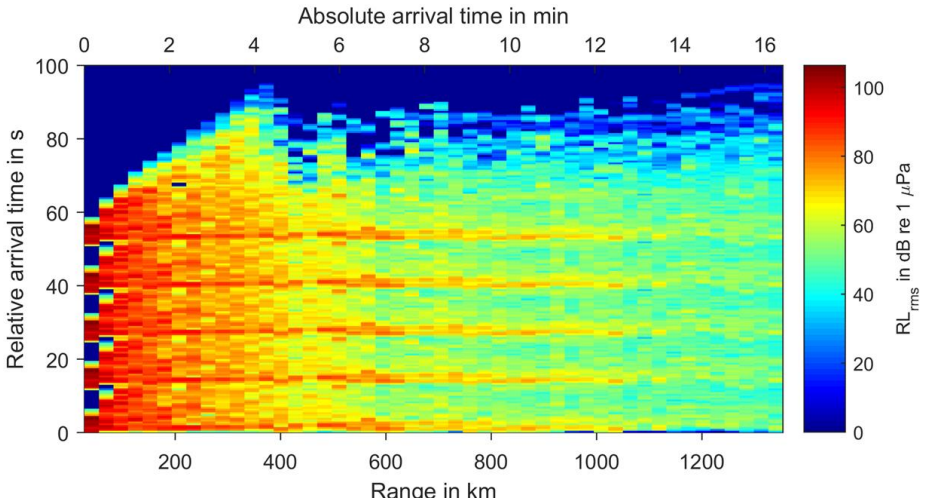

Supplementary Figure 2: Convolution of fin whale pulse train (5 pulses and 12 s intervals) with modelled impulse response from the Raytracing model BELLHOP. Horizontal axis represents range and absolute arrival time and the vertical axis the relative arrival time (the time of first arrival at each receiver subtracted from the absolute arrival time) Color represents the received level.

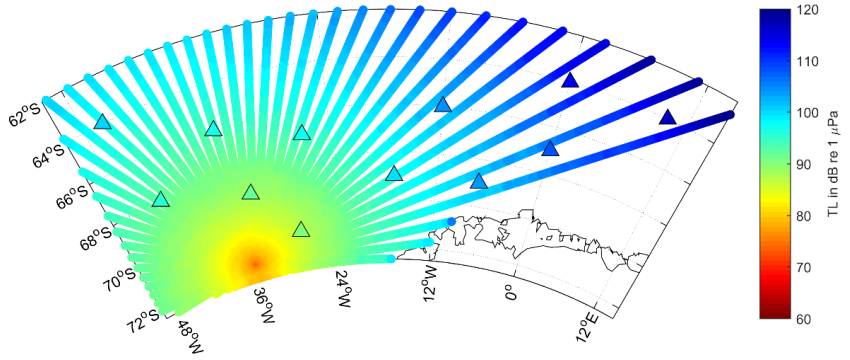

Supplementary Figure 3: Example of 2xN dimensional raytracing for calculating the TL matrix at 150 Hz. Colored slices show the TL slices calculated with Bellhop in 5° steps, and colored triangles the TL at the recorders locations, as interpolated from the TL slices.

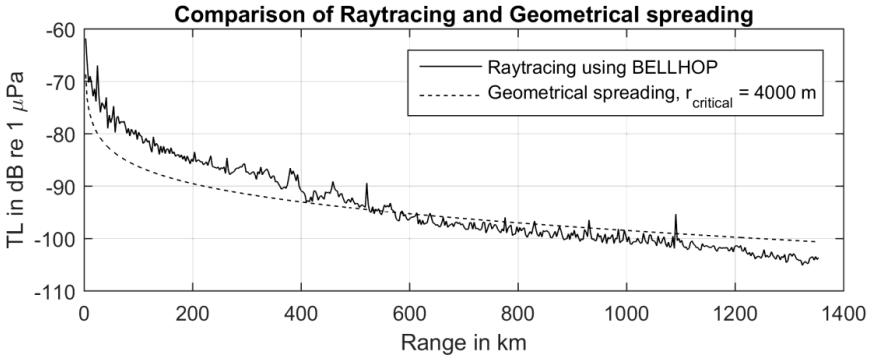

Supplementary Figure 4: Comparison of transmission loss models at 100 m depth and 150 Hz for the example transect presented in suppl. Figure 1.

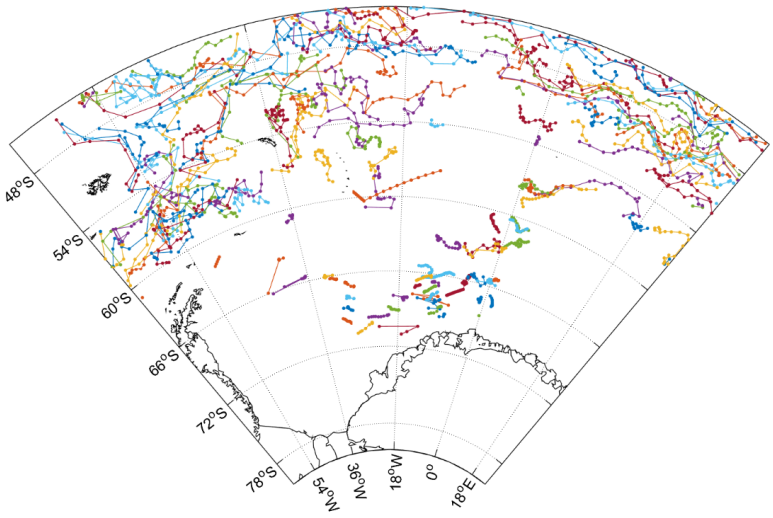

Supplementary Figure 5: Argo float tracks between the 1.1.2013 and 29.5.2013, obtained from the Coriolis Global Data Assembly Centre (http://www.argodatamgt.org/Access-to-data/Argo-data-selection). Each dot represents the location of an Argo float profile.

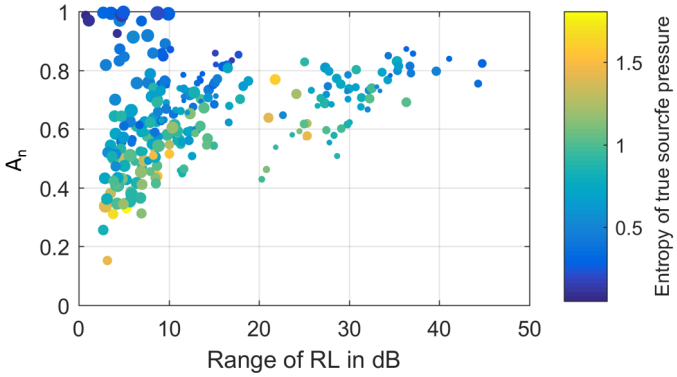

Supplementary Figure 6: Scatterplots comparing the normalized inversion accuracy (A_n within the trust zone) and the range of received levels. Marker size indicates the average distance between the true sources and recorders and color indicates the entropy of the true source distribution. Each dot represents one of the 250 random source distributions.

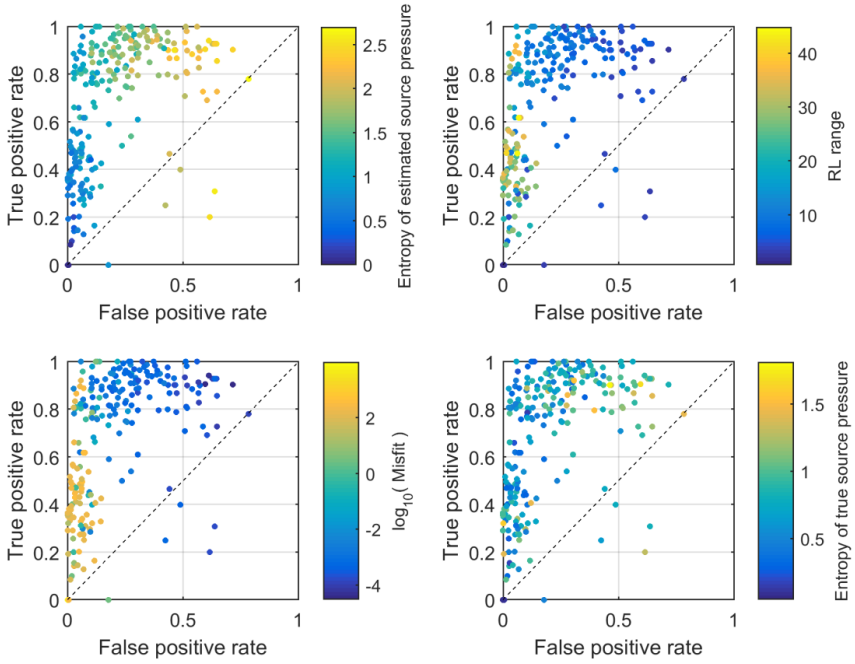

Supplementary Figure 7: Scatterplots comparing the true and false positive rate of the estimated source pressure grids (considering only source presence/absence) in relation to different metrics. Each dot represents one of the 250 random source distributions.

Graphic design: Communication Division, UiB / Print: Skipnes Kommunikasjon AS

uib.no

ISBN: 9788230840498 (print)
9788230856284 (PDF)